Molecular level insight to solvents

From understanding, via media effects, to developing a Hybrid Monte Carlo code

Dissertation
zur
Erlangung des Doktorgrades (Dr. rer. nat.)
der
Mathematisch-Naturwissenschaftlichen Fakultät
der
Rheinischen Friedrich-Wilhelms-Universität Bonn

vorgelegt von

Vahideh Alizadeh

aus
Maragheh, Iran

Bonn
2024

Angefertigt mit Genehmigung der Mathematisch-Naturwissenschaftlichen Fakultät der Rheinischen Friedrich-Wilhelms-Universität Bonn

Gutachterin/Betreuerin:	Prof. Dr. Barbara Kirchner
Gutachter:	Prof. Dr. Thomas Bredow

Tag der Promotion: 15.10.2024

Erscheinungsjahr: 2024

Me: What would you suggest and recommend to do
to be successful in life and science?

Always do the things you love.

— **Prof. Sigrid D. Peyerimhoff** —

Do what you love, not what you think you are supposed to do.

— **Prof. Daan Frenkel** —

Statement of Authorship

I, Vahideh Alizadeh, hereby declare that I am the sole author of this thesis. The ideas and work of others, whether published or unpublished, have been fully acknowledged and referenced in this thesis.

Publications

Parts of this thesis have already been published in peer-reviewed journals or are currently submitted for publication:

1. **V. Alizadeh**, F. Malberg, A. A. H. Pádua, B. Kirchner, “Are There Magic Compositions in Deep Eutectic Solvents? Effects of Composition and Water Content in Choline Chloride/Ethylene Glycol from Ab Initio Molecular Dynamics”, *J. Phys. Chem. B* **2020**, *124*, 7433–7443, DOI:10.1021/acs.jpcb.0c04844.
2. **V. Alizadeh**, D. Geller, F. Malberg, P. Sánchez, A. Padua, B. Kirchner, <updates-noreply@linkedin.com> Unsubscribe oteStrong Microheterogeneity in Novel Deep Eutectic Solvents, *ChemPhysChem* **2019**, *20*, 1786–1792, DOI:10.1002/cphc.201900307.
3. **V. Alizadeh**, L. Esser, B. Kirchner, “How is CO_2 Absorbed into a Deep Eutectic Solvent?”, *J. Chem. Phys.* **2021**, *154*, 094503, DOI:10.1063/5.0038093.
4. **V. Alizadeh**, B. Kirchner, “Molecular Level Insight into the Solvation of Cellulose in Deep Eutectic Solvents”, *J. Chem. Phys.* **2021**, *155*, 084501, DOI:10.1063/5.0058333.
5. B. Kirchner, J. Blasius, **V. Alizaeh**, A. Gansäuer, O. Hollóczki, “Chemistry Dissolved in Ionic Liquids. A Theoretical Perspective”, *J. Phys. Chem. B*, **2022**, *126 (4)*, 766–777, DOI:10.1021/acs.jpcb.1c09092.
6. **V. Alizaeh**, M. Garofalo, C. Urbach, and B. Kirchner, “A hybrid Monte Carlo study of argon solidification”*Z. Naturforsch. B*, **2024**, 79 (4), 283–291, DOI:10.1515/znb-2023-0107.

Further publications that are not part of the thesis:

7. T. Frömbgen, J. Blasius, **V. Alizadeh**, A. Chaumont, M. Brehm, B. Kirchner, “Cluster Analysis in Liquids: A Novel Tool in TRAVIS”, *J. Chem. Inf. Model.*, **2022**, *62 (22)*, 5634–5644, DOI:10.1021/acs.jcim.2c01244.
8. T. Frömbgen, J. Blasius, L. Dick, K. Drysch, **V. Alizadeh**, L. Wylie, B. Kirchner, “Reducing Uncertainties in and Analysis of Ionic Liquid Trajectories”, *Reference Module in Chemistry, Molecular Sciences and Chemical Engineering* **2023**. DOI:10.1016/B978-0-12-821978-2.00097-0.
9. W. Dong, **V. Alizadeh**, J. Blasius, L. Wylie, L. Dick, Z. Fan, B. Kirchner, “Locality in amino-acid based imidazolium ionic liquids”, *Phys. Chem. Chem. Phys.* **2023**, *25*, 24678-24685. DOI:10.1039/D3CP02671J.

Presentations and posters on conferences and workshops:

1. Poster on “Deep Eutetic solvent and water in touch: A molecular level study” at *55th Symposium on Theoretical Chemistry* in Rostock, 2019
2. Poster on “Which methodology and force field is able to describe deep eutectic solvents in a better way?” at *CECAM Workshop Beyond point charges: novel electrostatic developments in forcefields* in Lausanne, 2019
3. Contributed talk on “A molecular level look into deep eutectic solvents: Structure, interactions and microheterogeneity” at “GCC 2020 and SAMPL Satellite Workshop” online, 2020
4. Contributed talk on “Understanding deep eutectic solvents from ab initio molecular dynamics simulation” at “Workshop on Ionic Liquids” online, 2021
5. Contributed talk on “Molecular level insights to deep eutetic solvent properties and applications” at *ILMAT-VI* in Strasbourg, 2021
6. Poster on “Spectroscopy of neoteric solvents: Menthol-butanoic acid deep eutetic solvents” at *MolSim2022* in Erice, 2022
7. Contributed talk on “Ionic liquids modify radical catalysis: Ab initio molecular dynamics and metadynamics” at *CECAM workshop: 20 years of Metadynamics* in Lausanne, 2022
8. Poster and contributed talk on “Ion pairing in deep eutetic solvents” at *COIL-9* in Lyon, 2023

Abstract

With the increasing demand for resources in modern society and the impacts of climate change, there is a growing need for innovative and environmentally friendly solutions. Achieving sustainability in chemistry and materials science is crucial for enhancing human well-being and reducing energy consumption. In this context, solvents and their effects play a vital role in daily life, various chemical processes, as well as many research fields. This thesis focuses on understanding tunable classes of solvents, such as deep eutectic solvents and ionic liquids, and developing and implementing new computational techniques like Hybrid Monte Carlo. These efforts aim to advance the overarching goal of sustainability in chemistry.

Despite the growing number of studies on deep eutectic solvents and ionic liquids their working principles at the molecular level remain not fully understood. Multiscale theoretical approaches combined with suitable analysis tools are essential methods for gaining a more detailed insight into the microscopic behavior of solvents and solvent effects. Therefore, all projects were conducted from a computational chemistry perspective, employing various multiresolution and multiscale simulation methods such as classical molecular dynamics and ab initio molecular dynamics. In addition, a hybrid Monte Carlo method was developed and implemented as part of this doctoral thesis.

A perspective on the subject together with an outline of the investigated topics is provided in the introduction to this thesis with chapter 1). In chapter 2, the theoretical background is explained for the underlying concepts of ab initio molecular dynamics, density functional theory, classical molecular dynamics along with the working principles of hybrid Monte Carlo. Chapter 3, provides insights into the hydrogen bonding network's dependence on composition and water presence by ab initio molecular dynamics simulations, especially for the deep eutectic solvents mixture. This study could show that there is no strong dependency on the molecular level interactions on molar stoichiometry. This result implies the concept of the deep eutectic solvent should not be restricted by fixed proportions between the hydrogen bond acceptor and hydrogen bond donor. Based on this finding, the microheterogeneity in deep eutectic solvents and its tunability are investigated in more detail in chapter 4. The key findings reveal the impact of cation size on microheterogeneity and nanostructure in these solvents.

In the second part, solvent effects for CO_2 absorption, cellulose fiber, and titanocene catalyst are investigated in more detail. In the context of CO_2 absorption which is discussed in chapter 5, the choline chloride: ethylene glycol mixture demonstrated potential as a CO_2 absorbent. Ab initio molecular dynamics simulations uncovered the effects of anions, cations, and hydrogen bond donors on CO_2 solvation, emphasizing DESs' advantages over other liquids. Furthermore, biomass conversion reactions were explored in chapter 6 with MD simulations investigating

cellulose solvation in DESs. The study highlighted the influence of anion interactions on cellulose structure. Theoretical advancements and challenges for investigating titanocene catalysis in ionic liquids are discussed in chapter 7. This chapter underscores the importance of selecting an accurate electronic structure method for studying radical species. This highlights the complexity of theoretically handling radicals within ionic liquids through ab initio molecular dynamics simulations, necessitating further methodological advancements.

Finally, the chapter 8 intended to develop and implement a hybrid Monte Carlo method with a special focus on investigating phase transition, specifically the argon fluid solidification. Hybrid Monte Carlo method showed improved sampling compared to conventional molecular dynamics, making them a promising approach for investigating other solvents.

To summarize, this thesis provides new insights into deep eutectic solvents, ionic liquids, and their solvent effects in various applications from a theoretical perspective. Furthermore, effective simulation techniques for these solvents are developed and validated.

Contents

1. Introduction

As much as this doctoral thesis is a documentation of novel scientific insights on a class of solvents and their applications, it is also a documentation of scientific methodology. It offers instances of systematically breaking down a complex scientific issue into a sequence of smaller problems. An understanding and solutions on a long time scale are approached by a series of solutions on a shorter time scale. Although the secondary problems are often interesting in their own regard, the focus on the primary objective should be consistently maintained. Thus, each finding, understanding, and solution contribute to our progress toward elucidating the overreaching problem.

The overarching objective of this doctoral thesis is sustainability in chemistry (see section 1.1). With the increasing demand for resources in modern society and the impacts of climate change, there is a growing need for scientific and sustainable solutions to provide innovative and environmentally friendly solutions. Chemistry plays a vital role in providing sustainability for two crucial reasons. Firstly, it is essential to mitigate and reduce environmental pollution on a global scale. Simultaneously, chemistry plays a vital role in enhancing human well-being by offering diverse solutions in various domains like healthcare, nutrition, climate protection, and transportation. This includes the development of functional materials and products like medication, plastics, and electronics. Achieving the strategic goals for sustainable development in chemistry demands significant innovation in technical solutions and effective management practices, alongside robust collaboration and supportive political frameworks. Therefore, this thesis contributes to the understanding of modern solvents like ionic liquids and the novel solvent class of deep eutectic solvents (see section 1.2) and their applications such as radical catalysis, CO_2 absorption, and cellulose processing. To support this aim, this work also documents the implementation of new efficient simulation methods and techniques to reach better sampling in molecular simulations (see section 1.3).

1.1. Sustainability in chemistry

In 1987 the United Nations Brundtland Commission defined sustainability as "meeting the need for the present without compromising the ability of future generations to meet their own needs."[10] Since then, the United Nations has placed sustainable development at the forefront of their global objectives, with social equity, economic development, and environmental protection as fundamental pillars to this goal. Later in 2015, the 17 sustainable development goals (SDGs), also known as the global goals„ also known as the global goals, were announced by the United Nations as a universal call to action to end poverty, protect the planet, and ensure that by 2030 all people enjoy peace and prosperity. The 17 SDGs for 2030 aim to end poverty and hunger and bring gender equality, while also considering climate change and preserving forests and oceans.[11] The pillars of sustainability and 17 SDGs are important because they offer a framework to address sustainability challenges. The role of chemistry is to foster the industrial development of societies while adhering to the pillars of sustainability. This entails addressing specific challenges such as identifying or designing materials tailored to particular needs and applications. These materials need to be environmentally friendly, cost-efficient, and readily available or easily synthesizable (zero waste). Therefore, as a practical framework for sustainability in chemistry, chemists and material scientists may refer to the twelve principles of green chemistry.[12]

The twelve principles of green chemistry were introduced by Paul Anastas and John Warner in 1998 as a practical framework for making a greener chemical, process, or product.[13] For instance, the fifth principle entails the development and usage of safer solvents and auxiliaries, which highlights the importance of solvents in chemical process.[12] Solvents play crucial roles in mass and energy transfer, affecting reaction efficiency and overall process sustainability through its environmental impact and safety concerns. Efforts to develop new solvents should focus on optimizing their selection based on chemical suitability, reduced energy requirements, minimal toxicity, and environmental and safety considerations.

In the upcoming sections, the substances investigated and methods used in this thesis will be introduced. Also, the connection of this thesis with sustainability pillars and green chemistry principles will be elaborated on. Additionally, the role of molecular simulation in addressing green chemistry and sustainability challenges will be explored.

1.2. Substances

This thesis primarily focuses on studying the physicochemical properties of solvents and solvents effects on applications such as CO_2 absorption, cellulose processing, and catalysis. The three classes of solvents investigated are deep eutectic solvents (DESs), ionic liquids (ILs), and a Lennard-Jones (LJ) system (argon fluid). The need to understand solvents and their effects at the molecular level drives each project discussed in chapter 3 through chapter 8.

Ionic liquids (section 1.2.2) are solvents entirely composed of mobile ions. DESs (section 1.2.1) are mixtures of two or more substances which in combination form a liquid at much lower temperatures than the primary substances' melting points. For instance, a 1:2 molar ratio mixture of choline chloride ([Ch]Cl) and urea forms a DES with a melting point of 285 K, whereas the melting points of [Ch]Cl and urea are 575 K (decomposition point) and 406 K, respectively.[14]

To study the aforementioned substances, we applied multiscale computational methods ranging from ab initio to classical molecular dynamics. There are numerous strong arguments for investigating chemical systems using computer simulation techniques. Simulations eliminate the need for chemicals and costly, complex, and hazardous experimental setups, making computational chemistry a safer, more sustainable, and resource-efficient field. However, this approach requires access to high-performance computation facilities and efficient software and algorithms.

In this regard, we aimed to develop and implement the hybrid Monte Carlo method as an enhanced sampling technique. To obtain reliable results and predictions for complex systems and phenomena, it is essential to calibrate our models using well-known systems. Although the argon fluid and LJ potential are well-studied topics, they still attract significant research interest.[15–18] This approach allowed us to create a reliable framework for studying phase transitions before applying it to more complex systems like DESs and ILs. Understanding phase diagrams and the mechanisms of phase transitions is crucial in the field of DESs. This systematic and logical connection between all the projects and substances highlights the cohesive nature of this thesis.

1.2.1. Deep eutectic solvents

DESs were first introduced by Abbott and coworkers in 2003[14] and since then they have rapidly gained attention in various applications and fields such as separations,[19] gas capture,[20–23] battery technologies,[24,25] biocatalysis,[26,27] biomass processing,[28–30] and nanomaterial synthesis.[31–34] DESs can be designed, tailored, and customized for specific needs and applications, while also being economically and environmentally friendly.[35]

DESs are usually known as a mixture of two or more substances that is liquid at a much lower temperature than the melting points of either primary substance.[35] However, this general definition does not distinguish DESs from other classes of solvents by any specific characteristics, because eutectic phase behavior occurs in any mixture that is partially miscible in the liquid phase and immiscible in the solid phase, regardless of the chemical nature of the components.[36] Defining a mixture as a deep eutectic solvent is not straightforward, and current definitions need to be extended to address the nature of DESs more rigorously. Nevertheless, mixtures that exhibit significant melting point depressions (deep), allowing them to remain liquid over a wide range of temperatures and compositions, are known as deep eutectic solvents.[35,37]

Which solvent is a DES? Is the eutectic point deep enough to be considered a DES? Are there magic compositions in deep eutectic solvents? These and many other questions regarding the characterization of DESs were frequently asked upon their introduction in the literature. Given that DESs are inherently mixtures, they are best described using a thermodynamic framework for mixtures. The significant depression of the eutectic point temperature in a true DES, compared to an ideal mixture of its constituents, indicates that DESs are markedly non-ideal mixtures in thermodynamic terms. Several groups have previously employed mixture thermodynamics to quantify the non-ideality of DESs using various approaches. Martins et al.[37] proposed to define DESs based on the solid-liquid equilibrium phase diagram. Thus, the quantification of the eutectic point could be based on the difference between the actual eutectic temperature and a generally accepted reference temperature. To derive this reference temperature they suggested to use the classical thermodynamic equation given as

$$\ln x_i \gamma_i = -\frac{\Delta_{\mathrm{fus}} H_{m,i}}{R}\left(\frac{1}{T} - \frac{1}{T_i^*}\right) \tag{1.1}$$

where x_i is the mole fraction and γ_i the activity coefficient of compound i in the liquid mixture, T_i^* is the melting point, and $\Delta_{\mathrm{fus}} H_{m,i}$ is the enthalpy of fusion of the pure compound i, and T is the liquid temperature. The eutectic point ($x_\mathrm{e}, T_\mathrm{e}$) is at the intersection of the two liquids phase boundaries. Another approach to quantify DESs was used by López-Porfiri et al. measuring molar excess enthalpy values for four proposed DES systems at different compositions using calorimetry.[38] Kollau and coworkers described DES non-ideality using an effective interaction parameter derived from regular solution theory and examined different entropy of mixing models for DESs.[39] Recently, van den Bruinhorst and Costa Gomes introduced a closely-related metric D_e, which is a normalized version of the eutectic temperature depression. This dimensionless D_e metric represents the percent change in the eutectic temperature of a non-ideal mixture relative to its ideal eutectic temperature.[40] These efforts underscore the importance of measuring or predicting the solid–liquid phase diagram for mixtures, whether through experimental methods or computational techniques. Despite significant progress from various perspectives, especially from a thermodynamic viewpoint, the literature still lacks a rigorous definition that is widely accepted across the field.[41,42]

The various DESs studied thus far fall into five categories.[35,43] Type I combines a quaternary ammonium salt and a metal chloride, Type II includes a quaternary ammonium salt and a metal chloride hydrate, Type III consists of a quaternary ammonium salt and a hydrogen bond donor (typically an organic molecular component such as an amide, carboxylic acid, or polyol), Type IV comprises a metal chloride hydrate and hydrogen bond donor, and Type V is composed of only nonionic, molecular hydrogen bond acceptors and hydrogen bond donors. Given that most research has focused on the properties and applications of mixtures of quaternary ammonium salts and hydrogen bond donors, we primarily concentrate on “Type III” DESs. With a rough estimate, there could be around $10^6 - 10^8$ possible binary combinations for DES III which allows for customization using inexpensive, low-toxicity, and biodegradable components. However, optimizing DES mixtures for specific applications can be overwhelming with a trial-and-error approach, underscoring the need for systematic studies to develop predictive models. In this regard, many researchers focused on the interactions between DES components because the diversity and strength of intermolecular interactions form the foundation of the solvent properties and applications.[35,44] My research also investigates their working principles at the molecular level, including hydrogen bonding and the network’s dependence on composition and water presence, as discussed in chapter 3. Additionally, chapter 4 delves into the microheterogeneity in deep eutectic solvents. Furthermore, the solvent effects of DESs on CO_2 absorption and cellulose fiber are examined in chapter 5 and chapter 6, respectively.

1.2.2. Ionic liquids

Ionic liquids (ILs) are substances composed entirely of mobile ions and typically remain liquid at moderate temperatures, usually with a melting point below 100°C.[45] ILs have emerged as a more environmentally friendly option compared to traditional organic solvents due to their low volatility and flammability.[45] However, there are comprehensive discussions about the ILs toxicity.[46] These solvents possess unique characteristics that have led to their use in broad and various applications in many fields such as pharmaceutics,[47,48] energy storage,[49] biomass,[46,50] gas absorptions,[51,52] and catalytic applications.[53]. The tunability of ILs, achieved by selecting the constituent ions appropriately, allows for customization of their properties to fit a specific application. One of the primary applications of ILs is as solvents.

In this thesis, we examine the use of ILs as solvents for catalytic reactions, especially their ability to stabilize radical intermediates in reactions. In particular, the focus will be on titanocene complexes, since titanium is a readily accessible and environmentally friendly metal, which makes it an attractive candidate in designing organometallic catalysts.[54] Titanocene catalysts are reagents widely used in radical and organometallic chemistry.[54–56] They are highly attractive due to their high chemoselectivity and are ideal reagents for sustainable processes and green chemistry that require mild conditions. They provide tremendous opportunities for catalytic C–C and C–O bond formation reactions. In addition, titanocene-catalyzed radical reactions have also developed as highly sustainable reactions since the oxidative additions and reductive eliminations can happen in single electron steps since titanium is easily accessible in oxidation state from III to IV. Since the titanocene(IV) complexes are more strongly solvated than their titanocene(III) counterparts, solvent effects can be assumed to be substantial. Reactions with cationic titanocene(III) complexes are particularly sensitive to solvent effects.[57] Solvent coordination to titanocene can thus affect the overall rate of electron transfer to substances.[57,58] Therefore, choosing an appropriate solvent is an efficient way to modulate catalyst reactivity and stability. Here, specifically designed ILs can be an optimal solvent for accelerating the titanocene radical catalysis.

A key challenge for designing ILs, however, is the possible number of cation and anion combinations, which puts them into a similar range of candidates as DESs. Furthermore, the impact of ILs as a solvent on the reaction mechanism remains an unaddressed question, where computational simulations can bring necessary insights. The computational challenges of simulating ILs especially for radical catalysis are discussed in detail in chapter 7.

1.2.3. Lennard-Jones systems and Argon fluids

An LJ interaction model can adequately describe most nonpolar solvents, which assumes nearly spherical symmetry of the solvent molecules and interactions limited to dispersion and repulsion.[59] Within these constraints, LJ models can provide a wide range of insights into solvent structures, dynamics, and thermodynamics. Argon fluids and LJ systems are extensively studied in research due to their simplicity and the monoatomic nature of noble gases, which make them ideal for tests and benchmarks. Argon simulations are relevant across a wide range of physical contexts.

Despite their utility, several challenges persist in these simulations, primarily in formulating accurate potentials and specifying simulation details and conditions. The accuracy of molecular simulations heavily depends on the quality of the force field and intermolecular potentials used. Advanced studies have highlighted the importance of three-body interactions. In conclusion, argon and Lennard-Jones simulations remain foundational in computational research due to their simplicity and the fundamental insights they provide.

1.3. Hybrid Monte Carlo (HMC)

The simulation of rare events poses particular challenges for computational chemistry. While molecular dynamics and Monte Carlo methods are powerful tools for simulating the potential energy surface, they require long timescales or huge sample sizes to cover rare events like crossing reaction barriers or phase transitions. For molecular dynamics several schemes to overcome these limitations have been proposed, such as local elevation,[60] four-dimensional molecular dynamics,[61] metadynamics,[62,63] multiple time-scale molecular dynamics,[64,65] transition path sampling,[66,67] and advanced Monte Carlo and sampling algorithms.[68,69]

In this context, the Hybrid Monte Carlo (HMC) method has demonstrated significant promise in condensed matter simulations.[70,71] Currently there are two distinct approaches for HMC, either by implementation into molecular dynamics packages like LAMMPS,[72] GROMACS,[73] and NAMD,[74] or developed as separate Monte Carlo module such as TriMem,[75] a special implementation for modeling lipid membranes. While these implementations are valuable, they do not fully exploit the potential of HMC algorithms, as they are limited by the flexibility of the molecular dynamics package. Furthermore, there is a recognized need for HMC implementations optimized for GPU machines. To address relevant chemical applications, more examples of implementations, applications, and case studies are essential. Thus, as part of this thesis, chapter 8 aims to take initial steps toward this goal by developing a GPU-accelerated HMC package and testing it for rare events like phase transitions with argon solidification serving as a case study.

2. Theoretical Background

2.1. Molecular simulations

Molecular simulations can be concisely described as computational statistical mechanics, i.e., numerical methods combined with computer power to address physicochemical problems arising in condensed matter systems.[76–78] Statistical mechanics is the branch of physics that studies macroscopic systems from a microscopic or molecular point of view and provides the theoretical framework for understanding the behavior of molecular systems in molecular simulations. Statistical properties of large ensembles of particles are governed by the laws of classical or quantum mechanics. In the context of molecular simulations, statistical mechanics allows us to relate the macroscopic properties of a system to the microscopic interactions between its constituent molecules providing enormous potential for both explaining and predicting properties of molecules and materials on an atomic scale.

To providing a better explanation, of molecular simulation in chemistry, the potential energy surface (PES) is defined as a central concept in computational chemistry.[79] A PES is a mathematical function describing the energy of a molecule as a function of its geometry. To model the PES and its dynamics the Hamiltonian formed as follows can be used

$$\hat{H} = \hat{K} + \hat{V} \tag{2.1}$$

where $\hat{V}$ is the potential energy describing the form and shape of the PES and $\hat{K}$ is the kinetic energy described the dynamics on the PES.

There is a hierarchy of computational methods to model the PES which are arranged in different levels of accuracy, efficiency, and computational cost across a wide range of length and time scales. For instance, quantum mechanics provides energy functions based on the electronic structure, which are exact in principle and applicable for any molecule. However, in practice, approximate quantum mechanical methods are used for their more feasible computational cost. Another type of energy functions is provided by classical molecular mechancis based on the geometry of the molecule parameterized in stretches, bends, torsions, etc. Any approximate model however can have limitations in the systems it can describe well, e.g. bond breaking or formation is not well described in most classical molecular mechanics. Furthermore, the availability of suitable parameters for the chemical system is crucial for the application of any approximate energy model.

In this chapter, the focus is going to be on the ab initio molecular dynamics (AIMD), classical molecular dynamics (MD), and hybrid Monte Carlo method (HMC). The AIMD theory is introduced initially, starting from Schrödinger's time-dependent wave equation (section 2.2). Following this, classical MD and force field methods are discussed (section 2.3). Finally in section 2.4 HMC is discussed.

2.2. Ab initio molecular simulations

The basic idea in AIMD methods is to compute the forces acting on the nuclei from the electronic structure "on-the-fly" as the molecular dynamics trajectory is generated. In this way, the electronic variables are considered active degrees of freedom in each molecular dynamics step. This implies that the approximation in a molecular simulation is shifted from the level of selecting the model potential to the level of selecting a particular approximation for solving Schrödinger's equation. Furthermore, this implies that AIMD methods allow "chemically complex" systems to be treated implicitly in an unbiased manner with a suitable approximate solution to the many-electron problem. A chemically complex system refers to systems characterized by either (i) a wide variety of atom or molecule types resulting in numerous interatomic interactions requiring parameterization, or (ii) a system under study with significant changes in electronic structure with bond-breaking and bond-forming during simulation. AIMD theory can be derived from either classical approaches or quantum mechanics.[80–83] This section aims to drive the classical molecular dynamics starting from Schrödinger's time-dependent wave equation.

$$i\hbar\frac{\partial}{\partial t}\Phi(\{\mathbf{r}_i\},\{\mathbf{R}_I\};t) = \hat{\mathcal{H}}\Phi(\{\mathbf{r}_i\},\{\mathbf{R}_I\};t) \tag{2.2}$$

which $\Phi(\{\mathbf{r}_i\},\{\mathbf{R}_I\};t)$ is the total wavefunction that depends on time and on both electronic coordinates ($\{\mathbf{r}_i\}$) and nuclear coordinates ($\{\mathbf{R}_I\}$). The full Hamiltonian to describe a system can be written as follows

$$\begin{aligned}
\hat{\mathcal{H}} &= \underbrace{-\sum_I \frac{\hbar^2}{2M_I}\nabla_I^2 - \sum_i \frac{\hbar^2}{2m_e}\nabla_i^2}_{\text{kinetic energy}} \underbrace{+\sum_{I<J}\frac{e^2 Z_I Z_J}{\mid R_I - R_J \mid} + \sum_{i<j}\frac{e^2}{\mid r_i - r_j \mid} - \sum_{i,I}\frac{e^2 Z_I}{\mid R_I - r_i \mid}}_{\text{potential energy}} \\
&= -\sum_I \frac{\hbar^2}{2M_I}\nabla_I^2 - \sum_i \frac{\hbar^2}{2m_e}\nabla_i^2 + V(\{\mathbf{r}_i\},\{\mathbf{R}_I\}) \\
&= -\sum_I \frac{\hbar^2}{2M_I}\nabla_I^2 + \hat{\mathcal{H}}_e(\{\mathbf{r}_i\},\{\mathbf{R}_I\}) \qquad (2.3)
\end{aligned}$$

here the total Hamiltonian is written as a summation of kinetic energy and potential energy of nuclear and electrons. In the potential energy term of the Hamiltonian only the electron–electron, electron–nuclear, and nuclear–nuclear coulomb interactions are taken into account which depends on the relative distance of each particle. The first step to solve Schrödinger's time-dependent wave equation (eq. (2.2)) is to separate nuclear and electronic contribution to the total wavefunction by applying a simple product ansatz (see eq. (2.4)). An ansatz is an approach in physics and mathematics for solving equations, especially differential equations.[84] It involves making an educated guess or an additional assumption to assist in problem-solving, which is subsequently validated by its outcomes. In eq. (2.4) the total wavefunction is separated into the nuclear wavefunction $\chi(\{\mathbf{R}_I\};t)$ and electronic wavefunction $\Psi(\{\mathbf{r}_i\};t)$, each of which is separately normalized at every instant of time, i.e. $\langle\chi;t \mid \chi;t\rangle = 1$ and $\langle\Psi;t \mid \Psi;t\rangle = 1$.

$$\Phi(\{\mathbf{r}_i\},\{\mathbf{R}_I\};t) \approx \Psi(\{\mathbf{r}_i\};t)\chi(\{\mathbf{R}_I\};t) = \Psi\ \chi \tag{2.4}$$

Please note that in the following electronic and nuclear coordinates are omitted, Ψ and χ represent the electronic and nuclear wavefunctions, respectively, for simplicity and brevity in deriving the AIMD. Then Schrödinger's time-dependent wave equation can be written as

$$i\hbar\frac{\partial}{\partial t}\Psi\chi = \left[-\sum_I \frac{\hbar^2}{2M_I}\nabla_I^2 - \sum_i \frac{\hbar^2}{2m_e}\nabla_i^2 + V(\{\mathbf{r}_i\},\{\mathbf{R}_I\})\right]\Psi\chi \tag{2.5}$$

The following relations for χ and Ψ yield after multiplying eq. (2.5) from the left by $\langle\Psi \mid$ and $\langle\chi \mid$ and imposing energy conservation $\frac{d\langle\mathcal{H}\rangle}{dt} = 0$.

$$i\hbar\frac{\partial\Psi}{\partial t} = -\sum \frac{\hbar^2}{2m_e}\nabla_i^2\Psi + \left\{\int dR\ \chi^\star\left(-\sum \frac{\hbar^2}{2M_I}\nabla_I^2 + V(\{\mathbf{r}_i\},\{\mathbf{R}_I\})\right)\chi\right\}\Psi \tag{2.6}$$

$$i\hbar\frac{\partial\chi}{\partial t} = -\sum \frac{\hbar^2}{2M_I}\nabla_I^2\chi + \left\{\int dr\ \Psi^\star\mathcal{H}_e(\{\mathbf{r}_i\},\{\mathbf{R}_I\})\Psi\right\}\chi \tag{2.7}$$

Thus, both electrons and nuclei move quantum mechanically within time-dependent effective potentials derived from averages over the other set of degrees of freedom. Therefore, the product ansatz (eq. (2.4)) provides a mean-field representation of the coupled nuclear-electronic quantum dynamics, resulting in a straightforward separation of electronic and nuclear variables. This set of equations was first introduced by Dirac in 1930 and is known as the foundation of the time-dependent self-consistent field (TDSCF) method.[85] The subsequent stage in classical molecular dynamics derivation involves approximating the nuclei as classical point particles. A well-known route to extract classical mechanics from quantum mechanics[86] in general starts with rewriting the corresponding wavefunction

$$\chi(\{\mathbf{R}_I\};t) = A(\{\mathbf{R}_I\};t)\ \exp\left[iS(\{\mathbf{R}_I\};t)/\hbar\right] \tag{2.8}$$
$$\chi = A\ \exp\left[iS/\hbar\right]$$

in terms of an amplitude factor $A(\{\mathbf{R}_I\};t)$ (simplified as A) and a phase $S(\{\mathbf{R}_I\};t)$ (simplified as S) which are both considered to be real. After transforming the nuclear wave function in eq. (2.7) accordingly and after separating the real and imaginary parts, the TDSCF equation for the nuclei is re-expressed in terms of the new variables A and S.

$$\frac{\partial S}{\partial t} + \sum_I \frac{1}{2M_I}(\nabla_I S)^2 + \int dr\Psi^\star\mathcal{H}_e\Psi = \hbar^2\sum_I \frac{1}{2M_I}\frac{\nabla_I^2 A}{A} \tag{2.9}$$

$$\frac{\partial A}{\partial t} + \sum_I \frac{1}{M_I}(\nabla_I A)(\nabla_I S) + \sum_I \frac{1}{2M_I}A(\nabla_I^2 S) = 0 \tag{2.10}$$

This set of equations for solving the time-dependent Schrödinger equation is known as the quantum fluid dynamical representation.[87,88] Using the identity for the nuclear density $|\chi|^2 \equiv A^2$ eq. (2.10) can be reformulated as a continuity equation, reflecting the conservation of particle probability in the presence of a flux.

Note, the relation for S (eq. (2.9)) depends on $\hbar$ and this contribution in the classical limit $\hbar \to 0$ in the χ is

$$\frac{\partial S}{\partial t} + \sum_I \frac{1}{2M_I}(\nabla_I S)^2 + \int dr \Psi^\star \mathcal{H}_e \Psi = 0 \tag{2.11}$$

The resulting equation has a similar form of equations of the motion in the Hamiltonian–Jacobi formulation[89,90] given as

$$\frac{\partial S}{\partial t} + \mathcal{H}(\{\mathbf{R}_I\}, \{\nabla_I S\}) = 0 \tag{2.12}$$

As mentioned earlier, a Hamiltonian can be written as the sum of the kinetic and potential parts. Considering the general classical Hamiltonian function as follows, where $\{\mathbf{R}_I\}$ and $\{\mathbf{P}_I\}$ represent (generalized) coordinates and their conjugate momenta, respectively.

$$H(\{\mathbf{R}_I\}, \{\mathbf{P}_I\}) = T(\{\mathbf{P}_I\}) + U(\{\mathbf{R}_I\}) \tag{2.13}$$

With comparing the Hamiltonians in the eq. (2.12) and eq. (2.13)

$$\mathbf{P}_I \equiv \nabla_I S \tag{2.14}$$

the Newtonian equation of motion $\mathbf{P}_I = -\nabla U(\{\mathbf{R}_I\})$ of the classical nuclei corresponding to eq. (2.11) are

$$\frac{d\mathbf{P}_I}{dt} = -\nabla_I \int d\mathbf{r} \Psi^\star \mathcal{H}_e \Psi \tag{2.15}$$

or alternatively can be written as

$$M_I \ddot{\mathbf{R}}_I(t) = -\nabla_I \int d\mathbf{r} \Psi^\star \mathcal{H}_e \Psi = -\nabla_I V_e^E(\{\mathbf{R}_I(t)\}) \tag{2.16}$$

Thus, the nuclei move according to classical mechanics in an effective potential V_e^E due to the electrons. The effective potential V_e^E often called the Ehrenfest potential. This potential is a function of only the nuclear positions at time t as a result of averaging $\mathcal{H}_e$ over the electronic degree of freedom. In other words, computing the quantum expectation value of $\int d\mathbf{r} \Psi^\star \mathcal{H}_e \Psi$, while the nuclear positions are kept fixed at their instance values $\{\mathbf{R}_I(t)\}$. Please note, the nuclear wavefunction still occurs in the TDSCF equation for the electronic degree of freedom eq. (2.6). This nuclear wavefunction has to be replaced by the nuclei positions in the classical limits for consistency. Thus, the classical limits lead to a time-dependent wave equation for the electrons

$$\begin{aligned} i\hbar \frac{\partial \Psi}{\partial t} &= -\sum_i \frac{\hbar^2}{2m_e} \nabla_i^2 \Psi + V_{ne}(\{\mathbf{r}_i\}, \{\mathbf{R}_I(t)\}) \Psi \\ &= \mathcal{H}_e(\{\mathbf{r}_i\}, \{\mathbf{R}_I(t)\})\ \Psi \end{aligned} \tag{2.17}$$

which is solved self-consistently in the presence of the classically propagated nuclei (eq. (2.16)). In the eq. (2.17) the classical and quantum degree of freedom is incorporated since the $\mathcal{H}_e$ and Ψ depend parametrically on the classical nuclear positions $\{R_I(t)\}$ at time t through $V_{ne}(\{r_i\}, \{R_I(t)\})$. The method of solving eq. (2.16) together with eq. (2.17) is termed “Ehrenfest molecular dynamics” in honor of Ehrenfest who pioneered the derivation of Newtonian classical dynamics from Schrödinger’s wave equations. In Ehrenfest molecular dynamics, it is important to note that the interaction between classical and quantum degrees of freedom is incorporated bidirectionally, albeit in a mean-field manner. The Hamiltonian that governs the quantum particles varies with time due to its dependence on the positions of the classical particles in motion. Conversely, the movement of the classical particles is determined by the gradient of the expected value of the quantum mechanical Hamiltonian. Ehrenfest AIMD is a nonadiabatic method and is particularly suitable for studying nonadiabatic processes such as photochemistry and dynamics near conical intersections.[91] There is no restriction for staying on a PES and multiple electronic states can be evolved. Ehrenfest molecular dynamics also has its limitations. It is computationally demanding, requiring substantial computational resources and time. Moreover, it is an accurate method in many applications, it often struggles to fulfill detailed balance requirements effectively.[92]

In addition to Ehrenfest molecular dynamics, there are other methods categorized as ab initio molecular dynamics that aim to include electronic structure into molecular dynamics simulations such as Car–Parrinello molecular dynamics and Born–Oppenheimer ab initio molecular dynamics (BO-AIMD). In the following section, BO-AIMD is elaborated upon as it is the specific AIMD method utilized in the research reported in this thesis.

2.2.1. Born-Oppenheimer ab initio molecular dynamics

In BO ansatz eq. (2.18) the wavefunctions of nuclei and electrons can be treated separately, based on the fact that the electrons are much lighter and faster than the nuclei.[93]

$$\Phi_{BO}(\{\mathbf{r}_i\}, \{\mathbf{R}_I\}; t) = \sum_{k=0}^{\infty} \tilde{\Psi}_k(\{\mathbf{r}_i\}, \{\mathbf{R}_I\})\tilde{\chi}_k(\{\mathbf{R}_I\}; t) \tag{2.18}$$

where the electronic wavefunction $\tilde{\Psi}_k(\{\mathbf{r}_i\}, \{\mathbf{R}_I\})$ is considered time-independent and the nuclear wavefunction $\tilde{\chi}_k(\{\mathbf{R}_I\}; t)$ is propagated. To solve the electronic wavefunction, the nuclei are considered fixed and are only interacting with the average potential of the electronic cloud. The nuclear wavefunction is obtained by propagating the nuclear positions based on the relaxed (averaged) electron distribution. With this, the BO approximation effectively separates the electronic and nuclear motion. The resulting total energy of the electrons will depend on the nuclear configuration; this electronic energy, together with the energy of the mutual repulsion of the nuclei, determines the PES governing the motion of the nuclei. Therefore, BO-AIMD includes the electronic structure in molecular dynamics simulations by straightforwardly solving the static electronic structure problem in each molecular dynamics step given the set of fixed nuclear positions at that instance of time. The time-dependence of the electronic structure is a consequence of nuclear motion, and not intrinsic as in Ehrenfest molecular dynamics, making

BO-AIMD a good choice and computationally efficient for adiabatic processes in which the electronic state remains on a single PES, like the ground state.

In BO-AIMD simulations, various levels of theories could be utilized to describe the electronic structure, such as Hartree-Fock methods,[94,95] density functional theory (DFT),[96] and semi-empirical methods[97–99]. Considering both accuracy and computational cost, in this thesis DFT is applied as the level of theory, which will be briefly explained in the following section.

2.2.2. Density functional theory (DFT)

The time-independent Schrödinger equation is the foundation of the electronic structure methods. It is given by the following eigenvalue equation

$$\hat{\mathcal{H}} \mid \Psi\rangle = E \mid \Psi\rangle \tag{2.19}$$

where E is the energy of the system and Ψ is the total wave function. The electronic Hamiltonian with considering the BO approximation eq. (2.18) is given as

$$\begin{aligned} \hat{\mathcal{H}}_e &= \hat{T}_e + \hat{V}_{ee} + \hat{V}_{ext} \\ &= \underbrace{-\frac{1}{2}\sum_{i}^{N}\nabla_i^2}_{\text{electron kinetic energy}} \underbrace{+\sum_{i=1}^{N}\sum_{j=i+1}^{N}\frac{1}{\mid r_i - r_j \mid} - \sum_{i=1}^{N}\sum_{I}\frac{Z_I}{\mid r_i - R_I \mid}}_{\text{potential energy}} \end{aligned} \tag{2.20}$$

Please note that in this context (eq. (2.20)), $\hat{V}_{\text{ext}}$ refers to nuclear–electron potential, and the atomic units are applied in this section for simplicity in representing equations. Thus, the constants $\hbar$ and e are set equal one. For solving the time-independent Schrödinger equation, Kohn–Sham density functional theory (KSDFT; in the following simplified as DFT) relies on a functional that maps the density of the ground state to the external potential $\hat{V}_{ext}$. It describes the interaction between electrons using an observable in three-dimensional space, the electron density ρ. To obtain the wavefunction (Ψ) which yields the ground state electron density ρ, the non-interacting system ($\hat{V}_{ee} = 0$) is solved by minimizing the kinetic energy

$$T_s[\rho] = min_{\Psi\rightarrow\rho}\langle\Psi \mid \hat{T} \mid \Psi\rangle \tag{2.21}$$

where T_s is the kinetic energy of the KS system. Since $\hat{T}$ is an one-electron operator the resulting Kohn–Sham (KS) wavefunction can be expressed as Slater determinant

$$\Psi = \Phi(1,2,\cdots,N) = \frac{1}{\sqrt{N!}}\begin{vmatrix} \psi_1(1) & \psi_2(1) & \cdots & \psi_N(1) \\ \psi_1(2) & \psi_2(2) & \cdots & \psi_N(2) \\ \vdots & \vdots & \ddots & \vdots \\ \psi_1(N) & \psi_2(N) & \cdots & \psi_N(N) \end{vmatrix} \tag{2.22}$$

where $\Phi(1,2,\cdots,N)$ is Slater determinant of N number of electrons and $\psi_i(j)$ is ith molecular orbitals describing electron j. Slater determinants ensure proper antisymmetrization of the wavefunction upon exchange of the electrons ($\Phi(1, 2, \cdots, N) = -\Phi(2, 1, \cdots, N)$). The density ρ of the system is obtained from the molecular orbitals given as

$$\rho = \sum_{i}^{N} n_i \mid \psi_i \mid^2 \tag{2.23}$$

where n_i is the occupation number of the ith molecular orbital. The DFT ground state energy can be expressed as a functional of the electron density by

$$E[\rho] = T_s[\rho] + U_H[\rho] + E_{xc}[\rho] + V_{ext}[\rho] \tag{2.24}$$

where U_H is the Hartree energy (or also called Coulomb energy), E_{xc} is the exchange-correlation energy and V_{ext} is the external potential energy. The exchange-correlation energy describes the energy difference between the non-interacting KS system and the fully interacting system as

$$E_{xc}[\rho] = \underbrace{\langle \hat{T} \rangle - T_s[\rho]}_{c} + \underbrace{\langle \hat{V}_{ee} \rangle - U_H[\rho]}_{c/x} \tag{2.25}$$

The $\langle \hat{T} \rangle$ and $T_s[\rho]$ terms represent the true kinetic energy and approximated kinetic energy, respectively. Similarly, $\langle \hat{V}_{ee} \rangle$ and $U_H[\rho]$ stand for the true electron-electron interaction and Hartree energy. The exchange terms (x) include the constraint on the states of indistinguishable particles within the potential terms of eq. (2.25). The correlation (c) energy is a measure of how much the presence of all other electrons influences the movement of one electron. Correlation terms involve both kinetic and potential correlations. The real expression for the E_{xc} is computationally expensive, and thus approximated expressions are used in DFT methods to make them computationally feasible. The crucial difference of DFT methods lies in the treatment of the exchange-correlation E_{xc} term in eq. (2.24). The approximate exchange-correlation functional can also be written as follows:

$$\begin{aligned} Exc[\rho] &= E_x[\rho] + E_c[\rho] \\ &= E_x^{SL}[\rho] + E_x^{NL}[\rho] + E_c^{SL}[\rho] + E_c^{NL}[\rho] \end{aligned} \tag{2.26}$$

which introduces a further partition of exchange and correlation energy into semi-local (SL) and non-local (NL) components. It should be noted that the E_{xc} partitioning in eq. (2.26) is arbitrary which suggested by Predew to categorize Jacob's ladder of density functional approximations for the exchange-correlation energy.[100] Based on Jacob's ladder approximate exchange-correlation functionals are categorized in five rungs from local density approximation (LDA),[101] generalized gradient approximation (GGA),[102,103] meta-GGA,[104] hybrid[105] to double-hybrid,[106] respectively. Here, functionals are grouped according to their degree of approximation or the expected accuracy and computational cost and the information they use, such as the local density (electron density), density gradients, higher derivatives, non-local components in exchange or correlations such as Fock exchange and perturbative correlation terms. Functionals up to rung three (LDA, GGA and meta-GGA) do not include Fock exchange and are termed local or semi-local functionals, whereas hybrid and double-hybrid functionals incorporate Fock exchange at rung four (hybrid) and Fock exchange and pertubative correlation at rung five (double-hybrid). Since calculating Fock exchange poses a computational challenge, semi-local functionals tend to be more computationally efficient than hybrid and double-hybrid ones. While these categories stem from fundamental theoretical principles, suggesting improved accuracy with higher rungs, there can be significant performance variations among functionals within the same rung. Therefore, comprehensive benchmark studies evaluating each functional performance against the desired property are essential. Nonetheless, Jacob's ladder categorization provides a rough estimate of systematic functional errors and helps classify functionals by their computational efficiency.

Two significant errors in current DFT approximations are the self-interaction error (SIE) [107,108] and the absence of long-range correlation effects, particularly London dispersion. [109,110] While the inadequate representation of long-range correlation is a fundamental limitation of semi-local DFT, it can now be effectively addressed by incorporating one of several established dispersion corrections, such as D4 and D3. [109,111] The SIE occurs due to an artificial interaction of an electron with itself, stemming from the imperfect cancellation between the approximate exchange-correlation functional and the self-Coulomb interaction. It is a challenging error to rectify. This error is prevalent in all semi-local (m)GGA functionals (rungs 1–3), such as PBE [102,103] or BLYP [112,113]. Hybrid functionals aim to mitigate the SIE by substituting a portion of the approximate DFT exchange with Fock exchange (e.g., B3LYP with 20% and PBE0 with 25%). Another approach to deal with SIE in the DFT is including (adding) Hubbard parameters to the DFT which there known as DFT+U methods. [114,115]

2.3. Classical molecular dynamics

Classical molecular dynamics (MD) simulations are a technique for computing the equilibrium and transport properties of a classical many-body system. MD simulations can be applied to study molecule systems ranging in size and complexity from small to large systems with many thousands to millions of atoms. MD simulation could be considered as part of molecular mechanics which uses classical mechanics to model molecular systems. In this context, classical means the potential energy of all systems is calculated as a function of the nuclear coordinates called force fields. Force fields are functional forms of the potential energies with parameter sets to describe the forces between atoms within molecules (intramolecular) or between molecules (intermolecular). In molecular mechanics, the BO approximation is assumed valid. Thus, the potential energy of all systems is calculated as a function of the nuclear coordinates. Their motion follows the laws of classical mechanics, specifically Newton's laws of motion given as

$$F_I = M_I \ddot{R}_I \tag{2.27}$$

where the force is equal to mass (M) times acceleration ($\ddot{R}$). Also, the relation between the force and potential energy is known as

$$F_I = -\nabla_I V \tag{2.28}$$

which allows to compute the momenta of the atoms by integration of the forces with

$$p_I = -M_I \int_0^\tau \nabla_I V dt \tag{2.29}$$

From the momenta the kinetic energy is computed via

$$K = \sum_I \frac{p_I^2}{2M_I} \tag{2.30}$$

thereby the system can be described by the Hamiltonian in eq. (2.3) as $H = K + V$. The Hamiltonian allows to predict the state of the system at any future time from the current state and the potential energy governing the system. In the MD the trajectory is indeed the sequence of configurations and the properties are usually obtained by the time average.

This section aims to focus on some aspects of MD simulations such as force field in section 2.3.1 and equation of motion in section 2.3.2. For more information on classical molecular dynamics, including different conditions, ensembles, and technical details, refer to the literature by Allen and Tildesley,[78] Frenkel and Smit,[76] Leach,[116] and Alavi[77] which are the primary references for this section.

2.3.1. Force fields

In the BO-AIMD (see section 2.2.1) the separation of electronic and nuclear motions allows for determining the PES on which nuclei move. In classical molecular dynamics simulations, it is assumed that if the form of potential energy based on nuclear coordinates ($E(\{R\})$, for simplicity in the representations $\{R\}$ is going to skipped in the following equations) or an approximation can be determined, classical mechanics can then calculate nuclear motions on this surface over time. In classical mechanics, the total potential energy or force field is approximated as the sum of intramolecular and intermolecular contributions which in some references are called bonded and nonbonded contributions, respectively. The specific decomposition of terms depends on the force field types but a general form for the total energy can be written as:

$$E_{total} = E_{\text{intra}} + E_{\text{inter}} \tag{2.31}$$

The intramolecular energy terms ensure proper bond lengths, bond angles, and dihedral angles while allowing some shape flexibility. Incorrect modeling of these contributions can lead to distorted molecular structures and inaccurate simulations. Classical intramolecular potentials typically do not account for the breaking and formation of chemical bonds, as these processes disrupt electronic distributions and simple classical representations cannot capture these changes in atom–atom bond interactions.

$$E_{\text{intra}} = \sum_{ij} E_{\text{bond}}(R_{ij}) + \sum_{ijk} E_{\text{angle}}(\theta_{ijk}) + \sum_{ijkl} E_{\text{dihedral}}(\phi_{ijkl}) \tag{2.32}$$

where R_{ij} is the distance between atom i and j, θ_{ijk} is bond angle in the atom triple i, j, k, and ϕ_{ijkl} is the dihedral angle defined by the four bonded atoms i, j, k, and l. The intermolecular interaction usually consists of two main parts, van der Waals (vdW) and electrostatic interactions.

$$E_{\text{inter}} = \sum_{ij'} f \cdot E_{\text{elec}}(R_{ij'}) + \sum_{ij'} f \cdot E_{\text{VdW}}(R_{ij'}) \tag{2.33}$$

where f is a scaling factor for the pairs depending on whether they are bonded or unbonded. As mentioned, there are different types of classical force field forms and parameter sets, with the most popular ones being OPLS, AMBER, and CHARMM force fields. The AMBER (Assisted Model Building with Energy Refinement) force field originally developed by Peter Kollman and his coworkers and it has been refined over many years.[117,118] AMBER uses the following functional form to represent the force field of a molecule:

$$\begin{aligned} E =& \sum_{ij} K_{R,ij}(R_{ij} - R_{ij,0})^2 + \sum_{ijk} K_{\theta,ijk}(\theta_{ijk} - \theta_{ijk,0})^2 \\ &+ \sum_{ijkl} \frac{V_{\phi,ijkl}}{2}\Big(1 - \cos[m \cdot \phi_{ijkl} - \delta]\Big) + \sum_{i<j} f \left(\frac{A_{ij}}{R_{ij}^{12}} - \frac{B_{ij}}{R_{ij}^{6}} + \frac{q_i q_j}{4\pi\varepsilon_0\varepsilon_r R_{ij}} \right) \end{aligned} \tag{2.34}$$

The AMBER force field provides a table of constant parameters such as $K_{R,ij}$, $K_{\theta,ijk}$, $V_{\phi,ijkl}$, and σ_{ii} for defined atom types and pairs. Charges for each atom or atom type in the AMBER force field were determined by the restrained electrostatic potential (RESP) charge[119] model specifically in each molecule. The f factor is 0.5 for the electrostatic and vdW interaction between atoms with 1-4 separation in the same molecule and it is 1 for the 1-5 or higher interactions. The Lennard-Jones potential parameters are reported for like atom pairs "*ii*" and the unlike atom types "*ij*", follow the Lorentz–Berthelot mixing rules[120,121] (combination rules) given as

$$\sigma_{ij} = \frac{\sigma_{ii} + \sigma_{jj}}{2} \qquad \text{and} \qquad \varepsilon_{ij} = \sqrt{\varepsilon_{ii}\varepsilon_{jj}} \tag{2.35}$$

The OPLS (Optimized Potentials for Liquid Simulations) force field has a functional form similar to the AMBER force field, but it differs in the dihedral terms, which are expressed as follows

$$E_{\text{dihedral}}(\phi_{ijkl}) = \frac{A_1}{2}\Big(1 + \cos[\phi_{ijkl}]\Big) + \frac{A_2}{2}\Big(1 + \cos[2\phi_{ijkl}]\Big) + \frac{A_3}{2}\Big(1 + \cos[3\phi_{ijkl}]\Big) \tag{2.36}$$

where $A_{1/2/3}$ are constants. In addition, in the OPLS force field the mixing rule for the vdW interactions are based on the geometric-mean mixing rule[122,123], given as

$$\sigma_{ij} = \sqrt{\sigma_{ii}\sigma_{jj}} \qquad \text{and} \qquad \varepsilon_{ij} = \sqrt{\varepsilon_{ii}\varepsilon_{jj}} \tag{2.37}$$

Combining different parameter sets, even with similar functional forms, requires caution. This was one of the challenges in the initial MD simulation of DESs, as there were different parameter sets for each component but no specifically developed force field for their mixtures as DESs. Similar caution was applied when choosing force fields for solvation effect simulations, such as cellulose solvation in DESs. Another important consideration is the availability of parameter sets in the tools used to generate simulation inputs. In this regard, during this thesis, some of the DES solvent parameter sets were included in the TRAVIS programm.[124]

2.3.2. Equation of motion

The equations of motion are equations that describe the behavior of a physical system in terms of its motion as a function of time. More specifically, the equations of motion describe the behavior of a physical system as a set of mathematical functions in terms of dynamic variables. As mentioned, in the MD these variables are usually coordinates and time. In MD simulations the differential equation of motion obtained based on Newton's second law by considering the eq. (2.27) equal to eq. (2.28) is

$$M_I \ddot{R}_I = -\nabla_I V \qquad \text{or} \qquad \frac{d^2 R_I}{dt^2} = -\frac{\nabla_I V}{M} \tag{2.38}$$

The finite difference methods are applied to integrate the eq. (2.38) and solve the equation of the motion numerically. Due to the complex potential energies and many-body effects, an analytical solution is usually not possible. The essential idea of finite difference methods is to break down the left side of the equation into many small time steps each separated by fixed small time steps (Δt). There is a class of numerical integration schemes based on various algorithms. The desired algorithm to have successful simulations is supposed to be fast and use small space/memory on the computers. In addition, It should permit the use of a large time step Δt while satisfying the conservation laws for energy and momentum and be time-reversible.

The Verlet algorithm, proposed by Loup Verlet in 1967, applies Taylor expansions for position and momentum. Thus, the Verlet is a semi-implicit integration scheme, consisting of the following two consecutive steps:

$$\begin{aligned}\mathbf{R}_I(t+\Delta t) &= 2\ \mathbf{R}_I(t) - \mathbf{R}_I(t-\Delta t) + \frac{\Delta t^2}{M_I}\frac{\partial V}{\partial \mathbf{R}_I}(t) \\ \mathbf{p}_I(t+\Delta t) &= \frac{M_I}{2\Delta t}\Big[\mathbf{R}_I(t+\Delta t) - \mathbf{R}_I(t-\Delta t)\Big]\end{aligned} \tag{2.39}$$

The Verlet algorithm for moving to the next step in the trajectory ($R_I(t+\Delta t)$) needs two initial positions, position at time t and position $\Big(R_I(t)\Big)$ and one step back $\Big(R_I(t-\Delta t)\Big)$.

The value of $\Big(R_I(t)\Big)$ can be given as an initial condition at the start of the simulation and $\Big(R_I(t-\Delta t)\Big)$ can be estimated by using the Euler algorithm with a time step of $-\Delta t$. Please note that in many references,[76,77] the equations of the algorithms are presented using velocity instead of momentum. If m is an object's mass and $\mathbf{v}$ is its velocity, then the object's momentum $\mathbf{p}$ is given by $\mathbf{p} = m\mathbf{v}$. However, the Verlet algorithm has energy conservation and numerical stability, it has its own associated problems. For instance, the error in the position /velocities scales as $\Delta t^4/\Delta t^2$. The accuracy of the trajectories generated with the Verlet algorithm is not impressive. In addition, since it treats the positions and velocities asymmetrically, leads to problems in implementing thermostat and barostat algorithms.[77] A simple algorithm that overcomes these setbacks is the Leapfrog algorithm given as

$$\begin{aligned}
\mathbf{p}_I(t+\frac{\Delta t}{2}) &= \mathbf{p}_I(t) - \frac{\Delta t}{2}\frac{\partial V}{\partial \mathbf{R}_I}(t) \\
\mathbf{R}_I(t+\Delta t) &= \mathbf{R}_I(t) + \Delta t\ \mathbf{p}_I(t+\frac{\Delta t}{2}) \\
\mathbf{p}_I(t+\Delta t) &= \mathbf{p}_I(t+\frac{\Delta t}{2}) - \frac{\Delta t}{2}\frac{\partial V}{\partial \mathbf{R}_I}(t+\Delta t)
\end{aligned} \tag{2.40}$$

The Leapfrog algorithm consists of three consecutive steps. In this algorithm, the integration involves updating positions and momentum at interleaved time points. Thus, the updates to position and the momentum are not done simultaneously but are offset of each other in $\frac{1}{2}\Delta t$ time. Two primary strengths of the Leapfrog algorithm are its time-reversibility and simplicity. The global truncation errors in the velocity and position from the leapfrog algorithm are of order Δt^3.[77] Leapfrog is a second-order integration scheme; however, integration schemes of arbitrary order can be constructed. For instance, the Second-order-Minimal-Norm (2MN) integration scheme[125,126] is designed to minimize the norm of the residual integration error by using an additional parameter λ, at the cost of two extra steps given as

$$\begin{aligned}
\mathbf{p}_I(t+\lambda\Delta t) &= \mathbf{p}_I(t) - \lambda\Delta t\frac{\partial V}{\partial \mathbf{R}_I}(t) \\
\mathbf{R}_I(t+\frac{\Delta t}{2}) &= \mathbf{R}_I(t) + \frac{\Delta t}{2}\ \mathbf{p}_I(t+\lambda\Delta t) \\
\mathbf{p}_I\Big(t+(1-\lambda)\Delta t\Big) &= \mathbf{p}_I(t+\lambda\Delta t) - (1-2\lambda)\Delta t\ \frac{\partial V}{\partial \mathbf{R}_I}(t+\frac{\Delta t}{2}) \\
\mathbf{R}_I(t+\Delta t) &= \mathbf{R}_I(t+\frac{\Delta t}{2}) + \frac{\Delta t}{2}\ \mathbf{p}_I\Big(t+(1-\lambda)\Delta t\Big) \\
\mathbf{p}_I(t+\Delta t) &= \mathbf{p}_I\Big(t+(1-\lambda)\Delta t\Big) - \lambda\Delta t\frac{\partial V}{\partial \mathbf{R}_I}(t+\Delta t)
\end{aligned} \tag{2.41}$$

When $\lambda = 0.5$, the 2MN integrator becomes equivalent to the Leapfrog algorithm. However, the standard value for the additional parameter is approximately $\lambda \approx 0.19$,[126] though it can be adjusted to enhance the integrator performance for a particular problem. Omelyan et al. have shown that the integrators commonly used in simulations have limitations and are far from perfect. More efficient algorithms, such as the fourth-order scheme (OMF4, Omelyan-Mryglod-Folk), have been identified and tested for various levels of precision, significantly improving integration efficiency. OMF4 is an extension of 2MN to higher orders, consisting of a total of 11 steps and four parameters.[126] These algorithms accurately replicate key properties of conservative systems, ensuring stability, ergodicity, and detailed balance.[76] OMF4 algorithms are cost-effective to implement and optimized to minimize numerical uncertainties.

2.4. Hybrid Monte Carlo

There are two distinct molecular mechanics approaches in molecular simulations to compute the observable properties of classical many-body systems. One method is molecular dynamics as shown in section 2.3 generates an approximate solution to Newton's equations of motion, producing a trajectory in phase space. Using MD, we can compute time averages of both static properties (e.g., structural and thermodynamic observables) and dynamic properties (e.g., transport coefficients). In contrast, the idea behind the Monte Carlo (MC) method, or more precisely the Markov-Chain Monte Carlo method, is based on probabilities, with properties determined from ensemble averages.

Each of the MD and MC methods has its advantages and disadvantages. MD simulations can provide information about the time evolution of a system and be used to compute transport properties. Meanwhile, the strength of MD simulations can also be a limitation, especially if the dynamics is slow. This limits MD simulations to explore all accessible states of a system. MC methods suffer less from this drawback, as they can efficiently sample states even when the dynamics are slow. Thus, MC methods could have better sampling and be applied to any system that can exist in a large number of states, provided we can compute the relative probabilities of these states (e.g., the Boltzmann weight).

The basic principle of the MC is to sample from the distribution $\exp[-U(\{r_i\})]$ defined by the energy function $U(\{r_i\})$. The energy function can be a classical force field and any type of potential that can describe the investigated system. Given a configuration, denoted as o for old, a displacement is performed to reach a new configuration, denoted as n. The displacement step is accepted based on the Boltzmann weight defined by the energy function for configuration n. The main principle governing the MC algorithm is the detailed balance condition

$$N(o)\sum_{n}\pi(o\rightarrow n)=\sum_{n}N(n)\pi(n\rightarrow o) \tag{2.42}$$

where π is the probability for accepting a displacement step and N is the population of the respective configuration. The detailed balance ensures the MC displacement steps are fully reversible.

The Hybrid Monto Carlo method, also known as Hamiltonian Monto Carlo and abbreviated as HMC, combines MD with MC.[127] HMC represents a Markov-Chain Monte Carlo method where the trial moves are carried out by MD integration. Given a time-reversible MD integration scheme, the detailed balance is satisfied in the HMC scheme by construction. The starting point of HMC is an artificial Hamiltonian given as

$$H_{\mathrm{MC}}(\{\mathbf{p}_i\},\{\mathbf{r}_i\}) = \sum_i \frac{|\mathbf{p}_i|^2}{2} + U(\{r_i\}) \tag{2.43}$$

where $\mathbf{p}_i$ are the canonical momenta introduced as an auxiliary quantity and sampled from a standard normal distribution, i.e. $\mathbf{p}_i \propto \mathcal{N}_{0,1}$ for each of the cartesian components of $\mathbf{p}_i$. Based on these canonical momenta the equations of motion are defined as

$$\frac{d\mathbf{r}_i}{d\tau} = \frac{\partial H_{\mathrm{MC}}}{\partial \mathbf{p}_i} \qquad \text{and} \qquad \frac{d\mathbf{p}_i}{d\tau} = -\frac{\partial H_{\mathrm{MC}}}{\partial \mathbf{r}_i} \tag{2.44}$$

where τ is an artificial time variable. With the defined trajectory length τ_0 and the starting configuration $\{r_i\}$, the integration of the equation of motion is carried out with finite step size $\Delta\tau$ as described in section 2.3.2. The possible new configuration obtained by solving the equations of motion, is denoted with $\{\mathbf{p}_i'\}$ and $\{\mathbf{r}_i'\}$. This configuration is accepted based on the Boltzmann weight defined by the Hamiltonian as

$$P_{\mathrm{acc}} = \min\Big\{1,\ \exp\Big[-\Big(H_{\mathrm{MC}}(\{\mathbf{p}_i'\},\{\mathbf{r}_i'\}) - H_{\mathrm{MC}}(\{\mathbf{p}_i\},\{\mathbf{r}_i\})\Big)\Big]\Big\} \tag{2.45}$$

If the configuration is accepted, $\{\mathbf{r}_i'\}$ are used as new system coordinates, otherwise the original coordinates are kept. The canonical momenta are resampled from the standard normal distribution regardless of acceptance or rejection of the step. With an exact integration of the equations of motion, the Hamiltonian is preserved and all proposed displacement steps are accepted. However, with a finite step-size $\Delta\tau$ the acceptance rate is dependent on the chosen step size, therefore the choice of step size is crucial for a high acceptance ratio in the HMC algorithm. Due to the Boltzmann weighted acceptance of steps the generated distribution does not depend on the choice of time step and HMC is exact.

3. Are There Magic Compositions in Deep Eutectic Solvents? Effects of Composition and Water Content in Choline Chloride/Ethylene Glycol from Ab Initio Molecular Dynamics

Vahideh Alizadeh,* , Friedrich Malberg,* Agílio A. H. Pádua,† and Barbara Kirchner*

Received: 29 May 2020, Published online: 29 July 2020.

Reprinted in Appendix A with permission‡ from

V. Alizadeh, F. Malberg, A. A. H. Pádua, B. Kirchner, *J. Phys. Chem. B* **2020**, *124*, 7433-–7443, *doi:10.1021/acs.jpcb.0c04844.*

For this article, Supporting Information is available free of charge at:
https://pubs.acs.org/doi/10.1021/acs.jpcb.0c04844.

Contributions to the manuscript

- Development of the concept
- Performing all simulations, analysis, and calculations
- Interpretation of the results
- Writing of the manuscript

---

* Mulliken Center for Theoretical Chemistry, Clausius Institute for Physical and Theoretical Chemistry, University of Bonn, Beringstr. 4–6, 53115 Bonn, Germany

† Chemistry Laboratory, École Normale Supérieure de Lyon & CNRS, 69007 Lyon, France

‡ Permission requests to reuse material from this chapter should be directed to the American Chemical Society.

Before this study, the predominant belief in the DES community was that the DES solvent could be achieved in the eutectic point, which was assumed to exist at specific, seemingly fixed stoichiometric proportions.[37,44] The proportions in DES solvents (mixtures) were thought to correspond to a unique arrangement of a complex in the liquid phase, considered responsible for the formation of the eutectic point.[37,128] Thus, we attempt to contribute to the elucidation of whether mixtures at specific compositions exhibit significantly different physical and solvation properties. Additionally, we aim to investigate how the presence of impurities or other molecules, such as water, may alter the structure and solvation properties of the studied DES. A full reprint of this work[1] can be found in appendix A.

Three systems consist of 1:1 and 1:2 molar proportions (ratio) of choline chloride: ethylene glycol ([Ch]Cl:EG) mixtures, and 1:2:1 mixture of [Ch]Cl:EG:water, are investigated using AIMD simulations. [Ch]Cl:EG DES mixtures are chosen as the case studied because it is one of the most studied DES and applied in multiple applications.[129–134] Structural analysis (radial distribution functions (RDFs) and number integrals (NIs)) show that the overall structure of the ion-ion and ion-EG interactions is minimally affected by the addition of water or by altering the proportion of EG molecules, except for the Cl^--Cl^- and EG-Cl^- interactions. However, the first peak shapes for the cation-anion RDFs imply different patterns which relate to Cl^- anion potential sites to interact with cation, forming a strong $O-H\cdots Cl$ hydrogen bond (hydrogen bond coordination) or interacting with the ammonium headgroup (ionic coordination). These features in the solvation shell could have structural and chemical consequences. Although, gauche conformation of the cation makes it possible for Cl^- anion to interact with both the ammonium headgroup and hydroxyl group of $[Ch]^+$ cation simultaneously which gauche conformers are dominant in the cation in all systems. A closer look at the conformational analysis of EG molecule shows the gauche to the trans ratio of EG is 2.0, 1.2, and 2.3 in the 1:1, 1:2, and 1:2:1 systems respectively. However, the gauche conformation is the preferred conformation for EG in its pure liquid state with the gauche to the trans ratio of 4.0.[135] All of these effects are subtle, and the conformational analysis does not demonstrate a striking composition effect.

Given the critical role of hydrogen bonding in the formation and properties of DESs, the details of hydrogen bonding in all systems are being investigated. Thus, the strongest hydrogen bonds are observed in the shortest distances between Cl^- anions and the hydroxyl group of EG molecules then between Cl^- anions and the hydroxyl group hydrogen atom of $[Ch]^+$ cation. The strength of hydrogen bonds involving the anion decreases with dilution, transitioning from a 1:1 ratio to 1:2 and further to 1:2:1. However, the NIs as the representative number of coordination shells show with increasing the concentration of EG in 1:2 the anion's first solvation shell is more involving the neutral EG molecules rather ionic hydrogen bond between cation and anion in 1:1 which highlights the importance of $Cl\cdots EG$ interactions in the [Ch]Cl:EG mixtures. Additionally, the combined distribution function (CDF) and RDF analyses indicate a 2-fold hydrogen bond morphology in the hydrogen bond network of Cl^- with EG in the 1:1 system. Conversely, the 1:2 system exhibits a more flexible network of hydrogen bonds between Cl^- and EG which may be one reason for the lower melting point in the 1:2 system compared to the 1:1 system. When examining the hydrogen bonds among all available OH groups, it is observed that there are exceedingly minor cation-cation hydrogen bonds. However, a prominent interaction between the hydroxyl groups is the interaction of the hydrogen atom of the cation hydroxyl ($\mathrm{H_O}$) and the EG oxygen atom ($\mathrm{O_E}$) as an acceptor. Nonetheless, the $\mathrm{H_O} \cdots \mathrm{O_E}$ hydrogen bond weakens with dilution as EG-EG hydrogen bonds are strengthened. The presence of water in the 1:2:1 system slightly decreases the EG-EG interaction due to potential interactions with the hydrogen and oxygen of the hydroxyl group in EG.

In addition, charge analysis is utilized to examine charge delocalization and transfer among all components within the DES. Two methods for charge calculations are applied namely Mulliken[136] and Blöchl charges[137]. The obtained charge value is known to depend on the methods applied. Both charge calculation methods exhibit consistent trends. The resulting charge distributions indicate that water and EG molecules are not neutral in the studied DES mixtures, with charge transfers occurring between ions and somewhat toward the EG and water molecules. The charge analysis is in good agreement with structural analysis.

Our findings imply that there are no particular or exceptional occurrences in the liquid phase and solvation properties at specific molar stoichiometry with lower melting points. Therefore, the concept of DESs should not be confined by fixed proportions between the hydrogen bond donor (HBD) and hydrogen bond acceptor (HBA). However, stoichiometric ratios could be applied to optimize the composition of DES, maximizing its performance for desired applications. Thus, there is no magic composition in the DES. As the last point, it is worth mentioning, back to the time this investigation was done and published, 1:2 molar ratio of [Ch]Cl:EG was known as the eutectic mixture which later is shown as the real eutectic point for this mixture is between 1:4 and 1:5 (1:4.74) molar ratio of [Ch]Cl:EG.[138–140]

4. Strong Microheterogeneity in Novel Deep Eutectic Solvents

Vahideh Alizadeh,[*] David Geller,[*] Friedrich Malberg,[*] PabloB. Sánchez,[†] Agílio A. H. Pádua,[‡] and Barbara Kirchner[*]

Reprinted in Appendix B with permission[§] from

V. Alizadeh, D. Geller, F. Malberg, P. Sánchez, A. Padua, B. Kirchner, "Strong Microheterogeneity in Novel Deep Eutectic Solvents", *ChemPhysChem* **2019**, *20*, 1786–1792, *doi:10.1002/cphc.201900307*.

For this article, Supporting Information is available free of charge at:
https://doi.org/10.1002/cphc.201900307.

Contributions to the manuscript

- Co-performing simulations, analysis, and visualizations
- Interpretation of the results
- Co-writing of the manuscript

---

[*] Mulliken Center for Theoretical Chemistry, Clausius Institute for Physical and Theoretical Chemistry, University of Bonn, Beringstr. 4–6, 53115 Bonn, Germany

[†] Dpto.FísicaAplicada, Facultadde Ciencias, Universidad de Vigo, CampusLagoas-Marcosendes/n, 36310VIGO–Spain

[‡] Chemistry Laboratory, École Normale Supérieure de Lyon & CNRS, 69007 Lyon, France

[§] Permission requests to reuse material from this chapter should be directed to Wiley-VCH GmbH.

DESs can be utilized as functional materials, with unique molecular-level structures (nanostructure) emerging depending on the chemical composition of their components, while the system maintains macroscopic homogeneity as a liquid.[141,142] For example, molecular ionic clusters were observed via neutron scattering in choline chloride:urea:water DES mixtures, where an unusual transition from an ionic mixture to an aqueous solution could occur with varying water concentrations.[143] Another example arises in hydrophobic DESs when alkyl chain functionalizations are introduced to the molecular compounds.[28,144] The liquid reveals a nanosegregation into polar and nonpolar domains (phases), which is commonly known and denoted as microheterogeneity. Microheterogeneity in solvents enables template effects or structure-directing for synthesis, extraction processes, and catalytic reactions.[145–148] As the use of template-assisted syntheses grows in DESs and hydrophobic DESs prove effective in extraction processes where microheterogeneity is crucial, there is a need for suggestions for novel DESs with pronounced microheterogeneity.[142,149–151] Moreover, the literature lacks a molecular-level understanding of DESs containing long-side chains. Therefore, in this project, microheterogeneity is investigated in novel DESs. A full reprint of this work can be found in appendix B.

Classical MD simulations are being employed to investigate a total of ten DES systems, composed of choline chloride ([Ch]Cl) and several previously unreported choline derivatives as hydrogen-bond acceptors, combined with ethylene glycol (EG) as a hydrogen-bond donor, in a molar ratio of 1:2. Experimental data is available only for choline chloride:ethylene glycol ([Ch]Cl:EG). The remaining nine in silico systems are being proposed and theoretically studied as potential targets for synthesis. These in silico systems include variations such as a) altering one of the alkyl (methyl) side chains ($[\mathrm{C_RCh}]^+$ R=4, 6, 8), b) modifying the alcohol substitute side chain ($[\mathrm{ChC}_x\mathrm{OH}]^+$ x=4, 6, 8, 10, 12), and c) increasing all methyl groups to n-butyl ($[(\mathrm{C_4})_3\mathrm{Ch}]^+$).

In the initial analysis, the electrostatic surface potential (ESP) is plotted to illustrate charge distributions. This information is subsequently utilized to define polar and nonpolar parts (domains) in domain analysis. Chloride anion, EG molecule, hydroxyl, and ammonium group of cations along with the neighbor $\mathrm{CH_2}$ are considered polar parts while the rest of the elongated side chains are treated as nonpolar subgroups. The domain counts show the connectivity of different sub-molecular groups.[152] The larger number of the domain counts indicates the dispersion and separation of parts while the domain count number close to one indicates high connectivity between them. For all systems, the domain count number for polar groups is one, i.e., the polar parts are completely connected and form one polar domain. However, for the systems with side chain lengths of four carbon units, the nonpolar parts tend to be fully dispersed within the polar parts. Meanwhile, the systems with eight carbon lengths or longer have distinguished nonpolar and polar parts each from one fully connected microphase. Furthermore, fully separated microphases are observed in $[(\mathrm{C_4})_3\mathrm{Ch}][\mathrm{Cl}]$:EG, a level of microheterogeneity (segregation) that is typically only seen in the case of the $[\mathrm{ChC_{12}OH}]^+$ cation.

The conformation of the side chains is being investigated to gain a better understanding of the molecular structure. The intramolecular distance distribution function from the nitrogen atom to the terminal heavy atom of the side chain, namely the oxygen (in $[\mathrm{ChC}_x\mathrm{OH}]^+$) or the carbon (in $[\mathrm{C_RCh}]^+$ and $[(\mathrm{C_4})_3\mathrm{Ch}]^+$) atom, indicates that the side chains are predominantly stretched rather than crumbled, regardless of their length. These stretched conformations maximize potential interaction sites for both polar and nonpolar components. However, the distinction between the gauche (crumpled) and trans (stretched) conformations is less clear in the $[\mathrm{ChC}_x\mathrm{OH}]^+$ cations compared to the alkyl side-chain series based on the spatial distribution functions. The side chain structure supporting the picture of the stronger microheterogeneity obtained with the same substitute side chain length by altering one or all of the alkyl (methyl) side chains rather than modifying the alcohol substitute side chain.

Additionally, the influence of microheterogeneity on the hydrogen bond network of polar domains is explored through structural analyses such as the combined distribution function, radial distribution function, and number integrals (NIs). All systems have shown a strong hydrogen bond network. However, a subtle indirect effect of the longer alkyl chain can also be observed. For instance, the NIs of $\mathrm{Cl}\cdots\mathrm{O}$ (cation) decrease by elongating side chains as a hint of slightly stronger separation of polar groups. This observation although small (minor) supports the stronger microheterogeneity obtained by domain analysis for systems with longer side chains.

In conclusion, the novel DESs investigated in this study exhibit MH, with some cases demonstrating strong MH. Strong MH, characterized by both polar and non-polar parts forming completely connected domains, becomes apparent with side chain lengths of eight carbon units or more. Notably, bulky $[(\mathrm{C}_4)_3\mathrm{Ch}][\mathrm{Cl}]$:EG appears to be a special case, displaying MH at a level comparable to $[\mathrm{ChC}_{12}\mathrm{OH}][\mathrm{Cl}]$:EG. These findings highlight the potential of these compounds as valuable candidates for synthesis and utilization in processes such as extraction or template-assisted synthesis, where strong microheterogeneity is required.

5. How is CO_2 Absorbed into a Deep Eutectic Solvent?

Vahideh Alizadeh,[*] Lars Esser,[*] Barbara Kirchner [*]

Received: November 19 2020, Published online: February 07 2021.

Reprinted in Appendix C with permission[†] from

V. Alizadeh, L. Esser, B. Kirchner, "How is CO_2 Absorbed into a Deep Eutectic Solvent?", *J. Chem. Phys.* **2021**, *154*, 094503, *doi:10.1063/5.0038093.*

For this article, Supporting Information is available free of charge at:
https://doi.org/10.1063/5.0038093.

Contributions to the manuscript

- Development of the concept
- Performing all simulations, analysis, and calculations
- Interpretation of the results
- Writing of the manuscript

---

[*] Mulliken Center for Theoretical Chemistry, Clausius Institute for Physical and Theoretical Chemistry, University of Bonn, Beringstr. 4–6, 53115 Bonn, Germany

[†] Permission requests to reuse material from this chapter should be directed to the American Institute of Physics.

Investigating CO_2 capture and storage is essential for addressing environmental concerns and mitigating climate change.[153,154] There is an urgent need for continued research to discover more eco-friendly, non-toxic, and cost-effective alternatives for CO_2 absorption. This involves identifying easily synthesized and affordable materials and methods to scale up CO_2 absorption. DESs are known for their favorable physical and thermodynamic properties, non-toxicity, low price (affordability), and environmental friendliness and therefore hold promise for CO_2 capture.[35,44] While some experimental investigations support their use in CO_2 processing and absorption, there is limited molecular-level understanding of CO_2 capture mechanisms in DESs. This study represents the first attempt in the literature to use AIMD simulation techniques to explore CO_2 absorption in DESs. A full reprint of this work can be found in appendix C.

In this study, CO_2 absorption has been investigated in the 1:2 molar ratio of [Ch]Cl:EG DES mixture. Simulation boxes were prepared based on the experimental findings of Leron et al.[155,156] Their results demonstrate that the solubility of CO_2 increases with pressure and decreases with increasing temperature. The first system referred to as System A, contains 48 EG molecules, 24 [Ch]Cl ion pairs, and one CO_2 molecule. System B consists of 48 EG molecules, 24 [Ch]Cl ion pairs, and six CO_2 molecules. These systems vary in the number of CO_2 molecules and pressure, system A simulated under 1 Mpa and system B under 6 Mpa.

Initially, the overall structure of the DES was analyzed to check the pressure and CO_2 effect on [Ch]Cl:EG DES. The conformation of EG molecules remained unchanged regardless of pressure or the number of CO_2 molecules, with the gauche conformer being dominant in both systems. The $[Ch]^+$ cation showed a preference for the gauche conformation in both systems. However, there was an increased preference for the trans-conformer in system B due to higher pressure, resulting in a more packed structure. RDFs between DES species showed minor differences between systems, primarily due to packing effects rather than solute–solvent interactions. The strong interaction between DES components, particularly between Cl^- anion and $[Ch]^+$ cation and EG molecule, remained consistent across systems. The structure of [Ch]Cl:EG DES, driven by strong cation-anion and hydrogen bond interactions, showed no significant differences even in the presence of CO_2 molecules and under high pressures, similar to observations in ionic liquids.[157]

Afterward, RDFs and NIs applied to investigate the solvation shell and location of CO_2 relative to the [Ch]Cl:EG DES components and other CO_2 molecules. In system A (lower pressure), EG molecules are closest to CO_2 molecule, followed by Cl^- anions. In contrast, in system B (higher pressure), Cl^- anions are closest, followed by EG molecules. Furthermore, the ratio of peak heights for CO_2-Cl^- and CO_2-EG interactions changes. In system B, the CO_2-Cl^- interaction peak is more pronounced compared to system A, while the reverse is observed for CO_2-EG interaction. This suggests a transition from physical absorption (system A) to chemical absorption (system B).[158,159] In the first solvation shell of the CO_2 based on the NI analysis the number of the anions and EG molecules increased in system B, indicating a denser structure under pressure.

As further investigation, Voronoi analysis show as pressure increases, the CO_2 coverage by ions rises, where as the EG coverage of CO_2 decreases, that again indicates the change in solvation of

CO_2. Furthermore, at high pressure, both the ionic part and EG molecules tend to self-aggregate. The spatial distribution function (SDF) provides additional analysis of how ions and EG molecules organize around the CO_2 molecule. This detailed arrangement of ions and molecules emphasizes the significance of interaction types in CO_2 absorption within DESs, with anions absorbing more in system B and EG molecules interacting strongly in system A. SDF results are consistent with RDFs and Voronoi analysis. EG molecules interact parallel to the O−C−O axis, while cations tend to orient perpendicularly similar to our previous observation in ionic liquids.[160] Based on SDF analysis, the Cl^- anions position around CO_2 molecules change with pressure from diagonally in system A to interact directly with the carbon atom of CO_2 in system B. Further analysis like CDFs and RDFs provides additional evidence that supports the SDFs observations regarding the positioning of Cl^- ions around CO_2 molecules. It is worth to mention, the distance of Cl^- and carbon of CO_2 aligns with values observed in ionic liquids.[157,160]This suggests that under pressure (system B), the ionic part plays a significant role in CO_2 absorption, whereas in the lower pressure (system A), CO_2 is primarily absorbed by hydrogen bond donors like the EG molecule.

The O−C−O angle of CO_2 molecules could provide insights into distinguishing between chemical and physical absorption.[158,159] A bent O−C−O angle and strong interaction with an anion indicate chemical adsorption, while a linear CO_2 structure with weak interactions suggests physical adsorption. The O−C−O angular distribution function analysis (ADF) and the temporal evaluation show similarities in both systems with a maximum around 173∘ (more physical adsorption side). Additionally, temporal analysis shows fluctuations and bending of O−C−O angles over time.

In conclusion, the first solvation shell of CO_2 changes with pressure. Therefore, the DES exhibits a similar CO_2 absorption advantage to that observed in ionic liquids. Moreover, the presence of a second component, typically a hydrogen bond donor, offers an opportunity to guide and enhance CO_2 absorption in DES.

6. Molecular Level Insight into the Solvation of Cellulose in Deep Eutectic Solvents

Vahideh Alizadeh,* Barbara Kirchner*

Received: May 28 2021, Published online: August 05 2021.

Reprinted in Appendix D with permission† from

V. Alizadeh, B. Kirchner, "Molecular Level Insight into the Solvation of Cellulose in Deep Eutectic Solvents", *J. Chem. Phys.* **2021**, *155*, 084501, *doi:10.1063/5.0058333.*

For this article Supporting Information is available free of charge at:
https://doi.org/10.1063/5.0058333.

Contributions to the manuscript

- Development of the concept
- Performing all simulations, analysis, and calculations
- Interpretation of the results
- Writing of the manuscript

---

* Mulliken Center for Theoretical Chemistry, Clausius Institute for Physical and Theoretical Chemistry, University of Bonn, Beringstr. 4–6, 53115 Bonn, Germany

† Permission requests to reuse material from this chapter should be directed to the American Institute of Physics.

Cellulose is an important biopolymer widely used in various industries, including paper, textiles, and food.[161,162] It is also a promising material for the development of sustainable and renewable products, such as biofuels, bioplastics, and biomedical materials.[163] Solvents play a vital role in the research and development of cellulose because cellulose often needs to be dissolved for processing, modification, and characterization. In contrast, cellulose is a highly crystalline and insoluble material. Therefore, the search for and selecting an appropriate solvent is crucial for the sustainable processing, dissolution, and characterization of cellulose.[164–166] The choice of solvent can also affect the efficiency, cost, and environmental impact of cellulose processing. DESs as designable solvents hold promise for driving a transition towards a greener and more sustainable chemical product cycle.[167,168] Numerous factors can influence the processing and dissolution of cellulose in DESs.[169–172] Although different DESs types can dissolve certain cellulose types for instance in the choline based DESs amorphous cellulose (lignin and starch) are dissolved while crystallized cellulose types such as α-cellulose and cellulose nanocrystals remain unaffected.[171,173–175] Given the factors discussed it is important to understand the cellulose solvation in the DESs. Regardless of whether DES dissolves cellulose or not, investigating solvation remains essential. In this work, the interplay of cellulose is studied in two DESs choline acetate ([Ch][OAc]) mixed with urea and choline chloride ([Ch]Cl) mixed with urea using classical molecular dynamics simulations. A full reprint of this work[4] can be found in appendix D.

Cellulose solvation is simulated in two DES mixtures, [Ch]Cl:urea and [Ch][OAc]:urea, with applying OPLS-AA based force fields[176–179]. These DESs are chosen for their distinct anions, $[\mathrm{OAc}]^-$ and Cl^-, which are both strong hydrogen bond acceptors. Similar interactions also observed with the ionic liquids in which anions with hydrogen bond acceptors play a vital role in dissolving and separating cellulose in ionic liquids.[180,181] Similarly, in ionic liquids anions play a vital role as hydrogen bond acceptors in dissolving and separating cell. Each simulation box contained a cellulose model within DES mixtures of 250 ion pairs and 500 urea molecules. A beta-cellulose microfibril, composed of ten glucose octamer chains, is selected as the cellulose model.[182]

The properties of DES solvents are determined by the nature of their components, leading us to initially investigate their overall structure and dynamics. We examined the structures of [Ch]Cl:urea and [Ch][OAc]:urea using RDFs and NIs between the DES components. Chloride ions had slightly fewer molecules in their first solvent shell than acetate ions. However, considering urea molecules in the first solvent shell of the anions, chloride ions have more neighbours compared to acetate ions. The first solvation shell of the cation showed a slight increase in chloride ions compared to acetate ions, but vice versa for the anions. The urea self-interaction and cation-cation interplay were increased in [Ch]Cl:urea DES compared to [Ch][OAc]:urea DES, allowing chloride ions to “act more freely.” The diffusion coefficient, obtained from the mean square displacements, indicates the diffusion of DES components is higher in [Ch][OAc]:urea than in [Ch]Cl:urea, almost two times faster. The origin of this behavior is the central role of anion in the liquid structure. The strong interactions between DES components are hindering diffusion.

As the initial analysis to investigate cellulose in DES, we examined the variation in cellulose structure during the simulation. This was done by plotting the time development of the cellulose microfibril volume and the distance between the last glucoses ring in the cellulose microfibril chains (taking into account the nearest neighbor conditions) over the production run. Despite fluctuations in cellulose volume and distances, no significant change in structural features is observed. This suggests that cellulose dissolution in the studied DESs did not occur, consistent with experimental and theoretical studies.[182,183] However, the selected cellulose model demonstrates the capability of MD simulations to replicate cellulose dissolution in specific ionic liquids.[182] A closer examination reveals that cellulose volume and last sugar unit distances are larger in the [Ch]Cl:urea system compared to the [Ch][OAc]:urea system (slight swelling of the cellulose in the [Ch][Cl]:urea).

The hydrogen bonds between DES components and cellulose are examined in detail using RDFs, NIs, Sankey diagrams, and surface coverage from Voronoi analysis to understand molecular-level behaviors. It is important to mention that hydrogen bonds play a crucial role in cellulose solvation. Analysis of RDFs and NIs revealed significant hydrogen bonding between anions and cellulose, with Cl^- exhibiting higher probabilities despite shorter distances observed for oxygen of the acetate and the hydrogens of the cellulose. This suggests that Cl^- enter the cellulose frame, potentially causing the observed swelling. Sankey diagrams depicted hydrogen bond topology, showing Cl^- accepting more hydrogen bonds, highlighting differences between[Ch]Cl:urea and [Ch][OAc]:urea systems. Despite similarities to cellulose-ionic liquid interactions[181], DESs-cellulose interactions have fewer hydrogen bonds, indicating that investigated DESs may not dissociate cellulose chains due to strong intermolecular hydrogen bonding among DES components. Furthermore, the surface coverage and temporal evolution of cellulose coverage by the DES components, as determined by Voronoi analysis, reveal intriguing details regarding cellulose solvation in DESs, consistent with previous analyses.

In conclusion (summary), DESs show promise as sustainable solvents for cellulose processing and various applications. Therefore, understanding cellulose solvation in DESs is crucial for designing and utilizing DESs effectively in cellulose processing and novel applications. However, the DESs studied in this research do not dissolve cellulose, making them suitable candidates for applications where a solvent is required to maintain the cellulose structure intact for instance in cellulose applications as 3D printer ink.[170]

7. Chemistry Dissolved in Ionic Liquids. A Theoretical Perspective

Barbara Kirchner,* Jan Blasius,* Vahideh Alizadeh,* Andreas Gansäuer,† and Oldamur Hollóczki‡*

Received: 19 October 2021, Published online: 17 January 2022.

Reprinted in Appendix E with permission§ from

B. Kirchner, J. Blasius, V. Alizadeh, A. Gansäuer, and O. Hollóczki, *J. Phys. Chem. B* **2022**, *126*, 766–777, *doi:10.1021/acs.jpcb.1c09092.*

Contributions to the manuscript

- Performing of all calculations presented in section "Radical Problems in Ionic Liquids"
- Interpretation of the results presented in section "Radical Problems in Ionic Liquids"
- Writing of section "Radical Problems in Ionic Liquids"
- Co-writing of the other parts

---

* Mulliken Center for Theoretical Chemistry, Clausius Institute for Physical and Theoretical Chemistry, University of Bonn, Beringstr. 4–6, 53115 Bonn, Germany

† Kekulé-Institut für Organische Chemie und Biochemie, Gerhard-Domagk-Str. 1, University of Bonn, 53121 Bonn, Germany

‡ Department of Physical Chemistry, Faculty of Science and Technology, University of Debrecen, 4010 Debrecen, Hungary

§ Permission requests to reuse material from this chapter should be directed to the American Chemical Society.

This perspective underscores and highlights recent methodological advances and persisting challenges in the theoretical modeling of ILs. Three main areas of advanced IL research are explored for this purpose: 1) chemical reactions, 2) chirality transfer, and 3) radicals in ILs. All of these areas require the concurrent application of realistic models and precise methods. In this context, "realistic models" demand a careful consideration of simulation time, system size, and complexity, while "accurate methods" are essential for describing electronic structure. By carefully considering both realistic and accurate aspects, IL research can achieve predictiveness and stay aligned with the latest research trends. This perspective explores methodological advancements for the selected examples and introduces additional case studies central to this summary. For a comprehensive reading, the full work is available in appendix E.

To describe chemical reactions in ILs, the explicit treatment of the electronic structure is crucial to describe chemical bond breaking and bond formation. Consequently, classical simulations based on force fields are unsuitable for describing reactivity in MD simulations. On the other hand, reactions can be observed in AIMD simulations only if the reaction barrier is lower than approximately thermal energy $k_B T$. Under these prerequisites, AIMD simulations allow the investigation of spontaneous reactions. To overcome reaction barriers above the thermal energy alternative approaches like free energy methods can be used.

The case studies outlined herein focus on CO_2 absorption studies in ILs and Grotthuss diffusion in ILs. By studying CO_2-ILs mixtures with AIMD, physical absorption of CO_2 without chemical reaction can be found for ILs such as 1-n-butyl-3-methylimidazolium hexafluorophosphate ($[C_4C_1Im][PF_6]$)[184] and ethylammonium nitrate ($[N_2HHH][NO_3]$)[157], while chemical absorption of CO_2 is observed for amino acid-based and imidazolium acetate ILs.[185] Since the choice of the ILs influenced the gas absorption, the modifications in ILs like side-chain elongation and the introduction of an aromatic π-system establishes the step that controls the AIMD and static quantum chemical method computational cost. AIMD simulations exploring CO_2 absorption in choline chloride:ethylene glycol DES at different pressures which is part of this thesis (chapter 5 and appendix C) revealed varying roles of cations and anions; at lower pressure, the cation and ethylene glycol interactions with CO_2 are predominant, while at higher pressure, the anion played a more significant role in the physical absorption of CO_2.[3] While these case studies demonstrate the feasibility of investigating CO_2 absorption in ILs and DESs with AIMD simulations, limitations include the short simulation time and small system size, impacting sampling quality and often confining applications to small molecules. Potential strategies to address these challenges are further explored in appendix E, such as the utilization of tight-binding semiempirical methods for describing electronic structure.

Chirality transfer in ILs is the second example which poses a challenge due to the necessity of a careful description of intermolecular forces and interactions and their influence on the bonding within the molecules required to obtain satisfying spectra. Time correlation function techniques are applied to obtain spectra from molecular dynamics trajectories.[186,187] AIMD simulations offer an advantage by explicitly modeling electronic structures, enabling vibrational circular dichroism (VCD) spectra calculations for a deeper understanding of chirality transfer. However, their limitation to small system sizes restricts the study of local phenomena. Furthermore, because of the immense computational demand of these calculations, it is necessary to implement new methodologies like the cluster weighting approach[188] based on the quantum cluster equilibrium theory[189] that allows for accurate results with faster calculations.

Our final example of radicals in ILs poses challenges due to their complex electronic structures, demanding accurate methodologies. Even in electronic structure calculations complications such as self-interaction error and time scale problems must be overcome. Employing computationally expensive yet precise methods like hybrid functionals is often impractical for AIMD simulations due to their computational intensity. To illustrate, reaction energies for four gas phase exchange reactions involving a titanocene complex's chloride ligand and an IL anion are calculated using various functionals levels of theory such as GGA (BLYP,[112,190] PBE,[102] rev-PBE[191]), GGA+U[114] (PBE+U) meta-GGA (TPPS[192]) and Hybrid functional (PBE0[102], B3LYP[112,190]) with DZVP and TZVP basis sets. Comparisons between functionals demonstrate a significant increase in computational time, with hybrid functionals like PBE0 exhibiting a 200-fold increase compared to revPBE. Although the auxiliary density matrix method[193] for hybrid functionals reduces this to a factor of five, the increased computational cost limits the widespread use of hybrid functionals in AIMD simulations. This underscores the complexity of theoretically handling radicals within ILs through MD simulations, necessitating further methodological advancements.

8. A Hybrid Monte Carlo Study of Argon Solidification

Vahideh Alizadeh,[*] Marco Garofalo [†] Carsten Urbach,[†] Barbara Kirchner [*]

Received: 13 December 2023, Accepted: 20 December 2023.

Reprinted in Appendix F (accepted manuscript) with permission[‡] from

V. Alizadeh, M. Garofalo, C. Urbach, and B. Kirchner, *Z. Naturforsch.* **2024**, *79*, 283–291, *doi:10.1515/znb-2023-0107*.

For this article, Supporting Information is available free of charge at:
https://www.degruyter.com/document/doi/10.1515/znb-2023-0107/html.

Contributions to the manuscript

- Development of the concept
- Co-performing simulations
- Conducting the analysis, visualizations, and calculations
- Interpretation of the results
- Writing of the manuscript
- Co-implementing HMC code

---

[*] Mulliken Center for Theoretical Chemistry, Clausius Institute for Physical and Theoretical Chemistry, University of Bonn, Beringstr. 4–6, 53115 Bonn, Germany

[†] HISKP (Theory), Rheinische Friedrich-Wilhelms-Universität Bonn, Nussallee 14-16, 53115, Bonn, Germany

[‡] Permission requests to reuse material from this chapter should be directed to De Gruyter.

In recent decades, computational methods have transformed chemical and material simulations, allowing deeper exploration of molecular and material properties. Advances in computer hardware, software, and theoretical approaches have driven rapid evolution in computational chemistry and material science. Traditional techniques like molecular dynamics and Monte Carlo simulations perform well at short time scales and high-probability regions but struggle with rare events requiring longer simulations and efficient phase space sampling. This has led to the development of innovative algorithms and approaches. In this regard, we aim to develop and implement hybrid Monte Carlo (HMC) methods, also known as Hamiltonian Monte Carlo. Originally, Duane et al. first reported the HMC method in 1987 for systems in particle physics, such as quantum chromodynamics, which contained fermionic degrees of freedom.[127] Furthermore, HMC method has also gained attention and found application in the fields of chemistry and material science.[70,194] In the HMC algorithm, molecular dynamics techniques guide Monte Carlo moves. There are two ways to implement the HMC algorithm: one is as an interface in existing molecular dynamics packages such as LAMMPS,[72] GROMACS,[73] and NAMD[74]; the other is as standalone software for specific applications, such as the TriMem software[75] for simulating lipid membranes. Despite these valuable implementations, they do not fully leverage the potential of HMC algorithms. Therefore, optimized HMC implementations for GPU machines, tailored to various chemical applications, are needed. This work aims to take the first steps in that direction by implementing standalone HMC code and providing more examples and case studies for phase transition phenomena such as argon solidification. A full reprint of this work[6] can be found in appendix F.

As mentioned in section 2.4, HMC algorithm[127] represents an MCMC method in which the MC moves are guided by molecular dynamics techniques. We have implemented HMC using the Kokkos C++ library[195–197], which allows efficient parallel execution and data management for performance-portable applications. This enables the code to be compiled for both CPU and GPU architectures without modifications. The source code is modular, with key components like force and potential computation functions designed using the strategy pattern. In the context of this work, the Lennard-Jones potential and forces were made available as the mainly tested potential. While the Lennard-Jones potential is simple, it already allows to investigation of complex processes. Therefore, to focus on the difference in the integration schemes, the Lennard-Jones potential is chosen as the optimal starting point. The code structure however allows easy addition of other potentials. Currently, the program supports different integration schemes for the equations of motion, including Leapfrog, 2MN, and OMF4[126].

In this work, as a first step, the argon fluid simulation with two initial densities is conducted using HMC and MD to validate HMC. All the simulations are done in the canonical ensemble by maintaining constant NVT (N, number of particles; V, volume; and T, temperature) during the simulations.As shown in the HMC theory in section 2.4 HMC methods are based on the canonical ensemble. Meanwhile, MD theory is based on the microcanonical ensemble (constant NVE: N, number of particles; V, volume; and E, energy). To maintain the system temperature in the MD simulations in NVT ensemble with LAMMPS,[198] the Nosé-Hoover thermostat[199,200] are applied. To investigate the solidification of argon, we used a 5 × 5 × 5 face-centered cubic (fcc) supercell with a lattice size of 5.36 Å. HMC simulations at elevated temperatures generated the liquid phase, which was then used as the starting structure for each temperature. Consistency checks using MD simulations employed the same initial geometry. We studied factors affecting the solidification process, such as voids, system size effects, and temperature-dependent LJ parameters. Voids and defects were introduced by randomly removing argon atoms before generating the liquid phase. Each HMC trajectory ran for 1.1×10^5 sweeps after 1×10^5 sweeps of thermalization. Additionally, larger system sizes were simulated using a $10 \times 10 \times 10$ fcc supercell with a 5% void. Periodic boundary conditions were applied in all directions.

Comparing systems with and without voids showed that the solidification temperature decreases with the introduction of voids. This result was further supported by radial distribution functions, which indicated a transition to the solid state at lower temperatures. Larger voids contribute to a more well-structured solid, and cluster analysis shows that more voids lead to increased cluster distances throughout the process. Comparing large and small system sizes revealed challenges in investigating solidification with small systems and emphasizes the importance of using larger system sizes to achieve satisfactory results in solidification. A smooth solidification curve was observed with 4000 particles highlighting the need for larger system sizes in simulations. Simulations with temperature-dependent potentials did not improve the results which might be due to simulations being limited to small system sizes.

In conclusion, this work serves as an initiation for new implementations and research, showcasing the potential of HMC methods in investigating phase transitions such as solidification. It also underscores improvements in sampling and highlights bottlenecks such as system size and force field parameters. Furthermore, there is a need for further development in the HMC code to enhance its capabilities. This expansion would facilitate the exploration of a broader array of options and conditions, thereby enabling the investigation of more complex chemical phenomena.

9. Summary and Outlook

This thesis focused on a deeper understanding of solvents and solvent effects from several angles. Firstly, I investigated the interactions, especially hydrogen bonds, within DES along with their structural and dynamical properties as pure liquids.[1,2] Secondly, their interplay with solutes such as water, cellulose, and CO_2 gas was studied.[1,3,4] Finally, I investigated the challenges and tradeoffs in choosing a suitable computational method when exploring how ILs as solvents interact with radical molecules, like a titanocen catalyst.[5] Both ILs and DESs are designable and tunable solvents, allowing for tailoring to specific tasks. Therefore, understanding their physicochemical, structural, and dynamical properties is essential for customizing and optimizing their performance in desired applications.

All results were based on the application of different state-of-the-art simulation methods and required the development of extended simulation strategies.[5] In this work, the methods of choice were quantum chemical calculations, AIMD, and classical MD simulations.

Due to the complexity of interactions among all components in the liquid phase of DESs, AIMD simulations were applied first to understand the microscopic structure of choline chloride:ethylene glycol ([Ch]Cl:EG) mixtures (chapter 3). I also examined the influence of composition and water content on the hydrogen bonding network. This comprehensive study revealed that hydrogen bonding in these systems slightly depends on the composition. However, the presence of a fluctuating hydrogen bond network in the [Ch]Cl:EG mixture with a 1:2 molar ratio may contribute to the lower melting point of this system compared to the 1:1 system.

This study has significant implications (profound consequences) for the DES field in several aspects. First, at the molecular level, it shows that there are no specific interactions at a specific molar ratio (eutectic composition) or a "magic number" in the phase diagram that defines a DES. This concept has been embraced by the DES community and other experimental and theoretical groups have subsequently supported our findings.[41,201] These findings have altered the definition of a DES to introduce molar ratio as a parameter to tune DES properties rather than strictly defining them, which had a significant impact on the DES community.

The charge analysis agreed well with the structural analysis, indicating that charge distribution is not affected by composition. However, charge transfer occurs not only between ions but also towards the EG (hydrogen bond donor) and water molecules. This result and insight, that the ion's charge in DES type III is not fixed but variable, highlights the need for the development of specific force fields for DESs to consider this effect. Thus, the second significant impact of this paper is its support for the new developments and parametrization of force fields in the DES community. The AIMD trajectories were shared and utilized in several studies, for example by Goloviznina et al.,[202,203] Chaumont et al.,[204] and Maglia de Souza et al,[205] as a benchmark for assessing new force field parametrization for [Ch]Cl:EG DES mixtures.

In chapter 4, I dealt with the important phenomenon of nanostructuring in DESs, named polar-nonpolar microheterogeneity. Indeed microheterogeneity is the separation of polar and nonpolar parts and fundamental properties for the versatility of the solvents. The impact and influence of these properties extend to the solvation of various molecules, as well as its potential to act as a structure-directing or templating agent. Specifically, the incorporation of hydrophobic units in the form of alkyl groups of varying lengths allows for the adjustment of the microheterogeneous behavior of DESs and makes them interesting options as potential reaction media and extractants.

Classical MD simulations were employed to facilitate the simulation of large-scale systems since a large system size is crucial for capturing and quantifying this complex structural effect.[2] The simulations were applied to study ten DESs. Herein the investigated systems are [Ch]Cl:EG in 1:2 molar ratio and some of in silico DESs which are constructed by elongating the alkyl chains of $[\mathrm{Ch}]^+$ cation, either by a) altering one of the alkyl (methyl) side chains ($[\mathrm{C_RCh}]^+$ R=butyl, hexyl, octyl) or b) modifying the alcohol substitute side chain ($[\mathrm{ChC}_x\mathrm{OH}]^+$ x=butyl, hexyl, octyl, decyl, dodecyl) or c) substituting both methyl groups by n-butyl ($[(\mathrm{C_4})_3\mathrm{Ch}]^+$). The work demonstrated that even small differences in cation size influence the microheterogeneity and nanostructure of DESs. This affects the solvation of certain compounds and may allow the utilization of the structure-directing effect of DES as a solvent in the synthesis or extraction process. Moreover, the literature lacked a molecular-level understanding of DESs containing long-side chains. Given the relevance of these investigations, it is believed that the findings reported herein will contribute to the general molecular level understanding of the DESs.

In a further study (chapter 5), the [Ch]Cl:EG mixture with a 1:2 molar ratio was selected as a sustainable solvent for CO_2 absorption, given the significant potential of deep eutectic solvents (DESs) as CO_2 absorbents reported by experiments. To explore this potential, AIMD simulations were conducted in the isothermal–isobaric ensemble at pressures of 1 MPa and 5 MPa. These simulations aimed to investigate the principal interactions, structural characteristics, and underlying mechanisms of CO_2 absorption within DESs. The results revealed that there is a substantial influence of the anion and hydrogen bond donor (EG), alongside a relatively minor influence of the cation, on CO_2 solvation. Specifically, at lower pressures, the interaction between EG and CO_2 is the predominant factor, whereas at higher pressures, the interaction between chloride ions and CO_2 becomes more pronounced. This demonstrates that the DES exhibits similar advantages in CO_2 absorption as seen in ionic liquids. Moreover, the presence of a second component, which often serves as a hydrogen bond donor, can be strategically used to direct and enhance CO_2 absorption. The findings highlight the pressure effect, versatility, and efficiency of DESs in applications and underscores the potential for further development and fine-tuning of DESs to meet specific requirements in various industrial processes.

Afterwards in chapter 6, I studied the interaction of cellulose fiber in two DESs; namely choline acetate:urea ([Ch][OAc]:urea; 1:2) and choline chloride:urea([Ch]Cl:urea; 1:2).[4] Cellulose is the most abundant biopolymer on Earth and solvents play a crucial role in cellulose processing and applications. Understanding the interactions between the solvent and cellulose is essential for the rational design of solvents for cellulose processing, such as separation and purification. In this study, MD simulations with atomistic force fields were used to investigate the system's physical properties, employing a larger representation in terms of the number of molecules and time scales. The dissolution of cellulose was not observed in the studied liquids, in agreement with experimental studies found in literature. Cellulose solvation in DESs is governed by the overall structure and interactions of the ions and urea molecules with each other. In the [Ch]Cl:urea DES the Cl^- anion "acts more freely" compared to the $[OAc]^-$ anion in the [Ch][OAc]:urea DES. As a consequence, a slight swelling of cellulose was observed in the chloride-based solvent.

chapter 7 discusses the challenges associated with modeling the electronic structure and intermolecular interactions present in ILs and DESs. The trend in current research towards using more realistic models and accurate methodologies, highlights the need to enhance predictability in theoretical calculations and for conducting simulations. It is worth noting that these challenges especially extend to the computational study of DESs, given their increased complexity compared to ILs.In an extensive literature review several case studies based on AIMD investigating reaction chemistry, chirality, and radicals in ILs were presented. Especially for reactions and chirality in ILs the importance of an description of the electronic structure was emphasized. Furthermore, shortcomings could be mainly attributed to too short simulation times and too small system sizes.

For radicals in ILs the main challenge is that due to their complex electronic structures, their description demands accurate methodologies. Even in electronic structure calculations issues such as self-interaction errors and time scale problems must be addressed. To illustrate the computational bottleneck and the difficulty of functional choice, an artificial gas phase exchange reaction was calculated. This gas phase exchange reaction takes place between the chloride ligand of a titanocene complex and an anion from an IL ion pair. Overall, five ILs were investigated which were constructed by combination of three types of cations ($[C_4C_1Im]^+$ 1-n-butyl-3-methylimidazolium, $[pyrH_4]^+$ N-butylpyrrolidinium, and $[NH_{122}]^+$ diethylmethylammonium) with two types of anions ($[NTf_2]^-$ bis(trifluoromethylsulfonyl)imide and $[OTf]^-$ trifluoromethanesulfonate). These ILs were chosen to be investigated in order to evaluate how different anions and cations may affect this reaction. The calculation of such processes is highly attractive for the development of catalysts and reaction design, as quantitative predictions about the (reversible) modulation of the catalysts' redox potentials can be made. Based on the reaction energy of the exchange reaction, an obvious anion effect is visible. The reaction is energetically more favorable when $[OTf]^-$ is the solvent anion compared to when $[NTf_2]^-$ is the solvent anion. However, the cation effect is more subtle. Nevertheless, the use of a good electronic structure method is important to obtain a proper description of these complicated systems. This simple consideration shows that the theoretical treatment of radicals in ionic liquids is far from being solved.

As a last step, I dived into the implementation of the HMC method in chapter 8. With all the existence common methods, still computational chemistry requires access to high-performance computation facilities and efficient software and algorithms. The HMC method was implemented with the OMF4 integration scheme and utilizes the Kokkos C++ framework for efficient execution on both GPU and CPU based computer architectures. As an initial case study of typical chemical phenomena such as phase transitions, argon solidification was explored. To validate our HMC implementation, I compared the structure of fluid-like argon phases from HMC simulations with those from classical molecular dynamics simulations. Solidification is the process of transformation of a liquid to a solid. Therefore, each system is simulated by starting from a higher temperature (liquid state) and cooled down to a lower temperature (solid state). Both MD and HMC simulations demonstrate similar trends in the solidification of argon fluids. However, notable differences between HMC and MD appear, with an offset and differing behavior in the transition region.

Comparing systems with and without voids revealed that introducing voids decreased the solidification temperature. Structural analyses indicated that the presence of voids leads to the formation of a well-structured solid state at lower temperatures. Comparing very large and small system sizes highlighted the challenge of achieving satisfactory solidification with small systems. This emphasizes the importance of larger system sizes in solidification simulations. Simulations with a temperature-dependent potential did not improve our results, likely due to the small system size limitations. Future work will focus on further enhancing the HMC code, expanding its capabilities to explore a broader range of conditions and more complex chemical phenomena.

10. Bibliography

[1] V. Alizadeh, F. Malberg, A. A. Pádua, B. Kirchner, *J. Phys. Chem. B* **2020**, *124*, 7433–7443.

[2] V. Alizadeh, D. Geller, F. Malberg, P. B. Sánchez, A. Padua, B. Kirchner, *ChemPhysChem* **2019**, *20*, 1786–1792.

[3] V. Alizadeh, L. Esser, B. Kirchner, *J. Chem. Phys.* **2021**, *154*, 094503.

[4] V. Alizadeh, B. Kirchner, *J. Chem. Phys.* **2021**, *155*, 084501.

[5] B. Kirchner, J. Blasius, V. Alizadeh, A. Gansäuer, O. Hollóczki, *J. Phys. Chem. B* **2022**, *126*, 766–777.

[6] V. Alizadeh, M. Garofalo, C. Urbach, B. Kirchner, *Zeitschrift für Naturforschung B* **2024**, *79*, 283–291.

[7] T. Frömbgen, J. Blasius, V. Alizadeh, A. Chaumont, M. Brehm, B. Kirchner, *J. Chem. Inf. Model.* **2022**, *62*, 5634–5644.

[8] T. Frömbgen, J. Blasius, L. Dick, K. Drysch, V. Alizadeh, L. Wylie, B. Kirchner **2023**.

[9] W. Dong, V. Alizadeh, J. Blasius, L. Wylie, L. Dick, Z. Fan, B. Kirchner, *Phys. Chem. Chem. Phys.* **2023**, *25*, 24678–24685.

[10] *The United Nations Brundtland Commission definition of sustainability*, https://www.un.org/en/academic-impact/sustainability (accessed: 25.04.2024).

[11] *Sustainable Development Goals (17 SDGs)*, https://www.undp.org/sustainable-development-goals (accessed: 25.04.2024).

[12] *12 Principles of Green Chemistry*, https://www.acs.org/greenchemistry/principles/12-principles-of-green-chemistry.html (accessed: 25.04.2024).

[13] P. T. Anastas, J. C. Warner, *Green chemistry: theory and practice*, Oxford university press, **2000**.

[14] A. P. Abbott, G. Capper, D. L. Davies, R. K. Rasheed, V. Tambyrajah, *Chem. Commun.* **2003**, 70–71.

[15] G. T. Craven, N. Lubbers, K. Barros, S. Tretiak, *J. Chem. Phys.* **2020**, *153*, 104502 (13 pages).

[16] D. Heyes, D. Dini, S. Pieprzyk, A. Brańka, *J. Chem. Phys.* **2023**, *158*, 134502 (18 pages).

[17] M. K.-H. Kiessling, *J. Chem. Phys.* **2023**, *159*, 014301 (6 pages).

[18] J. Losey, R. J. Sadus, *J. Phys. Chem. B* **2019**, *123*, 8268–8273.

[19] X. Liu, D. Xu, B. Diao, L. Zhang, J. Gao, D. Liu, Y. Wang, *J. Mol. Liq.* **2019**, *275*, 347–353.

[20] G. García, S. Aparicio, R. Ullah, M. Atilhan, *Energy Fuels* **2015**, *29*, 2616–2644.

[21] S. Sarmad, J.-P. Mikkola, X. Ji, *ChemSusChem* **2017**, *10*, 324–352.

[22] C. Ma, S. Sarmad, J.-P. Mikkola, X. Ji, *Energy Procedia* **2017**, *142*, 3320–3325.

[23] G. Wang, Y. Dai, X. Hu, F. Xiao, Y. Wu, Z. Zhang, Z. Zhou, *J. Mol. Liq.* **2012**, *168*, 17–20.

[24] A. Boisset, S. Menne, J. Jacquemin, A. Balducci, M. Anouti, *Phys. Chem. Chem. Phys.* **2013**, *15*, 20054–20063.

[25] G. Cong, Y.-C. Lu, *Chem* **2018**, *4*, 2732–2734.

[26] M. Pätzold, S. Siebenhaller, S. Kara, A. Liese, C. Syldatk, D. Holtmann, *Trends Biotechnol.* **2019**, *37*, 943–959.

[27] A. Zhu, T. Jiang, B. Han, J. Zhang, Y. Xie, X. Ma, *Green Chem.* **2007**, *9*, 169–172.

[28] D. J. van Osch, L. F. Zubeir, A. van den Bruinhorst, M. A. Rocha, M. C. Kroon, *Green Chem.* **2015**, *17*, 4518–4521.

[29] J. A. Sirviö, M. Visanko, H. Liimatainen, *Green Chem.* **2015**, *17*, 3401–3406.

[30] A. Satlewal, R. Agrawal, S. Bhagia, J. Sangoro, A. J. Ragauskas, *Biotechnol. Adv.* **2018**, *36*, 2032–2050.

[31] Z. Chen, B. McLean, M. Ludwig, R. Stefanovic, G. G. Warr, G. B. Webber, A. J. Page, R. Atkin, *J. Phys. Chem. C* **2016**, *120*, 2225–2233.

[32] V. S. Raghuwanshi, M. Ochmann, A. Hoell, F. Polzer, K. Rademann, *Langmuir* **2014**, *30*, 6038–6046.

[33] C. Gu, J. Tu, *Langmuir* **2011**, *27*, 10132–10140.

[34] A. Abo-Hamad, M. Hayyan, M. A. AlSaadi, M. A. Hashim, *CHEM ENG J* **2015**, *273*, 551–567.

[35] H. Benworth B., S. Stephanie, C. Brian, P. Derrick, Z. Yong, K. Jeffrey M., H. Alexandre, A. Laxmi, Z. Tamar, D. Brian W., G. Burcu, M. Edward J., R. Arthur, D. Mark, Z. Thomas A., B. Gary A., T. Mark E., S. Robert F., S. Joshua R., *Chem. Rev.* **2020**, *121*, 1232–1285.

[36] P. W. Atkins, J. De Paula, J. Keeler, *Atkins' physical chemistry*, Oxford university press, **2023**.

[37] M. A. Martins, S. P. Pinho, J. A. Coutinho, *J. Solution Chem.* **2018**, 1–21.

[38] P. López-Porfiri, J. F. Brennecke, M. Gonzalez-Miquel, *J. Chem. Eng. Data* **2016**, *61*, 4245–4251.

[39] L. J. Kollau, M. Vis, A. Van Den Bruinhorst, A. C. C. Esteves, R. Tuinier, *Chem. Commun.* **2018**, *54*, 13351–13354.

[40] A. van den Bruinhorst, M. C. Gomes, *Curr. Opin. Green Sustain. Chem.* **2022**, *37*, 100659.

[41] D. O. Abranches, J. A. Coutinho, *Annu. Rev. Chem. Biomol. Eng.* **2023**, *14*, 141–163.

[42] B. D. Like, C. E. Uhlenbrock, M. J. Panzer, *Phys. Chem. Chem. Phys.* **2023**, *25*, 7946–7950.

[43] D. O. Abranches, M. A. Martins, L. P. Silva, N. Schaeffer, S. P. Pinho, J. A. Coutinho, *Chem. Commun.* **2019**, *55*, 10253–10256.

[44] E. L. Smith, A. P. Abbott, K. S. Ryder, *Chem. Rev.* **2014**, *114*, 11060–11082.

[45] T. Welton, *Biophys. Rev.* **2018**, *10*, 691–706.

[46] K. Kuroda, *New J Chem* **2022**, *46*, 20047–20052.

[47] K. S. Egorova, E. G. Gordeev, V. P. Ananikov, *Chem. Rev.* **2017**, *117*, 7132–7189.

[48] R. M. Moshikur, M. R. Chowdhury, M. Moniruzzaman, M. Goto, *Green Chem.* **2020**, *22*, 8116–8139.

[49] T. Zhou, C. Gui, L. Sun, Y. Hu, H. Lyu, Z. Wang, Z. Song, G. Yu, *Chem. Rev.* **2023**, *123*, 12170–12253.

[50] A. Chinnappan, C. Baskar, H. Kim, *RSC Adv.* **2016**, *6*, 63991–64002.

[51] G. Li, K. Chen, Z. Lei, Z. Wei, *Chem. Rev.* **2023**, *123*, 10258–10301.

[52] D. Shang, X. Liu, L. Bai, S. Zeng, Q. Xu, H. Gao, X. Zhang, *Curr. Opin. Green Sustain. Chem.* **2017**, *5*, 74–81.

[53] P. McNeice, P. C. Marr, A. C. Marr, *Catal. Sci. Technol.* **2021**, *11*, 726–741.

[54] R. Flowers, U. N. Oloyede, *Dalton Trans.* **2024**.

[55] D. S. G. Henriques, E. Rojo-Wiechel, S. Klare, R. Mika, S. Höthker, J. H. Schacht, N. Schmickler, A. Gansäuer, *Angew. Chem. Int. Ed.* **2022**, *61*, e202114198.

[56] Z. Zhang, D. Slak, T. Krebs, M. Leuschner, N. Schmickler, E. Kuchuk, J. Schmidt, L. I. Domenianni, J. B. Kleine Buning, S. Grimme, et al., *J. Am. Chem. Soc.* **2023**, *145*, 26667–26677.

[57] A. Gansäuer, S. Hildebrandt, A. Michelmann, T. Dahmen, D. von Laufenberg, C. Kube, G. D. Fianu, R. A. Flowers, *Angew. Chem. Int. Ed.* **2015**, *54*, 7003–7006.

[58] Y. Wu, X. Wang, Y. Luo, J. Wang, Y. Jian, H. Sun, G. Zhang, W. Zhang, Z. Gao, *RSC Adv.* **2016**, *6*, 15298–15303.

[59] P. Schwerdtfeger, D. J. Wales, *J. Chem. Theory Comput.* **2024**, *20*, 3379–3405.

[60] T. Huber, A. E. Torda, W. F. van Gunsteren, *J. Comput.-Aided Mol. Des.* **1994**, *8*, 695–708.

[61] T. C. Beutler, W. F. van Gunsteren, *J. Chem. Phys.* **1994**, *101*, 1417–1422.

[62] G. Bussi, A. Laio, *Nat. Rev. Phys.* **2020**, *2*, 200–212.

[63] A. Barducci, M. Bonomi, M. Parrinello, *Wiley Interdiscip. Rev. Comput. Mol. Sci.* **2011**, *1*, 826–843.

[64] M. Tuckerman, B. J. Berne, G. J. Martyna, *J. Chem. Phys.* **1992**, *97*, 1990–2001.

[65] C. R. Abreu, M. E. Tuckerman, *Mol. Phys.* **2021**, *119*, e1923848.

[66] T. S. Van Erp, D. Moroni, P. G. Bolhuis, *J. Chem. Phys.* **2003**, *118*, 7762–7774.

[67] P. G. Bolhuis, D. W. Swenson, *Adv. Theory Simul.* **2021**, *4*, 2000237.

[68] P. Höllmer, A. C. Maggs, W. Krauth, *J. Chem. Phys.* **2022**, *156*, 084108.

[69] A. Haji-Akbari, *J. Chem. Phys.* **2018**, *149*, 072303.

[70] T. Tagawa, T. Kaneko, S. Miura, *Mol. Simul.* **2017**, *43*, 1291–1294.

[71] B. Mehlig, D. Heermann, B. Forrest, *Phys. Rev. B* **1992**, *45*, 679–685.

[72] J. Guo, A. Haji-Akbari, J. C. Palmer, *J. Theor. Comput. Chem.* **2018**, *17*, 1840002.

[73] M. Fernández-Pendás, B. Escribano, T. Radivojević, E. Akhmatskaya, *J. Mol. Model.* **2014**, *20*, 1–10.

[74] M. S. Barhaghi, B. Crawford, G. Schwing, D. J. Hardy, J. E. Stone, L. Schwiebert, J. Potoff, E. Tajkhorshid, *J. Chem. Theory Comput.* **2022**, *18*, 4983–4994.

[75] M. Siggel, S. Kehl, K. Reuter, J. Köfinger, G. Hummer, *J. Chem. Phys.* **2022**, *157*, 174801.

[76] D. Frenkel, B. Smit, *Understanding molecular simulation: from algorithms to applications*, Elsevier, **2023**.

[77] S. Alavi, *Molecular simulations: fundamentals and practice*, John Wiley & Sons, **2020**.

[78] M. P. Allen, D. J. Tildesley, *Computer simulation of liquids*, Oxford university press, **2017**.

[79] E. G. Lewars, *Computational Chemistry. Introduction to the Theory and Applications of Molecular and Quantum Mechanics.*, Wiley Online Library, **2016**.

[80] B. Kirchner, P. J. di Dio, J. Hutter in *Multiscale Molecular Methods in Applied Chemistry*, Vol. 307 of *Topics in Current Chemistry*, B. Kirchner, J. Vrabec (Eds.), Springer Berlin Heidelberg, **2012**, pp. 109–153.

[81] D. Marx, J. Hutter, *Modern methods and algorithms of quantum chemistry* **2000**, *1*, 141.

[82] C. Tully, John, *Mixed quantum-classical dynamics: mean-field and surface-hopping*, B. J. Berne, G. Ciccotti, D. F. Coker (Eds.), **1998**, pp. 489–514.

[83] M. E. Tuckerman, *Statistical mechanics: Theory and Molecular Simulation*, Oxford university press, **2010**.

[84] N. A. Gershenfeld, *The nature of mathematical modeling*, Cambridge university press, **1999**.

[85] P. A. Dirac in *Mathematical proceedings of the Cambridge philosophical society*, Cambridge University Press, pp. 376–385.

[86] J. J. Sakurai, E. D. Commins, *Modern quantum mechanics*, American Association of Physics Teachers, **1995**.

[87] B. K. Dey, A. Askar, H. Rabitz, *J. Chem. Phys.* **1998**, *109*, 8770–8782.

[88] F. S. Mayor, A. Askar, H. A. Rabitz, *J. Chem. Phys.* **1999**, *111*, 2423–2435.

[89] B. Houchmandzadeh, *Am. J. Phys.* **2020**, *88*, 353–359.

[90] S. Rajeev, *Annals of Physics* **2008**, *323*, 2265–2285.

[91] J. C. Tully, *Chem. Phys. Lett.* **2023**, *816*, 140396.

[92] P. V. Parandekar, J. C. Tully, *J. Chem. Theory Comput.* **2006**, *2*, 229–235.

[93] M. Born, R. Oppenheimer, *Annalen der Physik* **1927**, *389*, 457–484.

[94] D. R. Hartree in *Mathematical Proceedings of the Cambridge Philosophical Society*, Cambridge University Press, pp. 111–132. https://doi.org/10.1017/S0305004100011920.

[95] V. Fock, *Zeitschrift für Physik* **1930**, *61*, 126–148.

[96] W. Kohn, L. J. Sham, *Physical review* **1965**, *140*, A1133.

[97] J. J. Stewart, *Journal of Molecular modeling* **2007**, *13*, 1173–1213.

[98] D. Porezag, T. Frauenheim, T. Köhler, G. Seifert, R. Kaschner, *Physical Review B* **1995**, *51*, 12947.

[99] C. Bannwarth, E. Caldeweyher, S. Ehlert, A. Hansen, P. Pracht, J. Seibert, S. Spicher, S. Grimme, *Wiley Interdisciplinary Reviews: Computational Molecular Science* **2021**, *11*, e1493.

[100] J. P. Perdew, K. Schmidt in *AIP Conference Proceedings*, American Institute of Physics, pp. 1–20.

[101] S. H. Vosko, L. Wilk, M. Nusair, *Canadian Journal of physics* **1980**, *58*, 1200–1211.

[102] J. P. Perdew, K. Burke, M. Ernzerhof, *Phys. Rev. Lett.* **1996**, *77*, 3865.

[103] J. P. Perdew, K. Burke, M. Ernzerhof, *Physical Review Letters* **1997**, *78*, 1396.

[104] J. Tao, J. P. Perdew, V. N. Staroverov, G. E. Scuseria, *Physical review letters* **2003**, *91*, 146401.

[105] A. D. Beck, *J. Chem. Phys* **1993**, *98*, 5648–6.

[106] S. Grimme, F. Neese, *The Journal of chemical physics* **2007**, *127*.

[107] J. L. Bao, L. Gagliardi, D. G. Truhlar, *J. Phys. Chem. Lett.* **2018**, *9*, 2353–2358.

[108] K. Sharkas, K. Wagle, B. Santra, S. Akter, R. R. Zope, T. Baruah, K. A. Jackson, J. P. Perdew, J. E. Peralta, *Proc. Natl. Acad. Sci. U.S.A.* **2020**, *117*, 11283–11288.

[109] S. Grimme, A. Hansen, J. G. Brandenburg, C. Bannwarth, *Chem. Rev.* **2016**, *116*, 5105–5154.

[110] J. Hermann, R. A. DiStasio Jr, A. Tkatchenko, *Chem. Rev.* **2017**, *117*, 4714–4758.

[111] E. Caldeweyher, S. Ehlert, A. Hansen, H. Neugebauer, S. Spicher, C. Bannwarth, S. Grimme, *The Journal of chemical physics* **2019**, *150*.

[112] C. Lee, W. Yang, R. G. Parr, *Phys. Rev. B* **1988**, *37*, 785.

[113] B. Miehlich, A. Savin, H. Stoll, H. Preuss, *Chemical Physics Letters* **1989**, *157*, 200–206.

[114] M. Capdevila-Cortada, Z. Łodziana, N. López, *ACS Catal.* **2016**, *6*, 8370–8379.

[115] A. C. Ulpe, K. C. Bauerfeind, L. I. Granone, A. Arimi, L. Megatif, R. Dillert, S. Warfsmann, D. H. Taffa, M. Wark, D. W. Bahnemann, et al., *Z. Naturforsch. B* **2020**, *234*, 719–776.

[116] A. R. Leach, *Molecular modelling: principles and applications*, Pearson education, **2001**.

[117] P. K. Weiner, P. A. Kollman, *J. Comput. Chem.* **1981**, *2*, 287–303.

[118] W. D. Cornell, P. Cieplak, C. I. Bayly, I. R. Gould, K. M. Merz, D. M. Ferguson, D. C. Spellmeyer, T. Fox, J. W. Caldwell, P. A. Kollman, *J. Am. Chem. Soc.* **1995**, *117*, 5179–5197.

[119] R. Woods, R. Chappelle, *J. Mol. Struct.* **2000**, *527*, 149–156.

[120] D. Berthelot, *Compt. Rendus* **1898**, *126*, 15.

[121] H. A. Lorentz, *Ann. Phys.* **1881**, *248*, 127–136.

[122] A. Hagler, E. Huler, S. Lifson, *J. Am. Chem. Soc.* **1974**, *96*, 5319–5327.

[123] S. Lifson, A. Hagler, P. Dauber, *J. Am. Chem. Soc.* **1979**, *101*, 5111–5121.

[124] M. Brehm, M. Thomas, S. Gehrke, B. Kirchner, *J. Chem. Phys.* **2020**, *152*.

[125] H. Yoshida, *Phys. Lett. A* **1990**, *150*, 262–268.

[126] I. Omelyan, I. Mryglod, R. Folk, *Comput. Phys. Commun.* **2003**, *151*, 272–314.

[127] S. Duane, A. D. Kennedy, B. J. Pendleton, D. Roweth, *Phys. Lett. B* **1987**, *195*, 216–222.

[128] A. H. Turner, J. D. Holbrey, *Phys.Chem.Chem.Phys* **2019**, *21*, 21782–21789.

[129] S. Zahn, B. Kirchner, D. Mollenhauer, *ChemPhysChem* **2016**, *17*, 3354–3358.

[130] S. Kaur, A. Malik, H. K. Kashyap, *J. Phys. Chem. B* **2019**, *123*, 8291–8299.

[131] N. Fanjul-Mosteirín, C. Concelló, V. del Amo, *Org. Lett.* **2016**, *18*, 4266–4269.

[132] A. R. Harifi-Mood, R. Buchner, *J. Mol. Liq.* **2017**, *225*, 689–695.

[133] A. Yadav, J. R. Kar, M. Verma, S. Naqvi, S. Pandey, *Thermochim. Acta* **2015**, *600*, 95–101.

[134] H. Shekaari, M. T. Zafarani-Moattar, A. Shayanfar, M. Mokhtarpour, *J. Mol. Liq.* **2018**, *249*, 1222–1235.

[135] A. Jindal, S. Vasudevan, *J. Phys. Chem. B* **2017**, *121*, 5595–5600.

[136] R. S. Mulliken, *J. Chem. Phys.* **1955**, *23*, 1833–1840.

[137] P. Blöchl, *J. Chem. Phys.* **1995**, *103*, 7422–7428.

[138] Y. Zhang, H. Squire, B. Gurkan, E. J. Maginn, *J. Chem. Eng. Data* **2022**, *67*, 1864–1871.

[139] V. Agieienko, R. Buchner, *Phys. Chem. Chem. Phys.* **2022**, *24*, 5265–5268.

[140] H. J. Hayler, S. Perkin, *Chem. Commun.* **2022**, *58*, 12728–12731.

[141] J. N. Canongia Lopes, A. A. Pádua, *J. Phys. Chem. B* **2006**, *110*, 3330–3335.

[142] H.-G. Liao, Y.-X. Jiang, Z.-Y. Zhou, S.-P. Chen, S.-G. Sun, *Angew. Chem. Int. Ed.* **2008**, *47*, 9100–9103.

[143] O. S. Hammond, D. T. Bowron, K. J. Edler, *Angew. Chem. Int. Ed.* **2017**, *56*, 9782–9785.

[144] M. H. Zainal-Abidin, M. Hayyan, W. F. Wong, *J. Ind. Eng. Chem.* **2021**, *97*, 142–162.

[145] O. S. Hammond, A.-V. Mudring, *Chemical Communications* **2022**, *58*, 3865–3892.

[146] Q. Chen, L. Chaihu, X. Yao, X. Cao, W. Bi, J. Lin, D. D. Y. Chen, *ACS Sustain. Chem. Eng.* **2021**, *9*, 10083–10092.

[147] W. Zhang, J. Ru, Y. Hua, X. Geng, *J. Electrochem. Soc.* **2021**, *168*, 082505.

[148] O. Hollóczki, A. Berkessel, J. Mars, M. Mezger, A. Wiebe, S. R. Waldvogel, B. Kirchner, *ACS Catal.* **2017**, *7*, 1846–1852.

[149] J. R. Hunter, Q. Qiao, Y. Zhang, Q. Shao, C. Crofcheck, J. Shi, *Sci. Rep.* **2023**, *13*, 10585.

[150] X. Li, K. H. Row, *J. Sep. Sci.* **2016**, *39*, 3505–3520.

[151] Anjali, S. Pandey, *Langmuir* **2024**, *40*, 2254–2267.

[152] M. Brehm, H. Weber, M. Thomas, O. Hollóczki, B. Kirchner, *ChemPhysChem* **2015**, *16*, 3271–3277.

[153] C. Wu, Q. Huang, Z. Xu, A. T. Sipra, N. Gao, L. P. de Souza Vandenberghe, S. Vieira, C. R. Soccol, R. Zhao, S. Deng, et al., *Carbon Capture Sci. Technol.* **2024**, *11*, 100178.

[154] *IPCC, The Intergovernmental Panel on Climate Change.* https://www.ipcc.ch/.

[155] R. B. Leron, M.-H. Li, *Thermochim. Acta* **2012**, *546*, 54–60.

[156] R. B. Leron, M.-H. Li, *Thermochimica acta* **2013**, *551*, 14–19.

[157] D. S. Firaha, B. Kirchner, *J. Chem. Eng. Data* **2014**, *59*, 3098–3104.

[158] D. S. Firaha, O. Hollóczki, B. Kirchner, *Angew. Chem. Int. Ed.* **2015**, *54*, 7805–7809.

[159] D. S. Firaha, O. Hollóczki, B. Kirchner, *Angew. Chem.* **2015**, *127*, 7916–7920.

[160] O. Hollóczki, Z. Kelemen, L. Könczöl, D. Szieberth, L. Nyulászi, A. Stark, B. Kirchner, *ChemPhysChem* **2013**, *14*, 315.

[161] T. Heinze, O. A. El Seoud, A. Koschella, *Cellulose derivatives: synthesis, structure, and properties*, Springer, **2018**.

[162] A. Farrán, C. Cai, M. Sandoval, Y. Xu, J. Liu, M. J. Hernáiz, R. J. Linhardt, *Chem. Rev.* **2015**, *115*, 6811–6853.

[163] R. Portela, C. R. Leal, P. L. Almeida, R. G. Sobral, *Microb. Biotechnol.* **2019**, *12*, 586–610.

[164] F. S. Tekin, P. Z. ¸Culfaz-Emecen, *ACS Appl. Polym. Mater.* **2023**, *5*, 2185–2194.

[165] M. Ghasemi, M. Tsianou, P. Alexandridis, *Bioresource technology* **2017**, *228*, 330–338.

[166] L. König-Mattern, A. O. Komarova, A. Ghosh, S. Linke, L. K. Rihko-Struckmann, J. Luterbacher, K. Sundmacher, *Chemical Engineering Journal* **2023**, *452*, 139476.

[167] C. C. Okwuwa, F. Adam, F. M. Said, M. E. Ries, *J. Clean. Prod.* **2023**, 139166.

[168] Y.-L. Chen, X. Zhang, T.-T. You, F. Xu, *Cellulose* **2019**, *26*, 205–213.

[169] M. Francisco, A. van den Bruinhorst, M. C. Kroon, *Green Chem.* **2012**, *14*, 2153–2157.

[170] C.-W. Lai, S.-S. Yu, *ACS Appl. Mater. Interfaces* **2020**, *12*, 34235–34244.

[171] H. Ren, C. Chen, Q. Wang, D. Zhao, S. Guo, *BioResources* **2016**, *11*, 5435–5451.

[172] Y. Ma, Q. Xia, Y. Liu, W. Chen, S. Liu, Q. Wang, Y. Liu, J. Li, H. Yu, *ACS omega* **2019**, *4*, 8539–8547.

[173] M. Pan, G. Zhao, C. Ding, B. Wu, Z. Lian, H. Lian, *Carbohydr. Polym.* **2017**, *176*, 307–314.

[174] G. C. Dugoni, A. Mezzetta, L. Guazzelli, C. Chiappe, M. Ferro, A. Mele, *Green Chem.* **2020**, *22*, 8680–8691.

[175] P. Li, J. A. Sirviö, A. Haapala, H. Liimatainen, *ACS Appl. Mater. Interfaces* **2017**, *9*, 2846–2855.

[176] W. L. Jorgensen, D. S. Maxwell, J. Tirado-Rives, *J. Am. Chem. Soc.* **1996**, *118*, 11225–11236.

[177] W. Damm, A. Frontera, J. Tirado-Rives, W. L. Jorgensen, *J. Comput. Chem.* **1997**, *18*, 1955–1970.

[178] S. V. Sambasivarao, O. Acevedo, *J. Chem. Theory Comput.* **2009**, *5*, 1038–1050.

[179] E. S. Ferreira, I. V. Voroshylova, C. M. Pereira, M. N. DS Cordeiro, *J. Phys. Chem. B* **2016**, *120*, 10124–10137.

[180] Y. Cao, J. Wu, J. Zhang, H. Li, Y. Zhang, J. He, *Chem. Eng. J.* **2009**, *147*, 13–21.

[181] M. Brehm, M. Pulst, J. Kressler, D. Sebastiani, *J. Phys. Chem. B* **2019**, *123*, 3994–4003.

[182] C. J. Smith, D. V. Wagle, N. Bhawawet, S. Gehrke, O. Hollóczki, S. V. Pingali, H. O'Neill, G. A. Baker, *J. Phys. Chem. B* **2020**, *124*, 7647–7658.

[183] M. A. Smirnov, M. P. Sokolova, D. A. Tolmachev, V. K. Vorobiov, I. A. Kasatkin, N. N. Smirnov, A. V. Klaving, N. V. Bobrova, N. V. Lukasheva, A. V. Yakimansky, *Cellulose* **2020**, 1–13.

[184] B. Bhargava, S. Balasubramanian, *J. Phys. Chem. B* **2007**, *111*, 4477–4487.

[185] D. S. Firaha, B. Kirchner, *ChemSusChem* **2016**, *9*, 1591–1599.

[186] M. Thomas, M. Brehm, R. Fligg, P. Vöhringer, B. Kirchner, *Phys. Chem. Chem. Phys.* **2013**, *15*, 6608–6622.

[187] M. Thomas, B. Kirchner, *J. Phys. Chem. Lett.* **2016**, *7*, 509–513.

[188] J. Blasius, B. Kirchner, *J. Phys. Chem. B* **2020**, *124*, 7272–7283.

[189] M. von Domaros, E. Perlt, J. Ingenmey, G. Marchelli, B. Kirchner, *SoftwareX* **2018**, *7*, 356–359.

[190] A. D. Becke, *Phys. Rev. A* **1988**, *38*, 3098.

[191] J. P. Perdew, A. Ruzsinszky, G. I. Csonka, O. A. Vydrov, G. E. Scuseria, L. A. Constantin, X. Zhou, K. Burke, *Phys. Rev. Lett.* **2008**, *100*, 136406.

[192] J. Tao, J. P. Perdew, V. N. Staroverov, G. E. Scuseria, *Phys. Rev. Lett.* **2003**, *91*, 146401.

[193] M. Guidon, J. Hutter, J. VandeVondele, *J. Chem. Theory Comput.* **2010**, *6*, 2348–2364.

[194] S. Prokhorenko, K. Kalke, Y. Nahas, L. Bellaiche, *npj Comput. Mater.* **2018**, *4*, 80.

[195] H. C. Edwards, C. R. Trott, D. Sunderland, *J. Parallel.Distrib. Comput.* **2014**, *74*, 3202–3216.

[196] C. Trott, L. Berger-Vergiat, D. Poliakoff, S. Rajamanickam, D. Lebrun-Grandie, J. Madsen, N. Al Awar, M. Gligoric, G. Shipman, G. Womeldorff, *Comput. Sci. Eng.* **2021**, *23*, 10–18.

[197] C. R. Trott, D. Lebrun-Grandié, D. Arndt, J. Ciesko, V. Dang, N. Ellingwood, R. Gayatri, E. Harvey, D. S. Hollman, D. Ibanez, N. Liber, J. Madsen, J. Miles, D. Poliakoff, A. Powell, S. Rajamanickam, M. Simberg, D. Sunderland, B. Turcksin, J. Wilke, *IEEE Trans. Parallel Distrib. Syst.* **2022**, *33*, 805–817.

[198] A. P. Thompson, H. M. Aktulga, R. Berger, D. S. Bolintineanu, W. M. Brown, P. S. Crozier, P. J. in't Veld, A. Kohlmeyer, S. G. Moore, T. D. Nguyen, et al., *Comput. Phys. Commun.* **2022**, *271*, 108171.

[199] S. Nosé, *J. Chem. Phys.* **1984**, *81*, 511–519.

[200] W. G. Hoover, *Phys. Rev. A* **1985**, *31*, 1695.

[201] M. A. Martins, L. P. Silva, N. Schaeffer, D. O. Abranches, G. J. Maximo, S. P. Pinho, J. A. Coutinho, *ACS Sustain. Chem. Eng.* **2019**, *7*, 17414–17423.

[202] K. Goloviznina, Z. Gong, M. F. Costa Gomes, A. A. Pádua, *J. Chem. Theory Comput.* **2021**, *17*, 1606–1617.

[203] K. Goloviznina, Z. Gong, A. A. Padua, *Wiley Interdiscip. Rev. Comput. Mol. Sci.* **2022**, *12*, e1572.

[204] A. Chaumont, E. Engler, R. Schurhammer, *J. Phys. Chem. B* **2020**, *124*, 7239–7250.

[205] R. Maglia de Souza, M. Karttunen, M. C. C. Ribeiro, *J. Chem. Inf. Model.* **2021**, *61*, 5938–5947.

A. Are There Magic Compositions in Deep Eutectic Solvents? Effects of Composition and Water Content in Choline Chloride/Ethylene Glycol from Ab Initio Molecular Dynamics

Vahideh Alizadeh,[*] , Friedrich Malberg,[*] Agílio A. H. Pádua,[†] and Barbara Kirchner[*]

Received: 29 May 2020, Published online: 29 July 2020.

Reprinted in Appendix A with permission[‡] from

V. Alizadeh, F. Malberg, A. A. H. Pádua, B. Kirchner, *J. Phys. Chem. B* **2020**, *124*, 7433-–7443, *doi:10.1021/acs.jpcb.0c04844*.

For this article, Supporting Information is available free of charge at:
https://pubs.acs.org/doi/10.1021/acs.jpcb.0c04844.

Contributions to the manuscript

- Development of the concept
- Performing all simulations, analysis, and calculations
- Interpretation of the results
- Writing of the manuscript

---

[*] Mulliken Center for Theoretical Chemistry, Clausius Institute for Physical and Theoretical Chemistry, University of Bonn, Beringstr. 4–6, 53115 Bonn, Germany

[†] Chemistry Laboratory, École Normale Supérieure de Lyon & CNRS, 69007 Lyon, France

[‡] Permission requests to reuse material from this chapter should be directed to the American Chemical Society.

THE JOURNAL OF
PHYSICAL CHEMISTRY B

pubs.acs.org/JPCB
Article

Are There Magic Compositions in Deep Eutectic Solvents? Effects of Composition and Water Content in Choline Chloride/Ethylene Glycol from Ab Initio Molecular Dynamics

Published as part of The Journal of Physical Chemistry virtual special issue "Deep Eutectic Solvents".

Vahideh Alizadeh, Friedrich Malberg, Agílio A. H. Pádua,* and Barbara Kirchner*

Cite This: *J. Phys. Chem. B* 2020, 124, 7433−7443

Read Online

ACCESS | Metrics & More | Article Recommendations | Supporting Information

ABSTRACT: Ab initio molecular dynamics simulations at elevated temperature are carried out to investigate the microscopic structure of liquid mixtures (deep eutectic solvents) composed of 1:1 and 1:2 choline chloride:ethylene glycol ([Ch]Cl:EG) and 1:2:1 choline chloride:ethylene glycol:water ([Ch]Cl:EG:water). In the present study, we aim to understand the composition effect on the choline chloride:ethylene glycol deep eutectic solvent and whether there is a specific composition in these solvents with marked special behavior at the microscopic level. The role of hydrogen bonds between all components was investigated through distribution functions. The structures are governed by the balance of hydrogen bond networks and the different populations of the EG molecule conformations. In the water-containing system, water competes for association with the anion. Also, the charge distribution analysis, which is consistent with structural analysis, indicates that the results are not impacted by changing composition. In addition, the charge transfer observed between ions, EG, and water molecules appears to be significant.

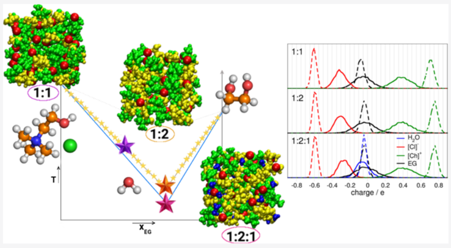

■ INTRODUCTION

Deep eutectic solvents (DESs) are known as a relatively new class of green solvents and a promising alternative for ionic liquids or conventional organic solvents, because DESs are eco-friendly, economically feasible, designer solvents (tunable), possess unique physicochemical properties, and most importantly are liquid at relatively low temperature, which is desired for many applications.[1] DESs have a great potential in different applications such as metal processing,[2−4] synthesis,[5−8] gas absorption,[9−11] and biotransformation,[12−15] among others.

DESs are mixtures of two or more substances which liquefy at a much lower temperature than the melting point (eutectic point) of the primary substances. They are classified into several main types depending on their constituents.[16] The presence of a eutectic point in the solid−liquid phase diagram of two immiscible solid and the liquid phase (which is miscible in all proportions) is characteristic of all mixtures,[17] even ideal mixtures. DESs are distinguished from usual eutectic mixtures and highlighted with the deep prefix, because their melting temperature is supposed to be significantly lower than the ideal eutectic temperature.[18] Definitions of DESs have been sought for and reported in the literature, and we adopt[19] what we consider some sensible ones: "*systems formed from a eutectic mixture of Lewis or Brønsted acids and bases which can contain a variety of anionic and/or cationic species*"[1] and "*DESs are two-component mixtures comprising hydrogen bond donor and acceptor moieties, HBD and HBA, respectively, in a molar ratio defined by the mixing itself*". These definitions need to be extended nowadays in order to address the nature of DESs more rigorously. Moreover, defining a mixture as a DES is not simple. First, in order to be able to identify and characterize mixtures as DESs, their phase diagrams should be known, which then allows evaluation of the nonideality of the liquid phase, and therefore of the solid−liquid phase diagram. In many situations, it is not possible even to calculate the ideal phase diagram due to lack of enthalpy of fusion data for the pure components.[18] Second, neither the presence of hydrogen bonding nor a hydrogen bond network in a mixture can guarantee the formation of a "deep" eutectic.[20] However, the hydrogen bonding ability and resulting network between DES components is appraised as a key feature for the decreasing melting point in DES based on experimental[21−24] and theoretical[25−29] investigations.

Another important aspect in the DES field is the choice of the "stoichiometric" proportion of the mixture. Generally, besides the temperature depression, a DES often is defined by a fixed molar ratio, which supposedly marks the eutectic point

Received: May 29, 2020
Revised: July 29, 2020
Published: July 29, 2020

https://dx.doi.org/10.1021/acs.jpcb.0c04844
J. Phys. Chem. B 2020, 124, 7433−7443

of that mixture. For example, the 1:2 molar ratio of the choline chloride:urea mixture is reported as a choline chloride:urea DES mixture.[30,31] However, what if the composition is slightly different from the exact integer ratio? Do the mixtures at those compositions exhibit significantly different physical and solvation properties? This leads to the question, are there special (integer mole ratio) compositions in deep eutectic solvents? We attempt to contribute to elucidate these questions.

Within this paper, we investigate the choline chloride:ethylene glycol ([Ch]Cl:EG) system at different compositions (1:1 and 1:2) and also the effect of water on the DES (1:2) through ab initio molecular dynamics (AIMD) simulations. We chose the [Ch]Cl:EG DES system because it is one of the most studied DESs in multiple fields such as in electrodeposition, in processing of metals,[3,32−34] and in the enhancement of drug solubility.[35] The experimental studies of [Ch]Cl:EG DES include physicochemical properties[36,37] and finding novel applications.[38,39] While AIMD simulations[26,40] as well as force field based MD simulations[41−44] have been employed to understand the molecular level structure, the nature of interactions emphasizing the specific role played by hydrogen bonding interactions between the [Ch]Cl:EG DES components in 1:2 molar ratio, to our knowledge no AIMD simulations have been carried out so far to understand the composition effect on DESs.

AIMD simulations were utilized because they are a well-suited level of theory to overcome theoretical challenges of treating the multiple intermolecular forces in DESs. This is due to the fact that the electronic structure is calculated on the fly explicitly in simulations with periodic boundary conditions.[45,46] Thus, polarization and charge transfer[40] are inherently described and many-body effects are present, contrary to classical molecular dynamics (MD) with non-polarizable force fields, which assume pairwise additivity. Although the chosen density functional theory (DFT) method applied in the present AIMD simulations is not the highest level of theory,[47,48] it is still superior with respect to the aforementioned effects compared to classical force field molecular dynamics, because it does not rely on parametrizations and combining rules for the many cross-interactions.

■ METHODS

In order to understand the microscopic structure of the [Ch]Cl:EG mixture as well as the influence of composition and water content on the hydrogen bonding network, we studied three DES systems from ab intio molecular dynamics simulations. Illustrative snapshots of the liquids can be found in Figure 1, and the system sizes are provided in Table 1.

The experimental densities at $T = 373.15$ K were calculated from eq 1 of Yadav et al.[36] ($\rho = \rho_0 + aT + bT^2$) and found to be 1.0677 g cm^{-3} for [Ch]Cl:EG 1:2 and 1.0531 g cm^{-3} for the [Ch]Cl:EG + water 1:2:1 mixture.

Generation of the Starting Structures. The starting structures for the AIMD simulations were generated from classical MD simulations utilizing the LAMMPS program package.[49] Choline chloride was modeled using the Canongia Lopes and Pádua (CL&P) force field for ionic liquids, with charges scaled by 0.8, which enables better agreement with experimental transport properties.[50] The parameters for ethylene glycol were taken from the OPLS-AA force field,[51] and water was represented by the SPC/E model.[52] First, the initial configuration of each cell was generated under periodic boundary conditions using the fftool[53] and Packmol utilities.[54] By minimizing the energy of the configuration, possible hotspots were removed. The nonbonded interactions were computed within a cutoff radius of 10 Å. Coulombic interactions beyond this distance were computed via the particle−particle particle−mesh solver[55] with an accuracy of 1 × 10^{-4}.

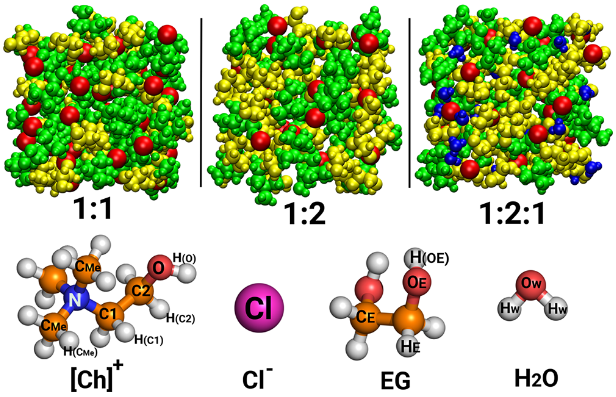

Figure 1. Top images: representations of simulation boxes with molecular color codes ([Ch]$^+$, green; Cl$^-$, red; EG, yellow; water, blue). Bottom molecular structures: ball-and-stick representations of the different species with atom color codes (C, orange; N, blue; O, red; Cl, purple; H, white).

Table 1. Simulation Parameters for Different System Compositions

system composition	1:1	1:2	1:2:1
[Ch]Cl ion pairs	32	24	24
EG molecules	32	48	48
water molecules			24
T/K	373.15	373.15	373.15
ρ/g cm^{-3}	1.0741	1.0666	1.0675
t_{sim}/ps	50	37	44.5

Subsequently, the systems were simulated in the *NPT* ensemble for at least 0.5 ns to relax the systems to the equilibrium density for the applied force field parameters. A Nosé−Hoover-chain thermostat ($T = 323.15$ K, $\tau = 100$ fs) and a Nosé−Hoover-chain barostat ($p = 1$ bar, $\tau = 500$ fs)[56,57] were applied to control temperature and pressure. The cell volume was averaged over the last 0.1 ns. By deforming the cell volume in the *NVT* ensemble over 0.1 ns, the systems were mildly perturbed so they could relax to the equilibrium volume. To control the temperature again, a Nosé−Hoover-chain thermostat ($T = 323.15$ K, $\tau = 100$ fs) was applied. After an equilibration of 0.5 ns in the *NVT* ensemble, a short run in the *NVE* ensemble was performed for 0.5 ns. The last configuration of this run as well as the average cell volume were taken as the starting configurations for the AIMD simulations.

AIMD Simulation Details. All AIMD simulations were carried out using the QUICKSTEP module[58] of the CP2K program package, where the hybrid Gaussian and plane waves (GPW) approach is used to calculate the energies and forces on the atoms. The molecularly optimized double-ζ basis set (MOLOPT-DZVP-SR-GTH)[59] was applied to all atoms together with the generalized gradient approximation (GGA) Becke−Lee−Yang−Parr (BLYP)[60,61] functional and the corresponding BLYP Goedecker−Teter−Hutter (GTH) pseudopotentials for core electrons.[62−64] A 400 Ry density CUTOFF criterion with the finest grid level was employed together with five multigrids (NGRID 5 and REL-CUTOFF 40) and a smoothing algorithm for the electron density (NN10-SMOOTH) and its derivative (NN10).[58] Dispersion interactions for the BLYP functional were corrected using the atom-based dispersion correction (D3) scheme with Becke−Johnson damping.[65,66] The direct inversion of the iterative subspace (DIIS) minimizer[67] as well as the FULL-SINGLE-INVERSE preconditioner[68] was used to achieve a fast and robust orbital transformation. The maximum number of SCF iterations to be performed for one iteration was set to 100, while a maximum of 10 iterations was performed for outer SCF loops. For the SCF calculation, 1×10^{-6} was used as the target accuracy for the SCF convergence.

Periodic boundary conditions were applied to avoid boundary effects. The simulation boxes were equilibrated for 30 ps using the canonical (*NVT*) ensemble with Nosé−Hoover thermostats for individual atoms with a time constant of 50 fs and with a time step of 0.5 fs.[56,57] The temperature for equilibration and production runs was set to 373.15 K. The production simulations were run for 50, 37, and 44.5 ps for 1:1 [Ch]Cl:EG, 1:2 [Ch]Cl:EG, and 1:2:1 [Ch]Cl:EG:H_2O systems, respectively. The time constant and the time step was kept the same as during equilibration.

AIMD, although being superior to the standard force field insofar as the intermolecular forces are calculated in each time step and thus accounting for polarizability and related effects, suffers on the other hand from small system sizes and short simulation times. Hence, we do not recommend calculating properties such as diffusion coefficients unless certain measures are taken in order to enhance sampling or otherwise correct for these shortcomings. For an in-depth discussion, we refer the reader to ref 58.

Trajectory Analysis. Our open source software TRAVIS was used for trajectory analysis.[69−73] We calculated radial distribution functions (RDFs), which give the probability to find two atoms separated by a certain distance (normalization of the average density), and also calculated number integrals (NI) showing the coordination of one species around another.

■ RESULTS AND DISCUSSION

Overall Structure. Plots of RDFs and number integrals (coordination numbers) are shown in Figure 2. The $[Ch]^+$−$[Ch]^+$ structure of the 1:2 composition is only slightly affected by either the addition of water or by changing the proportion of EG molecules. Similarly, only small effects are observed on the $[Ch]^+$−Cl^- spatial correlations. However, larger effects are visible in the Cl^-−Cl^- RDFs, in which the main peak widens and shifts to slightly larger distances. In the 1:1 system, which has higher salt concentration, the chloride anions are found with higher probability at shorter distances of 650 pm instead of 700 pm at 1:2 concentration. Comparing the water-containing system with the 1:2 system, the Cl^-−Cl^- typical distances are even larger (800 pm) and a prepeak at very short distances (450 pm) appears. This is in line with AIMD simulation results for ILs with the Cl^- anion in the presence of water, where a strong water solvation of Cl^- has been observed.[74]

The choline cation is relatively small with the positive charge (Figure 3a) located mainly on the nitrogen atom and distributed on the alkyl groups bonded to it (the ammonium headgroup). The polar hydroxyl group shows a slight negative polarization on the oxygen atom (indicated by faint red color) and positive charge on the hydrogen atom. Thus, the Cl^- anion has two potential sites to interact with the cation, forming a strong O−H···Cl hydrogen bond (hydrogen bond coordination) or interacting with the ammonium headgroup (ionic coordination); see Figure 3b. These motifs have been discussed previously for [Ch]Cl ion pairs in the gas phase.[75,76] Different first peak shapes for the cation−anion RDFs imply different coordination patterns, which have structural and chemical consequences (Figure 3b). In the 1:1 system (black curve), the first peak of the $[Ch]^+$−Cl^- RDFs shows three features—we call them features because they are not really distinguishable peaks. Meanwhile, the 1:2 system possesses a distinguished two-feature pattern (see Figure 3c), while the water containing 1:2:1 shows rather a plateau-like region. These findings of the ion−ion structure are in good agreement with the results by Chaumont et al.[77] The short distance entry corresponds to Cl^- in the region around the ammonium headgroup, and the feature or peak further away corresponds to Cl^- in the hydroxyl head region. From comparison of the $[Ch]^+$−Cl^- RDF peaks of the 1:1 system (Figure 3c, black line) with the 1:2 system (Figure 3c, red line), hydrogen bond coordination appears to be growing in the 1:2 system compared to the 1:1 system, marking the growing role of hydrogen bonds around the eutectic point. The broad peak shape of the 1:2:1 system indicates that in the presence of water there is no preference of any particular coordination pattern between cation and anion. Different coordination patterns will be evaluated further, from the point of view of conformation and contact structures in the next two sections.

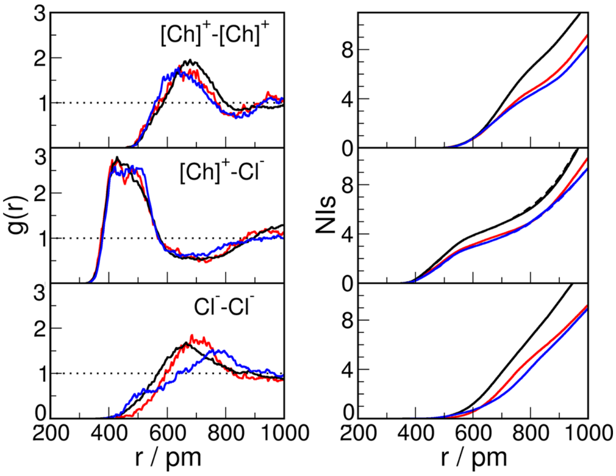

Figure 2. Center of mass RDFs and number integrals (NIs) for the counter and like ions of all three systems: 1:1 [Ch]Cl, black; 1:2 [Ch]Cl, red; 1:2:1 [Ch]Cl:EG:H_2O, blue. Note that the NIs for $[Ch]^+$−Cl^- are almost the same as those for Cl^-−$[Ch]^+$.

The behavior of the ethylene glycol molecules is illustrated in Figure 4. Altogether, the effects of composition are small. Nevertheless, it is obvious that water weakens the EG−$[Ch]^+$ and EG−Cl^- interplay. Increasing the amount of ethylene glycol molecules as well as the water presence weakens the EG−Cl^- correlation; namely, the prepeak is less pronounced. The prepeaks of EG−Cl^- are located around 320 pm, which is an indication of a strong interaction between EG molecules and Cl^-. This close contact will be discussed in detail in the

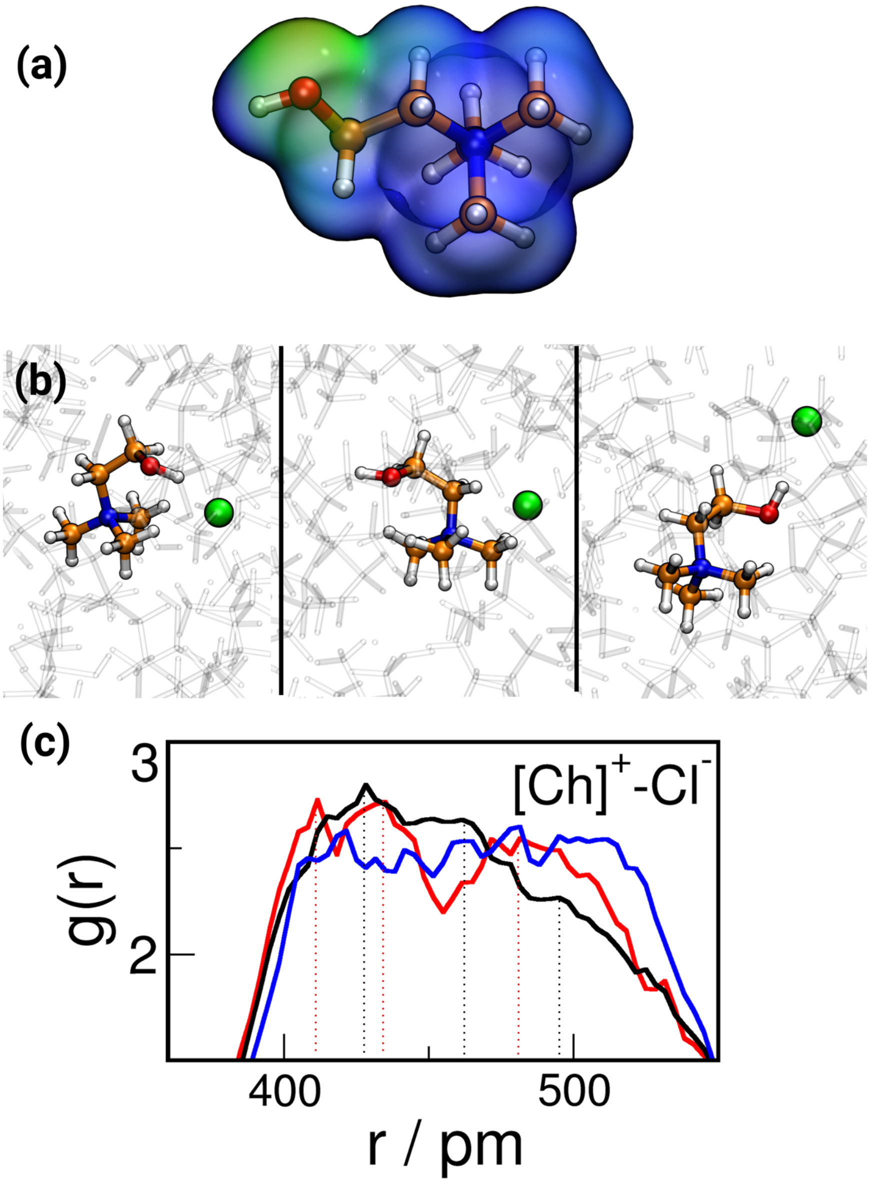

Figure 3. (a) Electrostatic potential mapped onto the $[Ch]^+$ cation. Red, negative; blue, positive; green, neutral. (b) Different snapshots from the trajectory of the systems, showcasing the close contacts between one $[Ch]^+$ cation and one Cl^- anion. (c) Zoom on the first peak in the $[Ch]^+-Cl^-$ center of mass RDFs.

contact structure section after analysis of the relative orientations of EG molecules with respect to the anion. The EG molecule possesses various possible conformations that affect its orientations with regard to other ions and molecules. The EG–EG interactions are enhanced with ethylene glycol and water addition. For example, the amount of ethylene glycol molecules in the first shell doubles from 3 to 6, which is due to the additional EG molecules and illustrates the clustering as observed before by Turner and Holbrey.[21]

The solvation structure of water in the 1:2:1 system is depicted in Figure 5. Water is closest to other water molecules (blue curve in Figure 5) and forms the usual hydrogen bonds between water molecules. However, the interaction between Cl^- anion and water is most pronounced at 300 pm and shows the highest peak. The broad peak around 400 pm related to EG molecules can be observed. $H_2O-[Ch]^+$ correlations are the weakest among those considered around 470 pm, which can be attributed to the size of the choline cations. Considering the NIs calculated to the first minimum of the RDFs depicted in Figure 5, each water molecule is surrounded by 0.5 water molecules and one Cl^- anion at close distance along with four EG molecules and three $[Ch]^+$ cations at further distance.

Altogether, we observe that an EG concentration variation and water addition mostly affects the Cl^- interaction with the EG molecules and with itself. However, the observed double peak and prepeaks (Figure 4, middle $EG-Cl^-$ panel) indicate special interactions with structural and chemical consequences which we will discuss in detail in the next section. However, there are no profound changes in the microscopic structure of the DES among the different compositions studied.

Conformational Analysis. Before analyzing the contact structure and plethora of possible hydrogen bonds, the

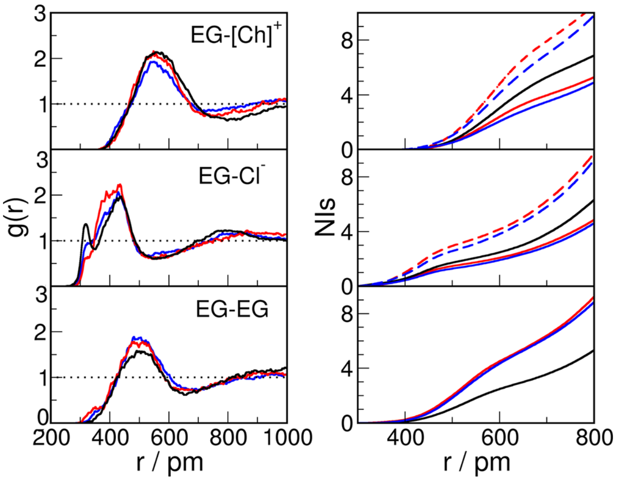

Figure 4. Center of mass RDFs and NIs for the EG molecules with themselves and the ions of all three systems: 1:1 [Ch]Cl:EG, black; 1:2 [Ch]Cl:EG, red; 1:2:1 [Ch]Cl:EG:H_2O, blue. Please note that, if only one set of NIs are shown for mixed functions, then they are identical. Otherwise, the solid lines represent EG−[Ch]$^+$ or EG−Cl$^−$ and the dashed lines are for [Ch]$^+$−EG or Cl$^−$−EG.

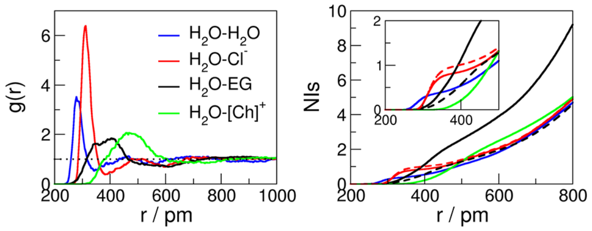

Figure 5. Center of mass RDFs and NIs of water molecules with themselves, ions, and ethylene glycol molecules in the 1:2:1 system. Please note that if only one set of NIs are shown for mixed functions then they are identical. Otherwise, solid lines represent H_2O−X and dashed lines are for X−H_2O, where X refers to Cl$^−$, EG, or [Ch]$^+$.

conformational flexibility of the cation and EG molecule is analyzed. Gauche conformers are dominant in the cation (Figure 6, left plots), with r(N−O) = 320 pm and d(NCCO)= 70°, in all systems. In the 1:1 system (black), the trans conformer is slightly preferred compared to the other systems (r(N−O) = 380 pm), whereas the preference for the N−C−C−O dihedral angle at ±180° in the 1:1 system is less marked than that in the 1:2 system. Addition of water has no influence on the cation conformations. A preference for the gauche conformation of choline cation has previously been reported in the solid, solution, and gas phase.[75,78,79]

On the right side of Figure 6, the distance distribution O_E−O_E and dihedral angle O_E−C−C−O_E of the EG molecules are presented. Due to the molecular structure of EG, two stable conformations are possible, a gauche conformation with the O_E−C−C−O_E dihedral angle of ±60° and O_E−O_E distance of 305 pm and a trans conformation with ±180° and 370 pm, respectively. The O_E−C−C−O_E dihedral angle distribution of the 1:2 system is different from that of the pure EG liquid,[80] from that of the 1:1 system, and from that of the 1:2:1 system. The gauche to trans ratio for the O_E−C−C−O_E dihedral angle is observed to be 2.0 (1:1 system), 1.2 (1:2 system), and 2.3 (1:2:1 system). Interestingly, in the pure EG liquid, a gauche to trans ratio of 4.0 is reported, which means the gauche conformation is the preferred conformation for EG in its pure liquid state.[80] Conversely, the trans conformation population of EG is almost the same as that of the gauche conformer for the 1:2 system, which also possesses the lowest melting point. This difference in dihedral angle distribution indicates a special morphology for the 1:2 system that is absent with less EG (1:1) and also in the presence of water (1:2:1), leading to a mixture with the lowest melting point. Similarly, the O_E−O_E distance distribution (Figure 6, right top) shows that the trans conformers with an O_E−O_E distance of 370 pm are slightly populated (1:2 = 1:1 > 1:2:1) in all systems, while the gauche conformer is highly populated with an O_E−O_E distance of 300 pm. All of these effects are only subtle and thus in parallel with the liquid phase structure; the conformational analyses do not show striking composition effects.

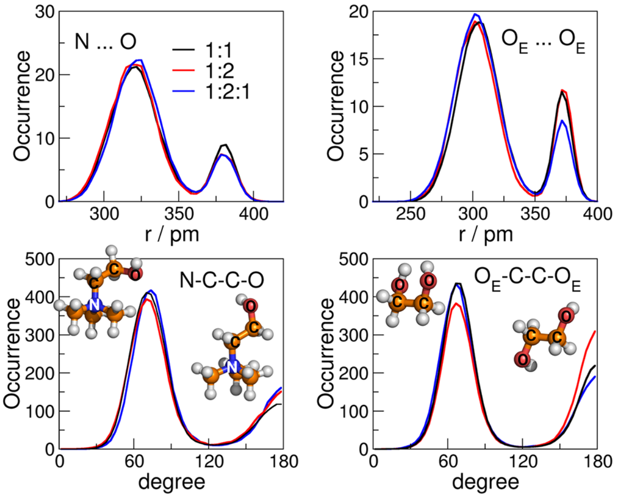

Figure 6. Conformational analysis of the cation (left) and EG (right). The distance distribution functions and dihedral distribution function show the occurrence plotted against the specific distances and dihedral angle, which reflect the conformation.

Contact Structure: Details of Hydrogen Bonding. In this section, the contact structures, i.e., the closest atoms of different molecules, in particular, the hydrogen bonding between all species, are investigated.

Figure S1 and Figure S2 depict the RDFs for each possible interaction between the Cl$^−$ anion and the hydrogen atoms of the EG molecule as well as the [Ch]$^+$ cation, and the corresponding distances and NI values are listed in Table 2. The shortest hydrogen bond distances r_{max} involving the Cl$^−$ anion are formed between the hydroxyl group oxygen atom of the EG molecule and the hydroxyl group hydrogen atom of the [Ch]$^+$ cation. The remaining hydrogen bonds which are donated by carbon atoms are longer, indicating a weaker character.

All hydrogen bonds involving the anion weaken with dilution from 1:1 over 1:2 to 1:2:1. With increasing EG concentration in 1:2 compared to 1:1, the amount of $H_{(OE)}$ atoms in the first solvation shell of Cl$^−$ increases from 0.75 to 1.0. However, the amount of $H_{(O)}$ atoms (cation) in the first shell of Cl$^−$ decreases from 0.7 to 0.5. These shifts in NIs highlight the importance of Cl$^−$−$H_{(OE)}$ (EG) interaction in [Ch]Cl:EG mixtures and especially in the 1:2 composition, as well as the transition from an ionic hydrogen bond between cation and anion in 1:1 to a hydrogen bond involving the neutral EG molecule with the anion.

Table 2. Position in First Maximum r_{max} and Minimum r_{min} in Selected Site−Site RDFs and Number Integrals (NIs) Which Were Determined to the First Minima in the RDFs[a]

		1:1		1:2		1:2:1	
center	shell	r_{max} (r_{min})	NIs	r_{max} (r_{min})	NIs	r_{max} (r_{min})	NIs
Chloride−EG							
Cl$^-$	H$_{(OE)}$	213.5 (300)	0.75/0.75	214.1 (300)	1.0/0.5	214.8 (300)	0.9/0.4
Chloride−Choline							
Cl$^-$	H$_{(O)}$	209.2 (300)	0.7	210.3 (300)	0.5	210.3 (300)	0.5
Cl$^-$	H$_{(C1)}$	265.4 (350)	0.6	264.9 (370)	0.5	263.3 (370)	0.4
Cl$^-$	H$_{(CMe)}$	272.5 (360)	0.6	275.3 (360)	0.5	275.3 (350)	0.35
EG−EG							
O$_E$	H$_{(OE)}$	181.2 (250)	0.06	180.0 (250)	0.22	178.7 (250)	0.18
EG−Choline							
O$_E$	H$_{(O)}$	177.8 (250)	0.18	177.7 (250)	0.15/0.3	175.5 (250)	0.08/0.15
O	H$_{(OE)}$	181.9 (250)	0.07	185.7 (250)	0.05/0.07	182.3 (250)	0.15/0.07

[a] All distances are in pm. The second number for NIs gives the value for the atom combination the other way around.

The interaction of the Cl$^-$ anion with cation H-sites occurs between distances of 300 and 370 pm; see Table 2 and Figure S2. The center of mass RDFs for $[Ch]^+$−Cl$^-$ suggest that the Cl$^-$ anion assumes a strong correlation through ion−ion attraction with the ammonium headgroup as well as through hydrogen bonding to the hydroxyl moiety of the $[Ch]^+$ cation. Also, the conformational analysis indicates the predominance of the gauche conformation for the $[Ch]^+$ cation (Figure 6, lower left) which enables multiple hydrogen bond donor sites for the Cl$^-$ anion in all systems. The latter motif (the Cl$^-$ anion is located between the OH and the ammonium group) is the most favorable one for the $[Ch]^+$−Cl$^-$ interactions and has been observed previously.[21,25,75] In the 1:2 system (the composition with the lower melting point), the exact same number integrals of 0.5 are observed for all combinations of Cl$^-$ anion with the cation H-sites. This suggests that the Cl$^-$ anion has an equal preference toward the nitrogen headgroup and to the hydroxyl moiety but with a closer distance to the H$_{(O)}$ hydrogen atom than to the other hydrogen atoms of the cation. With a smaller relative amount of EG molecules in the 1:1 system, there is a similar trend with slightly higher preference to the hydroxyl moiety. Opposed to this, in the presence of water (system 1:2:1), the Cl$^-$ anion is found more around H$_{(O)}$ (hydroxyl headgroup) and less around H$_{(CMe)}$ and H$_{(C1)}$ (ammonium headgroup).

To obtain a complete picture of the interaction between the Cl$^-$ anion and the EG molecule as well as the $[Ch]^+$ cation, we analyzed the hydrogen bond network between the Cl$^-$ anion and the most acidic hydrogen atoms H$_{(O)}$ (cation) and H$_{(OE)}$ (EG) in terms of combined distribution functions (CDFs). Figure S3 depicts CDFs for the distances Cl$^-$−H$_{(OE)}$ (left side, EG) and Cl$^-$−H$_{(O)}$ (right side, cation) on the x-axis and the angles O$_E$−H$_{(OE)}$−Cl (left side, EG) and O−H$_{(O)}$−Cl (right side, cation) Cl$^-$ on the y-axis. The strong peak around 210 pm/180° corresponds to these hydrogen bonds. Obviously, these peaks are very intense in all three systems, indicating that these hydrogen bonds are present all the time.

We also investigated the morphology of the hydrogen bonding network present between the Cl$^-$ anion and the most acidic hydrogen atoms (H$_{(O)}$ and H$_{(OE)}$). Thus, the probability of observing anion coordination simultaneously to two different cations or to two different EG molecules or two different water molecules is considered next. We observe in Figure S4 a more localized and intense probability at the "hydrogen bond positions" (i.e, $x = 300$ pm and $y = 300$ pm) in the system 1:1 rather than 1:2. However, water addition (system 1:2:1) increases the probability of coordination of a single anion simultaneously with two different cations, which reflects that the presence of water is pulling the ions toward each other. These observations are in agreement with the NI shifts of Table 2 and with the RDFs of Figure 2.

The EG molecules possess two hydroxyl groups, which raises the question regarding the hydrogen bond network of whether the Cl$^-$ anion is connected to one EG molecule by a single hydrogen bond or by two hydrogen bonds simultaneously; i.e., does the EG molecule display 2-fold[81] hydrogen bonds? Figure 7 depicts CDFs for two distances: the x-axis represents the distances between the first Cl$^-$−H$_{(OE)}$, and the y-axis represents the distances between the second Cl$^-$−H$_{(OE)}$. We observe strong peaks at $x = 210$ pm and $y = 210$ pm for the 1:1 system and a more diffuse distribution for the 1:2 system (Figure 7, 1:2). The high probability of the gauche conformer of EG in system 1:1 makes this kind of interaction possible. This observation along with the conformational analysis allows us to conclude that the large prepeak in the center of mass RDFs of EG−Cl$^-$ (Figure 4) of the 1:1 system arises from the interaction of a Cl$^-$ anion with an EG molecule by a 2-fold hydrogen bond, while the 1:2 system might rather show a flexible (fluctuating) network of hydrogen bonds similar to pure water, which may be one reason behind the lower melting point in the 1:2 system compared to the 1:1 system.

The hydrogen bonds between all possible OH group combinations are illustrated in Figure S5 and Figure S6. No cation−cation hydrogen bond can be observed, which is reflected in the RDFs with no significant peaks (see Figure S5), O−H$_{(O)}$. The interaction between the EG oxygen atom (EG as HB acceptor) and the hydrogen atom of the cationic hydroxyl group (cation as HB donor) (see Figure S5), O$_E$−H$_{(O)}$, are prominent interactions between hydroxyl groups, as indicated by the intense first peak. The hydrogen bonds between H$_{(O)}$ and O$_E$ weaken with dilution. While the O$_E$ are surrounded by less H$_{(O)}$, the H$_{(O)}$ are surrounded by more O$_E$ upon dilution (see NIs in Table 2). Another possible hydrogen bond between cations and EG molecules is the interaction of the $[Ch]^+$ cation oxygen atom with the hydrogen atom of EG hydroxyl groups (O−H$_{(OE)}$), in which the cation plays the role of HB acceptor and EG that of hydrogen bond donor. The O−H$_{(OE)}$ bonds have a slight enhancement in the 1:2 system, when compared to the systems with a lack of EG (1:1) and water addition (1:2:1).

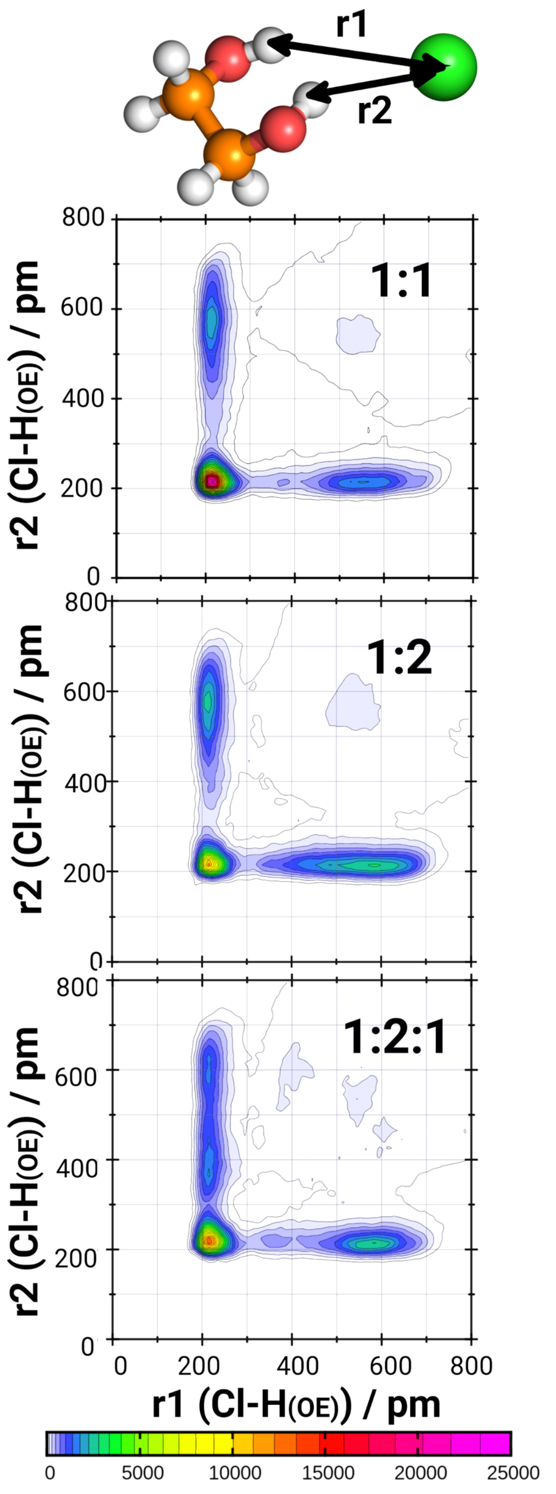

Figure 7. Combined distribution functions showing the possibility of the EG molecule to form a 2-fold hydrogen bond.[81]

The O_E–$H_{(OE)}$ RDFs show the highest occurrence in 1:2 rather than 1:2:1 and 1:1 systems. This indicates that hydrogen bonds between EG–EG (self-association), next to the weakening of ion–ion networks, are important factors contributing to a decrease in the melting point. Please note that the O_E–$H_{(OE)}$ RDFs and NIs slightly decrease upon water addition, since water also has the possibility to interact with $H_{(OE)}$ and O_E as well.

A closer look at the water contact structure is presented in Figure S7 and Table 3. Although the H_W atoms of the water molecules mainly interact with Cl^- anions at 219.3 pm, the O_W atoms interact with the acidic hydrogen atoms of the EG molecules ($H_{(OE)}$) and the $[Ch]^+$ cations ($H_{(O)}$) at 180.1 and 175.1 pm, respectively (see Table 3).

Table 3. Position in the First Maximum (r_{max}) and Minimum (r_{min}) in Selected Site–Site RDFs and Number Integrals (NIs) Which Were Determined to First Minima in the RDFs[a]

center	shell	1:2:1	
		r_{max} (r_{min})/pm	NIs
		Water–Chloride	
Cl	H_W	219.3 (290)	0.4
		Water–Choline	
O_W	$H_{(O)}$	175.1 (250)	0.14/0.002
O	H_W	183.3 (250)	0.08
		Water–EG	
O_W	$H_{(OE)}$	180.1 (250)	0.2/0.1
O_E	H_W	182.4 (250)	0.06/0.12
		Water–Water	
O_W	H_W	182.9 (250)	0.08

[a] The second number for NIs gives the value for the atom combination the other way around; otherwise, it is the same.

Charge Analysis. Charge delocalization and charge transfer between the cation, anion, and hydrogen bond donor molecules through hydrogen bonds play an eminent role in the suppression of melting points and formation of DESs.[40] In the following section, we carry out a charge analysis. It is well-known that the values calculated for charge depend on the method.[82,83] Our objective is to shed light on the charge distribution, not on obtaining absolute values. To illustrate this, we show two charge sets, namely, Mulliken[84] and Blöchl[85] charges. Figure 8 shows the charge distributions for the cations, anions, EG molecules, and water molecules in the 1:1, 1:2, and 1:2:1 systems. The obtained charge distributions

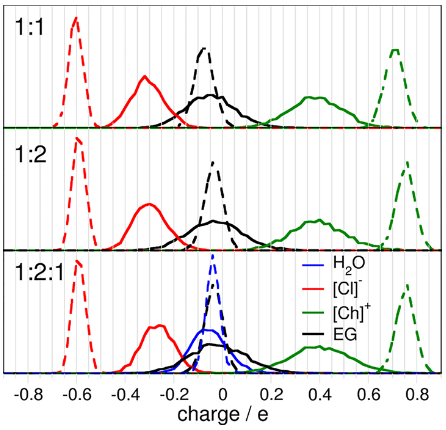

Figure 8. Total charge distribution of the cations, anions, EG molecules, and water molecules in systems 1:1, 1:2, and 1:2:1. The solid lines are Blöchl charges, and the dashed lines are Mulliken charges.

https://dx.doi.org/10.1021/acs.jpcb.0c04844
J. Phys. Chem. B 2020, 124, 7433−7443

Table 4. Total Average Charge ($\bar{q}$) and Full Width at Half-Maximum (FWHM) of Total Charge Distribution Graphs of the Cations, Anions, EG Molecules, and Water Molecules in Systems 1:1, 1:2, and 1:2:1[a]

	1:1		1:2		1:2:1	
	$\bar{q}$	fwhm	$\bar{q}$	fwhm	$\bar{q}$	fwhm
$[Ch]^+$	0.37 (0.70)	0.26 (0.1)	0.33 (0.75)	0.24 (0.09)	0.38 (0.75)	0.28 (0.09)
Cl^-	−0.32 (−0.62)	0.15 (0.07)	−0.30 (−0.60)	0.16 (0.07)	−0.27 (−0.60)	0.16 (0.07)
EG	−0.05 (−0.08)	0.23 (0.09)	−0.03 (−0.05)	0.25 (0.09)	−0.05 (−0.05)	0.27 (0.09)
water					−0.06 (−0.05)	0.18 (0.06)

[a] The numbers in parentheses were obtained from the Mulliken method, and the others were obtained from the Blöchl method.

do not depend on the box size.[40] It is noteworthy that the Mulliken and Blöchl charges are in agreement with each other in terms of trends but not in terms of absolute values, as explained above. Generally, the values in Figure 8 and Table 4 show that charges are not integer but fractional and are not impacted much by the composition of the systems. Another fact is that charges are not fixed but they vary along with the simulation and that they fluctuate in Gaussian distribution. The full width at half-maximum (fwhm) of charge distribution suggests the charge variation range, which is high in the case of the cation and EG molecule, rather than the anion (see Table 4). The charge distribution graphs obtained from the Blöchl method possess a larger fwhm than those from the Mulliken method (see Figure 8 and Table 4).

It is interesting that water and EG molecules are not neutral in the studied liquids (mixtures or DESs). It seems that charge transfer not only happens between ions, but it also occurs somewhat toward the EG and water molecules, with the variation in charge transfer with composition and water addition confirmed by the relative position of charge graphs (see Figure 8 and Table 4). In other words, cations and anions are losing their charge, which is especially evident for the anions in the presence of water molecules. The relative position of the charge distributions of the water molecules exhibits a pick on the negative side (−0.06*e*), which implies that part of the charge of the anions has shifted to the water molecules. The charge analysis is in good agreement with structural analysis which presents strong water solvation of Cl^-.

In system 1:2 compared to system 1:1, upon dilution (increasing EG), the total average charge decreases in absolute value (see Table 4,) which means more polarization and charge transfer effects occur through dilution from 1:1 to 1:2, probably due to the cooperative effect of EG networking in the 1:2 system. However, with water addition in system 1:2:1, the absolute amount of positive charge on the cation increased and the negative charge on the Cl^- anion decreased by spreading (transferring) more on EG molecules and water molecules. The atomic charge distribution graphs (see Figure S7) indicate the charge transfer toward the $[Ch]^+$ cation and EG molecule is similar in the systems 1:1 and 1:2. Also, it is equally distributed on the ammonium and hydroxyl headgroup of the $[Ch]^+$ cation. However, adding water in system 1:2:1 induced more charge transfer on the hydroxyl group of the $[Ch]^+$ cation. The blue curve on O seems less shifted to negative, and that on $H_{(O)}$, very slightly less shifted to positive (see Figure S7).

■ CONCLUSIONS

In this Article, we presented a comprehensive study on the structure of [Ch]Cl:EG mixtures and the [Ch]Cl:EG:water mixture. Three systems were considered: [Ch]Cl:EG mixtures at 1:1 and 1:2 molar proportion, to evaluate the composition effect, and the [Ch]Cl:EG:water mixture with molar ratio 1:2:1.

A variety of hydrogen bonds are present in these mixtures, formed between all components (cations, anions, EG molecules, and water). The geometry of the hydrogen bonds present in the systems is slightly dependent on the composition. The Cl^- anion forms hydrogen bonds with the $[Ch]^+$ cation with both the ammonium headgroup and the hydroxyl group, made possible simultaneously by the gauche conformation of the cation. In systems 1:2 and 1:1, the $[Ch]^+-Cl^-$ interaction is conserved and there is an equal preference to the nitrogen headgroup and hydroxyl moiety, with closer distance to $H_{(O)}$. However, adding water shifts the $[Ch]^+-Cl^-$ interaction toward more hydrogen bonds.

A strong hydrogen bond between the Cl^- anion and the $H_{(OE)}$ of the EG molecule was observed in all systems. The radial distribution functions (RDFs) and combined distribution (CDF) analyses allow us to conclude that the Cl^- anion interacts with an EG molecule by a 2-fold hydrogen bond in the 1:1 system, while the 1:2 system might rather show a flexible (fluctuating) network of hydrogen bonds similar to pure water. The high probability of the gauche conformer of the EG molecule in the 1:1 system and the trans conformation in the 1:2 system make these kinds of interactions possible. The presence of a fluctuating network of hydrogen bonds may be one reason for the lower melting point in the 1:2 system compared to the 1:1 system. In addition, the EG−EG hydrogen bond is found to be different from those in pure liquid EG because of the different dominant conformation of EG molecules. The gauche to trans ratio for the $O_E-C-C-O_E$ dihedral angle is observed to be 2.0 (1:1 system), 1.2 (1:2 system), and 2.3 (1:2:1 system), while, in the pure EG liquid, a gauche to trans ratio of 4.0 is reported.

The charge analysis is in good agreement with the structural analysis. The charge graphs show that the charge distribution is not impacted by the composition. Also, charge transfer occurs not only between ions but also somewhat toward the EG and water molecules. In the presence of water, some transfer of charge takes place from the anion and hydroxyl group of the cation to water molecules.

In all, the structural and conformational features, the main characteristics of H-bonding, and charge transfer do not exhibit marked contrasts induced by changes in composition. One conclusion that becomes clear from the present work is that there are no magic compositions in deep eutectic solvents. However, there are a few differences between the 1:1 system and the 1:2 system, namely, the fluctuating network of hydrogen bonds, which explains the large melting point depression in the 1:2 system.

■ ASSOCIATED CONTENT

Supporting Information

The Supporting Information is available free of charge at https://pubs.acs.org/doi/10.1021/acs.jpcb.0c04844.

> Additional figures containing the center of mass and site−site interval RDFs (Figure S1), the site−site RDFs−NIs (Figures S2, S3, S5, and S6), and CDFs (Figures S4 and S5) along with the atomic charge distribution with the Blöchl method (Figure S8). (PDF)

■ AUTHOR INFORMATION

Corresponding Authors

Agílio A. H. Pádua − *Chemistry Laboratory, École Normale Supérieure de Lyon & CNRS, 69007 Lyon, France;* orcid.org/0000-0002-7641-6526; Email: agilio.padua@ens-lyon.fr

Barbara Kirchner − *Mulliken Center for Theoretical Chemistry, University of Bonn, D-53115 Bonn, Germany;* orcid.org/0000-0001-8843-7132; Email: kirchner@thch.uni-bonn.de

Authors

Vahideh Alizadeh − *Mulliken Center for Theoretical Chemistry, University of Bonn, D-53115 Bonn, Germany*

Friedrich Malberg − *Mulliken Center for Theoretical Chemistry, University of Bonn, D-53115 Bonn, Germany*

Complete contact information is available at: https://pubs.acs.org/10.1021/acs.jpcb.0c04844

Notes

The authors declare no competing financial interest.

■ ACKNOWLEDGMENTS

We are thankful to Alain Chaumont (University of Strasbourg) and Rachel Schurhammer (University of Strasbourg) for fruitful exchanges and suggestions. Also, we would like to thank the DFG for the project number 406232243.

■ REFERENCES

(1) Smith, E. L.; Abbott, A. P.; Ryder, K. S. Deep eutectic solvents (DESs) and their applications. *Chem. Rev.* **2014**, *114*, 11060−11082.

(2) Abbott, A. P.; Capper, G.; Davies, D. L.; McKenzie, K. J.; Obi, S. U. Solubility of metal oxides in deep eutectic solvents based on choline chloride. *J. Chem. Eng. Data* **2006**, *51*, 1280−1282.

(3) Gamarra, J. D.; Marcoen, K.; Hubin, A.; Hauffman, T. Electrode-electrolyte interactions in choline chloride ethylene glycol based solvents and their effect on the electrodeposition of iron. *Electrochim. Acta* **2019**, *312*, 303−312.

(4) Abbott, A. P.; Al-Bassam, A. Z.; Goddard, A.; Harris, R. C.; Jenkin, G. R.; Nisbet, F. J.; Wieland, M. Dissolution of pyrite and other Fe−S−As minerals using deep eutectic solvents. *Green Chem.* **2017**, *19*, 2225−2233.

(5) Himeur, F.; Stein, I.; Wragg, D. S.; Slawin, A. M.; Lightfoot, P.; Morris, R. E. The ionothermal synthesis of metal organic frameworks, Ln (C9O6H3)((CH3NH) 2CO) 2, using deep eutectic solvents. *Solid State Sci.* **2010**, *12*, 418−421.

(6) Meng, Y.; Liu, J.-L.; Zhang, Z.-M.; Lin, W.-Q.; Lin, Z.-J.; Tong, M.-L. Ionothermal synthesis of two oxalate-bridged lanthanide (III) chains with slow magnetization relaxation by using a deep eutectic solvent. *Dalton Trans* **2013**, *42*, 12853−12856.

(7) Hammond, O. S.; Edler, K. J.; Bowron, D. T.; Torrente-Murciano, L. Deep eutectic-solvothermal synthesis of nanostructured ceria. *Nat. Commun.* **2017**, *8*, 14150.

(8) Hong, S.; Doughty, R. M.; Osterloh, F. E.; Zaikina, J. V. Deep eutectic solvent route synthesis of zinc and copper vanadate n-type semiconductors−mapping oxygen vacancies and their effect on photovoltage. *J. Mater. Chem. A* **2019**, *7*, 12303−12316.

(9) Korotkevich, A.; Firaha, D. S.; Padua, A. A.; Kirchner, B. Ab initio molecular dynamics simulations of SO2 solvation in choline chloride/glycerol deep eutectic solvent. *Fluid Phase Equilib.* **2017**, *448*, 59−68.

(10) Waite, S. L.; Li, H.; Page, A. J. NO2 Solvation Structure in Choline Chloride Deep Eutectic Solvents-The Role of the Hydrogen Bond Donor. *J. Phys. Chem. B* **2018**, *122*, 4336−4344.

(11) Garcia, G.; Aparicio, S.; Ullah, R.; Atilhan, M. Deep eutectic solvents: physicochemical properties and gas separation applications. *Energy Fuels* **2015**, *29*, 2616−2644.

(12) Zhao, H.; Baker, G. A.; Holmes, S. Protease activation in glycerol-based deep eutectic solvents. *J. Mol. Catal. B: Enzym.* **2011**, *72*, 163−167.

(13) Kim, K. H.; Dutta, T.; Sun, J.; Simmons, B.; Singh, S. Biomass pretreatment using deep eutectic solvents from lignin derived phenols. *Green Chem.* **2018**, *20*, 809−815.

(14) Liu, Q.; Zhao, X.; Yu, D.; Yu, H.; Zhang, Y.; Xue, Z.; Mu, T. Novel deep eutectic solvents with different functional groups towards highly efficient dissolution of lignin. *Green Chem.* **2019**, *21*, 5291−5297.

(15) Satlewal, A.; Agrawal, R.; Bhagia, S.; Sangoro, J.; Ragauskas, A. J. Natural deep eutectic solvents for lignocellulosic biomass pretreatment: Recent developments, challenges and novel opportunities. *Biotechnol. Adv.* **2018**, *36*, 2032−2050.

(16) Abranches, D. O.; Martins, M. A.; Silva, L. P.; Schaeffer, N.; Pinho, S. P.; Coutinho, J. A. Phenolic hydrogen bond donors in the formation of non-ionic deep eutectic solvents: the quest for type V DES. *Chem. Commun.* **2019**, *55*, 10253−10256.

(17) Levine, I. N. *Physical Chemistry*; Hodge, T. L., Oberbroeckling, S. R., Eds.; 2008.

(18) Martins, M. A.; Pinho, S. P.; Coutinho, J. A. Insights into the Nature of Eutectic and Deep Eutectic Mixtures. *J. Solution Chem.* **2019**, *48*, 962−982.

(19) Alizadeh, V.; Geller, D.; Malberg, F.; Sánchez, P. B.; Padua, A.; Kirchner, B. Strong microheterogeneity in novel deep eutectic solvents. *ChemPhysChem* **2019**, *20*, 1786−1792.

(20) Abranches, D. O.; Martins, R. O.; Silva, L. P.; Martins, M. A.; Pinho, S. P.; Coutinho, J. A. Liquefying Compounds by Forming Deep Eutectic Solvents: A Case Study for Organic Acids and Alcohols. *J. Phys. Chem. B* **2020**, *124*, 4174−4184.

(21) Turner, A. H.; Holbrey, J. D. Investigation of glycerol hydrogen-bonding networks in choline chloride/glycerol eutectic-forming liquids using neutron diffraction. *Phys. Chem. Chem. Phys.* **2019**, *21*, 21782−21789.

(22) Stefanovic, R.; Ludwig, M.; Webber, G. B.; Atkin, R.; Page, A. J. Nanostructure, hydrogen bonding and rheology in choline chloride deep eutectic solvents as a function of the hydrogen bond donor. *Phys. Chem. Chem. Phys.* **2017**, *19*, 3297−3306.

(23) Hammond, O. S.; Bowron, D. T.; Edler, K. J. Liquid structure of the choline chloride-urea deep eutectic solvent (reline) from neutron diffraction and atomistic modelling. *Green Chem.* **2016**, *18*, 2736−2744.

(24) Zhang, Y.; Poe, D.; Heroux, L.; Squire, H.; Doherty, B. W.; Long, Z.; Dadmun, M. D.; Gurkan, B. E.; Tuckerman, M. E.; Maginn, E. J. Liquid Structure and Transport Properties of the Deep Eutectic Solvent Ethaline. *J. Phys. Chem. B* **2020**, *124*, 5251−5264.

(25) Fetisov, E. O.; Harwood, D. B.; Kuo, I.-F. W.; Warrag, S. E.; Kroon, M. C.; Peters, C. J.; Siepmann, J. I. First-principles molecular dynamics study of a deep eutectic solvent: choline chloride/urea and its mixture with water. *J. Phys. Chem. B* **2018**, *122*, 1245−1254.

(26) Zahn, S. Deep eutectic solvents: similia similibus solvuntur? *Phys. Chem. Chem. Phys.* **2017**, *19*, 4041−4047.

(27) García, G.; Atilhan, M.; Aparicio, S. An approach for the rationalization of melting temperature for deep eutectic solvents from DFT. *Chem. Phys. Lett.* **2015**, *634*, 151−155.

(28) Kaur, S.; Sharma, S.; Kashyap, H. K. Bulk and interfacial structures of reline deep eutectic solvent: A molecular dynamics study. *J. Chem. Phys.* **2017**, *147*, 194507.

(29) Kumari, P.; Shobhna; Kaur, S.; Kashyap, H. K. Influence of hydration on the structure of reline deep eutectic solvent: a molecular dynamics study. *ACS omega* **2018**, *3*, 15246−15255.

(30) Abbott, A. P.; Capper, G.; Davies, D. L.; Rasheed, R. K.; Tambyrajah, V. Novel solvent properties of choline chloride/urea mixtures. *Chem. Commun.* **2003**, 70−71.

(31) Yadav, A.; Pandey, S. Densities and viscosities of (choline chloride+ urea) deep eutectic solvent and its aqueous mixtures in the temperature range 293.15 to 363.15 K. *J. Chem. Eng. Data* **2014**, *59*, 2221−2229.

(32) Jenkin, G. R.; Al-Bassam, A. Z.; Harris, R. C.; Abbott, A. P.; Smith, D. J.; Holwell, D. A.; Chapman, R. J.; Stanley, C. J. The application of deep eutectic solvent ionic liquids for environmentally-friendly dissolution and recovery of precious metals. *Miner. Eng.* **2016**, *87*, 18−24.

(33) Abbott, A. P.; Capper, G.; McKenzie, K. J.; Ryder, K. S. Electrodeposition of zinc−tin alloys from deep eutectic solvents based on choline chloride. *J. Electroanal. Chem.* **2007**, *599*, 288−294.

(34) Tran, M. K.; Rodrigues, M.-T. F.; Kato, K.; Babu, G.; Ajayan, P. M. Deep eutectic solvents for cathode recycling of Li-ion batteries. *Nat. Energy* **2019**, *4*, 339−345.

(35) Shekaari, H.; Zafarani-Moattar, M. T.; Shayanfar, A.; Mokhtarpour, M. Effect of choline chloride/ethylene glycol or glycerol as deep eutectic solvents on the solubility and thermodynamic properties of acetaminophen. *J. Mol. Liq.* **2018**, *249*, 1222−1235.

(36) Yadav, A.; Kar, J. R.; Verma, M.; Naqvi, S.; Pandey, S. Densities of aqueous mixtures of (choline chloride+ ethylene glycol) and (choline chloride+ malonic acid) deep eutectic solvents in temperature range 283.15−363.15 K. *Thermochim. Acta* **2015**, *600*, 95−101.

(37) Harifi-Mood, A. R.; Buchner, R. Density, viscosity, and conductivity of choline chloride+ ethylene glycol as a deep eutectic solvent and its binary mixtures with dimethyl sulfoxide. *J. Mol. Liq.* **2017**, *225*, 689−695.

(38) Fanjul-Mosteirín, N.; Concelló, C.; del Amo, V. L-Isoleucine in a choline chloride/ethylene glycol deep eutectic solvent: A reusable reaction kit for the asymmetric cross-aldol carboligation. *Org. Lett.* **2016**, *18*, 4266−4269.

(39) Hammond, O. S.; Li, H.; Westermann, C.; Al-Murshedi, A. Y.; Endres, F.; Abbott, A. P.; Warr, G. G.; Edler, K. J.; Atkin, R. Nanostructure of the deep eutectic solvent/platinum electrode interface as a function of potential and water content. *Nanoscale Horiz* **2019**, *4*, 158−168.

(40) Zahn, S.; Kirchner, B.; Mollenhauer, D. Charge spreading in deep eutectic solvents. *ChemPhysChem* **2016**, *17*, 3354−3358.

(41) Kaur, S.; Malik, A.; Kashyap, H. K. Anatomy of Microscopic Structure of Ethaline Deep Eutectic Solvent Decoded through Molecular Dynamics Simulations. *J. Phys. Chem. B* **2019**, *123*, 8291−8299.

(42) Kaur, S.; Gupta, A.; Kashyap, H. How Hydration Affects the Microscopic Structural Morphology in a Deep Eutectic Solvent. *J. Phys. Chem. B* **2020**, *124*, 2230−2237.

(43) Ferreira, E. S.; Voroshylova, I. V.; Pereira, C. M.; DS Cordeiro, M. N. Improved force field model for the deep eutectic solvent ethaline: Reliable physicochemical properties. *J. Phys. Chem. B* **2016**, *120*, 10124−10137.

(44) Perkins, S. L.; Painter, P.; Colina, C. M. Experimental and computational studies of choline chloride-based deep eutectic solvents. *J. Chem. Eng. Data* **2014**, *59*, 3652−3662.

(45) Kirchner, B.; di Dio, P. J.; Hutter, J. *Multiscale Molecular Methods in Applied Chemistry*; Springer, 2011; pp 109−153.

(46) Kirchner, B.; Hollóczki, O.; Canongia Lopes, J. N.; Pádua, A. A. Multiresolution calculation of ionic liquids. *Wiley Interdiscip. Rev. Comput. Mol. Sci.* **2015**, *5*, 202−214.

(47) Ruiz Pestana, L.; Mardirossian, N.; Head-Gordon, M.; Head-Gordon, T. Ab initio molecular dynamics simulations of liquid water using high quality meta-GGA functionals. *Chem. Sci.* **2017**, *8*, 3554−3565.

(48) Willow, S. Y.; Salim, M. A.; Kim, K. S.; Hirata, S. Ab initio molecular dynamics of liquid water using embedded-fragment second-order many-body perturbation theory towards its accurate property prediction. *Sci. Rep.* **2015**, *5*, 14358.

(49) Plimpton, S. Fast parallel algorithms for short-range molecular dynamics. *J. Comput. Phys.* **1995**, *117*, 1−19.

(50) Bhargava, B. L.; Balasubramanian, S. Refined potential model for atomistic simulations of ionic liquid [bmim] [PF6]. *J. Chem. Phys.* **2007**, *127*, 114510.

(51) Jorgensen, W. L.; Maxwell, D. S.; Tirado-Rives, J. Development and testing of the OPLS all-atom force field on conformational energetics and properties of organic liquids. *J. Am. Chem. Soc.* **1996**, *118*, 11225−11236.

(52) Berendsen, H.; Grigera, J.; Straatsma, T. The missing term in effective pair potentials. *J. Phys. Chem.* **1987**, *91*, 6269−6271.

(53) Padua, A. A. H. http://github.com/agiliopadua/fftool (2013).

(54) Martínez, L.; Andrade, R.; Birgin, E. G.; Martínez, J. M. PACKMOL: a package for building initial configurations for molecular dynamics simulations. *J. Comput. Chem.* **2009**, *30*, 2157−2164.

(55) Hockney, R.; Eastwood, J. *Computer Simulation Using Particles*; Adam Hilger: New York, 1989.

(56) Nosé, S. A unified formulation of the constant temperature molecular dynamics methods. *J. Chem. Phys.* **1984**, *81*, 511−519.

(57) Hoover, W. G. Canonical dynamics: Equilibrium phase-space distributions. *Phys. Rev. A: At., Mol., Opt. Phys.* **1985**, *31*, 1695.

(58) VandeVondele, J.; Krack, M.; Mohamed, F.; Parrinello, M.; Chassaing, T.; Hutter, J. Quickstep: Fast and accurate density functional calculations using a mixed Gaussian and plane waves approach. *Comput. Phys. Commun.* **2005**, *167*, 103−128.

(59) VandeVondele, J.; Hutter, J. Gaussian basis sets for accurate calculations on molecular systems in gas and condensed phases. *J. Chem. Phys.* **2007**, *127*, 114105.

(60) Becke, A. D. Density-functional exchange-energy approximation with correct asymptotic behavior. *Phys. Rev. A: At., Mol., Opt. Phys.* **1988**, *38*, 3098.

(61) Lee, C.; Yang, W.; Parr, R. G. Development of the Colle-Salvetti correlation-energy formula into a functional of the electron density. *Phys. Rev. B: Condens. Matter Mater. Phys.* **1988**, *37*, 785.

(62) Goedecker, S.; Teter, M.; Hutter, J. Separable dual-space Gaussian pseudopotentials. *Phys. Rev. B: Condens. Matter Mater. Phys.* **1996**, *54*, 1703.

(63) Hartwigsen, C.; Gœdecker, S.; Hutter, J. Relativistic separable dual-space Gaussian pseudopotentials from H to Rn. *Phys. Rev. B: Condens. Matter Mater. Phys.* **1998**, *58*, 3641.

(64) Krack, M. Pseudopotentials for H to Kr optimized for gradient-corrected exchange-correlation functionals. *Theor. Chem. Acc.* **2005**, *114*, 145−152.

(65) Grimme, S.; Antony, J.; Ehrlich, S.; Krieg, H. A consistent and accurate ab initio parametrization of density functional dispersion correction (DFT-D) for the 94 elements H-Pu. *J. Chem. Phys.* **2010**, *132*, 154104.

(66) Grimme, S.; Ehrlich, S.; Goerigk, L. Effect of the damping function in dispersion corrected density functional theory. *J. Comput. Chem.* **2011**, *32*, 1456−1465.

(67) VandeVondele, J.; Hutter, J. An efficient orbital transformation method for electronic structure calculations. *J. Chem. Phys.* **2003**, *118*, 4365−4369.

(68) Weber, V.; VandeVondele, J.; Hutter, J.; Niklasson, A. M. Direct energy functional minimization under orthogonality constraints. *J. Chem. Phys.* **2008**, *128*, 084113.

(69) Brehm, M.; Kirchner, B. TRAVIS-a free analyzer and visualizer for Monte Carlo and molecular dynamics trajectories. *J. Chem. Inf. Model.* **2011**, *51*, 2007−2023.

(70) Brehm, M.; Weber, H.; Pensado, A. S.; Stark, A.; Kirchner, B. Liquid Structure and Cluster Formation in Ionic Liquid/Water Mixtures−An Extensive ab initio Molecular Dynamics Study on 1-

Ethyl-3-Methylimidazolium Acetate/Water Mixtures—Part II. *Z. Phys. Chem.* **2013**, *227*, 177−204.

(71) Brehm, M.; Weber, H.; Thomas, M.; Hollóczki, O.; Kirchner, B. Domain Analysis in Nanostructured Liquids: A Post-Molecular Dynamics Study at the Example of Ionic Liquids. *ChemPhysChem* **2015**, *16*, 3271−3277.

(72) Hollóczki, O.; Malberg, F.; Welton, T.; Kirchner, B. On the origin of ionicity in ionic liquids. Ion pairing versus charge transfer. *Phys. Chem. Chem. Phys.* **2014**, *16*, 16880−16890.

(73) Brehm, M.; Thomas, M.; Gehrke, S.; Kirchner, B. TRAVIS-A free analyzer for trajectories from molecular simulation. *J. Chem. Phys.* **2020**, *152*, 164105.

(74) Macchieraldo, R.; Esser, L.; Elfgen, R.; Voepel, P.; Zahn, S.; Smarsly, B. M.; Kirchner, B. Hydrophilic ionic liquid mixtures of weakly and strongly coordinating anions with and without water. *ACS Omega* **2018**, *3*, 8567−8582.

(75) Ashworth, C. R.; Matthews, R. P.; Welton, T.; Hunt, P. A. Doubly ionic hydrogen bond interactions within the choline chloride−urea deep eutectic solvent. *Phys. Chem. Chem. Phys.* **2016**, *18*, 18145−18160.

(76) Davies, A. S.; George, W. O.; Howard, S. T. Ab initio and DFT computer studies of complexes of quaternary nitrogen cations: trimethylammonium, tetramethylammonium, trimethylethylammonium, choline and acetylcholine with hydroxide, fluoride and chloride anions. *Phys. Chem. Chem. Phys.* **2003**, *5*, 4533−4540.

(77) Chaumont, A.; Engler, E.; Schurhammer, R. Is charge scaling really mandatory when developing force fields for Deep Eutectic Solvents? *J. Phys. Chem. B* **2020**, DOI: 10.1021/acs.jpcb.0c04907.

(78) Tanzi, L.; Benassi, P.; Nardone, M.; Ramondo, F. Vibrations of bioionic liquids by ab initio molecular dynamics and vibrational spectroscopy. *J. Phys. Chem. A* **2014**, *118*, 12229−12240.

(79) Hjortås, J.; Sørum, H. A re-investigation of the crystal structure of choline chloride. *Acta Crystallogr., Sect. B: Struct. Crystallogr. Cryst. Chem.* **1971**, *27*, 1320−1323.

(80) Jindal, A.; Vasudevan, S. Conformation of ethylene glycol in the liquid state: intra-versus intermolecular interactions. *J. Phys. Chem. B* **2017**, *121*, 5595−5600.

(81) Reckien, W.; Kirchner, B.; Peyerimhoff, S. D. Frequency analysis of amide-linked rotaxane mimetics. *J. Phys. Chem. A* **2006**, *110*, 12963−12970.

(82) Rigby, J.; Izgorodina, E. I. Assessment of atomic partial charge schemes for polarisation and charge transfer effects in ionic liquids. *Phys. Chem. Chem. Phys.* **2013**, *15*, 1632−1646.

(83) Kohagen, M.; Brehm, M.; Thar, J.; Zhao, W.; Müller-Plathe, F.; Kirchner, B. Performance of quantum chemically derived charges and persistence of ion cages in ionic liquids. A molecular dynamics simulations study of 1-n-butyl-3-methylimidazolium bromide. *J. Phys. Chem. B* **2011**, *115*, 693−702.

(84) Mulliken, R. S. Electronic population analysis on LCAO−MO molecular wave functions. I. *J. Chem. Phys.* **1955**, *23*, 1833−1840.

(85) Blöchl, P. Electrostatic decoupling of periodic images of plane-wave-expanded densities and derived atomic point charges. *J. Chem. Phys.* **1995**, *103*, 7422−7428.

B. Strong Microheterogeneity in Novel Deep Eutectic Solvents

Vahideh Alizadeh,* David Geller,* Friedrich Malberg,* PabloB. Sánchez,† Agílio A. H. Pádua,‡ and Barbara Kirchner*

Reprinted in Appendix B with permission§ from

V. Alizadeh, D. Geller, F. Malberg, P. Sánchez, A. Padua, B. Kirchner, "Strong Microheterogeneity in Novel Deep Eutectic Solvents", *ChemPhysChem* **2019**, *20*, 1786–1792, *doi:10.1002/cphc.201900307.*

For this article, Supporting Information is available free of charge at:
https://doi.org/10.1002/cphc.201900307.

Contributions to the manuscript

- Co-performing simulations and analysis
- Interpretation of the results
- Co-writing of the manuscript

---

* Mulliken Center for Theoretical Chemistry, Clausius Institute for Physical and Theoretical Chemistry, University of Bonn, Beringstr. 4–6, 53115 Bonn, Germany

† Dpto.FísicaAplicada, Facultadde Ciencias, Universidad de Vigo, CampusLagoas-Marcosendes/n, 36310VIGO–Spain

‡ Chemistry Laboratory, École Normale Supérieure de Lyon & CNRS, 69007 Lyon, France

§ Permission requests to reuse material from this chapter should be directed to Wiley-VCH GmbH.

ChemPubSoc Europe

DOI: 10.1002/cphc.201900307

CHEMPHYSCHEM
Communications

Very Important Paper

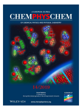

Strong Microheterogeneity in Novel Deep Eutectic Solvents

Vahideh Alizadeh,[a, b] David Geller,[a] Friedrich Malberg,[a] Pablo B. Sánchez,[c] Agilio Padua,[d] and Barbara Kirchner*[a]

With the increasing application of template assisted syntheses in deep eutectic solvents and successful application of hydrophobic deep eutectic solvents in extraction processes, where microheterogeneity plays a major role, suggestions for novel deep eutectic solvents which exhibit strong microheterogeneity are desirable. Therefore, classical molecular dynamics simulations were carried out on deep eutectic solvent systems constructed of choline chloride and some of its derivatives mixed with ethylene glycol in a molar composition of 1:2 since this is the optimal parent composition. The derivatives consisted of a series of elongated alkyl side chains and elongated alcohol side chains. Of these series only choline chloride ethylene glycol has been investigated experimentally, the other systems are suggested and theoretically investigated as possible target for synthesis. Our domain analysis supported by the clear distinction of polar and nonpolar parts from the electrostatic potentials reveals that strong microheterogeneity within these novel hypothetical deep eutectic solvents exists. Rather stretched than crumbled side chains maximize possible interaction sites for both polar and nonpolar parts which make the suggested compounds valuable objectives for experiments in order to exploit the microheterogeneity in deep eutectic solvents.

A deep eutectic solvent (DES)[1–5] can be obtained by mixing two substances which are in the majority of cases solids to obtain a low-melting mixture near the eutectic composition. These two substances are often a salt – hence the kinship to ionic liquids (ILs)[6–14] – and a hydrogen-bond donor or other molecular compound.[1–3] DESs are mostly made of cheap, readily available and rather safe starting compounds.[2] Their applications are widespread, for example in metal processing[15,16] and synthesis or biomass processing and catalysis as well as extraction,[17] but many more applications can be found and will be discovered in the future.[2,3,18–20] Calculations on DESs are rather sparse compared to experiments and often concentrate on the understanding of the hydrogen bonding behavior since a plethora of hydrogen bonds are available, examples are Refs. [5,18,21–24].

A very important kind of nanostructuring, namely, molecular ionic clusters within a complex and disordered hydrogen bonding network was observed by Edler and coworkers.[25–27] Biswas and coworkers found various type of aggregats depending on the anion and temperature.[28] So far only a few studies about polar-nonpolar microheterogeneity (MH) – which is the separation of polar and nonpolar molecular parts –[29] has occurred in literature. However, microheterogeneity has been extensively investigated in ILs[12,30–34] and recently in the context of the template or structure-directing effects in ILs.[34] As template assisted syntheses have been carried out in DESs as well[35,36] and this can be often connected to microheterogeneity, suggestions for DESs which exhibit strong MH are desirable.

MH studies in DES started when hydrophobic DES were presented and successfully applied in extraction processes.[17,37] A nanoscale spatial heterogeneity was found from molecular dynamics simulations of acetamide with $Li^+ ClO_4^-$ and propionamide with $Li^+ ClO_4^-$.[38] Analyzing the distinction into polar and nonpolar groups was carried out on the choline chloride glycerol system.[29] Further evidence for MH in standard DESs was found in a combined IR and molecular dynamics (MD) simulations work.[39] Recently a study of alkylammonium bromide mixed with glycerol appeared with the side chains increased to four units length demonstrating MH via neutron diffraction experiments and MD simulations.[40]

The lack of molecular level insight for very long side chain systems prompts the further study with respect to novel DESs systems. The herein investigated DESs (see Figures 1 and 2) are constructed of choline chloride ($T_m = 575$ K) and some of its derivatives – all of which have not been reported so far –, mixed with ethylene glycol (EG) ($T_m = 260$ K), a hydrogen-bond donor, in an optimal molar composition of 1:2 for the parent DES. We created these kind of varying DES systems in silico in order to explore strong microheterogeneity and give suggestions which of them may be valuable targets to investigate experimentally. The in silico systems include a variation a) in one of the alkyl (methyl) side chains, b) the alcohol substituted side chain, and c) an increase of all methyl groups to n-butyl groups.

From the electrostatic potential (ESP) plots mapped onto the density in Figure 1, the charge distribution is available. While any cationic head group is mainly colored in blue indicating the distribution of the positive charge over the ammonium-group, all alcohol groups are red close to the

---

[a] V. Alizadeh, D. Geller, Dr. F. Malberg, Prof. Dr. B. Kirchner
Mulliken Center for Theoretical Chemistry, University of Bonn, Beringstraße 4+6, D-53115 Bonn, Germany
E-mail: kirchner@thch.uni-bonn.de
[b] V. Alizadeh
Department of Chemistry, Institute for Advanced Studies in Basic Sciences (IASBS), Zanjan, Iran
[c] Dr. P. B. Sánchez
Dpto. Física Aplicada, Facultad de Ciencias, Universidad de Vigo, Campus Lagoas-Marcosende s/n, 36310 VIGO – Spain
[d] Prof. Dr. A. Padua
École Normale Supérieure de Lyon, Laboratoire de Chimie 46, allée d'Italie, 69364 Lyon cedex 07, France

Supporting information for this article is available on the WWW under https://doi.org/10.1002/cphc.201900307

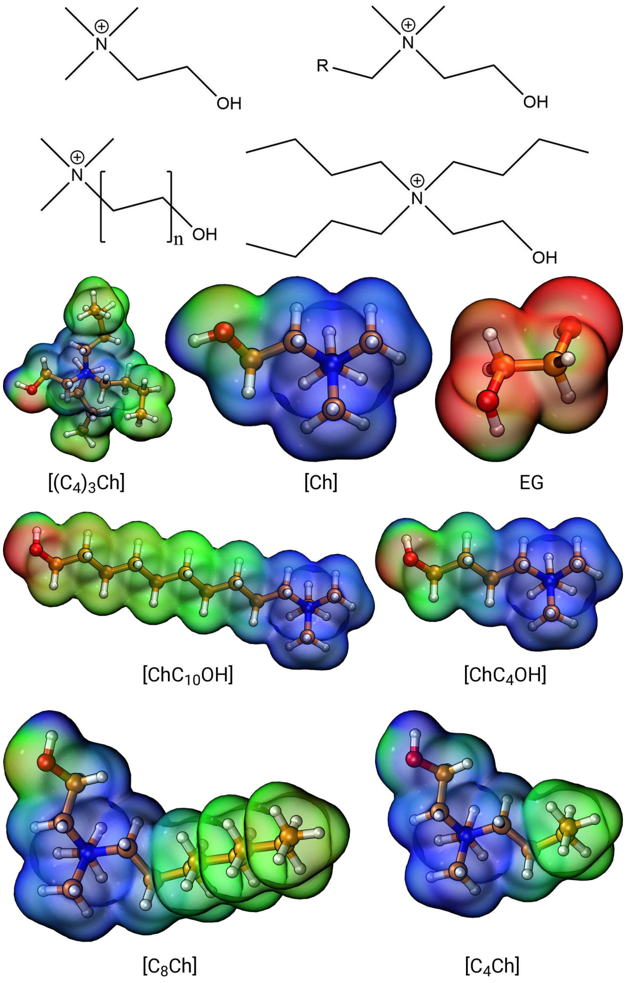

Figure 1. Components of the investigated DESs systems. First line gives the Lewis structures of the cations investigated in the following order: Choline $[Ch]^+$, alkyl-choline with R = 4,6,8 denoted as $[C_RCh]^+$, choline with an increased alcohol substituted side chain, denoted as $[ChC_xOH]^+$ with x = 4,6,8,10,12 and the tri-n-butyl-choline denoted as $[(C_4)_3Ch]^+$. Note, the counterion is always the chloride anion and the neutral molecular compound is always ethylene glycol abbreviated EG. Below we see the electrostatic potential[41] mapped onto the density (details can be found in the SI) on some choosen examples. Red: negative, blue: positive and green: neutral. The distinction into polar (red and blue) and nonpolar (green) parts is clearly visible.

oxygen atoms and blue close to the proton, see f.e. $[(C_4)_3Ch]^+$ cation in Figure 1. This is also valid for EG explaining the strong cation-EG interaction. The long alkyl chains exhibit green color indicating their neutrality or non-polarity – a better word may be lipophilicity – which is observable from the systems with increased OH-substituted alkyl group (second last row of choline-derivatives in Figure 1), but also in the elongated alkyl groups (last row of choline-derivatives in Figure 1).

All systems as listed in Figure 1 were also investigated from molecular dynamics (MD) simulations at elevated temperature of 423.15 K, details see supporting information (SI). The higher temperature was chosen in order to decrease viscosity and sampling and thus to allow for better statistics.

Table 1. Calculated densities (ρ_{cal} in $g \cdot cm^{-3}$)[42] and domain count[33,43] (last six columns) for all different DESs at 423 K. The domain count is a measure for the connectivity, i.e., 1: all subunits are connected; values ≥1: the parts are dispersed. The following subunits combinations have been chosen: 1. N: all nonpolar parts and P: all polar parts, see Figure 1; 2. N and P(I): ionic polar parts separated from EG molecules, and 3. N and P(C): cationic polar parts and EG + Cl: EG and anion.

cation	ρ_{cal}	N	P	P(I)	EG	P(C)	EG + Cl
$[Ch]^+$	1.035	–	1.0	1.2	1.0	1.0	2.2
$[C_4Ch]^+$	0.985	21.4	1.0	1.2	1.0	1.1	2.6
$[C_6Ch]^+$	0.952	3.0	1.0	1.2	1.2	1.2	3.1
$[C_8Ch]^+$	0.927	1.2	1.0	1.2	2.0	1.2	3.2
$[(C_4)_3Ch]^+$	0.919	1.0	1.0	2.3	2.2	10.2	3.8
$[ChC_4OH]^+$	1.006	100.6	1.0	1.1	1.1	1.1	2.0
$[ChC_6OH]^+$	0.977	12.9	1.0	1.1	1.2	1.2	2.7
$[ChC_8OH]^+$	0.951	2.1	1.0	1.3	1.7	1.5	3.5
$[ChC_{10}OH]^+$	0.932	1.1	1.0	1.5	2.4	1.9	4.0
$[ChC_{12}OH]^+$	0.917	1.0	1.0	1.8	3.0	2.4	4.3

Table 1 lists in the second column the calculated densities. The densities for all investigated liquids (the choline chloride/EG system as well as the suggested ones) lie in the range of 0.9 to 1.0 $g \cdot cm^{-3}$ at 423 K. Obviously, for the novel systems no experimental densities are available. However, the experimental density at lower temperature for [Ch][Cl]/EG was extrapolated to 1.045 $g \cdot cm^{-3}$ at 423 K which is in acceptable agreement to our simulated density of 1.035 $g \cdot cm^{-3}$. Furthermore, the elongation of the side chain rightfully leads to decreased densities (thus to less dense systems) probably due to the increased space requirement of the longer side chains. This trend is confirmed by the experimental hydrophobic DES study of Kroon and coworkers.[44]

Table 1 also gives the domain count[33,34,43,45–49] which indicates with numbers close to one high connectivity of different sub-molecular groups and for numbers greater than one dispersed or non-connected parts. The domain count[33,34,43,45–49] stems from a radical Voronoi tesselation of the investigated systems where the different sub-molecular groups are connected when they share at least one Voronoi face with each other. For a more detailed explanation on the methodology of the used domain analyses the reader is referred to.[33] According to the ESP analysis (Figure 1) EG is counted as polar as well as all cationic head groups with one spacer CH_2 element and/or the terminal methyl groups. Further, the OH-group and the neighbouring CH_2 element are considered as being polar, while the rest of the elongated side chains are treated as nonpolar subgroup, see also Figure 2. Similarly, the long alkyl side chain is counted as nonpolar group. With this distinction we always obtain one polar completely connected domain (domain count = 1), see in Table 1 the 4th column P, which is in agreement with the behavior of IL systems.[33,34,45] All nonpolar groups are heavily dispersed in the polar parts for side chain length of less or equal than four carbon units, see entry for DES containing the $[C_4Ch]^+$ and the $[ChC_4OH]^+$ cation 3rd column in Table 1. From the side chain length of eight carbon units, the nonpolar parts of the DES stick together as well and real MH can be observed in that the polar and the nonpolar parts each form one fully connected microphase which shows that in order

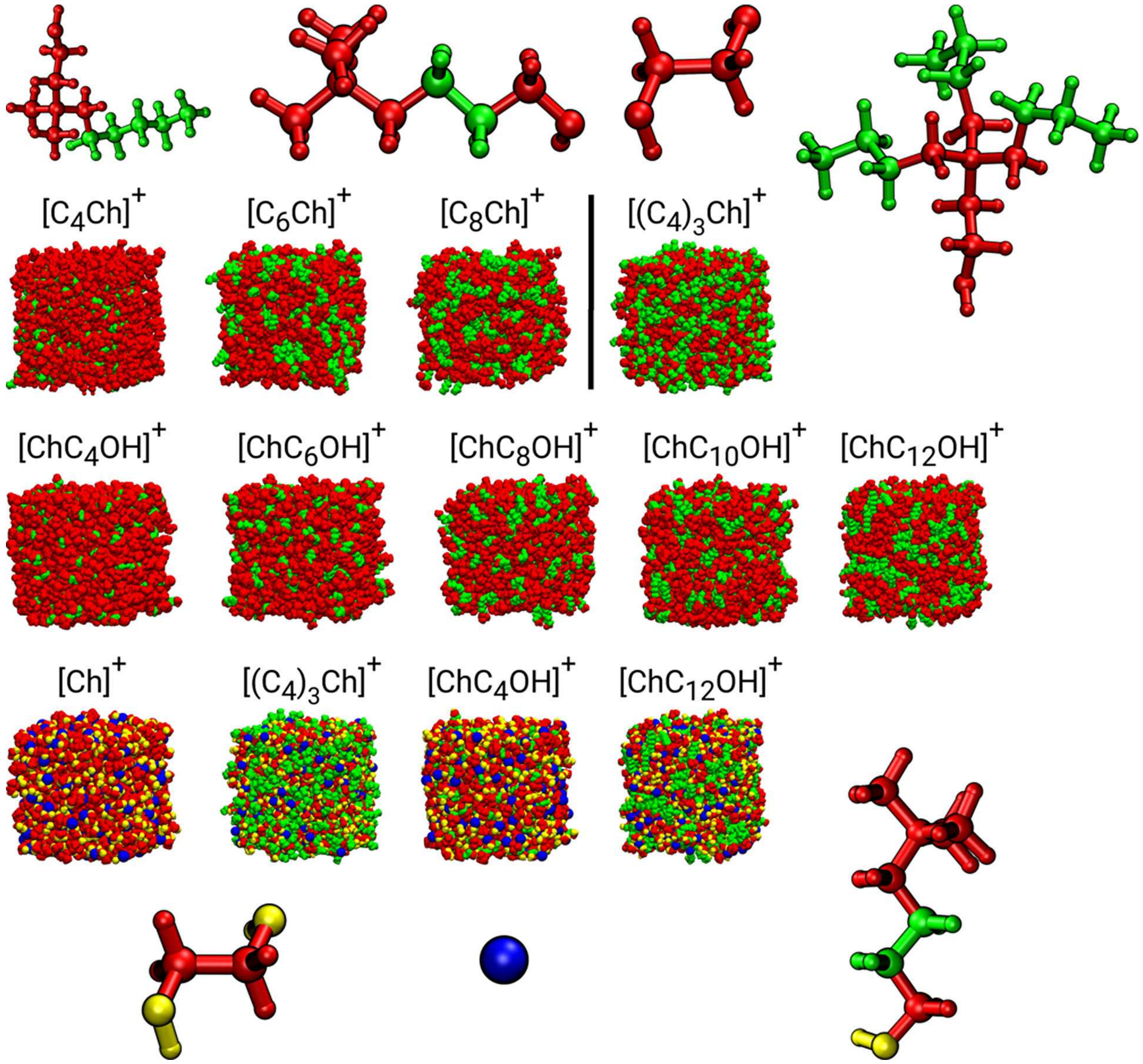

Figure 2. Ball and stick representation of the simulation boxes for all investigated DES systems. The first and the last row shows the chosen colour code at the example of $[C_6Ch]^+$, $[ChC_4OH]^+$, EG, $[(C_4)_3Ch]^+$ (above), EG, Cl^-, $[ChC_4OH]^+$ (below). The strong MH is clearly visible for the systems with side chain lengths of eight carbon units or more. For the alkyl-side chain family, the MH is stronger than for the OH-substituted side chain compounds. Furthermore, it can be observed that the chloride anion is strongly shared between the red and yellow parts.

to exploit MH these suggested compounds should be chosen by the according experiments. In the case of $[(C_4)_3Ch][Cl]$/EG we also observe fully separated microphases when considering the N and P column in Table 1. Such a strong separation is otherwhise only observed in the case of the $[ChC_{12}OH]^+$ cation. Thus, $[(C_4)_3Ch][Cl]$/EG might be suitable candidate for template synthesis as well. Further distinction into nonpolar, polar ionic and molecular subsystems (column 3, 5, and 6 in Table 1 and Table 3 in the SI) shows that the polar parts are slightly disrupted if the EG molecules are counted separately, thus the molecular parts truly belong to the polar parts of the whole system. For the cations with short side chains (less than six) all EG molecules are contributing to one domain – for the ones with longer side chain they are also more disrupted. Interestingly, all polar part perturbations are related to increasing side chain length of the nonpolar part, i.e., the longer the nonpolar part the more dispersion is observed in the polar part. This indicates a small but maybe non-negligible change in the micro-structure of the polar parts. This dispersion of the polar parts is even more obvious when a distinction between cationic polar part and other polar parts are made. Again $[(C_4)_3Ch][Cl]$/EG seems to be a special case, because the dispersion of the polar (cationic) part is not small at all, but clearly present when considered individually. Since both – ethylene glycol and the chloride anion – are rather small compared to the polar part of some of the choline cations, the effect on the connectivity of the polar parts (except for $[(C_4)_3Ch][Cl]$) is rather small. Most likely, with larger anions or larger hydrogen bond donors the effect on the connectivity of the polar parts will be more significant as was observed for ionic liquids.[50] Counting chloride within the ethylene glycol subunits (see column 7 and 8 in Table 1 and Table 3 in the SI) leads again to a disruption of this domain, which suggests that only if all polar subunits are accounted for, i. e., cation, anion and EG, the fully interconnected polar microphase can be obtained.

For understanding the conformation of the side chains, we depict in Figure 3 the intramolecular distance distribution function of the nitrogen atom to the terminal heavy atom of the side chain, namely the oxygen (left: hydroxyalkyl side chain cations) or the carbon (right: alkyl side chain cations) atom. Keeping in mind that with increasing side chain dilution-effects with respect to larger amount of nonpolar parts are possible, we refrain from discussing the decreasing peak height. Common features are visible with respect to the different side chains, see black, red, and, blue curves in Figure 3 where approximately a constant change by 200–250 pm in peak location per side chain unit can be observed. With larger side chain the peaks are less distinct, see the change from three peaks to one common peak for the $[ChC_xOH]^+$ series. For the $[ChC_xOH]^+$ series the side chain with the OH-group in gauche conformation stays the most important, with small after-peaks or -shoulders indicating some population of the fully stretched trans conformation. For the $[C_xCh]^+$ series the majority of the trans fully stretched is only present in the $[C_4Ch]^+$, for x = 6 and 8 the gauche fully stretched conformation is dominant. In total, the side chains are rather stretched than crumbled independent of length which maximizes possible interaction sites for both polar and nonpolar parts.

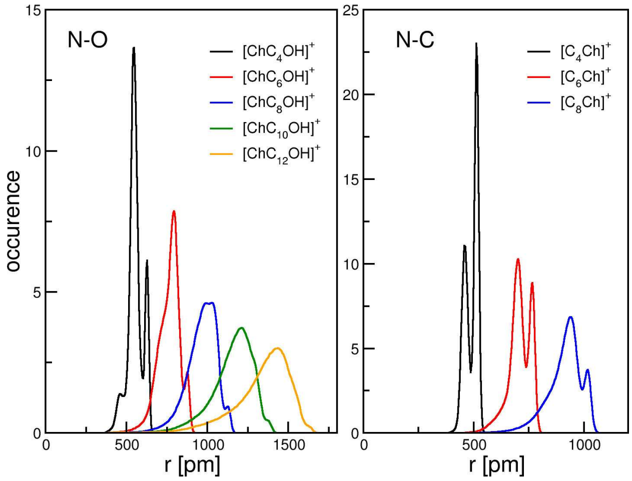

Figure 3. Intramolecular distance distribution function of nitrogen atom to oxygen atom for the $[ChC_xOH]^+$ systems (left) and to terminal carbon atom for the $[C_RCh]^+$ substances (right). N–C Curve for $[(C_4)_3Ch]^+$ matches $[C_4Ch]^+$ why it is neglected.

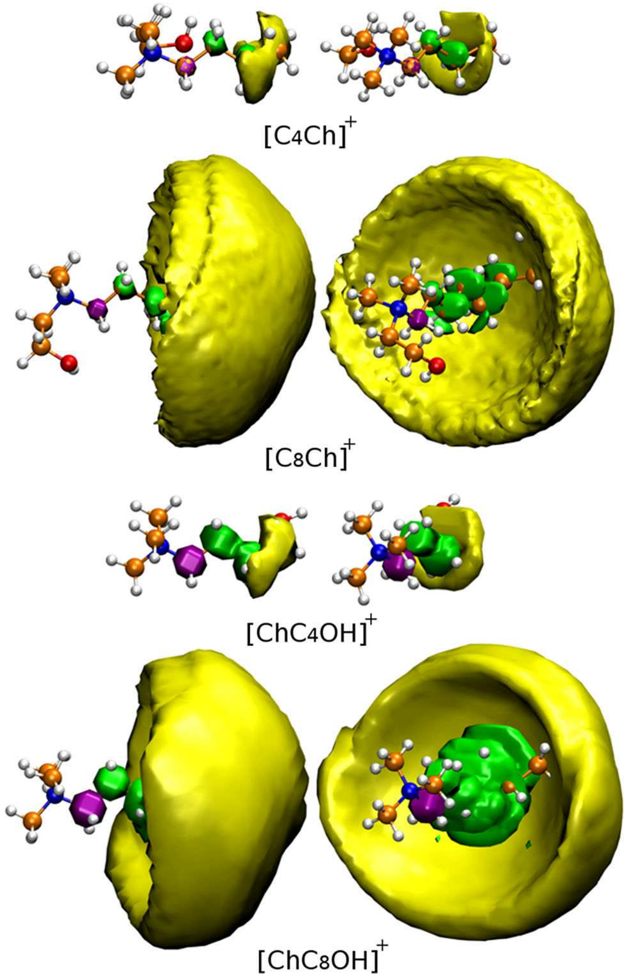

Figure 4. Spatial distribution function[43,51] in order to illustrate the side chain conformers. For each side chain series two examples are chosen, the one with C4 and C8. The carbon atom in neighbourhood to the nitrogen is colored in purple, all the carbon atoms inbetween are colored in green and the terminal carbon atom is colored in yellow. For the isosurface we choose 1% of the maximum value for all colors in all systems.

Similarly, as indicated by the intramolecular distribution functions of Figure 3, the spatial distribution functions of Figure 4 show that different conformers for the cations can be occupied. We marked in this plot the neighbouring carbon atom purple, the terminal yellow and the carbon atoms inbetween green. For the longer side chains obviously much more possibilities exists which leads to the broadening of the peaks in the intramolecular distribution function (Figure 3), see for example yellow, but also green and purple isosurface for the C8 versus the C4 series. Comparing the alkyl side chain series to the alcohol side chain series, we observe that spheres for the latter are much more smeared out, i. e., they are less distinct than in the alkyl side chain series which is reflected in the more pronounced peaks for the alkyl side chain series in Figure 3.

Indirect subtle effects of the long side chains might be observed for the polar hydrogen bonded network. Because hydrogen bonds were subject to many extensive discussions in literature,[18,21,52–54] we show in Figure 5 only for selected examples the corresponding combined distribution function for the hydrogen bonds between chloride and the cation as well as the EG. It is clear from these examples and from literature[18,21,52–54] that the hydrogen bonds in the different DES

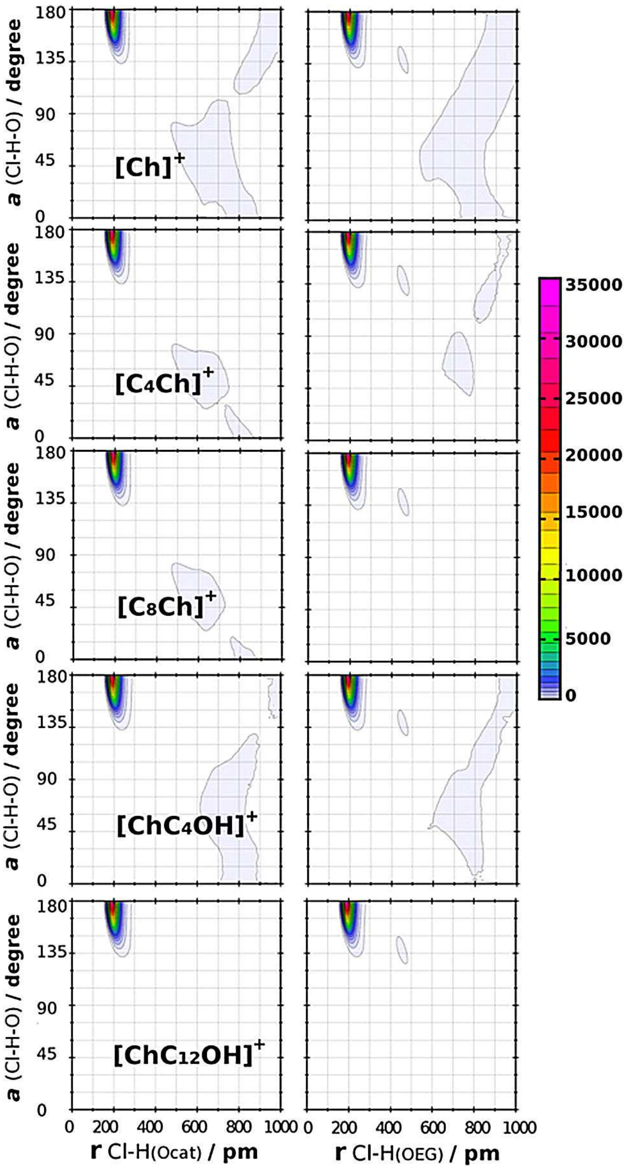

Figure 5. Combined distribution function[43,51] in order to illustrate the presence of a hydrogen bond. On the left the hydrogen bond between the chloride anion and the OH group of the cation is depicted and on the right the one between the chloride and the OH group of the EG is shown. The Cl–H–O angle **a** in degrees is plotted versus the Cl···H distance **r** in pm.

are all very strong, because they exhibit an extremely directional behavior, i.e., angles **a** (Cl–H–O) are close to 180 degrees and the peaks extend only to 165 degrees. This is different for aprotic ionic liquids, see for example [51,55,56], where usually such a directionaly cannot be achieved, because the donor atom often is a carbon atom. Furthermore, differences with respect to the chosen hydrogen bond and with respect to the different cations are too subtle to be discussed in details. The only point worth mentioning is, that for increasing side chain, less entries away from the major peak at approximately 180 degrees and a distance of 180 pm can be observed.

In Figure 6 we show the corresponding radial distribution functions (RDFs) and number intergrals (NI) which give insight into certain atom-atom distance probability and corresponding coordination numbers, further RDFs can be found in the SI. Considering the Cl–O(cation) pair (see Figure 6 left row), a strong peak is observed at 290/292 pm and the Cl anion is surrounded in the first solvent shell by 0.9/0.8 oxygen atoms if one considers the family with increasing alkyl/hydroxyalkyl side chain. Differences – i.e., drops in the coordination number with longer side chain – only occur from a distance larger than 450 pm on, which hints to a slightly stronger seperation of the polar groups and thus an increase in the size of the non-polar domains, supporting the picture of a stronger MH in the systems with longer side chains. In Figure 6 right row (Cl–O (EG)) the RDFs show a large peak at around 290 pm for all substances again indicating hydrogen bonding. In the first solvent shell, the Cl atom is surrounded by approximatley 3.0 oxygen atoms. For larger distances, the NIs for the Cl–O(EG) interactions show similar coordination numbers for all investigated systems, except for the bulky $[(C_4)_3Ch][Cl]$. Nonetheless, these simple analyses of the hydrogen bond network show that only subtle effects of the MH can be found for the hydrogen bond interactions.

In conclusion, with the clear distinction between polar and nonpolar groups provided by the electrostatic potential (see Figure 1) and a domain analysis the novel DESs investigated in this work all show MH and in some cases even strong MH. For all systems, the polar groups are always completely connected forming one domain, while the nonpolar groups tend to be highly dispersed within the polar parts for side chain lengths of four carbon units. Strong microheterogeneity, where both polar and non-polar parts form one completely connected domain each, can be observed from side chain lengths of eight carbon units and more, making those compounds valuable targets for synthesis. Intermolecular distance distribution functions of the nitrogen atom to the terminal heavy atom within the side chains of the cations show that these side chains are rather stretched not crumbled which maximizes the possible interaction sites for both polar and nonpolar parts. Subtle indirect effects of the MH can also be observed within the hydrogen bond network of the polar domains. The number integral of Cl–O(cation) hints to a slightly stronger separation of the polar groups for the systems with longer side chains and thus to an increase in the size of the non-polar domains, supporting the picture of the stronger MH obtained from the domain analysis. Several processes such as template assisted synthesis and extraction processes utilize strong MH which make these suggested substances valuable targets for synthesis.

Acknowledgements

We would like to thank the DFG for the grant KI768/19-1 and the SPP 1708 project KI768/15-1 and the DAAD for providing funds for VA. PBS acknowledges Xunta de Galicia for his postdoctoral fellowship.

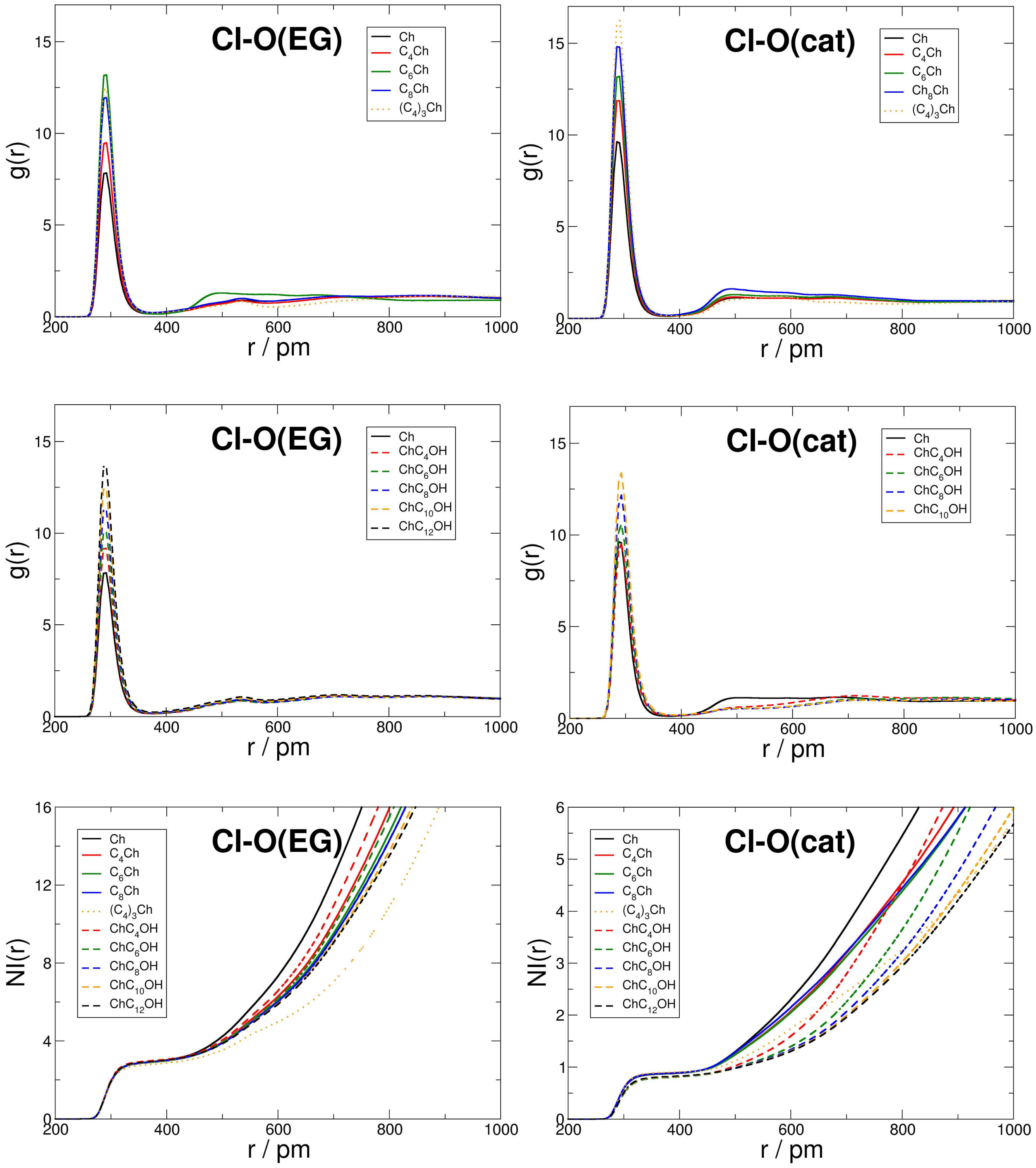

Figure 6. Radial distribution function in order to illustrate the hydrogen bond network. Upper and middle panel left: RDF between the Cl and the oxygen atom of the cation; Upper and middle panel right: RDF between the Cl and the oxygen atom of EG; Lower panel: Number integrals for the corresponding RDFs above.

Conflict of Interest

The authors declare no conflict of interest.

Keywords: Deep eutectic solvent · microheterogeneity · domain analysis · molecular dynamics simulations · neoteric solvents

[1] A. P. Abbott, D. Boothby, G. Capper, D. L. Davies, R. K. Rasheed, *J. Am. Chem. Soc.* **2004**, *126*, 9142–9147.

[2] Q. Zhang, K. D. O. Vigier, S. Royer, F. Jerome, *Chem. Soc. Rev.* **2012**, *41*, 7108–7146.

[3] E. L. Smith, A. P. Abbott, K. S. Ryder, *Chem. Rev.* **2014**, *114*, 11060–11082.

[4] D. V. Wagle, H. Zhao, G. A. Baker *Acc. Chem. Res.* **2014**, *47*, 2299–2308.

[5] S. L. Perkins, P. Painter, C. M. Colina, *J. Chem. Eng. Data* **2014**, *59*, 3652–3662.

[6] T. Welton, *Chem. Rev.* **1999**, *99*, 2071–2083.

[7] S. Zhang, X. Lu, Q. Zhou, X. Li, X. Zhang, S. Li, *Ionic Liquids: Physicochemical Properties*; Elsevier: **2009**.

[8] D. R. MacFarlane, K. R. Seddon, *Aust. J. Chem.* **2007**, *60*, 3–5.

[9] R. Hayes, G. G. Warr, R. Atkin, *Chem. Rev.* **2015**, *115*, 6357–6426.

[10] Z. Lei, B. Chen, Y. M. Koo, D. R. MacFarlane, *Chem. Rev.* **2017**, *117*, 6633–6635.

[11] E. I. Izgorodina, Z. L. Seeger, D. L. Scarborough, S. Y. Tan, *Chem. Rev.* **2017**, *117*, 6696–6754.

[12] B. Kirchner, O. Hollóczki, J. N. Canongia Lopes, A. A. H. P'adua, *WIREs Comput. Mol. Sci.* **2014**, 202–214.

[13] D. S. Firaha, M. Kavalchuk, B. Kirchner, *J. Solution Chem.* **2015**, *44*, 838–849.

[14] D. S. Firaha, O. Hollóczki, B. Kirchner, *Angew. Chem.* **2015**, *127*, 7916–7920; *Angew. Chem. Int. Ed.* **2015**, *54*, 7805–7809.

[15] A. P. Abbott, M. Azam, K. S. Ryder, S. Saleem, *Transactions of the IMF* **2018**, *96*, 297–303.

[16] W. O. Karim, A. P. Abbott, S. Cihangir, K. S. Ryder, *Transactions of the IMF* **2018**, *96*, 200–205.

[17] C. Florindo, L. Branco, I. Marrucho, *Fluid Phase Equilib.* **2017**, *448*, 135–142.

[18] S. Zahn, *Phys. Chem. Chem. Phys.* **2017**, *19*, 4041–4047.

[19] M. Rumyantsev, S. Rumyantsev, I. Y. Kalagaev, *J. Phys. Chem. B* **2018**, *122*, 5951–5960.

[20] S. Kaur, S. Sharma, H. K. Kashyap, *J. Chem. Phys.* **2017**, *147*, 194507.

[21] S. Zahn, B. Kirchner, D. Mollenhauer, *ChemPhysChem* **2016**, *17*, 3354–3358.

[22] C. R. Ashworth, R. P. Matthews, T. Welton, P. A. Hunt, *Phys. Chem. Chem. Phys.* **2016**, *18*, 18145–18160.

[23] M. Gilmore, L. M. Moura, A. H. Turner, M. Swadzba-Kwasny, S. K. Callear, J. A. McCune, O. A. Scherman, J. D. Holbrey, *J. Chem. Phys.* **2018**, *148*, 193823.

[24] E. O. Fetisov, D. B. Harwood, I. F. W. Kuo, S. E. E. Warrag, M. C. Kroon, C. J. Peters, J. I. Siepmann, *J. Phys. Chem. B* **2018**, *122*, 1245–1254.

[25] O. S. Hammond, D. T. Bowron, K. J. Edler, *Green Chem.* **2016**, *18*, 2736–2744.

[26] O. S. Hammond, D. T. Bowron, K. J. Edler, *Angew. Chem. Int. Ed.* **2017**, *56*, 9782–9785; *Angew. Chem.* **2017**, *129*, 9914–9917.

[27] O. S. Hammond, D. T. Bowron, K. J. Edler, *Angew. Chem.* **2017**, *129*, 9914–9917; *Angew. Chem. Int. Ed.* **2017**, *56*, 9782–9785.

[28] B. Guchhait, S. Das, S. Daschakraborty, R. Biswas, *J. Chem. Phys.* **2014**, *140*, 104514.

[29] A. Korotkevich, D. S. Firaha, A. A. H. Pádua, B. Kirchner, *Fluid Phase Equilib.* **2017**, *448*, 59–68.

[30] J. N. Canongia Lopes, A. A. H. Pádua, *J. Phys. Chem. B* **2006**, *110*, 16816–16818.

[31] A. Triolo, O. Russina, H. J. Bleif, E. D. Cola, *J. Phys. Chem. B* **2007**, *111*, 4641–4644.

[32] J. N. Canongia Lopes, A. A. H. Pádua, *J. Phys. Chem. B* **2006**, *110*, 3330–3335.

[33] M. Brehm, H. Weber, M. Thomas, O. Hollóczki, B. Kirchner, *ChemPhysChem* **2015**, *16*, 3271–3277.

[34] R. Elfgen, O. Hollóczki, B. Kirchner, *Acc. Chem. Res.* **2017**, *50*, 2949–2957.

[35] H. G. Liao, Y. X. Jiang, Z. Y. Zhou, S. P. Chen, S. G. Sun, *Angew. Chem. Int. Ed.* **2008**, *47*, 9100–9103; *Angew. Chem.* **2008**, *120*, 9240–9243.

[36] H. G. Liao, Y. X. Jiang, Z. Y. Zhou, S. P. Chen, S. G. Sun, *Angew. Chem.* **2008** *120*, 9240–9243.

[37] D. J. van Osch, L. F. Zubeir, A. van den Bruinhorst, M. A. Rocha, M. C. Kroon, *Green Chem.* **2015**, *17*, 4518–4521.

[38] S. Kaur, A. Gupta, H. K. Kashyap, *J. Phys. Chem. B* **2016**, *120*, 6712–6720.

[39] Y. Cui, D. G. Kuroda, *J. Phys. Chem. A* **2018**, *122*, 1185–1193.

[40] S. McDonald, T. Murphy, S. Imberti, G. G. Warr, R. Atkin, *J. Phys. Chem. Lett.* **2018**, *9*, 3922–3927.

[41] F. Neese, *WIREs Comput. Mol. Sci.* **2012**, *2*, 73–78.

[42] S. Plimpton, *J. Comput. Phys.* **1995**, *117*, 1–19.

[43] M. Brehm, B. Kirchner, *J. Chem. Inf. Model.* **2011**, *51*, 2007–2023.

[44] D. J. van Osch, L. F. Zubeir, A. van den Bruinhorst, M. A. Rocha, M. C. Kroon, *Green Chem.* **2015**, *17*, 4518–4521.

[45] O. Hollóczki, M. Macchiagodena, H. Weber, M. Thomas, M. Brehm, A. Stark, O. Russina, A. Triolo, B. Kirchner, *ChemPhysChem* **2015**, *16*, 3325–3333.

[46] R. Macchieraldo, L. Esser, R. Elfgen, P. Voepel, S. Zahn, B. M. Smarsly, B. Kirchner, *ACS Omega* **2018**, *3*, 8567–8582.

[47] O. Hollóczki, A. Berkessel, J. Mars, M. Mezger, A. Wiebe, S. R. Waldvogel, B. Kirchner, *ACS Catal.* **2017**, *7*, 1846–1852.

[48] P. Ray, R. Elfgen, B. Kirchner, *Phys. Chem. Chem. Phys.* **2019**, *21*, 4472–4486.

[49] O. Hollóczki, R. Macchieraldo, B. Gleede, S. R. Waldvogel, B. Kirchner, *J. Phys. Chem. Lett.* **2019**, *10*, 1192–1197.

[50] H. Weber, O. Hollóczki, A. S. Pensado, B. Kirchner, *J. Chem. Phys.* **2013**, *139*, 084502.

[51] S. Gehrke, M. von Domaros, R. Clark, O. Hollóczki, M. Brehm, T. Welton, A. Luzar, B. Kirchner, *Faraday Discuss.* **2018**, *206*, 219–245.

[52] Q. Xia, Y. Liu, J. Meng, W. Cheng, W. Chen, S. Liu, Y. Liu, J. Li, H. Yu, *Green Chem.* **2018**, *20*, 2711–2721.

[53] C. R. Ashworth, R. P. Matthews, T. Welton, P. A. Hunt, *Phys. Chem. Chem. Phys.* **2016**, *18*, 18145–18160.

[54] A. Faraone, D. V. Wagle, G. A. Baker, E. Novak, M. Ohl, D. Reuter, P. Lunkenheimer, A. Loidl, E. Mamontov, *J. Phys. Chem. B* **2018**, *122*, 1261–1267.

[55] S. B. C. Lehmann, M. Roatsch, M. Schöppke, B. Kirchner, *Phys. Chem. Chem. Phys.* **2010**, *12*, 7473–7486.

[56] V. Kempter, B. Kirchner, *J. Mol. Struct.* **2010**, *972*, 22–34.

Manuscript received: March 27, 2019
Revised manuscript received: May 16, 2019
Accepted manuscript online: May 16, 2019
Version of record online: June 26, 2019

C. How is CO_2 Absorbed into a Deep Eutectic Solvent?

Vahideh Alizadeh,[*] Lars Esser,[*] Barbara Kirchner [*]

Received: November 19 2020, Published online: February 07 2021.

Reprinted in Appendix C with permission[†] from

V. Alizadeh, L. Esser, B. Kirchner, "How is CO_2 Absorbed into a Deep Eutectic Solvent?", *J. Chem. Phys.* **2021**, *154*, 094503, *doi:DOI:10.1063/5.0038093.*

For this article, Supporting Information is available free of charge at:
https://doi.org/10.1063/5.0038093.

Contributions to the manuscript

- Development of the concept
- Performing all simulations, analysis, and calculations
- Interpretation of the results
- Writing of the manuscript

---

[*] Mulliken Center for Theoretical Chemistry, Clausius Institute for Physical and Theoretical Chemistry, University of Bonn, Beringstr. 4–6, 53115 Bonn, Germany

[†] Permission requests to reuse material from this chapter should be directed to the American Institute of Physics.

The Journal of Chemical Physics ARTICLE scitation.org/journal/jcp

How is CO_2 absorbed into a deep eutectic solvent?

Cite as: J. Chem. Phys. **154**, 094503 (2021); doi: 10.1063/5.0038093
Submitted: 19 November 2020 • Accepted: 7 February 2021 •
Published Online: 1 March 2021

Vahideh Alizadeh, Lars Esser, and Barbara Kirchner[a)]

AFFILIATIONS

Mulliken Center for Theoretical Chemistry, University of Bonn, Beringstraße 4+6, D-53115 Bonn, Germany

Note: This paper is part of the JCP Special Collection in Honor of Women in Chemical Physics and Physical Chemistry.

[a)]Author to whom correspondence should be addressed: kirchner@thch.uni-bonn.de

ABSTRACT

Deep eutectic solvents show great potential as CO_2 absorbents, which is highly desirable for the sustainable development of CO_2 reduction and prevention of global climate changes. *Ab initio* molecular dynamics simulations in the isothermal–isobaric ensemble at pressures of 1 MPa and 5 MPa and at the corresponding experimental density are carried out to investigate the CO_2 absorption in choline chloride: ethylene glycol deep eutectic solvent. Based on the structural analysis, there is a strong anion and hydrogen bond donor effect and a minor cation effect on CO_2 solvation in the solvent. Instead of cooperation, a competition between the anion and the hydrogen bond donor (ethylene glycol) for the interaction with CO_2 is indicated. While at a lower pressure, the ethylene glycol–CO_2 interaction dominates, at a higher pressure, it is the chloride–CO_2 interaction. Thus, it is possible to use the same advantages within the deep eutectic solvent as the CO_2 absorbent as in ionic liquids, but in the hydrogen bond, a donor can be exploited.

I. INTRODUCTION

Deep eutectic solvents (DESs) as a new class of solvents and alternative (kinship) for ionic liquids (ILs) have attracted the interest of scientists over the last two decades due to their favorable physical and thermodynamic properties.[1] These include low vapor pressure, non-toxicity, and environmental friendliness. These fluids are mixtures of two compounds with a eutectic melting point significantly below the melting point of the pure compounds, which are classified into several main types according to their constituents.[1,2] Often, one compound is a salt, and one compound is a hydrogen bond donor (HBD) for which the importance of hydrogen bond interactions in them is well known.[3–5] DESs have many potential applications ranging from metal processes, synthesis, separation, and biomass.[6–11] In addition, DESs, which are similar to ILs, explored the potential as an alternative to conventional carbon dioxide (CO_2) absorbent fluids such as aqueous amines.[12–15] CO_2 capture is an area of universal interest in all scientific disciplines where ILs occupy a special place in the CO_2 capturing process.[16] CO_2 can be absorbed either physically or chemically in ILs.[17,18] There are already a large number of studies that have dealt with CO_2 absorption in various ionic liquids, on both an experimental and theoretical basis.[17,19–23] Furthermore, DESs as well as ILs possess high CO_2 solubilities, a very low vapor pressure, and high thermal stabilities. They are more eco-friendly, non-toxic, and most importantly cheap and easy to produce, making them suitable for large-scale application. In an effort to validate the use of DESs in CO_2 processing, the solubility of CO_2 was measured experimentally under different conditions such as different pressures, temperatures, and molar ratios between the two DES components and the effect of the hydrogen bond donor moiety. Most of the reported studies focused on choline chloride ([Ch][Cl]) based DESs.[24–27] In this context, Leron *et al.* investigated the solubility of CO_2 in DESs composed of [Ch][Cl]:urea and [Ch][Cl]:ethylene glycol at pressures up to 6 MPa. It was found that the solubility of CO_2 increases with pressure and decreases with rising temperature, and the solubility values were comparable to the solubility of CO_2 in 1-butyl-3-methylimidazolium- and 1-ethyl-3-methylimidazolium-based ILs.[28–30]

Most of the few studies available are on an experimental basis, and a handful of studies have used computational methods to determine the behavior at the molecular level of CO_2 absorption in the DES. Aparicio and co-workers used density functional theory (DFT) and classical molecular dynamics (MD) to demonstrate the effectiveness of choline-based DESs in CO_2 absorption.[31–34] In the above-mentioned studies, an attempt has been made to elucidate the mechanism of CO_2 capture at the molecular level using DESs. In order to complement the existing studies, we used *ab initio* molecular dynamics simulation (AIMD) to study CO_2 absorption in [Ch][Cl]:EG DES at two pressure levels. There are many open questions as follows: How does CO_2 dissolve in a DES? Which component is more important for CO_2 absorption: cation, anion, or HBD molecule? Does CO_2 incorporate in the hydrogen bond network? Does it stay in the nonpolar domains? How does the pressure affect CO_2 absorption? The knowledge gathered here will not only give an insight into CO_2 solubility in [Ch][Cl]:EG DES, but it will also extend our general understanding of influential factors on CO_2 solubility in [Ch][Cl]-based DESs.

II. COMPUTATIONAL DETAILS

To investigate the CO_2 adsorption in the [Ch][Cl]:EG DES, *ab initio* molecular dynamic simulations (AIMD) were performed with the CP2K package.[35] Based on the experimental data, two simulation boxes were created.[28,36] The first system consists of 48 EG molecules, 24 [Ch][Cl] ion pairs, and one CO_2 molecule, and it is abbreviated as system **A**. System **B** is a mixture of 48 EG molecules, 24 [Ch][Cl] ion pairs, and six CO_2 molecules. The investigated systems differ in the number of CO_2 molecules inside and in the pressure (see Table I and Fig. 1). The graphical representation of the components with the corresponding nomenclature is visualized in Fig. 2. The initial geometries for the AIMD simulations were pre-equilibrated by classical molecular dynamic simulations within periodic boundary conditions, using the LAMMPS program package.[37] The force field of Canongia, Lopes, and Padua (CLP) for [Ch][Cl] based on the OPLS force field and the OPLS force field for EG molecules were used to describe the intra- and intermolecular interactions during classical MD simulations.[38,39] After 9 ns in NPT and NVT ensembles, the final snapshot of the classical MD trajectories was selected as an initial geometry for AIMD simulations. The simulations temperature was set to 373.15 K, and the density was adjusted to the experimental values.[28]

After the MD simulations, the systems were equilibrated for 5 ps in an NVT ensemble employing massive Nosé–Hoover thermostats and then simulated for 10 ps at 373.15 K in an NVT ensemble by using regular Nosé–Hoover thermostats.[40,41] The production run for system A and system B in an NPT ensemble is 45 ps and 30 ps, respectively, using a Nosé–Hoover barostat. For the electronic structure calculations, the QUICKSTEP module[42] of the CP2K program package is applied, where the hybrid Gaussian and plane waves (GPW) approach is used to calculate the energies and forces on the atoms. The molecularly optimized double-ζ basis set (MOLOPT-DZVP-SR-GTH)[43] was applied to all atoms together with the generalized gradient approximation (GGA) Becke–Lee–Yang–Parr (BLYP)[44,45] functional and the corresponding BLYP Goedecker–Teter–Hutter (GTH) pseudopotentials to represent the core electrons.[46–48] Dispersion interactions for the BLYP functional were corrected using the atom-based dispersion correction (D3) scheme with Becke–Johnson damping.[49,50] For the SCF calculation, 10^{-6} was used as target accuracy for the SCF convergence. The direct inversion of the iterative subspace (DIIS) minimizer[51] and the FULL-SINGLE-INVERSE preconditioner[52] were used to achieve fast and robust orbital transformation. To obtain accurate and reliable results from GPW calculations, the convergence of a real space integration grid is required, which is determined by the energy cutoff.[42] A CUTOFF criterion for the density of 400 Ry with the finest grid level was employed for NVT ensembles together with five multigrids (NGRID5 and REL-CUTOFF 40) and a smoothing algorithm for the electron density (NN10-SMOOTH) and its derivative (NN10).[42] In the NPT ensemble, a larger cutoff equal to a value of 800 Ry was used due to grid sensitivity issues when the volume of the simulations can fluctuate.[53,54]

TABLE I. Compositions of the simulation boxes and physical chemical properties.

Quantity	A	B
No([Ch][Cl])	24	24
No(EG)	48	48
No(CO_2)	1	6
P (MPa)	1	5
T (K)	373.15	373.15
ρ (g cm^{-3})	1.077	1.094
ρ_{exp} (g cm^{-3})	1.0756	1.0769
t_{sim} (ps)	51	55

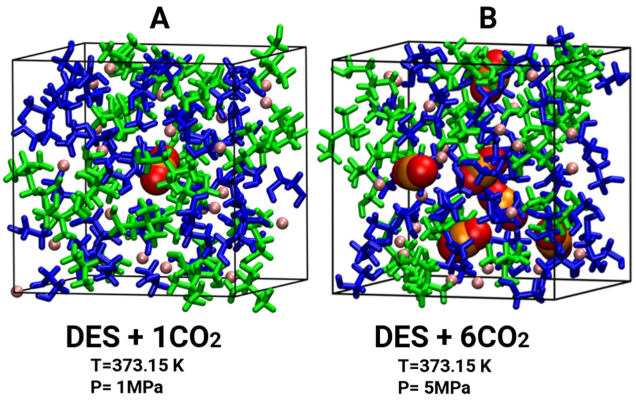

FIG. 1. Representative snapshot of the simulation boxes. The $[Ch]^+$ cation and the EG molecule in stick (cations in green and EG in blue), CO_2 in van der Waals, and the Cl^- anion in ball (pink) representation.

All analyses were performed with TRAVIS.[55,56] The diagrams presented in this article were created using the Xmgrace[57] with the running average option applied in plotted graphs.

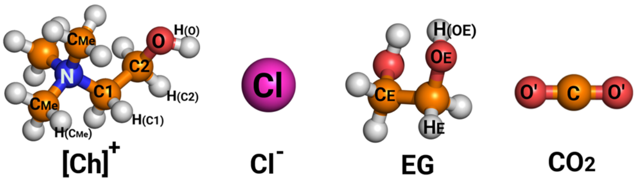

FIG. 2. Ball-and-stick representation of the cation, the anion, the EG molecule, and the CO_2 molecule. N: blue; C: orange; O: red, H: white, and Cl: purple.

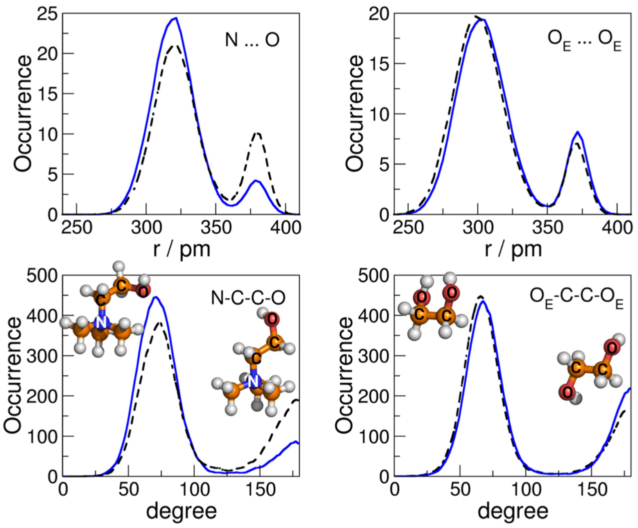

FIG. 3. Conformational analysis of the $[Ch]^+$ cation and the EG molecules; color code: blue: system A and black: system B.

III. RESULTS AND DISCUSSION

Before investigating the CO_2 absorption in the [Ch[Cl]:EG DES, the overall structure of the DES is analyzed. On the basis of intramolecular radial and angle distribution functions (RDFs), the EG molecule conformation does not change either with pressure or with the number of CO_2 molecules inside, and the gauche conformer is dominant with $r(O_E–O_E) = 300$ pm and $d(O_ECCO_E) = 60°$ in the both systems (Fig. 3, right panels). The gauche conformation of the $[Ch]^+$ cation is preferred in both systems [distinct with peaks at r(N–O) = 320 pm and d(NCCO) = 70°] that is similar to what was found before.[58–60] However, our results show an increased preference of the trans-conformer in system B compared to A, which is due to the high pressure in system B compared to previous AIMD studies[59,60] (Fig. 3, left panels, black dashed lines), so that the DES under high pressure has a more packed structure than in system A.

The simplest possible structural feature of [Ch][Cl]:EG DES is the location of the ions and EG molecules relative to each other. The radial distribution function between DES species is presented in Fig. 4. While the EG–EG graphs in systems A and B are almost identical and are not influenced by pressure, there are minor differences between the RDFs in $[Ch]^+$–$[Ch]^+$, Cl^-–Cl^-, and EG–$[Ch]^+$ in system B rather than system A, which are due to packing effects and not due to solute–solvent interactions. The peak around 400 pm in the RDFs presents the strong interaction between DES components that is related to the Cl^- anion with the $[Ch]^+$ cation and EG molecule. Interestingly, the first solvation shell of the Cl^- anion is different in system A than in system B. The EG–Cl^- peak at system B is centered at 400 pm, while in system A, the RDF has a double peak at 310 pm and 430 pm. The first peak (pre-peak) at 310 pm for system A represents two-fold hydrogen bond, which is discussed in

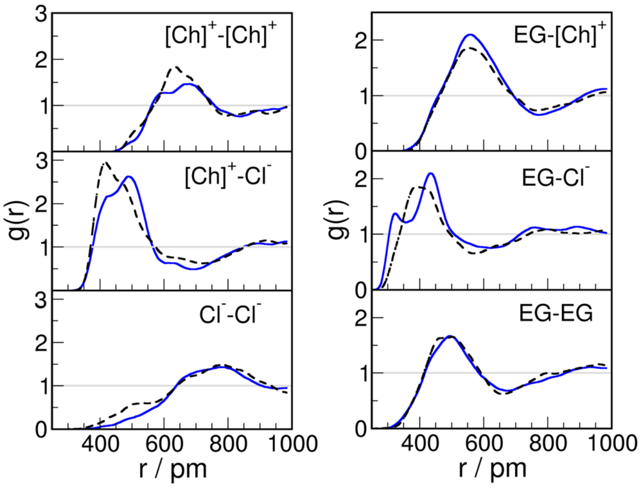

FIG. 4. Center of mass RDFs for the EG molecules and ions with themselves and each other in systems A and B. Blue solid lines depicts system A, and black dashed lines depicts system B.

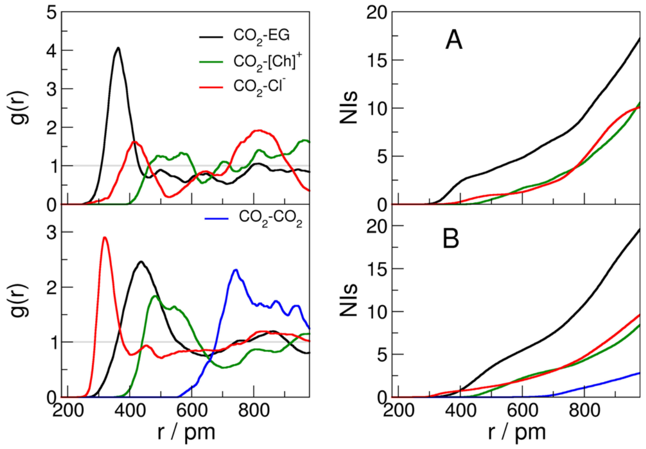

FIG. 5. Center of mass RDFs and number integrals (NIs) for the CO_2 molecules with themselves, the ions, and the EG molecules of the systems.

TABLE II. Surface coverage from Voronoi analysis. It is distinguished between the subsets: DES ions $\{Ch^+$ (cation), Cl^- (anion)$\}$, EG molecules, and CO_2 molecules.

	Ch^+ coverage				Cl^- coverage			
System	Ch^+	Cl^-	EG	CO_2	Ch^+	Cl^-	EG	CO_2
A	28.3	13.9	57.2	0.5	47.9	0.12	51.7	0.2
B	29.7	14.6	52.1	3.5	50.8	0.4	45.7	3.0
	EG coverage				CO_2 coverage			
	Ch^+	Cl^-	EG	CO_2	Ch^+	Cl^-	EG	CO_2
A	43.9	11.5	43.7	0.8	31.7	2.0	65.1	0
B	39.7	10.0	45.5	4.7	33.3	5.3	58.4	0.02

our previous study.[60] Furthermore, the peak for $[Ch]^+$–Cl^- at system A is slightly shifted to larger distances. The shape of the peak at $[Ch]^+$–Cl^- RDFs represented the subtle change from Coulombic interplay (Cl^- interacting with the ammonium head group of $[Ch]^+$) to hydrogen bonds (Cl^- interacting with the hydroxyl head group of $[Ch]^+$), and it was found more in system B than in system A. These observations suggest that the [Ch][Cl]:EG DES structure, which is driven by strong cation–anion and hydrogen bond interactions, shows no striking difference even in the presence of CO_2 molecules and under high pressures.[60] A similar observation has been reported for ionic liquids.[61]

Figure 5 shows the location of CO_2 relative to the [Ch][Cl]:EG DES component and other CO_2 molecules. Interestingly, the first solvation shell of CO_2 changes with pressure. In system A, the EG

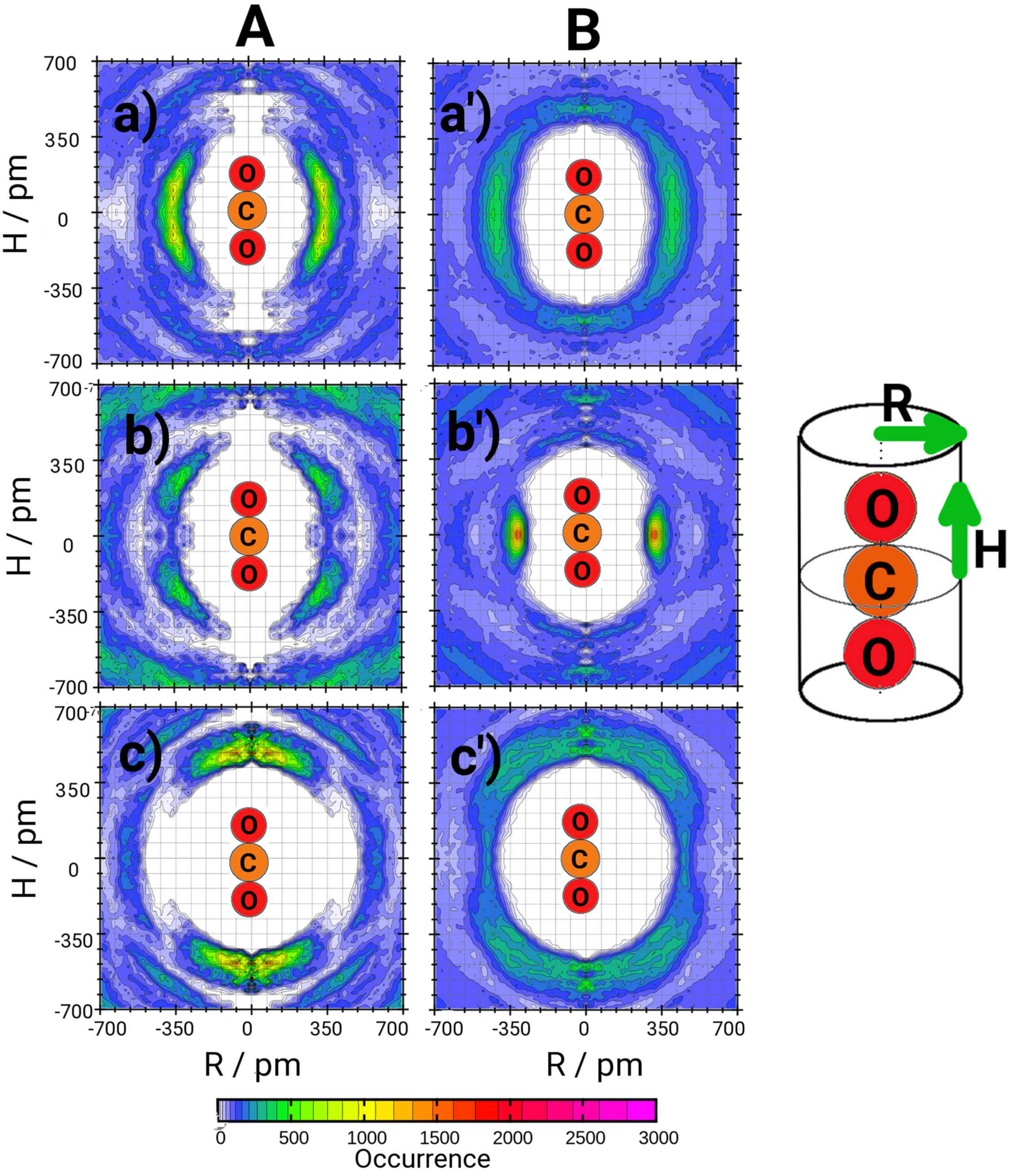

FIG. 6. Spatial distribution of the EG molecules COMs (a) anionic (b) and the cationic COMs (c) around CO_2.

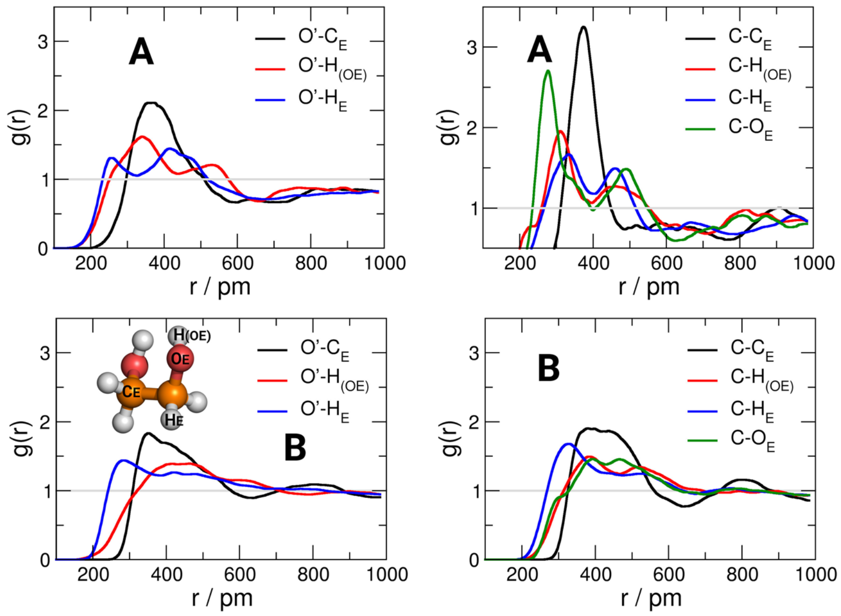

FIG. 7. RDF of CO_2–EG interaction sites in system A (top) and system B (bottom).

molecule is the closest to CO_2 molecules (the black line in Fig. 5 peaks at r = 360 pm) and then comes the Cl^- anion at r = 410 pm. Meanwhile, in system B, the Cl^- anion is the closest with a peak at r = 320 pm (the red line in Fig. 5) and next come the EG molecules with a peak at r = 440 pm. Furthermore, the peak of the CO_2–Cl^- interaction is very pronounced in system B compared to system A. The ratio of peak heights for CO_2–Cl^- and CO_2–EG changes from system A to system B. This indicates a first step from physical (system A) to chemical absorption, as was discussed by us previously.[17,18] Based on the number integral (NI) in the first solvation shell of the CO_2 molecules, there are 1.0 and 0.74 numbers of Cl^- anions and 3.0 and 6.30 numbers of the EG molecules in system A and system B, respectively. The cation in both systems is located in further distances (with a broad peak around 500 pm). The number of $[Ch]^+$ cations around CO_2 molecules is 1.9 in system A and 3.1 in system B. The increased number integrals represent

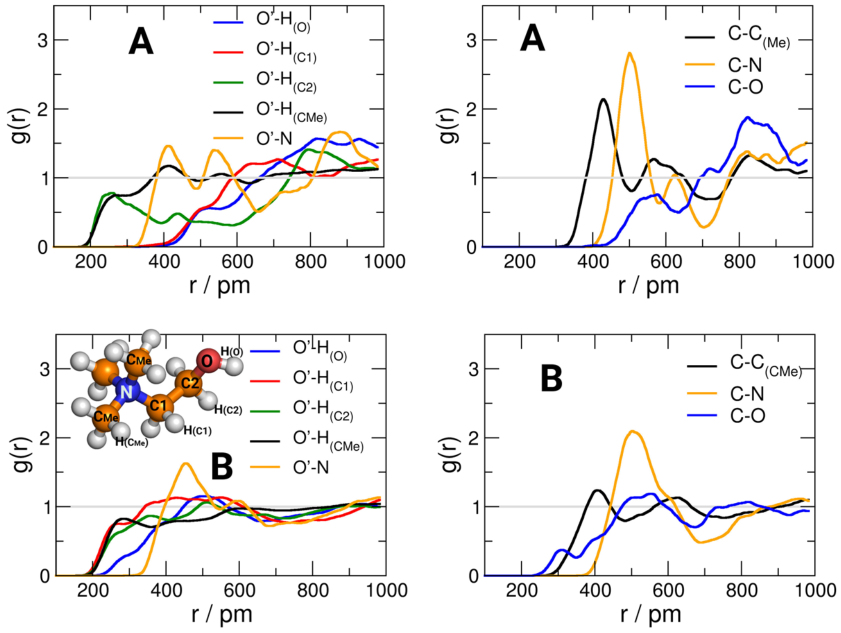

FIG. 8. RDF of CO_2–cation interaction sites in system A (top) and system B (bottom).

the packed structure in the pressurized system. If we compare the first solvation shell of the CO_2 molecules in DES and the previously investigated ILs,[20,61] it becomes clear that [Ch][Cl] in the DES behaves similar to pure ILs.

For further investigation, Voronoi analysis was carried out, as shown in Table II. This analysis shows the surface coverage of the CO_2 molecule by the ions and EG molecules. While the coverage of CO_2 by ions is increased by pressure, the EG coverage of CO_2 is reduced, which again indicates the change in solvation of CO_2 from system A to B. In addition, under high pressure, the ionic part and EG molecules prefer to self-aggregate.

The spatial distribution function (SDF) depicted in Fig. 6 is for further analysis of how ions and EG molecules arrange around the CO_2 molecule. This high local structuring of the ions and hydrogen bond donor molecules around the solute highlights the importance of the interaction type in CO_2 absorption in DESs. Due to the change from system A to system B, the absorption by the anion is more pronounced, whereas in system A, CO_2 interacts strongly with the EG molecule. The SDF results are consistent with the RDFs (Fig. 5) and the Voronoi analysis. Based on the center of mass SDFs, the EG molecules interact with the CO_2 molecule parallel to the O–C–O line (axis). The cation tends to have a perpendicular orientation to the

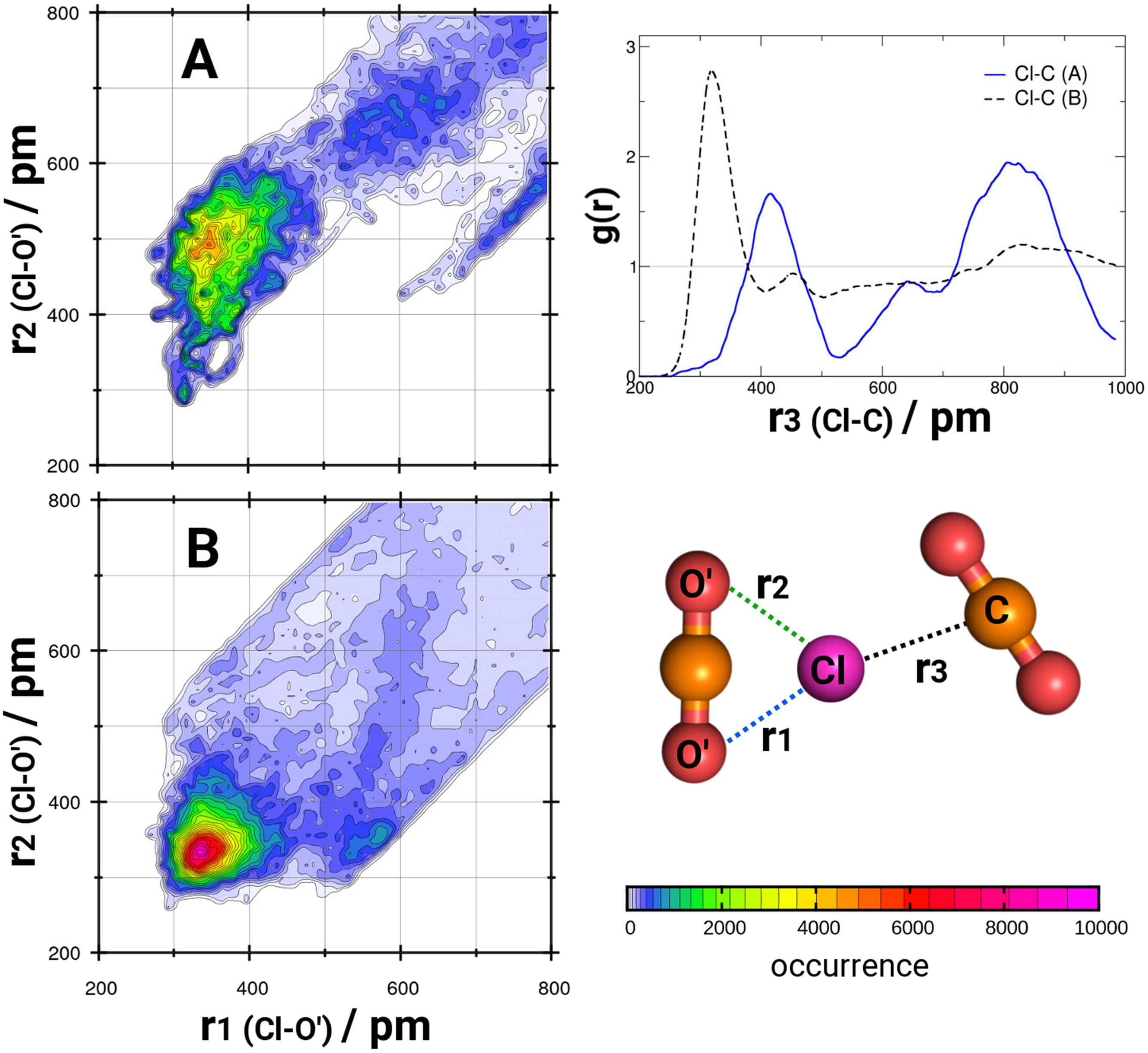

FIG. 9. CDFs and RDFs show the possible CO_2–Cl interactions.

O–C–O axis. This was observed previously by us for ionic liquids.[20] The arrangement of the EG molecule and the cation around CO_2 molecule in both systems is the same at the two different pressures but is more dispersed in system B. The contact structure of the $[Ch]^+$ cation and the EG molecule with the CO_2 molecule is shown in detail with the site–site RDFs in Figs. 8 and 7. The more dispersed SDF for the $[Ch]^+$ cation and the EG molecule around the CO_2 molecule in system B is reflected in the lower peak heights in Figs. 8 and 7.

It is obvious that CO_2 interacts with the polar [O_E and $H_{(OE)}$] and nonpolar (C_E and H_E) sides of the EG molecule. While in system A, both sides interact in a certain way with the CO_2 molecule, in system B, the interaction of the nonpolar side (O'–H_E, O'–C_E, O'–H_E, and O'–C_E RDFs) is dominant. The CO_2 molecule interacts (correlates) mainly with the ammonium head group [see C–$C_{(Me)}$, O–$H_{(CMe)}$ O'–N, and C–N RDFs] of the cation in both systems. However, in system B, we observe that the peaks belonging to the ammonium head group (C–N and O'–N RDFs) are slightly shifted to the larger distances, and the pre-peaks present refer to the hydroxyl head group [C–O, O'–$H_{(O)}$], which occur at shorter distances compared to system A. When comparing Figs. 7 and 8, it becomes clear that the correlations of EG–CO_2 are stronger (more pronounced) than those of $[Ch]^+$–CO_2.

Furthermore, according to the SDFs shown in Fig. 6 (middle panels), Cl^- location (and/or orientation) around the CO_2 molecule changes with pressure. In system A, Cl^- is located near CO_2 obliquely (diagonally), while (vice versa) in system B, the interaction is directed to the carbon atom of CO_2. In accordance with the SDF, CDFs and RDFs (Fig. 9) again show similar distributions. In system B, the Cl^-–$C(CO_2)$ distance is at 320 pm, which is in the same range as the anion(O)–$C(CO_2)$ for 1-ethyl-3-methylimidazolium acetate and ethylammonium nitrate ILs.[20,61] One could conclude that in the pressurized system, the ionic part is responsible to absorb CO_2, whereas in system A, CO_2 is mainly absorbed by the hydrogen bond donor, the EG molecule.

The O–C–O angle of the CO_2 molecules is also of interest because it can describe the chemical absorption vs physical absorption of CO_2.[17] We have previously shown for ionic liquids as CO_2 absorbents that a clear distinction between physical adsorption and chemical adsorption can be achieved according to CO_2 geometries and interactions. The bent O–C–O angle and strong interaction with an anion indicate chemical adsorption, while the linear CO_2 and weak interactions are presented in physical adsorption. Figure 10 represents the O–C–O angular distribution function (ADF) and the temporal evolution of the ADF in systems A and B for each CO_2 molecule. It is obvious that system A is not so different from system B. However, the ADF maximum is around 173° (more on the physical adsorption side). From temporal analysis, it is obvious that the O–C–O angles fluctuate and bend with time.

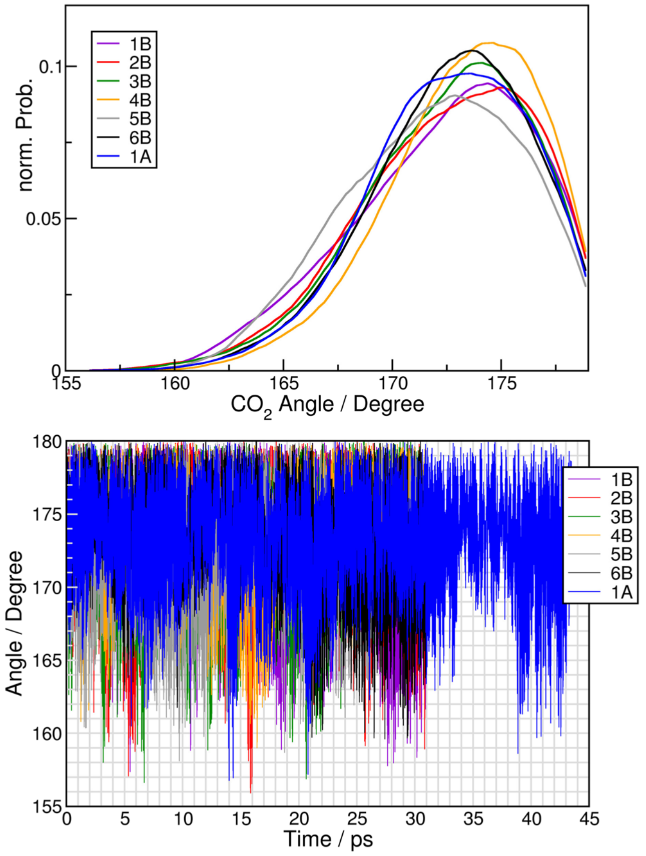

FIG. 10. Angular distribution function (ADF) and temporal evolution plots of the ADF for the CO_2 molecules in system A and system B. The plots are decomposed for system B to show the results for each CO_2 molecule in the systems.

IV. CONCLUSION

In this theoretical study, the interaction between CO_2 and [Ch][Cl]:EG DES was investigated by AIMD simulations under two pressure levels to gain an insight into the first step of CO_2 absorption in a DES. There is a strong anion and hydrogen bond donor effect and a minor cation effect on CO_2 solvation in the DES. Instead of cooperation, a competition between the anion and the hydrogen bond donor (EG) for the interaction with CO_2 is indicated. Meanwhile, at a lower pressure (system A), the EG–CO_2 interaction is dominant, and at a higher pressure (system B), it is the Cl–CO_2 interaction. Thus, the DES shows the same advantage of CO_2 absorption as in ionic liquids; however, in addition, the second component (often a hydrogen bond donor) can be used to direct and improve the CO_2 absorption.

DEDICATION

We dedicate this article to Sigrid Doris Peyerimhoff and Ruth Lynden-Bell for giving us directions in either electronic structure theory or molecular dynamics simulations.

ACKNOWLEDGMENTS

The authors thank the DFG for the financial support under Project No. 406232243.

DATA AVAILABILITY

The data that support the findings of this study are available from the corresponding author upon reasonable request.

REFERENCES

[1] E. L. Smith, A. P. Abbott, and K. S. Ryder, "Deep eutectic solvents (DESs) and their applications," Chem. Rev. **114**, 11060–11082 (2014).

[2] D. O. Abranches, M. A. R. Martins, L. P. Silva, N. Schaeffer, S. P. Pinho, and J. A. P. Coutinho, "Phenolic hydrogen bond donors in the formation of non-ionic deep eutectic solvents: The quest for type V DES," Chem. Commun. **55**, 10253–10256 (2019).

[3] Y. Dimitrova and S. D. Peyerimhoff, "Theoretical study of hydrogen-bonded formaldehyde complexes," Z. Phys. D: At., Mol. Clusters **32**, 241–247 (1994).

[4] Y. Dimitrova and S. D. Peyerimhoff, "Theoretical study of the $n \rightarrow \pi^*$ transitions in hydrogen-bonded formaldehyde complexes," Chem. Phys. Lett. **227**, 384–389 (1994).

[5] E. O. Fetisov, D. B. Harwood, I.-F. W. Kuo, S. E. E. Warrag, M. C. Kroon, C. J. Peters, and J. I. Siepmann, "First-principles molecular dynamics study of a deep eutectic solvent: Choline chloride/urea and its mixture with water," J. Phys. Chem. B **122**, 1245–1254 (2018).

[6] J. D. Gamarra, K. Marcoen, A. Hubin, and T. Hauffman, "Electrode-electrolyte interactions in choline chloride ethylene glycol based solvents and their effect on the electrodeposition of iron," Electrochim. Acta **312**, 303–312 (2019).

[7] G. R. T. Jenkin, A. Z. M. Al-Bassam, R. C. Harris, A. P. Abbott, D. J. Smith, D. A. Holwell, R. J. Chapman, and C. J. Stanley, "The application of deep eutectic solvent ionic liquids for environmentally-friendly dissolution and recovery of precious metals," Miner. Eng. **87**, 18–24 (2016).

[8] F. Himeur, I. Stein, D. S. Wragg, A. M. Z. Slawin, P. Lightfoot, and R. E. Morris, "The ionothermal synthesis of metal organic frameworks, Ln $(C_9O_6H_3)((CH_3NH)_2CO)_2$, using deep eutectic solvents," Solid State Sci. **12**, 418–421 (2010).

[9] A. Satlewal, R. Agrawal, S. Bhagia, J. Sangoro, and A. J. Ragauskas, "Natural deep eutectic solvents for lignocellulosic biomass pretreatment: Recent developments, challenges and novel opportunities," Biotechnol. Adv. **36**, 2032 (2018).

[10] K. H. Kim, T. Dutta, J. Sun, B. Simmons, and S. Singh, "Biomass pretreatment using deep eutectic solvents from lignin derived phenols," Green Chem. **20**, 809–815 (2018).

[11] C. G. Hanke, N. A. Atamas, and R. M. Lynden-Bell, "Solvation of small molecules in imidazolium ionic liquids: A simulation study," Green Chem. **4**, 107–111 (2002).

[12] S. Sarmad, J.-P. Mikkola, and X. Ji, "Carbon dioxide capture with ionic liquids and deep eutectic solvents: A new generation of sorbents," ChemSusChem **10**, 324–352 (2017).

[13] S. Babamohammadi, A. Shamiri, and M. K. Aroua, "A review of CO_2 capture by absorption in ionic liquid-based solvents," Rev. Chem. Eng. **31**, 383–412 (2015).

[14] K. Mulia, S. Putri, E. Krisanti, and Nasruddin, "Natural deep eutectic solvents (NADES) as green solvents for carbon dioxide capture," AIP Conf. Proc. **1823**, 020022 (2017).

[15] L. Moura, L. Kollau, and M. C. Gomes, *Deep Eutectic Solvents for Medicine, Gas Solubilization and Extraction of Natural Substances* (Springer, 2021), pp. 131–155.

[16] R. M. Lynden-Bell, M. G. Del Pópolo, T. G. A. Youngs, J. Kohanoff, C. G. Hanke, J. B. Harper, and C. C. Pinilla, "Simulations of ionic liquids, solutions, and surfaces," Acc. Chem. Res. **40**, 1138–1145 (2007).

[17] D. S. Firaha, O. Hollóczki, and B. Kirchner, "Computer-aided design of ionic liquids as CO_2 absorbents," Angew. Chem., Int. Ed. **54**, 7805–7809 (2015).

[18] D. S. Firaha, O. Hollóczki, and B. Kirchner, "Computer-gestütztes design ionischer flüssigkeiten zur CO_2-absorption," Angew. Chem. **127**, 7916–7920 (2015).

[19] D. S. Firaha and B. Kirchner, "Tuning the carbon dioxide absorption in amino acid ionic liquids," ChemSusChem **9**, 1591–1599 (2016).

[20] O. Hollóczki, Z. Kelemen, L. Könczöl, D. Szieberth, L. Nyulászi, A. Stark, and B. Kirchner, "Significant cation effects in carbon dioxide–ionic liquid systems," ChemPhysChem **14**, 315 (2013).

[21] Q. R. Sheridan, W. F. Schneider, and E. J. Maginn, "Role of molecular modeling in the development of CO_2–reactive ionic liquids," Chem. Rev. **118**, 5242–5260 (2018).

[22] J. F. Brennecke and B. E. Gurkan, "Ionic liquids for CO_2 capture and emission reduction," J. Phys. Chem. Lett. **1**, 3459–3464 (2010).

[23] D. Almantariotis, T. Gefflaut, A. A. H. Pádua, J.-Y. Coxam, and M. F. Costa Gomes, "Effect of fluorination and size of the alkyl side-chain on the solubility of carbon dioxide in 1-alkyl-3-methylimidazolium bis(trifluoromethylsulfonyl) amide ionic liquids," J. Phys. Chem. B **114**, 3608–3617 (2010).

[24] H. Wibowo, W. Liao, X. Zhou, C. Yu, D. A. Rahim, D. Hantoko, H. Qun, and M. Yan, "Study on the effect of operating parameters towards CO_2 absorption behavior of choline chloride–monoethanolamine deep eutectic solvent and its aqueous solutions," Chem. Eng. Process. **157**, 108142 (2020).

[25] M. B. Haider, D. Jha, B. Marriyappan Sivagnanam, and R. Kumar, "Thermodynamic and kinetic studies of CO_2 capture by glycol and amine-based deep eutectic solvents," J. Chem. Eng. Data **63**, 2671–2680 (2018).

[26] L. L. Sze, S. Pandey, S. Ravula, S. Pandey, H. Zhao, G. A. Baker, and S. N. Baker, "Ternary deep eutectic solvents tasked for carbon dioxide capture," ACS Sustainable Chem. Eng. **2**, 2117–2123 (2014).

[27] Y. Gu, Y. Hou, S. Ren, Y. Sun, and W. Wu, "Hydrophobic functional deep eutectic solvents used for efficient and reversible capture of CO_2," ACS Omega **5**, 6809–6816 (2020).

[28] R. B. Leron and M.-H. Li, "Solubility of carbon dioxide in a choline chloride–ethylene glycol based deep eutectic solvent," Thermochim. Acta **551**, 14–19 (2013).

[29] R. B. Leron, A. Caparanga, and M.-H. Li, "Carbon dioxide solubility in a deep eutectic solvent based on choline chloride and urea at $T = 303.15$–343.15 K and moderate pressures," J. Taiwan Inst. Chem. Eng. **44**, 879–885 (2013).

[30] S. N. V. K. Aki, B. R. Mellein, E. M. Saurer, and J. F. Brennecke, "High-pressure phase behavior of carbon dioxide with imidazolium-based ionic liquids," J. Phys. Chem. B **108**, 20355–20365 (2004).

[31] G. García, S. Aparicio, R. Ullah, and M. Atilhan, "Deep eutectic solvents: Physicochemical properties and gas separation applications," Energy Fuels **29**, 2616–2644 (2015).

[32] G. García, M. Atilhan, and S. Aparicio, "A theoretical study on mitigation of CO_2 through advanced deep eutectic solvents," Int. J. Greenhouse Gas Control **39**, 62–73 (2015).

[33] R. Ullah, M. Atilhan, B. Anaya, M. Khraisheh, G. García, A. ElKhattat, M. Tariq, and S. Aparicio, "A detailed study of cholinium chloride and levulinic acid deep eutectic solvent system for CO_2 capture via experimental and molecular simulation approaches," Phys. Chem. Chem. Phys. **17**, 20941–20960 (2015).

[34] T. Altamash, M. Atilhan, A. Aliyan, R. Ullah, G. García, and S. Aparicio, "Insights into choline chloride–phenylacetic acid deep eutectic solvent for CO_2 absorption," RSC Adv. **6**, 109201–109210 (2016).

[35] CP2K Open Source Molecular Dynamics Home Page, Official Webpage: https://www.cp2k.org; accessed 01 March 2013.

[36] R. B. Leron and M.-H. Li, "High-pressure volumetric properties of choline chloride–ethylene glycol based deep eutectic solvent and its mixtures with water," Thermochim. Acta **546**, 54–60 (2012).

[37] S. Plimpton, "Fast parallel algorithms for short-range molecular dynamics," J. Comput. Phys. **117**, 1–19 (1995).

[38] W. L. Jorgensen, D. S. Maxwell, and J. Tirado-Rives, "Development and testing of the OPLS all-atom force field on conformational energetics and properties of organic liquids," J. Am. Chem. Soc. **118**, 11225–11236 (1996).

[39] A. A. H. Padua, http://github.com/agiliopadua/fftool, 2013.

[40] S. Nosé, "A unified formulation of the constant temperature molecular dynamics methods," J. Chem. Phys. **81**, 511–519 (1984).

[41] W. G. Hoover, "Canonical dynamics: Equilibrium phase-space distributions," Phys. Rev. A **31**, 1695 (1985).

[42] J. VandeVondele, M. Krack, F. Mohamed, M. Parrinello, T. Chassaing, and J. Hutter, "Quickstep: Fast and accurate density functional calculations using a mixed Gaussian and plane waves approach," Comput. Phys. Commun. **167**, 103–128 (2005).

[43] J. VandeVondele and J. Hutter, "Gaussian basis sets for accurate calculations on molecular systems in gas and condensed phases," J. Chem. Phys. **127**, 114105 (2007).

[44] A. D. Becke, "Density-functional exchange-energy approximation with correct asymptotic behavior," Phys. Rev. A **38**, 3098 (1988).

[45] C. Lee, W. Yang, and R. G. Parr, "Development of the Colle-Salvetti correlation-energy formula into a functional of the electron density," Phys. Rev. B **37**, 785 (1988).

[46] S. Goedecker, M. Teter, and J. Hutter, "Separable dual-space Gaussian pseudopotentials," Phys. Rev. B **54**, 1703 (1996).

[47] C. Hartwigsen, S. Goedecker, and J. Hutter, "Relativistic separable dual-space Gaussian pseudopotentials from H to Rn," Phys. Rev. B **58**, 3641 (1998).

[48] M. Krack, "Pseudopotentials for H to Kr optimized for gradient-corrected exchange-correlation functionals," Theor. Chem. Acc. **114**, 145–152 (2005).

[49] S. Grimme, J. Antony, S. Ehrlich, and H. Krieg, "A consistent and accurate *ab initio* parametrization of density functional dispersion correction (DFT-D) for the 94 elements H-Pu," J. Chem. Phys. **132**, 154104 (2010).

[50] S. Grimme, S. Ehrlich, and L. Goerigk, "Effect of the damping function in dispersion corrected density functional theory," J. Comput. Chem. **32**, 1456–1465 (2011).

[51] J. VandeVondele and J. Hutter, "An efficient orbital transformation method for electronic structure calculations," J. Chem. Phys. **118**, 4365–4369 (2003).

[52] V. Weber, J. VandeVondele, J. Hutter, and A. M. N. Niklasson, "Direct energy functional minimization under orthogonality constraints," J. Chem. Phys. **128**, 084113 (2008).

[53] M. J. McGrath, J. I. Siepmann, I.-F. W. Kuo, C. J. Mundy, J. VandeVondele, J. Hutter, F. Mohamed, and M. Krack, "Isobaric–isothermal Monte Carlo simulations from first principles: Application to liquid water at ambient conditions," ChemPhysChem **6**, 1894–1901 (2005).

[54] L. R. Pestana, N. Mardirossian, M. Head-Gordon, and T. Head-Gordon, "*Ab initio* molecular dynamics simulations of liquid water using high quality meta-GGA functionals," Chem. Sci. **8**, 3554–3565 (2017).

[55] M. Brehm and B. Kirchner, "TRAVIS—A free analyzer and visualizer for Monte Carlo and molecular dynamics trajectories," J. Chem. Inf. Model. **4**, 2007 (2011).

[56] M. Brehm, M. Thomas, S. Gehrke, and B. Kirchner, "TRAVIS—A free analyzer for trajectories from molecular simulation," J. Chem. Phys. **152**, 164105 (2020).

[57] Grace Development Team, https://plasma-gate.weizmann.ac.il/Grace/, 1996–2008.

[58] C. R. Ashworth, R. P. Matthews, T. Welton, and P. A. Hunt, "Doubly ionic hydrogen bond interactions within the choline chloride–urea deep eutectic solvent," Phys. Chem. Chem. Phys. **18**, 18145–18160 (2016).

[59] A. Korotkevich, D. S. Firaha, A. A. H. Padua, and B. Kirchner, "Ab initio molecular dynamics simulations of SO_2 solvation in choline chloride/glycerol deep eutectic solvent," Fluid Phase Equilib. **448**, 59–68 (2017).

[60] V. Alizadeh, F. Malberg, A. A. H. Pádua, and B. Kirchner, "Are there magic compositions in deep eutectic solvents? Effects of composition and water content in choline chloride/ethylene glycol from ab initio molecular dynamics," J. Phys. Chem. B **124**, 7433–7443 (2020).

[61] D. S. Firaha and B. Kirchner, "CO_2 absorption in the protic ionic liquid ethylammonium nitrate," J. Chem. Eng. Data **59**, 3098–3104 (2014).

D. Molecular Level Insight into the Solvation of Cellulose in Deep Eutectic Solvents

Vahideh Alizadeh,[*] Barbara Kirchner[*]

Received: May 28 2021, Published online: August 05 2021.

Reprinted in Appendix D with permission[†] from

V. Alizadeh, B. Kirchner, "Molecular Level Insight into the Solvation of Cellulose in Deep Eutectic Solvents", *J. Chem. Phys.* **2021**, *155*, 084501, *doi:10.1063/5.0058333.*

For this article Supporting Information is available free of charge at:
https://doi.org/10.1063/5.0058333.

Contributions to the manuscript

- Development of the concept
- Performing all simulations, analysis, and calculations
- Interpretation of the results
- Writing of the manuscript

---

[*] Mulliken Center for Theoretical Chemistry, Clausius Institute for Physical and Theoretical Chemistry, University of Bonn, Beringstr. 4–6, 53115 Bonn, Germany

[†] Permission requests to reuse material from this chapter should be directed to the American Institute of Physics.

The Journal of Chemical Physics | ARTICLE | scitation.org/journal/jcp

Molecular level insight into the solvation of cellulose in deep eutectic solvents

Cite as: J. Chem. Phys. **155**, 084501 (2021); doi: 10.1063/5.0058333
Submitted: 28 May 2021 • Accepted: 5 August 2021 •
Published Online: 23 August 2021

Vahideh Alizadeh and Barbara Kirchner[a)]

AFFILIATIONS

Mulliken Center for Theoretical Chemistry, University of Bonn, Beringstraße 4+6, D-53115 Bonn, Germany

Note: This paper is part of the JCP Special Topic on Chemical Physics of Deep Eutectic Solvents.
[a)]Author to whom correspondence should be addressed: kirchner@thch.uni-bonn.de

ABSTRACT

Deep eutectic solvents as sustainable and new-generation solvents show potential in the field of cellulose dissolution. Although these novel materials are tested for numerous industrial, environmental, and medical applications, little is known about the structural features of cellulose interacting with deep eutectic solvents. In this work, the interplay of cellulose is studied in two deep eutectic solvents: choline acetate mixed with urea and choline chloride mixed with urea using classical molecular dynamics simulations. Dissolution of cellulose in the studied liquids was not observed to be in agreement with experimental work from the literature. However, a slight swelling in the chloride, as compared to the acetate-based solvent, is apparent. A possible rationale might be found in the stronger hydrogen bonding of the chloride anion compared to the acetate anion with the hydrogen atoms of the cellulose. Moreover, chloride approaches the outer glucose units comparatively more, which could be interpreted as the onset of entering and thus dissolving the cellulose as was previously observed. Specific hydrogen bonds between all units are analyzed and discussed in detail.

INTRODUCTION

Cellulose is the most abundant and renewable biopolymer that can be converted into various valuable materials, such as glucose, sorbitol, fibers, furan compounds, and biofuels.[1–3] Cellulose consists of linear chains of D-glucose monomers arranged in parallel and stabilized as flat sheets by multiple intra- and intermolecular hydrogen bonds.[1] Solvents play an important role in research and development in the field of cellulose because cellulose often needs to be dissolved for processing, modification, and characterization.[4,5] The presence of strong hydrogen bond interactions in cellulose makes the molecule reluctantly soluble. A variety of successful solvent systems for cellulose have extensively been studied and developed, such as *N*-methylmorpholine-*N*-oxide,[6] lithium chloride/*N*,*N*-dimethylacetamide,[7] ionic liquids,[8–10] and alkali/urea or alkali/thiourea aqueous solutions.[11] However, the search for more efficient, sustainable, and cost-effective solvents for various applications in the cellulose field continues.

Deep eutectic solvents (DESs), as a new class of solvents, have received considerable attention and are promising solvents for cellulose because of their ease of production, low cost, low toxicity, and environmental friendliness.[12–14] In 2012, Francisco *et al.* investigated the dissolution of lignin, starch, and cellulose in 26 DESs, such as choline chloride:urea, choline bromide:urea, and proline:malic acid.[15] They showed that lignin could be dissolved more than cellulose in the tested DESs. Furthermore, cellulose dissolution varies depending on the temperature and molar ratio of the DES components. Pretreatment of rice straw with the choline chloride:urea DES showed that amorphous cellulose in rice straw could be dissolved in choline chloride:urea, but the α-cellulose was almost not dissolved in the choline chloride:urea mixture.[16] Furthermore, treatment of Kraft cellulose using the choline acetate-based DESs showed that the selective solubilization of lignin and hemicellulose leads to cellulose purification.[17] Examination of cellulose solvation in ionic liquids and DESs, in terms of thermodynamics of solvation, revealed that the higher entropy of solvation is the driving force for the higher solubility of cellulose in ionic liquids compared to DESs.[18] Ren *et al.* tested the dissolution of cellulose in choline chloride-based eutectic solvents and found that the solubility of cellulose was enhanced by the use of ultrasound.[19] The result showed that the cellulose was dissolved directly and no other derivatives were produced while the choline chloride:imidazole exhibited the best dissolving ability of the cellulose due to its high hydrogen bond basicity, polarizability effects, and Hammett acidity function.

In addition, DESs were applied as novel solvents for cellulose nanofibril and nanocellulose production.[20–22] Cellulose nanofibrils produced with the application of DESs achieved good mechanical properties and thermal stability.[21] The synthesis of cellulose nanocrystals without significant chemical surface modification by applying a DES would expand the fields of application for cellulose nanocrystals.[22] Recently, a 3D printable ink made of cellulose nanocrystals, DESs, and ionically cross-linked polyacrylic acid was developed, offering new insights into the applications of cellulose and DESs as renewable materials.[23]

In view of the above, an in-depth understanding of the solvation of cellulose in DESs is needed to improve upon the various applications of DESs in the field of cellulose research. In this work, we will therefore investigate the solvation of cellulose in choline chloride:urea (ChCl:urea) and choline acetate:urea (ChOAc:urea) mixtures at the molecular level by conducting atomistic simulations.

COMPUTATIONAL DETAILS

To understand the solvation of cellulose in DESs, we simulated cellulose in two DESs that are ChCl:urea and ChOAc:urea mixtures (Fig. 1). These DESs were chosen with different anions, $[OAc]^-$ and Cl^-, which are both strong hydrogen bond acceptors.[24] The $[OAc]^-$ and Cl^- anions play the major role in the solvation and dissociation of cellulose in ionic liquids.[25,26]

The initial configuration of the simulation boxes was generated using the PACKMOL program package.[27] The systems contain a cellulose model in a DES consisting of 250 ion pairs and 500 urea molecules. A beta-cellulose microfibril consisting of ten glucose octamer chains was used as a model system for cellulose.[28]

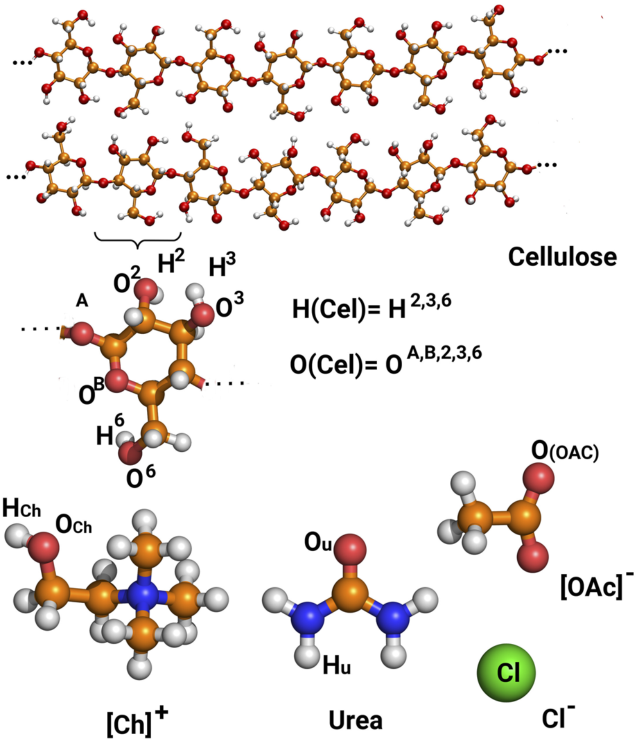

FIG. 1. Ball-and-stick representation and atom labels of the substances investigated in this study. N: blue, C: orange, O: red, H: white, and Cl: green.

Classical molecular dynamics (MD) simulations were performed using the large-scale atomic/molecular massively parallel simulator (LAMMPS) program package under periodic boundary conditions.[29] For chloride, acetate, and urea, we used the well-known optimized potentials for liquid simulations-OPLS-AA force field while for the choline cation, we opted for the force field developed by Acevedo and co-worker, which is also based on OPLS-AA force field.[30,31] For cellulose, the force field parameters of DAMM were used.[32] It should be noted that all applied force fields stem from the OPLS-AA family. At the moment, there is not a particular force field for cellulose in deep eutectic solvents. However, a cellulose force field in imidazolium-based ionic liquids was reported recently.[33] The force field combination, as mentioned earlier, was validated by Ferreira *et al.*[34] for pure DES and by Smith *et al.*[28] for investigating cellulose in a DES. The charge of the ions was scaled down by a factor of 0.8. Nonbonded interactions were described by the 6–12 Lennard-Jones potential and the geometric mixing rules were used to obtain parameters for pairs of different atoms.[35] For the calculation of Lennard-Jones and Coulombic interactions, a cutoff of 1.2 nm was chosen and a particle–particle particle–mesh solver was used to map the atomic charge onto a three-dimensional mesh.[36] Equilibration of the systems was obtained by simulating for 8.5 ns with NVE, NPT, and NVT ensembles. After initial energy minimization, the systems were simulated for 0.5 ns in an NVE ensemble with additional velocity scaling, deforming the simulation box to achieve a pre-equilibration density. Subsequently, the systems were simulated for 5 ns in an NpT ensemble by applying the Nosé–Hoover chain thermostats and barostats to achieve constant temperature and pressure ($T = 350$ K, $\tau = 100$ fs and $p = 1$ bar, $\tau = 2000$ fs, respectively).[37,38] Finally, using the average volume of the previous 1 ns as the final box volume, the system was equilibrated for an additional 3 ns in an NVT ensemble with the same thermostat settings. The subsequent production run consisted of a total simulation time of 20 ns in an NVT ensemble, with the same settings as for the equilibration. The time step was set to 1 fs throughout the procedure, and every 500th time step was saved in a trajectory for further processing. The obtained trajectories were analyzed with the TRAVIS code.[39,40] This tool provides different types of functions that allow the analysis of the interactions between the components of the systems. The latest TRAVIS version has now been extended including the force field parameters for choline and cellulose. Radial distribution functions (RDFs), number of integrals (NIs), diffusion coefficients, Voronoi analysis, and Sankey diagrams were calculated in this work.

RESULTS

Overall structure and dynamics of DESs

Since the nature of the DES components determines the properties of the liquid,[41] we first focus on the overall structure of the DESs. The structure of ChCl:urea and ChOAc:urea was investigated using the center of mass RDFs and the number of integrals (NIs) between the DES components (see Fig. 2 and Table I). Close inspection of the RDFs reveals for the chloride–urea RDF (at r_{max} = 395 pm) a higher peak than for the acetate–urea RDF (at r_{max} = 411 pm). Interestingly, the amount of Cl^- in the first solvent shell of urea is slightly less (1.7) than that of the $[OAc]^-$ anion (2.0), despite Cl^- being the smaller anion. Size plays a role when the urea molecules in the first solvent shell of the anions are considered

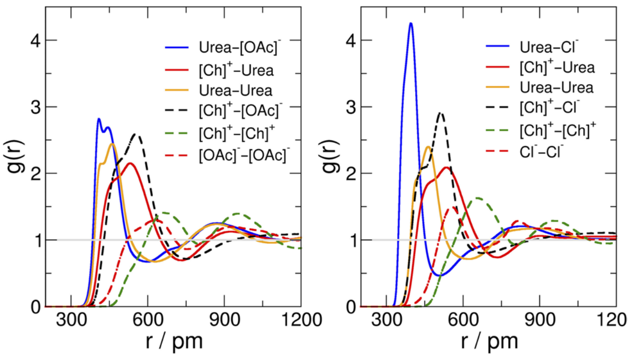

FIG. 2. Center of mass RDFs in the range of 250–1200 pm for the urea molecules and ions with themselves and each other.

TABLE I. Number of integrals (NIs), $r_{\min}$, and r_{max} from center of mass RDFs for the urea molecules and ions with themselves and each other.

		r_{max}(pm)	$r_{\min}$(pm)	NIs	$\overline{NIs}$
ChOAc:urea	Urea–$[\mathrm{OAc}]^-$	411	585	2.0	4.1
	$[\mathrm{Ch}]^+$–urea	534	730	8.0	4.5
	Urea–urea	463	630	4.6	⋯
	$[\mathrm{Ch}]^+$–$[\mathrm{OAc}]^-$	557	760	3.8	4.9
	$[\mathrm{Ch}]^+$–$[\mathrm{Ch}]^+$	665	800	3.8	⋯
	$[\mathrm{OAc}]^-$–$[\mathrm{OAc}]^-$	632	758	3.3	⋯
ChCl:urea	Urea–Cl^-	395	510	1.7	3.4
	$[\mathrm{Ch}]^+$–urea	530	735	9.0	4.5
	Urea–urea	468	618	4.7	⋯
	$[\mathrm{Ch}]^+$–Cl^-	518	685	4.1	4.1
	$[\mathrm{Ch}]^+$–$[\mathrm{Ch}]^+$	655	811	5.0	⋯
	Cl^-–Cl^-	556	668	2.2	⋯

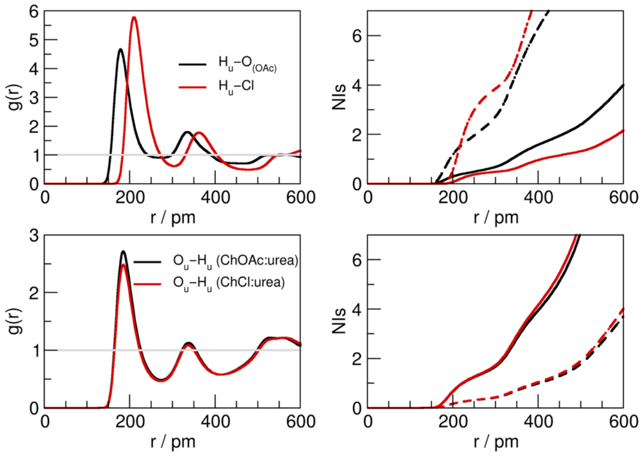

FIG. 3. RDFs and NIs representing the site–site interaction between the anion–urea and urea–urea. The solid lines for the NIs show H_u–$O_{(OAc)}$, H_u–Cl, and O_u–H_u, and the dashed lines represent the other way around.

TABLE II. Diffusion coefficients in 10^{-12} m^2 s^{-1} of the ions and urea in the simulated systems.

	$D_{[\mathrm{Ch}]^+}$	$D_{[\mathrm{OAc}]^-/(\mathrm{Cl}^-)}$	D_{urea}
ChOAc:urea	1.62	2.57	3.60
ChCl:urea	0.85	1.68	2.11

(Cl^-: 3.4 vs $[\mathrm{OAc}]^-$: 4.1). While the first solvation shell of the cations shows a slight increase in chloride anions (4.1) compared to the $[\mathrm{OAc}]^-$ anions (3.8), vice versa, that is, the Cl^- anions see significantly less cations (4.1) than the $[\mathrm{OAc}]^-$ anions (4.9), which again can be explained with the size of the anions. The urea self-interaction is somewhat increased, and the cation–cation interplay is strongly increased in the ChCl:urea DES compared to the ChOAc:urea DES, allowing the Cl^- anion to "act more freely" with respect to further coordination. Because of the counter-intuitive amount of Cl^- anions compared to the $[\mathrm{OAc}]^-$ anions around urea, we have a closer look at contact atoms. Figure 3 illustrates the site–site RDFs and NIs of

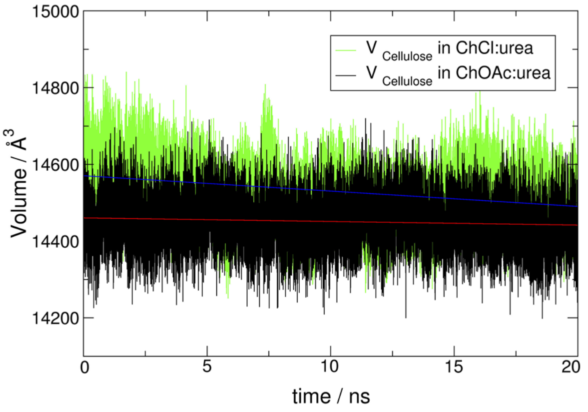

FIG. 4. Time development of the cellulose microfibril volume variation during the production runs. The lines are linear fits to the volume fluctuations, red for ChOAc:urea and blue for ChCl:urea.

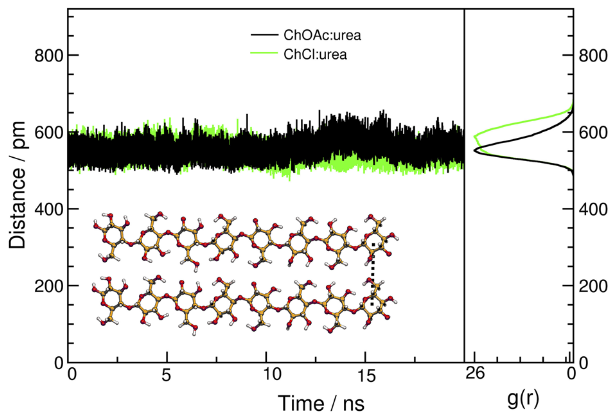

FIG. 5. RDFs and time development of RDFs for the center of the last glucose ring in the cellulose microfibril chains, considering the nearest neighbor conditions.

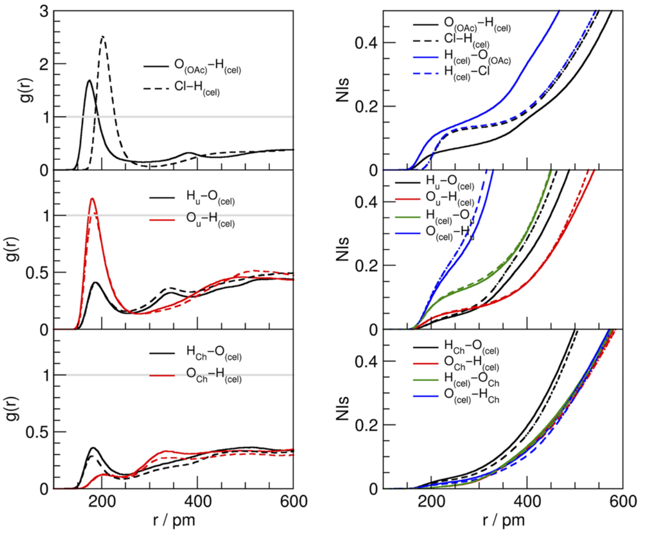

FIG. 6. RDFs representing the individual cellulose–solvents interactions. Solid lines are for cellulose–ChOAc:urea, and dashed lines are for cellulose–ChCl:urea.

H_u–$O_{(OAc)}$, H_u–Cl, and O_u–H_u. Consistent with the center of mass RDFs, the amount of the $O_{(OAc)}$ in the first solvation shell of the H_u is slightly higher than that of Cl^-; see the black solid line versus the red solid line in the upper left panel of Fig. 3. Due to multiple coordination sites, several prepeaks are observed in the functions involving urea, $[Ch]^+$ and $[OAc]^-$.

The diffusion coefficient obtained from the mean square displacement (Table II) shows that the diffusion of DES components is higher in ChOAc:urea than in ChCl:urea. Urea shows a faster diffusion rate than the ions in both systems similar to glycerol in ChCl:glycerol.[28] The diffusion constants of urea and the ions in the ChOAc:urea DES are almost twice as large as those of the ChCl:urea DES. The origin of this behavior is that anions play a central role in the liquid structure; the strong interactions between DES components are hindering the diffusion. This is in agreement with the observed overall structure in Fig. 2 and Table I. Ionic liquids based on the acetate anion[42,43] are less viscous than chloride-based ionic liquids.[44,45] Due to the inverse proportionality of the viscosity and diffusion coefficient, one could conclude that the diffusion coefficients of the ions in the chloride-based ionic liquids are smaller than those in the acetate-based ionic liquids. Interestingly, the exact same trend is observable in Table II for the DESs. The effect of the overall structure and dynamics of the DESs on cellulose will be evaluated in the next section.

Cellulose in DESs

The time development of the cellulose volume as well as the distance between the last sugar units in the cellulose chain considering the nearest neighbor condition during the MD simulations is shown in Figs. 4 and 5. Although the cellulose volume and the mentioned distances fluctuate, there is no significant change in structural features. Thus, the dissolution of cellulose in the studied DESs has not occurred, which is in agreement with experimental and other theoretical studies.[22,28,46] It is noteworthy that the selected cellulose model proves the ability of MD simulations to reproduce the dissolution of cellulose in certain ionic liquids by using this cellulose model.[47] A close examination of the studied systems in Figs. 4 and 5 shows that the volume and the last sugar unit distances in the cellulose chain are larger in the ChCl:urea system than in the ChOAc:urea system. Comparing the densities of both pure liquids does not provide an explanation for this phenomenon: $\rho_{\text{ChCl:urea}} = 1.25\ \text{g cm}^{-3}$ and $\rho_{\text{ChOAc:urea}} = 1.17\ \text{g cm}^{-3}$.[48]

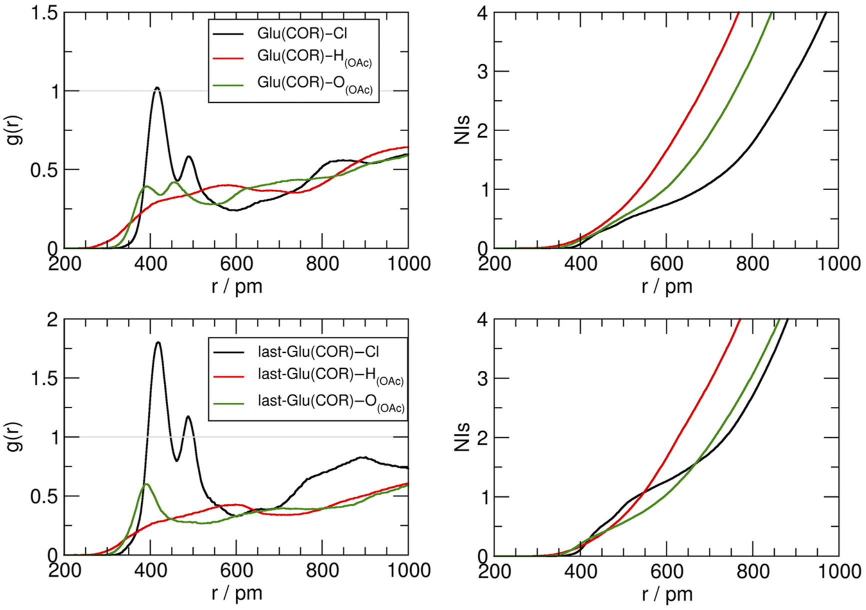

FIG. 7. RDFs and NIs representing the center of the ring (COR) of the glucose units with the atoms from the anions.

In order to gain more insight into molecular level behaviors and to obtain a possible explanation for the slight swelling of the cellulose in the ChCl:urea DES compared to the ChOAc:urea DES, we turn to the interactions of cellulose microfiber within the DES components. It is well known that hydrogen bonds play the main role in the solvation of cellulose.[49] Therefore, it is crucial to understand the hydrogen bond topology in our complex studied systems. The distance and height of the H$\cdots$X RDFs at the first maximum and the NIs at the first minimum of the RDFs are the simplest estimates for the hydrogen bonds formed with atom X.

Based on the RDFs and NIs (Fig. 6 and Figs. S1 and S2), among the many possible interactions between the DES components and cellulose, hydrogen bonding between anions and cellulose is prominently dominant. The $O_{(OAc)}$–$H_{(cel)}$ peak appears at a shorter distance than Cl–$H_{(cel)}$, while the latter has a much higher probability. Cl^- has more $H_{(cel)}$ in the first solvation shell than the $[OAc]^-$ anion. The other way around, the protons of the cellulose have approximately the same amount of oxygen and chloride in the first solvent shell. This may already provide the first explanation as to why the slight swelling of the cellulose in the ChCl:urea DES occurs compared to the ChOAc:urea DES.

The slight swelling of the cellulose in the case of Cl-based DES may be related to anions entering the cellulose frame as previously observed for the cellulose in ionic liquids.[9,50] In order to verify this, we plotted the RDFs of the center of the ring (COR) of the glucose units with the atoms from the anions (see Fig. 7). We observe a high probability of Cl^- being close to the COR, while the O/H atoms show a negligible probability (less than one) in the RDFs. The last COR in the cellulose chains "sees" more than one Cl^- anion in the first solvent shell but is surrounded by less (0.75) oxygen atoms of the $[OAc]^-$ anion.

The choline cation interacts with cellulose as the hydrogen bond donor (H_{ch}–$O_{(cel)}$) and hydrogen bond acceptor (O_{ch}–$H_{(cel)}$) although this happens only on rare occasions; see peaks below one in the lower panel of Fig. 6. Interestingly, urea also acts prominently as a hydrogen bond acceptor (O_u–$H_{(cel)}$ red lines in Fig. 6, middle panel), but not so much as a hydrogen bond donor, which may improve the process somehow, but, obviously, not enough.

There are different hydrogen bond donors and acceptors in the studied systems. The Sankey diagram presented in Fig. 8 shows the topology of hydrogen bonds. Figure 8 is an illustrative way to show the possible hydrogen bonds from the pairwise RDFs written as a matrix of numbers. Each panel corresponds to one of the studied systems. Three hydrogen bond donors were placed on the left side and four acceptors on the right side (see Fig. 1 for atom labels). The width of the bars is proportional to the average number of hydrogen bonds formed by the donor/acceptor atom of the specified kind. The numbers correspond to the average hydrogen bond count per donor/acceptor. The width of the bars being different on the left and right sides in each diagram is a reason for the different number of molecules.

The Sankey diagrams for both systems are quite similar, and the main difference relates to the anions. According to the average count of hydrogen bonds, the $[OAc]^-$ anion accepts less hydrogen bonds than the Cl^- anion. The average count of hydrogen bonds formed by the donor atom is slightly higher in the ChOAc:urea system. All the hydrogen bond acceptors on the right accept hydrogen bonds from all donors except O_{Ch}, which interacts only with H_u.

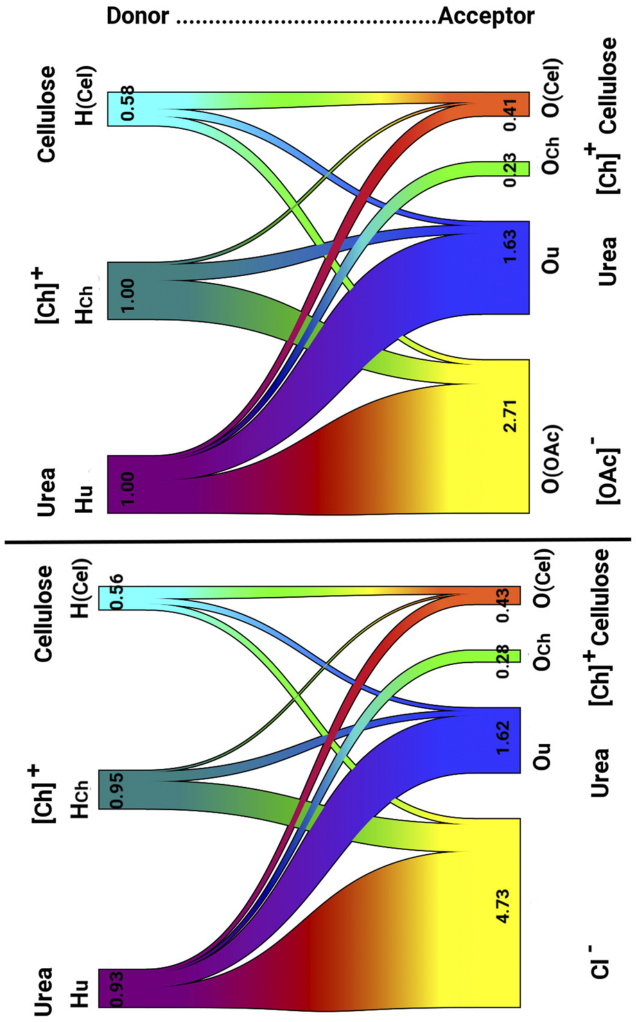

FIG. 8. Linear Sankey diagram representing the hydrogen bond topology of cellulose in the mixture of ChOAc:urea (top) and ChCl:urea (bottom).

This result is consistent with the simulation and experimental investigation of cellulose in ChCl:glycerol and ChCl:urea, and it also shows the dominant interaction of the anion with cellulose.[22,28]

A closer look at the hydrogen bond topology of cellulose–ionic liquids reveals the dominance of the hydrogen bond between anions and cellulose.[51] Moreover, the number of hydrogen bonds between cellulose and the ionic liquids is twice that of cellulose–DESs.[51] However, the possible role of the cation should not be underestimated.[52] For example, it was shown that the imidazolium cation can become chiral due a symmetry loss close to the glucose unit and plays a decisive role in the interaction with glucose units, which is also shown in the onset of a possible carbene[53,54] reaction.[52] Based on the hydrogen bond topology together with the persistent structure for

TABLE III. Surface coverage from Voronoi analysis in %. A distinction is made between the subsets DES ions {$[\mathrm{Ch}]^+$ (cation) and $[\mathrm{OAc}]^-/\mathrm{Cl}^-$ (anion)}, the urea molecules, and the cellulose. The second column lists the unit that is covered. While the following entries along a row list by what the unit is covered to what %.

		Cellulose	$[\mathrm{Ch}]^+$	Urea	$[\mathrm{OAc}]^-/(\mathrm{Cl}^-)$
ChOAc:urea	Cellulose	56.92	16.79	18.32	7.97
	$[\mathrm{Ch}]^+$	4.21	26.08	43.20	26.50
	Urea	4.32	40.63	34.54	20.50
	$[\mathrm{OAc}]^-$	3.58	47.41	38.98	10.04
ChCl:urea	Cellulose	56.93	17.36	21.25	4.46
	$[\mathrm{Ch}]^+$	4.34	34.24	48.98	12.44
	Urea	4.95	45.57	36.98	12.50
	Cl^-	4.13	46.04	49.71	0.11

the model cellulose microfibril, it may be concluded that these particular DESs are not active enough to dissociate the cellulose chains because of the strong intermolecular hydrogen bonding between the DES components.

Creating Voronoi cells in the system at each simulation step provides valuable information about the neighborhood of each component and the interaction surface between components. The average percentage coverage of different components from the surface of each component is shown in Table III. Comparing units that are covered by the anions shows that the $[\mathrm{OAc}]^-$ anions cover all the components more than the Cl^- anions, which is due to the anion size. Meanwhile, urea and cellulose cover the Cl^- anions in ChCl:urea more than the $[\mathrm{OAc}]^-$ anions in ChOAc:urea. This relates well to our previous observations.

The time development of the cellulose surface coverage by the DES components (see Fig. 9) also shows some intriguing details regarding the cellulose solvation in the DESs. The choline cation occupies the same amount of cellulose surface in both ChCl:urea and ChOAc:urea systems. The choline cation's weak hydrogen bonding with the cellulose suggests that its interfacial accumulation is mainly governed by its electrostatic attraction toward anions adsorbed on the surface. The urea molecules cover the largest fraction of the cellulose surface in both systems due to their multiple hydrogen bonds with the cellulose and ions. However, the fact that the urea molecules cover less cellulose surface in the ChOAc:urea mixtures than in the ChCl:urea liquid could be because of the stronger urea–anion interactions in ChOAc:urea DES. The order of interaction strengths results in a specific structure at the cellulose–DES interface, as shown in Fig. 9(c), right side. The spatial distribution of the different species at the surface appears to suggest the aggregation of DES components into separate domains, analogous to the microheterogeneity in DESs.[55]

CONCLUSIONS

The results reported here from MD simulations of a cellulose microfibril solvated in both ChOAc:urea and ChCl:urea mixtures shed light on the role of the DES components in cellulose solvation and dissolution. The dissolution of cellulose in the studied DESs was not observed. However, a slight swelling occurred in the ChCl:urea DES compared to the ChOAc:urea DES. Our analysis indicated close proximity of the chloride anion in contrast to the acetate anion to the glucose units at the end of each strand. This can be interpreted as the onset of an entering mechanism. Moreover, the cellulose hydrogen bonds accepted by the chloride anions were more pronounced than those of the acetate anions.

Cellulose solvation is governed by the overall structure and interactions of the ions and urea molecules with each other. For example, the urea self-interaction is slightly increased and the cation–cation interplay is greatly increased in the ChCl:urea DES compared to the ChOAc:urea DES, allowing the Cl anion to "act more freely" with respect to further coordination. The order of interaction strengths leads to a specific structure at the cellulose–DES interface.

SUPPLEMENTARY MATERIAL

See the supplementary material for additional figures containing snapshots of the simulation boxes (Fig. S1) and site–site RDFs (Figs. S2 and S3).

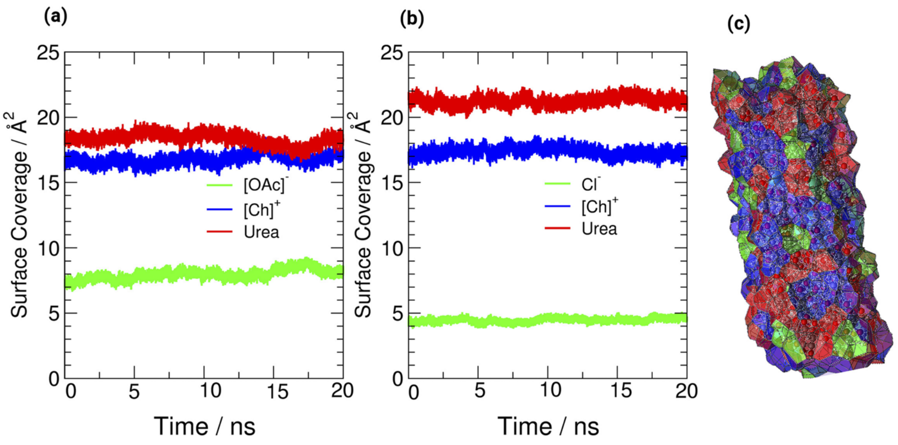

FIG. 9. Time development of the surface coverage of a cellulose microfibril in ChOAc:urea (a) and ChCl:urea (b) by the three components of the DES components, calculated using Voronoi analysis. $[\mathrm{Ch}]^+$ cation (blue), $[\mathrm{OAc}]^-/\mathrm{Cl}^-$ anion (green), and urea in red. (c) Ball-and-stick model of cellulose fibril with surfaces generated using Voronoi analysis of the ChOAc:urea system where the DES components at the interface are color-coded green ($[\mathrm{OAc}]^-$), blue ($[\mathrm{Ch}]^+$), and red (urea).

ACKNOWLEDGMENTS

The authors thank Dr. O. Hollóczki for providing cellulose model as input files. The authors also thank Jan Blasius and Henrrik Niemöller for carefully reading their manuscript. They would also like to thank the DFG for Project No. 406232243.

DATA AVAILABILITY

The data that support the findings of this study are available from the corresponding author upon request.

REFERENCES

[1] T. Heinze, O. A. El Seoud, and A. Koschella, *Cellulose Derivatives: Synthesis, Structure, and Properties* (Springer, 2018).

[2] A. Farrán, C. Cai, M. Sandoval, Y. Xu, J. Liu, M. J. Hernáiz, and R. J. Linhardt, "Green solvents in carbohydrate chemistry: From raw materials to fine chemicals," Chem. Rev. **115**, 6811–6853 (2015).

[3] R. Portela, C. R. Leal, P. L. Almeida, and R. G. Sobral, "Bacterial cellulose: A versatile biopolymer for wound dressing applications," Microbiol. Biotechnol. **12**, 586–610 (2019).

[4] T. Liebert, *Cellulose Solvents: For Analysis, Shaping and Chemical Modification* (ACS Publications, 2010), pp. 3–54.

[5] B. Medronho and B. Lindman, "Competing forces during cellulose dissolution: From solvents to mechanisms," Curr. Opin. Colloid Interface Sci. **19**, 32–40 (2014).

[6] T. Rosenau, A. Potthast, I. Adorjan, A. Hofinger, H. Sixta, H. Firgo, and P. Kosma, "Cellulose solutions in *N*-methylmorpholine-*N*-oxide (NMMO)–degradation processes and stabilizers," Cellulose **9**, 283–291 (2002).

[7] C. Zhang, R. Liu, J. Xiang, H. Kang, Z. Liu, and Y. Huang, "Dissolution mechanism of cellulose in *N*,*N*-dimethylacetamide/lithium chloride: Revisiting through molecular interactions," J. Phys. Chem. B **118**, 9507–9514 (2014).

[8] J. Zhang, J. Wu, J. Yu, X. Zhang, J. He, and J. Zhang, "Application of ionic liquids for dissolving cellulose and fabricating cellulose-based materials: State of the art and future trends," Mater. Chem. Front. **1**, 1273–1290 (2017).

[9] S. Velioglu, X. Yao, J. Devémy, M. G. Ahunbay, S. B. Tantekin-Ersolmaz, A. Dequidt, M. F. Costa Gomes, and A. A. Pádua, "Solvation of a cellulose microfibril in imidazolium acetate ionic liquids: Effect of a cosolvent," J. Phys. Chem. B **118**, 14860–14869 (2014).

[10] H. Zhao, C. L. Jones, G. A. Baker, S. Xia, O. Olubajo, and V. N. Person, "Regenerating cellulose from ionic liquids for an accelerated enzymatic hydrolysis," J. Biotechnol. **139**, 47–54 (2009).

[11] B. Xiong, P. Zhao, K. Hu, L. Zhang, and G. Cheng, "Dissolution of cellulose in aqueous NaOH/urea solution: Role of urea," Cellulose **21**, 1183–1192 (2014).

[12] E. L. Smith, A. P. Abbott, and K. S. Ryder, "Deep eutectic solvents (DESs) and their applications," Chem. Rev. **114**, 11060–11082 (2014).

[13] B. B. Hansen, S. Spittle, B. Chen, D. Poe, Y. Zhang, J. M. Klein, A. Horton, L. Adhikari, T. Zelovich, B. W. Doherty *et al.*, "Deep eutectic solvents: A review of fundamentals and applications," Chem. Rev. **121**, 1232 (2020).

[14] B. E. Gurkan, E. J. Maginn, and E. B. Pentzer, "Deep eutectic solvents: A new class of versatile liquids," J. Phys. Chem. B **124**, 11313 (2020).

[15] M. Francisco, A. van den Bruinhorst, and M. C. Kroon, "New natural and renewable low transition temperature mixtures (LTTMs): Screening as solvents for lignocellulosic biomass processing," Green Chem. **14**, 2153–2157 (2012).

[16] M. Pan, G. Zhao, C. Ding, B. Wu, Z. Lian, and H. Lian, "Physicochemical transformation of rice straw after pretreatment with a deep eutectic solvent of choline chloride/urea," Carbohydr. Polym. **176**, 307–314 (2017).

[17] G. C. Dugoni, A. Mezzetta, L. Guazzelli, C. Chiappe, M. Ferro, and A. Mele, "Purification of Kraft cellulose under mild conditions using choline acetate based deep eutectic solvents," Green Chem. **22**, 8680–8691 (2020).

[18] R. Häkkinen and A. Abbott, "Solvation of carbohydrates in five choline chloride-based deep eutectic solvents and the implication for cellulose solubility," Green Chem. **21**, 4673–4682 (2019).

[19] H. Ren, C. Chen, Q. Wang, D. Zhao, and S. Guo, "The properties of choline chloride-based deep eutectic solvents and their performance in the dissolution of cellulose," BioResources **11**, 5435–5451 (2016).

[20] P. Li, J. A. Sirviö, A. Haapala, and H. Liimatainen, "Cellulose nanofibrils from nonderivatizing urea-based deep eutectic solvent pretreatments," ACS Appl. Mater. Interfaces **9**, 2846–2855 (2017).

[21] Y. Ma, Q. Xia, Y. Liu, W. Chen, S. Liu, Q. Wang, Y. Liu, J. Li, and H. Yu, "Production of nanocellulose using hydrated deep eutectic solvent combined with ultrasonic treatment," ACS Omega **4**, 8539–8547 (2019).

[22] M. A. Smirnov, M. P. Sokolova, D. A. Tolmachev, V. K. Vorobiov, I. A. Kasatkin, N. N. Smirnov, A. V. Klaving, N. V. Bobrova, N. V. Lukasheva, and A. V. Yakimansky, "Green method for preparation of cellulose nanocrystals using deep eutectic solvent," Cellulose **27**, 4305–4317 (2020).

[23] C.-W. Lai and S.-S. Yu, "3D printable strain sensors from deep eutectic solvents and cellulose nanocrystals," ACS Appl. Mater. Interfaces **12**, 34235–34244 (2020).

[24] S. J. Pike, J. J. Hutchinson, and C. A. Hunter, "H-bond acceptor parameters for anions," J. Am. Chem. Soc. **139**, 6700–6706 (2017).

[25] Y. Cao, J. Wu, J. Zhang, H. Li, Y. Zhang, and J. He, "Room temperature ionic liquids (RTILs): A new and versatile platform for cellulose processing and derivatization," Chem. Eng. J. **147**, 13–21 (2009).

[26] M. Brehm, M. Pulst, J. Kressler, and D. Sebastiani, "Triazolium-based ionic liquids: A novel class of cellulose solvents," J. Phys. Chem. B **123**, 3994–4003 (2019).

[27] L. Martínez, R. Andrade, E. G. Birgin, and J. M. Martínez, "PACKMOL: A package for building initial configurations for molecular dynamics simulations," J. Comput. Chem. **30**, 2157–2164 (2009).

[28] C. J. Smith, D. V. Wagle, N. Bhawawet, S. Gehrke, O. Hollóczki, S. V. Pingali, H. O'Neill, and G. A. Baker, "Combined small-angle neutron scattering, diffusion NMR, and molecular dynamics study of a eutectogel: Illuminating the dynamical behavior of glyceline confined in bacterial cellulose gels," J. Phys. Chem. B **124**, 7647–7658 (2020).

[29] S. Plimpton, "Fast parallel algorithms for short-range molecular dynamics," J. Comput. Phys. **117**, 1–19 (1995).

[30] W. L. Jorgensen, D. S. Maxwell, and J. Tirado-Rives, "Development and testing of the OPLS all-atom force field on conformational energetics and properties of organic liquids," J. Am. Chem. Soc. **118**, 11225–11236 (1996).

[31] S. V. Sambasivarao and O. Acevedo, "Development of OPLS-AA force field parameters for 68 unique ionic liquids," J. Chem. Theory Comput. **5**, 1038–1050 (2009).

[32] W. Damm, A. Frontera, J. Tirado-Rives, and W. L. Jorgensen, "OPLS all-atom force field for carbohydrates," J. Comput. Chem. **18**, 1955–1970 (1997).

[33] E. Roos and M. Brehm, "A force field for bio-polymers in ionic liquids (BILFF) – part 1:[EMIm][OAc]/water mixtures," Phys. Chem. Chem. Phys. **23**, 1242 (2020).

[34] E. S. C. Ferreira, I. V. Voroshylova, C. M. Pereira, and M. N. D. S. Cordeiro, "Improved force field model for the deep eutectic solvent ethaline: Reliable physicochemical properties," J. Phys. Chem. B **120**, 10124–10137 (2016).

[35] J. E. Lennard-Jones, "Cohesion," Proc. Phys. Soc. **43**, 461 (1931).

[36] J. W. Eastwood, R. W. Hockney, and D. N. Lawrence, "P3M3DP—The three-dimensional periodic particle-particle/particle-mesh program," Comput. Phys. Commun. **19**, 215–261 (1980).

[37] S. Nose, "Constant-temperature molecular dynamics," J. Phys.: Condens. Matter **2**, SA115 (1990).

[38] W. G. Hoover, H. A. Posch, B. L. Holian, M. J. Gillan, M. Mareschal, and C. Massobrio, "Dissipative irreversibility from Nosé's reversible mechanics," Mol. Simul. **1**, 79–86 (1987).

[39] M. Brehm and B. Kirchner, "TRAVIS—A free analyzer and visualizer for Monte Carlo and molecular dynamics trajectories," J. Chem. Inf. Model. **51**, 2007–2023 (2011).

[40] M. Brehm, M. Thomas, S. Gehrke, and B. Kirchner, "TRAVIS—A free analyzer for trajectories from molecular simulation," J. Chem. Phys. **152**, 164105 (2020).

[41] S. Kaur, M. Kumari, and H. K. Kashyap, "Microstructure of deep eutectic solvents: Current understanding and challenges," J. Phys. Chem. B **124**, 10601–10616 (2020).

[42] K. R. Harris, "Temperature and pressure dependence of the viscosity of the ionic liquid 1-butyl-3-methylimidazolium acetate," J. Chem. Eng. Data **65**, 804–813 (2020).

[43] H. F. D. Almeida, H. Passos, J. A. Lopes-da-Silva, A. M. Fernandes, M. G. Freire, and J. A. P. Coutinho, "Thermophysical properties of five acetate-based ionic liquids," J. Chem. Eng. Data **57**, 3005–3013 (2012).

[44] F. Yang, X. Wang, H. Tan, and Z. Liu, "Improvement the viscosity of imidazolium-based ionic liquid using organic solvents for biofuels," J. Mol. Liq. **248**, 626–633 (2017).

[45] K. R. Seddon, A. Stark, and M.-J. Torres, "Viscosity and density of 1-alkyl-3-methylimidazolium ionic liquids," in *Clean Solvents: Alternative Media for Chemical Reactions and Processing* (American Chemical Society, 2002).

[46] I. Bodachivskyi, U. Kuzhiumparambil, and D. B. G. Williams, "Catalytic valorization of native biomass in a deep eutectic solvent: A systematic approach toward high-yielding reactions of polysaccharides," ACS Sustainable Chem. Eng. **8**, 678–685 (2020).

[47] S. Gehrke, K. Schmitz, and O. Hollóczki, "Is carbene formation necessary for dissolving cellulose in ionic liquids?," J. Phys. Chem. B **121**, 4521–4529 (2017).

[48] J. Hoppe, R. Drozd, E. Byzia, and M. Smiglak, "Deep eutectic solvents based on choline cation - Physicochemical properties and influence on enzymatic reaction with β-galactosidase," Int. J. Biol. Macromol. **136**, 296–304 (2019).

[49] B. Lindman, B. Medronho, L. Alves, C. Costa, H. Edlund, and M. Norgren, "The relevance of structural features of cellulose and its interactions to dissolution, regeneration, gelation and plasticization phenomena," Phys. Chem. Chem. Phys. **19**, 23704–23718 (2017).

[50] M. Zhang, S.-C. Wu, W. Zhou, and B. Xu, "Imaging and measuring single-molecule interaction between a carbohydrate-binding module and natural plant cell wall cellulose," J. Phys. Chem. B **116**, 9949–9956 (2012).

[51] M. Brehm, J. Radicke, M. Pulst, F. Shaabani, D. Sebastiani, and J. Kressler, "Dissolving cellulose in 1, 2, 3-triazolium- and imidazolium-based ionic liquids with aromatic anions," Molecules **25**, 3539 (2020).

[52] J. Blasius, R. Elfgen, O. Hollóczki, and B. Kirchner, "Glucose in dry and moist ionic liquid: Vibrational circular dichroism, IR, and possible mechanisms," Phys. Chem. Chem. Phys. **22**, 10726–10737 (2020).

[53] S. Gehrke and O. Hollóczki, "N-heterocyclic carbene organocatalysis: With or without carbenes?," Chemistry **26**, 10140 (2020).

[54] S. Gehrke and O. Hollóczki, "Are there carbenes in N-heterocyclic carbene organocatalysis?," Angew. Chem., Int. Ed. **56**, 16395–16398 (2017).

[55] V. Alizadeh, D. Geller, F. Malberg, P. B. Sánchez, A. Padua, and B. Kirchner, "Strong microheterogeneity in novel deep eutectic solvents," ChemPhysChem **20**, 1786–1792 (2019).

E. Chemistry Dissolved in Ionic Liquids. A Theoretical Perspective

Barbara Kirchner,[*] Jan Blasius,[*] Vahideh Alizadeh,[*] Andreas Gansäuer,[†] and Oldamur Hollóczki[‡][*]

Received: 19 October 2021, Published online: 17 January 2022.

Reprinted in Appendix E with permission[§] from

B. Kirchner, J. Blasius, V. Alizadeh, A. Gansäuer, and O. Hollóczki, *J. Phys. Chem. B* **2022**, *126*, 766–777, *doi:10.1021/acs.jpcb.1c09092.*

Contributions to the manuscript

- Performing of all calculations presented in section “Radical Problems in Ionic Liquids”
- Interpretation of the results presented in section “Radical Problems in Ionic Liquids”
- Writing of section “Radical Problems in Ionic Liquids”
- Co-writing of the other parts

---

[*] Mulliken Center for Theoretical Chemistry, Clausius Institute for Physical and Theoretical Chemistry, University of Bonn, Beringstr. 4–6, 53115 Bonn, Germany

[†] Kekulé-Institut für Organische Chemie und Biochemie, Gerhard-Domagk-Str. 1, University of Bonn, 53121 Bonn, Germany

[‡] Department of Physical Chemistry, Faculty of Science and Technology, University of Debrecen, 4010 Debrecen, Hungary

[§] Permission requests to reuse material from this chapter should be directed to the American Chemical Society.

THE JOURNAL OF PHYSICAL CHEMISTRY B
A JOURNAL OF THE AMERICAN CHEMICAL SOCIETY

pubs.acs.org/JPCB Perspective

Chemistry Dissolved in Ionic Liquids. A Theoretical Perspective

Barbara Kirchner,* Jan Blasius, Vahideh Alizadeh, Andreas Gansäuer, and Oldamur Hollóczki

Cite This: *J. Phys. Chem. B* 2022, 126, 766−777

Read Online

ACCESS | Metrics & More | Article Recommendations

ABSTRACT: The theoretical treatment of ionic liquids must focus now on more realistic models while at the same time keeping an accurate methodology when following recent ionic liquids research trends or allowing predictability to come to the foreground. In this Perspective, we summarize in three cases of advanced ionic liquid research what methodological progress has been made and point out difficulties that need to be overcome. As particular examples to discuss we choose reactions, chirality, and radicals in ionic liquids. All these topics have in common that an explicit or accurate treatment of the electronic structure and/or intermolecular interactions is required (accurate methodology), while at the same time system size and complexity as well as simulation time (realistic model) play an important role and must be covered as well.

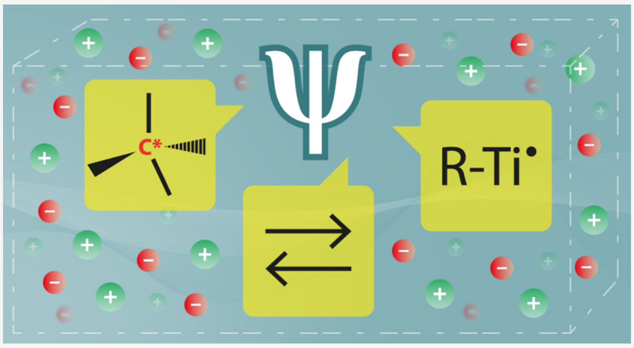

■ INTRODUCTION

Sustainable chemistry is a broad field with many materials and processes of interest, which may open possibilities to decrease our impact on the environment.[1−4] Among these, ionic liquids (ILs) have received particular scientific attention, leading to comprehensive discussions about their toxicity.[5,6] The research on ionic liquids was for a long time of two extremes: aiming at either very fundamental or very application-oriented questions. Interestingly, throughout the past years these two extremes started to approach each other to merge into interesting advanced academic ionic liquid applications. This bears significant challenges for theoretical chemists in many aspects if they are to follow or assist the experiments, such as the size of the systems[7] to consider and the accuracy of the results that are needed. Moreover, recently a new field related to ILs has emerged, deep eutectic solvents (DESs). In the theoretical research on DESs, the complexity of the system is a burdensome necessity, since this very property gives these mixtures their practically most important feature: their low melting point compared to the primary substances.[8]

Traditionally, ionic liquids (and DESs) have been studied computationally mainly from classical molecular dynamics simulations based on force fields.[9−22] Car−Parrinello or Born−Oppenheimer *ab initio* molecular dynamics (AIMD) simulations[23] based on the explicit description of the electronic structure concerning ionic liquids[24,25] and deep eutectic solvents[8,26−30] also appeared in the literature. Many contributions and clarifications came from static quantum chemical calculations.[31−37] As usual in static quantum chemistry, density functional theory (DFT) serves as workhorse for many calculations;[38,39] however, different methods were applied as well.[40−42] Polarizable force fields in all forms receive always special attention because they overcome many problems of traditional MD simulations.[43−47]

As Sharma et al. point out in their perspective about the differences of molten salts and ionic liquids,[48] general ionic liquid research tends to be always very broad and a myriad of excellent reviews exists for every special topic. In this Perspective we aim at considering only three wider ionic liquid applications without covering the literature completely as examples, which are not completely unaffected by each other, and they do not necessarily lead to industrial applications. These topics will, in our opinion, help identify and recognize the difficulties theoreticians face and will also highlight the accomplishments of computational chemistry in following the research to the aforementioned newly besieged more advanced stage.

Probably the most prominent applications of ionic liquids are related to energy devices.[49−51] The obvious connection of our three discussed examples to electrochemistry (echem) will be underscored where we deem it necessary. This will be, of course, far from being complete. Besides, several reviews with respect to calculations in echem applications and ionic liquids exist already.[52−56]

Received: October 19, 2021
Revised: January 2, 2022
Published: January 17, 2022

https://doi.org/10.1021/acs.jpcb.1c09092

As first example, we would like to recall that ionic liquids can be attractive solvents for reactions.[57,58] They can be used to dissolve substances, stabilize transition states and intermediates, or simply change the selectivity for different reasons. Early (experimental) studies with a molecular level focus were performed by the groups of Welton,[59] Croft and Harper,[60−63] D'Anna,[64,65] and Chiappe.[66] Connected to this are the IL applications regarding chirality. Chiral ionic liquids (CILs) were studied experimentally very early on by Seddon, Wasserscheid, and others, who introduced the possibility to include chirality in IL ions.[67−71] In amino acid-based ILs, the amino acid group can provide the cation and/or the anion.[72] A further challenge for theory is our third topic, "radicals in ionic liquids".[73,74] The difficulties lie in the complex electronic structure of these compounds, next to the intricacies of solvation in these highly structured solvents. Nonetheless, their importance is shown by the myriad of reactions in which radicals are involved, as will be shown below.

■ RESULTS AND DISCUSSION

Ionic Liquids as Reaction Media. An excellent review article about the main properties, i.e., the bulk polarity and the nanostructure[75] or that they are microheterogeneous liquids,[76] which make ILs good solvents, was provided by the D'Anna group recently.[65] One of the most important messages of their review is that the IL effect[59] can be influenced not only by the nature of the IL but also by the nature of the substrate, highlighting the complexity of the factors that govern reactivity in such media. Examples for a mechanism switch are provided.[65]

As trivial as it may sound, let us recall that, in describing reactivity, the challenge for theoretical studies is the need to treat the electronic structure explicitly, if a proper description of bond breaking and formation is to be achieved. Furthermore, describing the peculiar solvent effects of ionic liquids—often dependent on amphiphilic interactions and mesoscale micro-segregation—necessitates dealing with a large amount of particles. Several reactions in explicit ionic liquid solvents were studied from theory by the Acevedo group.[77,78] Acevedo and co-workers apply to this end mixed *ab initio* and molecular mechanics simulations (QM/MM), where the QM part delivers the explicit electronic structure, whereas the MM part—that can deal with the huge number of particles—can provide the description of influential long-range solvation effects. Large improvements of the results were observed if the QM part for the solute was described through exact exchange functionals of density functional theory[78] instead of only semiempirical methods.[77] Similarly, much effort was also put into improving the MM part that definitively leads to a superior solvent structure.[9−11]

Recently, the anion $[BF_4]^-$ is gaining interest in electrochemical applications. Already in the early days of the renaissance of ILs, Ken Seddon warned of the instability of $[BF_4]^-$ and $[PF_6]^-$, especially in aqueous solution.[79] This does not only raise questions about the inertness of the corresponding materials and their use in sustainable processes but also makes the simulation of such systems from classical MD nontrivial, considering that their spontaneous reactivity is their inherent feature. Standard classical simulations cannot describe reactivity, while in AIMD simulations, without the use of free energy methods, they can be observed only if the barrier is not higher than ca. k_BT (Boltzmann constant times temperature). Nonetheless, if this criterion is met, simple spontaneous reactions of or in ILs can be captured from full AIMD simulations. These include, for example, CO_2 absorption studies in ILs,[80−82] Grotthuss type mechanisms that are closely related to echem,[83] or decomposition reactions.[84]

CO_2−IL mixtures were studied from AIMD by Bhargava and Balasubramanian[81] where no chemical reaction occurred because the chosen ionic liquid (1-*n*-butyl-3-methylimidazolium hexafluorophosphate ($[C_4C_1Im][PF_6]$)) absorbs this gas physically.[85,86] Similarly, in a study of ethylammonium nitrate ($[N_{2HHH}][NO_3]$) a rationale could be provided for the missing swelling when CO_2 is being physically absorbed, but a chemical reaction did not occur.[87] Furthermore, AIMD simulations at 1 and 5 MPa were performed to investigate the CO_2 absorption in the choline chloride:ethylene glycol DES. While at lower pressure the cation and the ethylene glycol played the major role, at higher pressure the anion was more important in the physical absorption of CO_2.[26]

The chemical absorption of CO_2 by amino acid-based ionic liquids was studied from AIMD and static quantum chemical methods.[80,88] Reaction mechanisms were discussed, and the modification of the CO_2 adduct formation barrier (rate-determining step) was tested. It can be increased by side-chain elongation, the introduction of an aromatic π-system, and perfluorination.[80] The chemical absorption of CO_2 in imidazolium acetate ionic liquids has also been studied through AIMD.[88] It was found that CO_2 does not hinder the mobility of the most acidic ring proton and it seemed to rather induce it. It is worth mentioning that a couple of static quantum chemical investigations about CO_2 absorption in ILs exist as well, for example in refs 85, 86, and 88−91. First principles Monte Carlo simulations were applied by the Rai group to test the applicability of different functionals for the calculations of vapor−liquid equilibria of CO_2 in ILs.[82] Interestingly, the authors have a very good point about that classical MD can fail "when/where they are needed the most, i.e., when experiments are either difficult or nearly impossible to perform", which appears for systems under extreme pressure or temperature, or chemicals that are toxic, or for unknown materials.[82]

The Grotthuss diffusion of protons in aqueous solutions is a typical case for the applicability of AIMD. In certain ILs, similar structural diffusion can occur; thus, charge can move in space with a minimal movement of the atoms, if bonds can rearrange within a network of covalent and noncovalent interactions. The first Grotthuss diffusion process that was observed in ionic liquids from AIMD was that in mixtures of $[C_2C_1Im][Cl]$ and aluminum trichloride.[83] In these liquids, the anionic clusters of aluminum can transfer a chloride anion to a neutral cluster. Because the newly formed charged cluster can transfer another chloride at a different site, this mechanism provides a shortcut for charge transport. These theoretical findings, obtained by AIMD, gave a feasible explanation for the superb performance of these ILs in echem applications.[83] Analogously to aqueous solutions of acids and bases, a proton conduction mechanism for imidazole−acid mixtures has been observed.[92] These mixtures are often termed pseudo-ILs since they are not fully ionic but contain many neutral imidazole and acid molecules.[92] The proton transfer from one basic site to the other can therefore be conducted through a chain of acids and imidazolium compounds. By altering the substituents of the acid and the base, further pseudo-ILs were designed, which should show similarly remarkable conductive processes.[92] An interesting work of Bodo and co-workers considered the Grotthuss diffusion in amino acid-based ionic liquids. They observed in their AIMD simulations that the repulsive anion−anion interplay can be weakened to such an extent that a proton migration becomes possible also within the anionic component of the liquid.[93] Recently, a similar dynamic bond breaking and bond formation process has been observed for the mixtures of imidazolium halide ILs and phosphorus trihalides. It was observed through experiments and AIMD simulations that the anion coordinates to the phosphorus atom, forming a complex anion in a dynamic equilibrium. This process was suggested to offer a way for Grotthuss diffusion of anions.[94] The actual Grotthuss diffusion process was observed later in a PCl_3:$[C_4C_1Im][Cl]$ 3:1 mixture with AIMD[95] (see Figure 1). Through static calculations, the possible mechanisms of further anionic structural diffusion processes of ionic liquids have been comprehensively explored.[95]

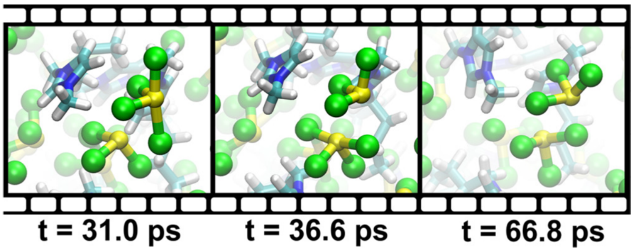

Figure 1. Selected snapshots from a simulation of a PCl_3:$[C_4C_1Im][Cl]$ 3:1 mixture: (P, yellow; C, cyan; Cl, green; H, white; N, blue). The transfer of a chloride from a $[PCl_4]^-$ complex anion to a PCl_3 can be observed, which is followed by the break of another P−Cl bond in the latter molecule, releasing a free chloride at the opposite end of the molecule. To highlight the time scale of the process, the physical time in the simulation is given for each snapshot. Reproduced with permission from ref 95.

An obvious drawback in all AIMD simulations is that the time scales are far below those of classical simulations. There are some promising approaches that we want to mention here. Sebastiani and co-workers[96,97] derived in the spirit of Monte Carlo simulations[98] a matrix formalism to be able to simulate proton dynamics for extended systems and time scales. This involves the construction of a Markov chain based on an AIMD run and the subsequent propagation of the proton distribution by means of transition matrices, which contain kinetic data from both ultrashort and intermediate (picoseconds) time scales.[96,97] Second, improved tight-binding semiempirical methods[99] that have been applied in ILs[100−102] may lead to larger and longer investigations of (organic) reactions in ILs and DESs due to the reduced costs of the electronic structure method. Quantum embedding for material chemistry based on domain separation and open subsystems might be another solution to these problems.[103] As such methods can provide a more sufficient sampling than traditional AIMD of wide conformational spaces, they enable theoretical investigations of, for example, the reactivity of large and flexible molecules. Moreover, they can contribute to the investigation of chiral phenomena like chiroptical response or chirality transfer, which necessitate the consideration of the electronic structure and a proper sampling of all relevant conformers.

Chirality: Complications from Asymmetry. Chiral induction effects in the amino acid-based ionic liquid 1-ethyl-3-methylimidazolium L-alaninate ($[C_2C_1Im][$L-ala$]$) were detected by Oulevey and co-workers.[104,105] Experimental vibrational circular dichroism (VCD) spectra were found to be dominated by the chiral anion, but Raman optical activity measurements revealed chiroptical activity of the achiral cation, thereby proving chirality transfer.[104,105] With the aid of theoretical investigations, a symmetry breaking in the conformational distribution of the cation was found to be the source for the chiroptical response, inasmuch as the energetic degeneration of two mirror-imaged conformations gets perturbed by the chiral anion.[104,105] This study exemplifies that experiments can definitely prove the occurrence of chiral induction effects, but theoretical methods can provide valuable mechanistic insights, not least with the aid of theoretical spectra which can be decomposed into contributions of different components.

However, an accurate modeling of phenomena like chiral induction poses severe challenges. The assessment through static approaches[106−109] can be achieved by calculations of diastereomeric complexes, that is, clusters in which a permanently chiral species interacts with different conformations of an achiral molecule. Based on the electronic energies of the clusters, indications for the most stable conformations of the achiral molecule in the presence of the chiral species can be obtained. However, since chiral induction is often a dynamic process[110,111] influenced by many species, the search for a representative ensemble of clusters is desirable but far from being straightforward. Although MD simulations can circumvent this ensemble issue,[112,113] great care has to be taken with respect to the force field employed. As discussed above, classical force fields are usually fitted to macroscopic properties of known substances, meaning they do not necessarily apply to unknown substances or deliver a reliable description of the correct intermolecular interactions and hence molecular-level speciation. Chirality transfer is often related to the formation of intermolecular complexes involving many particles. Therefore, the usage of either polarizable force fields or AIMD simulations is recommended, at the cost of limiting the system size to fewer molecules and restricting the analysis of the trajectories to local phenomena in the case of AIMD.

If the calculation of vibrational spectra and their decomposition into contributions of different species is desired, correlation functions can be employed in nonstatic approaches. A VCD spectrum can for instance be calculated from an MD trajectory by taking the Fourier transform of the time cross-correlation function of the electric dipole moment $\mu(t)$ and the magnetic dipole moment $m(t)$:[114]

$$\Delta A_{\mathrm{VCD}}(\tilde{\nu}) = \frac{N_{\mathrm{A}}}{12\varepsilon_0 c^2 k_{\mathrm{B}} T}\int_{-\infty}^{\infty} [\langle\dot{\mu}(\tau)\cdot\dot{m}(\tau+t)\rangle_\tau - \langle\dot{m}(\tau)\cdot\dot{\mu}(\tau+t)\rangle_\tau]\exp(-2\pi i c\tilde{\nu}t)\,\mathrm{d}t \qquad (1)$$

Herein, N_A is the Avogadro constant, t and τ represent the time, c is the speed of light, ε_0 is the vacuum permittivity, k_B is the Boltzmann constant, T is the average temperature of the simulation, and $\langle\dot{\mu}(\tau)\cdot\dot{m}(\tau+t)\rangle_\tau$ is the cross-correlation function[114] of the electric and magnetic dipole moments. For the calculation of the electric dipole moments we presented the so-called Voronoi tessellation which partitions the electron density in space.[115] Based on this partitioning scheme also the magnetic dipole moments can be obtained by solving the according partial differential equation.[116]

Following this approach, our investigations of different D-glucose isomers dissolved in the nonchiral ionic liquid 1-ethyl-3-methylimidazolium acetate ($[C_2C_1Im][OAc]$) revealed the occurrence of chiral induction effects with the aid of theoretical VCD spectra.[117] While the global spectra were dominated by the chiral D-glucose molecules, a decomposition into the contribu-

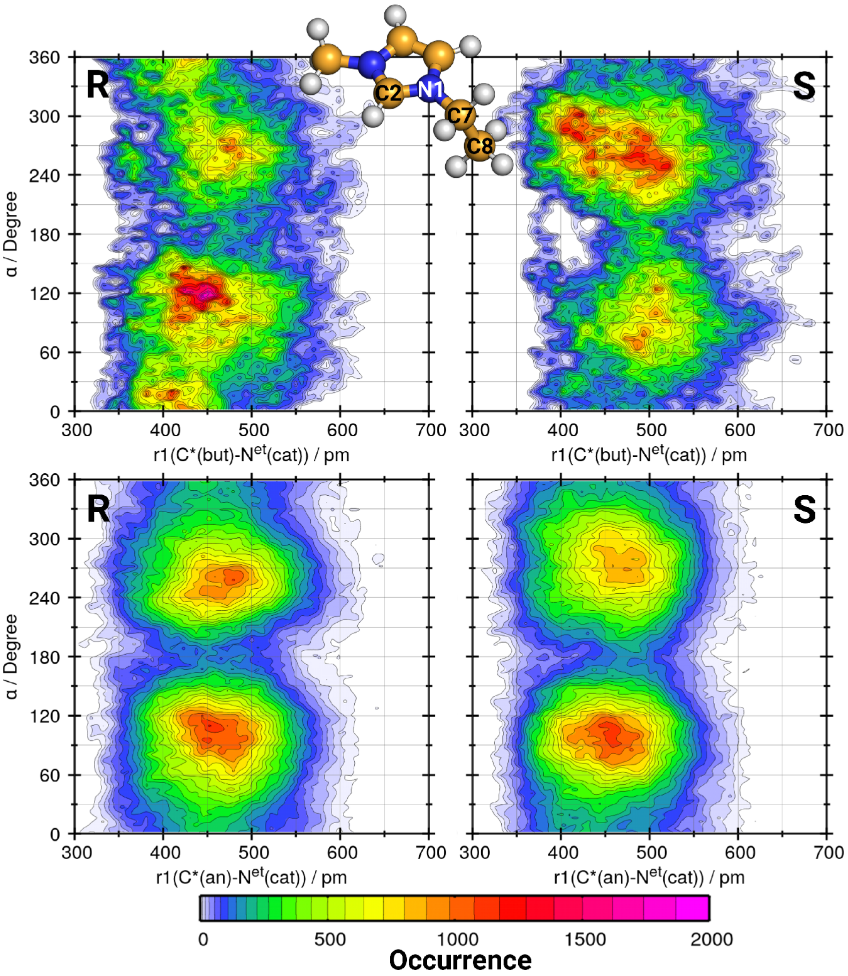

Figure 2. Combined distribution functions correlating the dihedral angle *α* (C2−N1−C7−C8) of the cation 1-ethyl-3-methylimidazolium with the distance between the chiral center of butan-2-ol (top) or the chiral center the anion L-alaninate (bottom) and the nitrogen atom N1 of the cation bound to the ethyl group. Note that only the closest cation with respect to butan-2-ol or the anion was taken into account. Reproduced with permission from ref 24.

tions of the different components clearly confirmed chiroptical activity of the achiral IL components. Opposed to the chirality transfer observed in neat [C_2C_1Im][L-ala], the chiral information does not stem from one of the IL components but from a solute. A deeper investigation of the intermolecular interactions revealed an involved network, causing the formation of tight complexes between the different species which can promote the chirality transfer. This highlights the importance to use computational methods that can describe the intermolecular speciation properly.

To investigate the influence of chiral induction on enantiomeric recognition, we performed AIMD simulations of (*R*)- and (*S*)-butan-2-ol dissolved in the chiral ionic liquid [C_2C_1Im][L-ala].[24] Depending on the chirality of the solute, the systems were termed as **R** (heterochiral) and **S** (homochiral). We observed that the heterochiral system is stabilized by ΔE = 18.8 kJ/mol compared to the homochiral one, indeed indicating the occurrence of chiral discrimination induced by the IL. Although this could be attributed to diastereomeric complexes formed between the permanently chiral [L-ala]$^-$ anion and the butan-2-ol enantiomers, chiral information induced on the cation might amplify this process.

A more detailed investigation of the effects of the [L-ala]$^-$ anions and the enantiomers of butan-2-ol on the structure of the cation is presented in Figure 2, which depicts combined distribution functions that correlate the dihedral angle *α* (C2−N1−C7−C8) of the cation (see sketch in Figure 2) with the distance between the nitrogen atom N1 of the cation and the chiral center of butan-2-ol (top) or the chiral center of the [L-ala]$^-$ anion (bottom).[24] To capture the local effects of the permanently chiral species on the achiral cation, only the closest cation with respect to butan-2-ol or the anion was taken into account. Around the [L-ala]$^-$ anion, the cation shows a slight preference to adopt structures with *α* around 120° (bottom panel). A preference for the same cation structure is observed around (*R*)-butan-2-ol (top left); however, around (*S*)-butan-2-ol we observe a preference for cation structures with opposite chirality, i.e., *α* around 270° (top right). Thus, the [L-ala]$^-$ anion and (*R*)-butan-2-ol induce the same chirality within the cation. As a consequence, the IL itself creates an environment in which (*R*)-butan-2-ol fits well, while (*S*)-butan-2-ol does not, ultimately leading to chiral discrimination effects caused by chiral induction.

To verify the observed chiral induction effects, we present in Figure 3 the calculated VCD spectra obtained from the AIMD trajectories. As observed in our previous study of D-glucose dissolved in [C_2C_1Im][OAc],[117] the global spectrum is dominated by the chiral compound in excess, here the [L-ala]$^-$

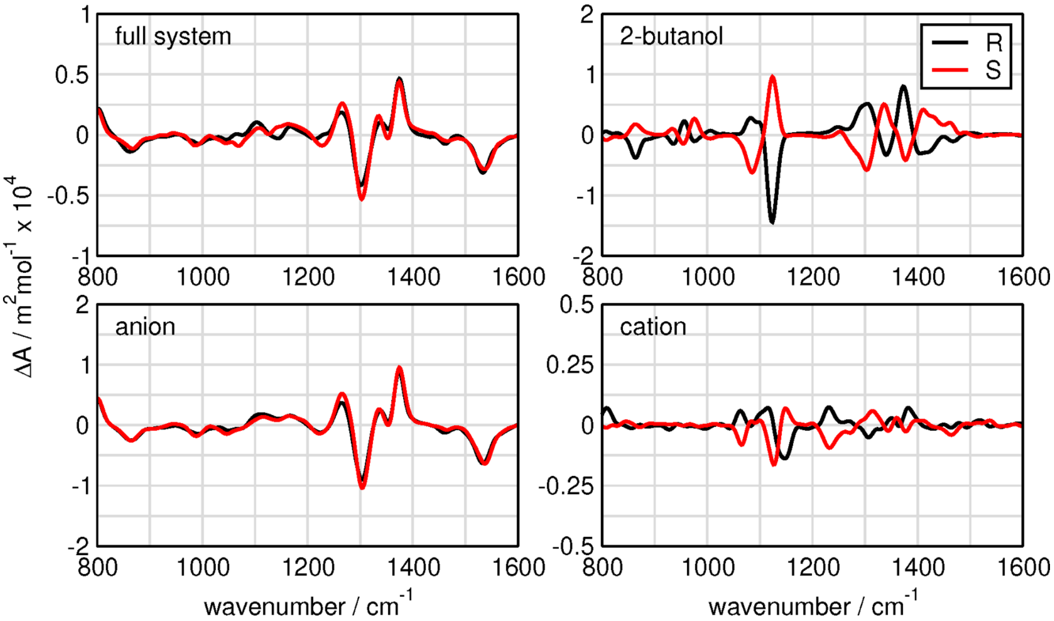

Figure 3. Vibrational circular dichroism spectra obtained from *ab initio* molecular dynamics simulations of (*R*)- and (*S*)-butan-2-ol in the ionic liquid 1-ethyl-3-methylimidazolium L-alaninate.

anion. Both butan-2-ol enantiomers show mirror-imaged spectra, as it is expected due to their opposite chirality. However, mirror-imaged VCD spectra are also observed for the achiral cation, clearly proving the existence of enantiomeric conformers and the occurrence of chirality transfer. The decreased intensity as compared to the [L-ala]$^-$ anion and butan-2-ol can be explained by the conformational analysis presented in Figure 2. Although the cation preferably adopts specific conformations around either the anion or butan-2-ol, conformations with opposite chirality are still present in the solution. Thus, the chiroptical response of those enantiomeric structures cancels out to some extent, and only chiral conformations being present in excess contribute to the spectrum.

While this study exemplifies that the approach presented above allows a theoretical investigation of chirality transfer from spectroscopy, it requires knowledge about the electronic structure whose calculation is computationally rather intense. As a computationally less expensive alternative for calculating bulk-phase spectra, we introduced a cluster weighting approach[109] based on the quantum cluster equilibrium theory,[118] and we are currently investigating the calculation of dipole moments based on partial charges.[113] Provided that a reliable description of dipole moments from partial charges can be achieved, polarizable force fields[43] could be employed for the calculation of bulk phase spectra. As another alternative, force fields specially fitted for the description of spectroscopic properties or reaction dynamics can be employed.[119] The development of such specialized force fields might also be a promising approach for the theoretical description of radicals and their dynamics in solution.

Radical Problems in Ionic Liquids. Early experimental studies by the Lagrost group considered the dimerization of acetophenone anion radicals in ionic liquids.[120] Interestingly, they found an increased kinetics in 1,3-dialkylimidazolium salts as compared to 1,2,3-trialkylimidazolium salts, which they could attribute to hydrogen bonding to the acidic proton of the imidazolium ring and hence to charge transfer between the radical anion and the cation.[120]

As pointed out by the López group,[4] DFT calculations can run into problems if the electronic structure becomes too complicated such as in complex spin configurations. A remedy can be the use of hybrid functionals in which the exchange term is based on Hartree−Fock, however, at the cost of computationally expensive calculations. For repeated force calculations (when molecular dynamics simulations are involved) of solvent effects in large systems, this might not pose a realistic possibility, and other approaches like the Hubbard model which is often abbreviated as DFT+U[4] must be sought for.

Izgorodina and co-workers pioneered quantum chemical calculations of radicals in ionic liquids by considering radicals combined with ion pairs in multiple conformations.[31,32,121,122] To be able to study the complicated electronic structure of such systems in ILs, they specifically developed a spin ratio scaled MP2 method termed SRS-MP2.[123]

It is worth mentioning that excess electrons[124,125] in ionic liquids have been studied from AIMD simulations as well. As Unterreiner and co-workers point out, a major task is to understand "the fate of excess electrons (and holes)", which needs the consideration of "various formation mechanisms considering structural and dynamical aspects".[125] Wang et al. investigated an excess electron in eight ion pairs of 1-methylpyridinium chloride already in 2010.[126] While they used the generalized gradient approximation (GGA) functional BLYP[127,128] to generate the trajectory, they added calculations employing exact exchange density functionals on top of these simulations at certain snapshots of the BLYP trajectory. Their analysis contained energy level plots, the density of states, and orbital analysis next to radial pair distribution functions. A similar choice (PBE[129] and B3LYP[127,128]) was taken by Margulis and co-workers[130] when studying a dry excess electron in ethyltrimethylammonium bis(trifluoromethane)sulfonimide ([N$_{1113}$][Tf$_2$N]). The reasons for this are that the unpaired electron in the singly occupied molecular orbital could suffer under the self-interaction error, and the valence-conduction

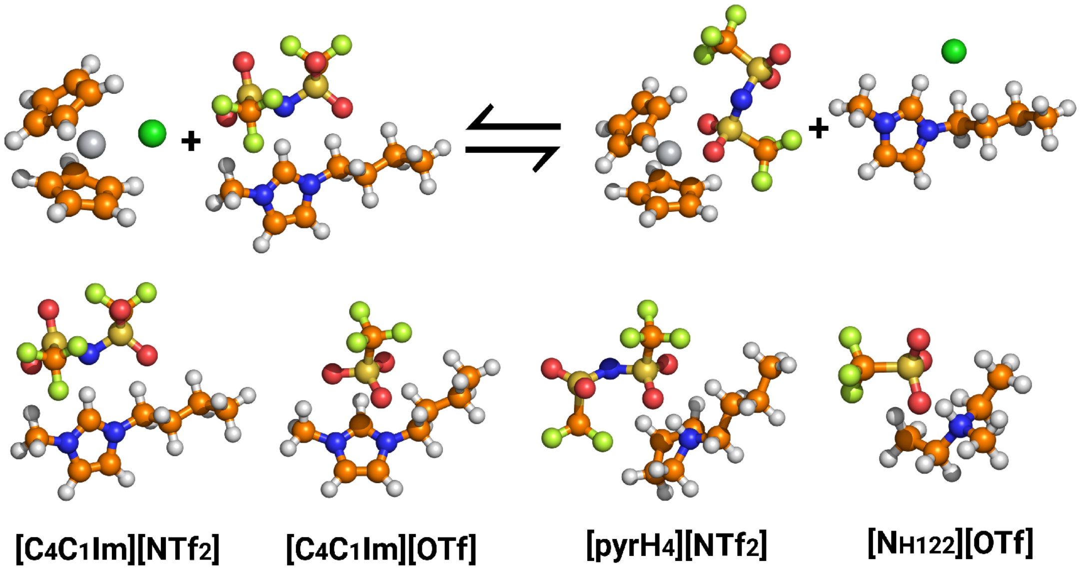

Figure 4. Top: illustration in ball-and-stick representation of the exchange reaction between the chloride ligand of a titanocene complex[138,139] and the $[NTf_2]^-$ anion of the 1-*n*-butyl-3-methylimidazolium bis(trifluoromethylsulfonyl)imide $[C_4C_1Im][NTf_2]$ ion pair. Bottom: different ion pairs as used in the calculations, from left to right: $[C_4C_1Im][NTf_2]$; $[C_4C_1Im][OTf]$ ([OTf]: trifluoromethanesulfonate anion), $[pyrH4][NTf_2]$ (cation: *N*-butylpyrrolidinium), and $[N_{H122}][OTf]$ (cation: diethylmethylammonium).

Table 1. Reaction Energy E^{IP} in kJ/mol of the Exchange Reaction (2)[a]

method	$E^{[C_4C_1Im][NTf_2]}$	$E^{[C_4C_1Im][OTf]}$	$E^{[pyrH4][NTf_2]}$	$E^{[N_{H122}][OTf]}$	RAD	$t(TiCp_2X)$
DZVP[134] basis set						
BLYP	97.8 (1.3)	41.8 (4.4)	69.6 (1.1)	31.7 (3.9)	2.7	371
PBE	97.5 (1.6)	35.1 (2.3)	65.0 (3.5)	24.6 (3.2)	2.7	475
revPBE	100.7 (1.6)	43.6 (6.2)	67.5 (1.0)	30.5 (2.7)	9.5	393
PBE+*U* (*U* = 5 eV)	78.1 (21.0)	21.4 (16.0)	45.7 (22.8)	10.8 (17.0)	19.2	558
PBE+*U* (*U* = 2 eV)	99.6 (0.5)	32.8 (4.6)	67.2 (1.3)	22.3 (5.5)	3.0	382
TPSS	91.5 (7.6)	34.3 (3.1)	63.2 (5.3)	26.0 (1.8)	4.5	617
B3LYP(ADMM)	105.2 (6.1)	49.7 (12.3)	77.0 (8.5)	39.7 (11.9)	9.7	1266
PBE0(ADMM)	104.2 (5.1)	42.8 (5.4)	71.5 (3.0)	26.0 (1.8)	3.8	1380
PBE0	99.1 (−)	37.4 (−)	68.5 (−)	27.8 (−)		60640
TZVP[134,145] basis set						
BLYP	89.1 (4.9)	32.8 (0.9)	67.8 (0.8)	29.3 (1.3)	2.0	806
PBE	87.4 (6.6)	26.3 (7.4)	61.6 (7.0)	22.1 (8.5)	7.3	852
TPSS	85.3 (8.7)	22.7 (11.0)	62.7 (5.9)	20.4 (10.2)	9.0	1350
B3LYP(ADMM)	97.2 (3.2)	40.0 (6.3)	75.9 (7.3)	37.1 (6.5)	5.8	1983
PBE0(ADMM)	94.0 (−)	33.7 (−)	68.6 (−)	30.6 (−)		2752

[a] Average timing $t(TiCp_2X)$ with X = Cl or anion in s of each single point calculation that includes Ti, running on 64 cores of a compute cluster with 2.3 GHz AMD-Opteron-CPUs and 128 GB RAM. The values in parentheses give the absolute deviation from the reference value, i.e., PBE0 for DZVP and PBE0(ADMM) for TZVP. RAD gives the average absolute deviation from the reference.

energy band gap could be underestimated. While the former one was found to be rather unimportant, the latter turned out to be relevant for the calculation of the optical absorbance spectrum.[130] The authors point out that self-interaction appears to be more relevant in positively charged systems generated by the removal of an electron and creation of a hole. In general, it is found that the excess electron can delocalize over cations or anions depending on the nature of the ions involved.[130]

Roy and Gill et al.[131,132] studied d-block metal ions (Ni^{2+}, Co^{2+}, and Cr^{3+}) in molten salts by a combined AIMD and experimental extended X-ray absorption fine structure (EXAFS) approach. They point out the importance of AIMD when studying such systems because the consideration of electronic interactions and spin polarization is necessary. They give a warning that the right prediction of the local dynamical coordination environment and chemical speciation of the complex solvent mixtures is necessary to allow high-quality predictions.[131,132]

Similarly, Salanne and co-workers used AIMD to study biredox ionic species in acetonitrile.[133] They used the GGA functional BLYP[127,128] in conjunction with the TZV2P basis set.[134] To describe the radical species properly, the scaled self-interaction correction[135,136] was applied. This work was later used to parametrize polarizable force fields because problems due to ad hoc developed force fields of radicals and the lack of polarization effects description for radical species can lead to inaccuracies in solvation and dynamics.[137]

To illustrate the difficulty of functional choice and computational time, we calculated the artificial gas phase exchange reaction (eq 2) of the chloride ligand of a titanocene complex[138,139] with an anion from an IL ion pair as illustrated in Figure 4. The calculation of such processes is highly attractive for catalysts, and reaction design as quantitative predictions about the (reversible) modulation of the catalysts' redox potentials can be made. All four structures (titanocene complexes and ion pairs) for each IL in eq 2 have been optimized with the PBE0[129]/def2-SVP[140] level of theory with unrestricted DFT by the orca package.[141] Subsequently, the single point energy calculations were performed from the CP2K package.[142] The following functionals and basis sets were chosen: PBE0,[129] PBE,[129] revPBE,[143] BLYP,[127,128] B3LYP,[127,128] TPSS,[144] DZVP,[134] and TZVP.[134,145] The auxiliary density matrix method (ADMM) for the hybrid functionals was tested.[146] Pseudopotentials were chosen from ref 134. A value of 10^{-6} was used as target accuracy for the SCF convergence (EPS SCF 1.0×10^{-6}). A 200 Ry density CUTOFF criterion was employed with multigrids number 5 (NGRID 5 and REL CUTOFF 30) by using the smoothing for the electron density (NN10 SMOOTH) and its derivative (NN10).[147]

$$\mathrm{TiCp_2Cl + cation{-}anion \rightleftharpoons TiCp_2anion + cation{-}Cl} \tag{2}$$

Table 1 summarizes the reaction energies of the exchange reaction (2), the average timing for the respective single point calculations, and the absolute deviations from the reference values. Additionally, we present RAD values which represent the averaged absolute deviation from the reference for a respective level of theory. Based on Table 1, an obvious anion effect is visible; that is, the reaction is on average by 60 kJ/mol energetically more favorable when $[\mathrm{OTf}]^-$ is chosen than when $[\mathrm{NTf2}]^-$ is the solvent anion. The cation effect is more subtle; when changing from $[\mathrm{C_4C_1Im}]^+$ to $[\mathrm{pyrH4}]^+$ the reaction becomes on average more favorable by about 28 kJ/mol and when changing from $[\mathrm{C_4C_1Im}]^+$ to $[\mathrm{N_{H122}}]^+$ by about 8 kJ/mol. Nevertheless, when changing the cation, the difference in the reaction energy is still greater than the deviation to the reference functional, i.e., above or within the RAD. We further see in Table 1 that different functionals perform differently for the reaction 2 (see RAD values). The consideration of the reaction only is of course a simplification because we did not treat transition states for which we expect larger differences to occur. However, we can observe a huge increase in computational time when hybrid functionals are being chosen. Without the ADMM approximation a factor of more than 40 has to be paid in computational costs. The comparison between revPBE and PBE0 (with ADMM) even yields a factor of 200 (5). When 100 ps with a time step of 0.5 fs is being targeted, 200000 steps need to be produced which shows again that a factor of 5 for each of these steps is difficult and a factor of 200 is unacceptable. Nevertheless, the use of a good electronic structure in such systems is important to obtain a proper description of these complicated systems. This simple consideration shows that the theoretical treatment of radicals in ionic liquids is far from being solved.

CONCLUSION

In this Perspective we discuss how theory can further approach complicated situations in ionic liquids (ILs). We showed at particular examples, namely reactions, chirality, and radicals in ILs, what progress was made and still has to be made in theoretical investigations to overcome the problems resulted from oversimplifications in models and methodologies. We chose these particular applications of IL research because they recently gained more importance, while exciting observations have also been made from purely academic research.

For reactions, one needs to consider that breaking and formation of bonds occur. This is solved by explicit *ab initio* molecular dynamics (AIMD) simulations, which treat the electronic structure on the fly. However, when applied to reactions, small system sizes and short simulation times become an obstacle to a realistic treatment. Solutions are given by simplified electronic structure methods, QM/MM as well as novel Monte Carlo techniques, or embedding methods that help to use more realistic time scales.

Chirality does not necessarily mean that reactions need to be considered, but again only a careful description of intermolecular forces allows the elucidation of the underlying intricate induction mechanisms. Identifying the chirality of the given molecule is often performed through spectroscopic methods, which provide a convenient connection between theory and experiments. To extract vibrational spectra from trajectories, time correlation function techniques are applied. To obtain satisfying spectra, the proper description of the intermolecular interactions and their influence on the bonding within the molecule is required, which again shows the advantages of describing the electronic structure explicitly. However, because of the immense computational demand of these calculations, it is necessary to implement new methodologies that allow for accurate results with faster calculations.

Our final example of radicals in ILs involves species with very complicated electronic structures. For such systems, only a handful of successful studies exists, in which force-field-based methods were employed. Furthermore, even in electronic structure calculations complications such as self-interaction error and time scale problems must be overcome. In some cases an elegant approach was applied, where a lower theoretical level was used to produce the trajectories, and the more accurate, higher level calculations were performed on top of the obtained structures. Alternatively, clusters of solute IL units can be treated by a high-level of quantum chemistry.

Thus, all the mentioned IL application examples have in common that the system size is large and complex, e.g., with many compounds, resulting in unknown and unexpected intermolecular interactions, while at the same time an explicit description of the electronic structure is in principle needed. For all of these advanced investigations that will dominate ionic liquid research in the next decades, theory will not be able to rely solely on standard force-field-based simulations. Again, many problems theoretical investigations will face in future will still be originated not only from system size or solvent effects but also in complex electronic structures. Polarizable force fields will often offer remedy, but they surely will not be sufficient in all cases.

AUTHOR INFORMATION

Corresponding Author

Barbara Kirchner − *Mulliken Center for Theoretical Chemistry, University of Bonn, D-53115 Bonn, Germany;* orcid.org/0000-0001-8843-7132; Email: kirchner@thch.uni-bonn.de

Authors

Jan Blasius − *Mulliken Center for Theoretical Chemistry, University of Bonn, D-53115 Bonn, Germany*

Vahideh Alizadeh − *Mulliken Center for Theoretical Chemistry, University of Bonn, D-53115 Bonn, Germany*

Andreas Gansäuer − *Kekulé-Institut für Organische Chemie und Biochemie, University of Bonn, D-53121 Bonn, Germany*

Oldamur Hollóczki – *Mulliken Center for Theoretical Chemistry, University of Bonn, D-53115 Bonn, Germany; Department of Physical Chemistry, Faculty of Science and Technology, University of Debrecen, H-4010 Debrecen, Hungary;* orcid.org/0000-0003-3105-7176

Complete contact information is available at: https://pubs.acs.org/10.1021/acs.jpcb.1c09092

Notes

The authors declare no competing financial interest.

Biographies

Barbara Kirchner holds a chair for theoretical chemistry at the Mulliken Center for Theoretical Chemistry in Bonn (Germany) where she is also currently head of the Department of Chemistry. Before that, she held the chair for Theoretical Chemistry at the University of Leipzig (Germany). She is a member of the transdisciplinary research areas "Building Blocks of Matter and Fundamental Interactions" and "Innovation and Technology for Sustainable Futures" at the University of Bonn. She is specialized in theoretical methods for liquids, for example ionic liquids and deep eutectic solvents. However, her research interests and impact reach far beyond the topic of ionic liquids; they cover a wide range of fields in theoretical, physical, (bio)organic, inorganic and sustainable chemistry, with a novel view on chemical problems. She investigates functional materials such as chemically active domains in liquids, bulk and interfacial liquid–liquid systems for extraction, and energy devices. Her research involves two larger software projects: Peacemaker and Travis. While the former program is gradually gaining more and more attention for predicting physical and chemical properties of liquids based on high level quantum chemical calculations, the latter allows a systematic characterization of molecular simulation trajectories and is used broadly in the international scientific community.

Jan Blasius is a Ph.D. student in the research group of Prof. Barbara Kirchner. He studied chemistry at the Rheinische Friedrich-Wilhelms-University of Bonn (Germany) and obtained his B.Sc. (2017) and M.Sc. degrees (2019) after work in the group of Barbara Kirchner. In his B.Sc. thesis he investigated a new theoretical approach for the prediction of mole fraction dependent acid dissociation. During his master studies he started to work in the field of molecular chirality and optical activity. In his M.Sc. thesis, he investigated and developed static and dynamic approaches for the calculation of vibrational circular dichroism spectra in the liquid state. He continues this work in his Ph.D. project and uses the developed methods to investigate chiral phenomena (e.g., chirality transfer) in the condensed phase.

Vahideh Alizadeh is pursuing her Ph.D. under the supervision of Prof. Barbara Kirchner at the University of Bonn (Germany). Her research focuses on molecular-level studies of interactions and reactions in deep eutectic solvents and ionic liquids by applying multiresolution computational methods such as AIMD, classical MD, and quantum chemistry methods. She is also one of Travis software developers. In her M.Sc., she investigated the electronic structure of lanthanide complexes and noncovalent interactions in organic compounds under the supervision of Prof. Mehdi D. Esrafili in Iran.

Andreas Gansäuer obtained his Ph.D. in the group of Prof. Reetz at the MPI für Kohlenforschung (Germany). After a postdoctoral position in the group of Prof. Trost at Stanford University (US), he completed his habilitation with Prof. Brückner. Since 2000 he is Professor of Organic Chemistry at the University of Bonn (Germany). His research interests include radical chemistry and catalysis. Both fields are ideally suited for mechanistic investigations in cooperation with theoretical and physical chemistry. These studies have led to the design of a number of novel catalytic radical reactions.

Oldamur Hollóczki received his Ph.D. in chemistry at the Budapest University of Technology and Economics (Hungary) in 2011. In 2012 he received the prestigious Alexander von Humboldt Fellowship, which allowed him to join the research group of Prof. Barbara Kirchner in Leipzig and later Bonn in Germany. From 2015 on, he was a leader of a junior research group at the University of Bonn (Germany), where he did his habilitation in 2021. Since 2021, he has a permanent position at the University of Debrecen (Hungary), where he is currently working on research in various fields, including organocatalysis, nanoplastics, and sustainable chemistry through quantum chemical calculations and classical and *ab initio* molecular dynamics simulations.

■ ACKNOWLEDGMENTS

The authors thank the DFG under the grant project number 406232243 for financial support and the University of Bonn for granting access to the Bonna cluster and the TRA matter for financial support. The authors also thank all the excellent researchers working on ionic liquids, especially those that did not enter this Perspective but nevertheless do not fail to impress us.

■ REFERENCES

(1) Pálvölgyi, Á. M.; Bitai, J.; Zeindlhofer, V.; Schröder, C.; Bica, K. Ion-Tagged Chiral Ligands for Asymmetric Transfer Hydrogenations in Aqueous Medium. *ACS Sustainable Chem. Eng.* **2019**, *7*, 3414−3423.

(2) Sang, S.; Unruh, T.; Demeshko, S.; Domenianni, L. I.; van Leest, N. P.; Marquetand, P.; Schneck, F.; Würtele, C.; de Zwart, F. J.; de Bruin, B.; et al. Photo-Initiated Cobalt-Catalyzed Radical Olefin Hydrogenation. *Chem.—Eur. J.* **2021**, *27*, 16978−16989.

(3) Hilche, T.; Reinsberg, P. H.; Klare, S.; Liedtke, T.; Schäfer, L.; Gansäuer, A. Design Platform for Sustainable Catalysis with Radicals: Electrochemical Activation of Cp2TiCl2 for Catalysis Unveiled. *Chem.—Eur. J.* **2021**, *27*, 4903−4912.

(4) Capdevila-Cortada, M.; Łodziana, Z.; López, N. Performance of DFT+U Approaches in the Study of Catalytic Materials. *ACS Catal.* **2016**, *6*, 8370−8379.

(5) Flieger, J.; Flieger, M. Ionic liquids toxicity—benefits and threats. *Int. J. Mol. Sci.* **2020**, *21*, 6267.

(6) Cho, C.-W.; Pham, T. P. T.; Zhao, Y.; Stolte, S.; Yun, Y.-S. Review of the toxic effects of ionic liquids. *Sci. Total Environ.* **2021**, *786*, 147309.

(7) Marion, S.; Vučemilović-Alagić, N.; Špadina, M.; Radenović, A.; Smith, A.-S. From Water Solutions to Ionic Liquids with Solid State Nanopores as a Perspective to Study Transport and Translocation Phenomena. *Small* **2021**, *17*, 2100777.

(8) Alizadeh, V.; Malberg, F.; Pádua, A. A. H.; Kirchner, B. Are there magic compositions in deep eutectic solvents? effects of composition and water content in choline chloride/ethylene glycol from ab initio molecular dynamics. *J. Phys. Chem. B* **2020**, *124*, 7433−7443.

(9) Doherty, B.; Zhong, X.; Acevedo, O. Virtual site OPLS force field for imidazolium-based ionic liquids. *J. Phys. Chem. B* **2018**, *122*, 2962−2974.

(10) Doherty, B.; Acevedo, O. OPLS force field for choline chloride-based deep eutectic solvents. *J. Phys. Chem. B* **2018**, *122*, 9982−9993.

(11) Zhong, X.; Velez, C.; Acevedo, O. Partial Charges Optimized by Genetic Algorithms for Deep Eutectic Solvent Simulations. *J. Chem. Theory Comput.* **2021**, *17*, 3078−3087.

(12) Neumann, J.; Golub, B.; Odebrecht, L.-M.; Ludwig, R.; Paschek, D. Revisiting imidazolium based ionic liquids: Effect of the conformation bias of the [NTf2] anion studied by molecular dynamics simulations. *J. Chem. Phys.* **2018**, *148*, 193828.

(13) Brehm, M.; Pulst, M.; Kressler, J.; Sebastiani, D. Triazolium-based ionic liquids: A novel class of cellulose solvents. *J. Phys. Chem. B* **2019**, *123*, 3994−4003.

(14) Gehrke, S.; Kirchner, B. Robustness of the hydrogen bond and ion pair dynamics in ionic liquids to different parameters from the reactive flux method. *J. Chem. Eng. Data* **2020**, *65*, 1146−1158.

(15) Alizadeh, V.; Geller, D.; Malberg, F.; Sánchez, P. B.; Padua, A.; Kirchner, B. Strong Microheterogeneity in Novel Deep Eutectic Solvents. *ChemPhysChem* **2019**, *20*, 1786−1792.

(16) Chaumont, A.; Engler, E.; Schurhammer, R. Is Charge Scaling Really Mandatory when Developing Fixed-Charge Atomistic Force Fields for Deep Eutectic Solvents? *J. Phys. Chem. B* **2020**, *124*, 7239−7250.

(17) Lewis, N. H. C.; Zhang, Y.; Dereka, B.; Carino, E. V.; Maginn, E. J.; Tokmakoff, A. Signatures of ion pairing and aggregation in the vibrational spectroscopy of super-concentrated aqueous lithium bistriflimide solutions. *J. Phys. Chem. C* **2020**, *124*, 3470−3481.

(18) Alizadeh, V.; Kirchner, B. Molecular level insight into the solvation of cellulose in deep eutectic solvents. *J. Chem. Phys.* **2021**, *155*, 084501.

(19) Gehrke, S.; Ray, P.; Stettner, T.; Balducci, A.; Kirchner, B. Water in Protic Ionic Liquid Electrolytes: From solvent separated ion pairs to water clusters. *ChemSusChem* **2021**, *14*, 3315−3324.

(20) Alfurayj, I.; Fraenza, C. C.; Zhang, Y.; Pandian, R.; Spittle, S.; Hansen, B.; Dean, W.; Gurkan, B.; Savinell, R.; Greenbaum, S.; et al. Solvation Dynamics of Wet Ethaline: Water is the Magic Component. *J. Phys. Chem. B* **2021**, *125*, 8888−8901.

(21) Zhang, Y.; Lewis, N. H. C.; Mars, J.; Wan, G.; Weadock, N. J.; Takacs, C. J.; Lukatskaya, M. R.; Steinrück, H.-G.; Toney, M. F.; Tokmakoff, A.; et al. Water-in-Salt LiTFSI Aqueous Electrolytes. 1. Liquid Structure from Combined Molecular Dynamics Simulation and Experimental Studies. *J. Phys. Chem. B* **2021**, *125*, 4501−4513.

(22) Livraghi, M.; Höllring, K.; Wick, C. R.; Smith, D. M.; Smith, A.-S. An Exact Algorithm to Detect the Percolation Transition in Molecular Dynamics Simulations of Cross-Linking Polymer Networks. *J. Chem. Theory Comput.* **2021**, *17*, 6449−6457.

(23) Schade, R.; Kenter, T.; Elgabarty, H.; Lass, M.; Schütt, O.; Lazzaro, A.; Pabst, H.; Mohr, S.; Hutter, J.; Kühne, T. D.; et al. Enabling Electronic Structure-Based Ab-Initio Molecular Dynamics Simulations with Hundreds of Millions of Atoms. arXiv preprint 16.04.2021, arXiv:2104.08245.

(24) Blasius, J.; Zaby, P.; Hollóczki, O.; Kirchner, B. Recognition in Chiral Ionic Liquids: The Achiral Cation Makes the Difference. *J. Org. Chem.* **2021**, DOI: 10.1021/acs.joc.1c00939.

(25) Esser, L.; Macchieraldo, R.; Elfgen, R.; Sieland, M.; Smarsly, B. M.; Kirchner, B. $TiCl_4$ Dissolved in Ionic Liquid Mixtures from Ab Initio Molecular Dynamics Simulations. *Molecules* **2021**, *26*, 79.

(26) Alizadeh, V.; Esser, L.; Kirchner, B. How is CO_2 absorbed into a deep eutectic solvent? *J. Chem. Phys.* **2021**, *154*, 094503.

(27) Fetisov, E. O.; Harwood, D. B.; Kuo, I.-F. W.; Warrag, S. E.; Kroon, M. C.; Peters, C. J.; Siepmann, J. I. First-principles molecular dynamics study of a deep eutectic solvent: Choline chloride/urea and its mixture with water. *J. Phys. Chem. B* **2018**, *122*, 1245−1254.

(28) Contreras, R.; Lodeiro, L.; Rozas-Castro, N.; Ormazábal-Toledo, R. On the role of water in the hydrogen bond network in DESs: an ab initio molecular dynamics and quantum mechanical study on the urea-betaine system. *Phys. Chem. Chem. Phys.* **2021**, *23*, 1994−2004.

(29) Zhang, Y.; Poe, D.; Heroux, L.; Squire, H.; Doherty, B. W.; Long, Z.; Dadmun, M.; Gurkan, B.; Tuckerman, M. E.; Maginn, E. J. Liquid structure and transport properties of the deep eutectic solvent ethaline. *J. Phys. Chem. B* **2020**, *124*, 5251−5264.

(30) Malik, A.; Dhattarwal, H. S.; Kashyap, H. K. Distinct Solvation Structures of CO_2 and SO2 in Reline and Ethaline Deep Eutectic Solvents Revealed by AIMD Simulations. *J. Phys. Chem. B* **2021**, *125*, 1852−1860.

(31) Wylie, L.; Seeger, Z. L.; Hancock, A. N.; Izgorodina, E. I. Increased stability of nitroxide radicals in ionic liquids: more than a viscosity effect. *Phys. Chem. Chem. Phys.* **2019**, *21*, 2882−2888.

(32) Wylie, L.; Oyaizu, K.; Karton, A.; Yoshizawa-Fujita, M.; Izgorodina, E. I. Toward improved performance of all-organic nitroxide radical batteries with ionic liquids: a theoretical perspective. *ACS Sustainable Chem. Eng.* **2019**, *7*, 5367−5375.

(33) Heid, E.; Hunt, P. A.; Schröder, C. Evaluating excited state atomic polarizabilities of chromophores. *Phys. Chem. Chem. Phys.* **2018**, *20*, 8554−8563.

(34) Seeger, Z. L.; Izgorodina, E. I. A Systematic Study of DFT Performance for Geometry Optimizations of Ionic Liquid Clusters. *J. Chem. Theory Comput.* **2020**, *16*, 6735−6753.

(35) Philippi, F.; Rauber, D.; Kuttich, B.; Kraus, T.; Kay, C. W. M.; Hempelmann, R.; Hunt, P. A.; Welton, T. Ether functionalisation, ion conformation and the optimization of macroscopic properties in ionic liquids. *Phys. Chem. Chem. Phys.* **2020**, *22*, 23038−23056.

(36) Philippi, F.; Pugh, D.; Rauber, D.; Welton, T.; Hunt, P. A. Conformational design concepts for anions in ionic liquids. *Chem. Sci.* **2020**, *11*, 6405−6422.

(37) Rowe, R.; Lovelock, K. R. J.; Hunt, P. A. Bi (III) halometallate ionic liquids: Interactions and speciation. *J. Chem. Phys.* **2021**, *155*, 014501.

(38) Perlt, E.; Ray, P.; Hansen, A.; Malberg, F.; Grimme, S.; Kirchner, B. Finding the best density functional approximation to describe interaction energies and structures of ionic liquids in molecular dynamics studies. *J. Chem. Phys.* **2018**, *148*, 193835.

(39) Rodríguez-Fernández, C. D.; Lago, E. L.; Schröder, C.; Varela, L. M. Non-additive electronic polarizabilities of ionic liquids: Charge delocalization effects. *J. Mol. Liq.* **2022**, *346*, 117099.

(40) Heid, E.; Fleck, M.; Chatterjee, P.; Schröder, C.; MacKerell, A. D., Jr. Toward prediction of electrostatic parameters for force fields that explicitly treat electronic polarization. *J. Chem. Theory Comput.* **2019**, *15*, 2460−2469.

(41) Low, K.; Tan, S. Y. S.; Izgorodina, E. I. An ab initio study of the structure and energetics of hydrogen bonding in ionic liquids. *Front. Chem.* **2019**, *7*, 208.

(42) Bodo, E.; Bonomo, M.; Mariani, A. Assessing the Structure of Protic Ionic Liquids Based on Triethylammonium and Organic Acid Anions. *J. Phys. Chem. B* **2021**, *125*, 2781−2792.

(43) Goloviznina, K.; Gong, Z.; Pádua, A. A. H. The CL &Pol polarizable force field for the simulation of ionic liquids and eutectic solvents. *Wiley Interdiscip. Rev. Comput. Mol. Sci.* **2021**, e1572.

(44) Goloviznina, K.; Canongia Lopes, J. N.; Costa Gomes, M.; Pádua, A. A. H. Transferable, Polarizable Force Field for Ionic Liquids. *J. Chem. Theory Comput.* **2019**, *15*, 5858−5871.

(45) Xu, L.; Izgorodina, E. I.; Coote, M. L. Ordered solvents and ionic liquids can be harnessed for electrostatic catalysis. *J. Am. Chem. Soc.* **2020**, *142*, 12826−12833.

(46) de Oliveira Cavalcante, A.; Chelli, R. Polarizability relaxation in water/ethanol mixtures. *J. Mol. Liq.* **2021**, *332*, 115839.

(47) Szabadi, A.; Elfgen, R.; Macchieraldo, R.; Kearns, F. L.; Woodcock, H. L.; Kirchner, B.; Schröder, C. Comparison between ab initio and polarizable molecular dynamics simulations of 1-butyl-3-methylimidazolium tetrafluoroborate and chloride in water. *J. Mol. Liq.* **2021**, *337*, 116521.

(48) Sharma, S.; Ivanov, A. S.; Margulis, C. J. A Brief Guide to the Structure of High-Temperature Molten Salts and Key Aspects Making Them Different from Their Low-Temperature Relatives, the Ionic Liquids. *J. Phys. Chem. B* **2021**, *125*, 6359−6372.

(49) Miao, L.; Song, Z.; Zhu, D.; Li, L.; Gan, L.; Liu, M. Ionic Liquids for Supercapacitive Energy Storage: A Mini-Review. *Energy Fuels* **2021**, *35*, 8443−8455.

(50) Stettner, T.; Balducci, A. Protic ionic liquids in energy storage devices: Past, present and future perspective. *Energy Storage Mater.* **2021**, *40*, 402−414.

(51) Liu, F.; Yu, J.; Qazi, A. B.; Zhang, L.; Liu, X. Metal-Based Ionic Liquids in Oxidative Desulfurization: A Critical Review. *Environ. Sci. Technol.* **2021**, *55*, 1419−1435.

(52) Scalfi, L.; Salanne, M.; Rotenberg, B. Molecular simulation of electrode-solution interfaces. *Annu. Rev. Phys. Chem.* **2021**, *72*, 189−212.

(53) Salanne, M. Ionic liquids for supercapacitor applications. *Top. Curr. Chem.* **2017**, *375*, 63.

(54) Dufils, T.; Jeanmairet, G.; Rotenberg, B.; Sprik, M.; Salanne, M. Simulating Electrochemical Systems by Combining the Finite Field Method with a Constant Potential Electrode. *Phys. Rev. Lett.* **2019**, *123*, 195501.

(55) Jonsson, E. Ionic liquids as electrolytes for energy storage applications-A modelling perspective. *Energy Storage Mater.* **2020**, *25*, 827−835.

(56) Groves, T. S.; Perez-Martinez, C. S.; Lhermerout, R.; Perkin, S. Surface Forces and Structure in a Water-in-Salt Electrolyte. *J. Phys. Chem. Lett.* **2021**, *12*, 1702−1707.

(57) Harper, J. B.; Kirchner, B.; Pavez, P.; Welton, T. Non-traditional solvent effects in organic reactions. *Phys. Chem. Chem. Phys.* **2021**, *23*, 26028−26029.

(58) Brzeczek-Szafran, A.; Wiecławik, J.; Barteczko, N.; Szelwicka, A.; Byrne, E.; Kolanowska, A.; Kwaśny, M. S.; Chrobok, A. Protic ionic liquids from di-or triamines: even cheaper Brønsted acidic catalysts. *Green Chem.* **2021**, *23*, 4421−4429.

(59) Hallett, J. P.; Welton, T. Room-Temperature Ionic Liquids: Solvents for Synthesis and Catalysis. 2. *Chem. Rev.* **2011**, *111*, 3508−3576.

(60) Tanner, E. E. L.; Hawker, R. R.; Yau, H. M.; Croft, A. K.; Harper, J. B. Probing the importance of ionic liquid structure: A general ionic liquid effect on an SN Ar process. *Org. Biomol. Chem.* **2013**, *11*, 7516−7521.

(61) Harper, J.; Kobrak, M. Understanding organic processes in ionic liquids: Achievements so far and challenges remaining. *Mini Rev. Org. Chem.* **2006**, *3*, 253−269.

(62) Harper, J. B.; Lynden-Bell, R. Macroscopic and microscopic properties of solutions of aromatic compounds in an ionic liquid. *Mol. Phys.* **2004**, *102*, 85−94.

(63) Yau, H. M.; Keaveney, S. T.; Butler, B. J.; Tanner, E. E.; Guerry, M. S.; George, S. R. D.; Dunn, M. H.; Croft, A. K.; Harper, J. B. Towards solvent-controlled reactivity in ionic liquids. *Pure Appl. Chem.* **2013**, *85*, 1979−1990.

(64) D'Anna, F.; Frenna, V.; Noto, R.; Pace, V.; Spinelli, D. Study of aromatic nucleophilic substitution with amines on nitrothiophenes in room-temperature ionic liquids: Are the different effects on the behavior of para-like and ortho-like isomers on going from conventional solvents to room-temperature ionic liquids related to solvation effects? *J. Org. Chem.* **2006**, *71*, 5144−5150.

(65) Marullo, S.; D'Anna, F.; Rizzo, C.; Billeci, F. Ionic liquids:"normal" solvents or nanostructured fluids? *Org. Biomol. Chem.* **2021**, *19*, 2076−2095.

(66) Chiappe, C.; Pieraccini, D. Ionic liquids: solvent properties and organic reactivity. *J. Phys. Org. Chem.* **2005**, *18*, 275−297.

(67) Wasserscheid, P.; Bösmann, A.; Bolm, C. Synthesis and properties of ionic liquids derived from the 'chiral pool'. *Chem. Commun.* **2002**, 200−201.

(68) Schulz, P. S.; Müller, N.; Bösmann, A.; Wasserscheid, P. Effective chirality transfer in ionic liquids through ion-pairing effects. *Angew. Chem., Int. Ed.* **2007**, *46*, 1293−1295.

(69) Bösmann, A.; Schulz, P. S.; Wasserscheid, P. Enhancing task specific ionic liquids' thermal stability by structural modification. *Monatsh. Chem.* **2007**, *138*, 1159−1161.

(70) Ding, J.; Armstrong, D. W. Chiral ionic liquids: synthesis and applications. *Chirality* **2005**, *17*, 281−292.

(71) Bica, K.; Gaertner, P. Applications of chiral ionic liquids. *Eur. J. Org. Chem.* **2008**, *2008*, 3235−3250.

(72) Ohno, H.; Fukumoto, K. Amino acid ionic liquids. *Acc. Chem. Res.* **2007**, *40*, 1122−1129.

(73) Strehmel, V. Radicals in ionic liquids. *ChemPhysChem* **2012**, *13*, 1649−1663.

(74) Wishart, J. F. *Ionic Liquids: Current State and Future Directions*; ACS: 2017; pp 251−272.

(75) Hayes, R.; Warr, G. G.; Atkin, R. Structure and Nanostructure in Ionic Liquids. *Chem. Rev.* **2015**, *115*, 6357−6426.

(76) Elfgen, R.; Holloczki, O.; Kirchner, B. A molecular level understanding of template effects in ionic liquids. *Acc. Chem. Res.* **2017**, *50*, 2949−2957.

(77) Allen, C.; Ghebreab, R.; Doherty, B.; Li, B.; Acevedo, O. Examining ionic liquid effects on mononuclear rearrangement of heterocycles using QM/MM simulations. *J. Phys. Chem. B* **2016**, *120*, 10786−10796.

(78) Velez, C.; Doherty, B.; Acevedo, O. Accurate Diels-Alder energies and Endo selectivity in ionic liquids using the OPLS-VSIL force field. *Int. J. Mol. Sci.* **2020**, *21*, 1190.

(79) Freire, M. G.; Neves, C. M. S. S.; Marrucho, I. M.; Coutinho, J. A. P.; Fernandes, A. M. Hydrolysis of Tetrafluoroborate and Hexafluorophosphate Counter Ions in Imidazolium-Based Ionic Liquids. *J. Phys. Chem. A* **2010**, *114*, 3744−3749.

(80) Firaha, D. S.; Kirchner, B. Tuning the carbon dioxide absorption in amino acid ionic liquids. *ChemSusChem* **2016**, *9*, 1591−1599.

(81) Bhargava, B.; Balasubramanian, S. Insights into the structure and dynamics of a room-temperature ionic liquid: ab initio molecular dynamics simulation studies of 1-n-butyl-3-methylimidazolium hexafluorophosphate ([bmim][PF6]) and the [bmim][PF6]- CO_2 mixture. *J. Phys. Chem. B* **2007**, *111*, 4477−4487.

(82) Goel, H.; Windom, Z. W.; Jackson, A. A.; Rai, N. Performance of density functionals for modeling vapor liquid equilibria of CO_2 and SO_2. *J. Comput. Chem.* **2018**, *39*, 397−406.

(83) Kirchner, B.; Seitsonen, A. P. Ionic Liquids from Car-Parrinello Simulations. 2. Structural Diffusion Leading to Large Anions in Chloraluminate Ionic Liquids. *Inorg. Chem.* **2007**, *46*, 2751−2754.

(84) Ballone, P.; Cortes-Huerto, R. Ab initio simulations of thermal decomposition and of electron transfer reactions in room temperature ionic liquids. *Faraday Discuss.* **2012**, *154*, 373−389.

(85) Firaha, D. S.; Hollóczki, O.; Kirchner, B. Computer-aided design of ionic liquids as CO_2 absorbents. *Angew. Chem., Int. Ed.* **2015**, *54*, 7805−7809.

(86) Firaha, D. S.; Hollóczki, O.; Kirchner, B. Computer-gestütztes Design ionischer Flüssigkeiten zur CO_2-Absorption. *Angew. Chem.* **2015**, *127*, 7916−7920.

(87) Firaha, D. S.; Kirchner, B. CO_2 absorption in the protic ionic liquid ethylammonium nitrate. *J. Chem. Eng. Data* **2014**, *59*, 3098−3104.

(88) Holloczki, O.; Firaha, D. S.; Friedrich, J.; Brehm, M.; Cybik, R.; Wild, M.; Stark, A.; Kirchner, B. Carbene formation in ionic liquids: spontaneous, induced, or prohibited? *J. Phys. Chem. B* **2013**, *117*, 5898−5907.

(89) Yamada, H. Comparison of solvation effects on CO_2 capture with aqueous amine solutions and amine-functionalized ionic liquids. *J. Phys. Chem. B* **2016**, *120*, 10563−10568.

(90) Luo, X. Y.; Lv, X. Y.; Shi, G. L.; Meng, Q.; Li, H. R.; Wang, C. M. Designing amino-based ionic liquids for improved carbon capture: One amine binds two CO_2. *AIChE J.* **2019**, *65*, 230−238.

(91) Shaikh, A. R.; Ashraf, M.; AlMayef, T.; Chawla, M.; Poater, A.; Cavallo, L. Amino acid ionic liquids as potential candidates for CO_2 capture: combined density functional theory and molecular dynamics simulations. *Chem. Phys. Lett.* **2020**, *745*, 137239.

(92) Ingenmey, J.; Gehrke, S.; Kirchner, B. How to harvest Grotthuss diffusion in protic ionic liquid electrolyte systems. *ChemSusChem* **2018**, *11*, 1900−1910.

(93) Le Donne, A.; Adenusi, H.; Porcelli, F.; Bodo, E. Structural features of cholinium based protic ionic liquids through molecular dynamics. *J. Phys. Chem. B* **2019**, *123*, 5568−5576.

(94) Hollóczki, O.; Wolff, A.; Pallmann, J.; Whiteside, R. E.; Hartley, J.; Grasser, M. A.; Nockemann, P.; Brunner, E.; Doert, T.; Ruck, M. Spontaneous Substitutions at Phosphorus Trihalides in Imidazolium Halide Ionic Liquids: Grotthuss Diffusion of Anions. *Chem.—Eur. J.* **2018**, *24*, 16323−16331.

(95) Hollóczki, O. Toward Anionic Structural Diffusion and Highly Conducting Ionic Liquid Electrolytes. *ACS Sustain. Chem. Eng.* **2019**, *7*, 2626−2633.

(96) Dreßler, C.; Kabbe, G.; Brehm, M.; Sebastiani, D. Exploring non-equilibrium molecular dynamics of mobile protons in the solid acid CsH2PO4 at the micrometer and microsecond scale. *J. Chem. Phys.* **2020**, *152*, 164110.

(97) Dreßler, C.; Kabbe, G.; Brehm, M.; Sebastiani, D. Dynamical matrix propagator scheme for large-scale proton dynamics simulations. *J. Chem. Phys.* **2020**, *152*, 114114.

(98) Urbach, C.; Jansen, K.; Shindler, A.; Wenger, U. HMC algorithm with multiple time scale integration and mass preconditioning. *Comput. Phys. Commun.* **2006**, *174*, 87−98.

(99) Bannwarth, C.; Caldeweyher, E.; Ehlert, S.; Hansen, A.; Pracht, P.; Seibert, J.; Spicher, S.; Grimme, S. Extended tight-binding quantum chemistry methods. *Wiley Interdiscip. Rev. Comput. Mol. Sci.* **2021**, *11*, e1493.

(100) Perlt, E.; Ray, P.; Hansen, A.; Malberg, F.; Grimme, S.; Kirchner, B. Finding the best density functional approximation to describe interaction energies and structures of ionic liquids in molecular dynamics studies. *J. Chem. Phys.* **2018**, *148*, 193835.

(101) Zentel, T.; Overbeck, V.; Michalik, D.; Kühn, O.; Ludwig, R. Hydrogen bonding in protic ionic liquids: structural correlations, vibrational spectroscopy, and rotational dynamics of liquid ethylammonium nitrate. *J. Phys. B: At. Mol. Opt. Phys.* **2018**, *51*, 034002.

(102) Karu, K.; Elhi, F.; Põhako-Esko, K.; Ivaništšev, V. Predicting Melting Points of Biofriendly Choline-Based Ionic Liquids with Molecular Dynamics. *Appl. Sci.* **2019**, *9*, 5367.

(103) Mosquera, M. A.; Jones, L. O.; Ratner, M. A.; Schatz, G. C. Quantum embedding for material chemistry based on domain separation and open subsystems. *Int. J. Quantum Chem.* **2020**, *120*, e26184.

(104) Oulevey, P.; Luber, S.; Varnholt, B.; Bürgi, T. Symmetry breaking in chiral ionic liquids evidenced by vibrational optical activity. *Angew. Chem., Int. Ed.* **2016**, *55*, 11787−11790.

(105) Oulevey, P.; Luber, S.; Varnholt, B.; Bürgi, T. Symmetriebruch in chiralen ionischen Flüssigkeiten: Nachweis durch vibratorisch-optische Aktivität. *Angew. Chem.* **2016**, *128*, 11962−11966.

(106) Ghidinelli, S.; Abbate, S.; Mazzeo, G.; Boiadjiev, S. E.; Lightner, D. A.; Longhi, G. Biliverdin chiral derivatives as chiroptical switches for pH and metal cation sensing. *Phys. Chem. Chem. Phys.* **2021**, *23*, 20138−20151.

(107) Koenis, M. A.; Nicu, V. P.; Visscher, L.; Kuehn, C.; Bremer, M.; Krier, M.; Untenecker, H.; Zhumaev, U.; Küstner, B.; Buma, W. J. Vibrational circular dichroism studies of exceptionally strong chirality inducers in liquid crystals. *Phys. Chem. Chem. Phys.* **2021**, *23*, 10021−10028.

(108) Weirich, L.; Merten, C. Induced VCD and conformational chirality in host-guest complexes of a chiral ammonium salt with crown ethers. *Phys. Chem. Chem. Phys.* **2021**, *23*, 18300−18307.

(109) Blasius, J.; Kirchner, B. Cluster-Weighting in Bulk Phase Vibrational Circular Dichroism. *J. Phys. Chem. B* **2020**, *124*, 7272−7283.

(110) Jähnigen, S.; Scherrer, A.; Vuilleumier, R.; Sebastiani, D. Chiral crystal packing induces enhancement of vibrational circular dichroism. *Angew. Chem., Int. Ed.* **2018**, *57*, 13344−13348.

(111) Jähnigen, S.; Scherrer, A.; Vuilleumier, R.; Sebastiani, D. VCD-Verstärkung durch chirale Packungseffekte in molekularen Kristallen. *Angew. Chem.* **2018**, *130*, 13528−13532.

(112) Le Barbu-Debus, K.; Bowles, J.; Jähnigen, S.; Clavaguéra, C.; Calvo, F.; Vuilleumier, R.; Zehnacker, A. Assessing cluster models of

solvation for the description of vibrational circular dichroism spectra: synergy between static and dynamic approaches. *Phys. Chem. Chem. Phys.* **2020**, *22*, 26047−26068.

(113) Kirchner, B.; Blasius, J.; Esser, L.; Reckien, W. Predicting Vibrational Spectroscopy for Flexible Molecules and Molecules with Non-Idle Environments. *Adv. Theory Simul.* **2021**, *4*, 2000223.

(114) Abbate, S.; Longhi, G.; Kwon, K.; Moscowitz, A. The use of cross-correlation functions in the analysis of circular dichroism spectra. *J. Chem. Phys.* **1998**, *108*, 50−62.

(115) Thomas, M.; Brehm, M.; Kirchner, B. Voronoi dipole moments for the simulation of bulk phase vibrational spectra. *Phys. Chem. Chem. Phys.* **2015**, *17*, 3207−3213.

(116) Thomas, M.; Kirchner, B. Classical magnetic dipole moments for the simulation of vibrational circular dichroism by ab initio molecular dynamics. *J. Phys. Chem. Lett.* **2016**, *7*, 509−513.

(117) Blasius, J.; Elfgen, R.; Hollóczki, O.; Kirchner, B. Glucose in dry and moist ionic liquid: vibrational circular dichroism, IR, and possible mechanisms. *Phys. Chem. Chem. Phys.* **2020**, *22*, 10726−10737.

(118) von Domaros, M.; Perlt, E.; Ingenmey, J.; Marchelli, G.; Kirchner, B. Peacemaker 2: Making clusters talk about binary mixtures and neat liquids. *SoftwareX* **2018**, *7*, 356−359.

(119) Koner, D.; Salehi, S. M.; Mondal, P.; Meuwly, M. Non-conventional force fields for applications in spectroscopy and chemical reaction dynamics. *J. Chem. Phys.* **2020**, *153*, 010901.

(120) André, F.; Hapiot, P.; Lagrost, C. Dimerization of ion radicals in ionic liquids. An example of favourable "Coulombic" solvation. *Phys. Chem. Chem. Phys.* **2010**, *12*, 7506−7512.

(121) Wylie, L.; Blesch, T.; Freeman, R.; Hatakeyama-Sato, K.; Oyaizu, K.; Yoshizawa-Fujita, M.; Izgorodina, E. I. Reversible Reduction of the TEMPO Radical: One Step Closer to an All-Organic Redox Flow Battery. *Chem. Eng.* **2020**, *8*, 17988−17996.

(122) Wylie, L.; Hakatayama-Sato, K.; Go, C.; Oyaizu, K.; Izgorodina, E. I. Electrochemical characterization and thermodynamic analysis of TEMPO derivatives in ionic liquids. *Phys. Chem. Chem. Phys.* **2021**, *23*, 10205−10217.

(123) Tan, S.; Barrera Acevedo, S.; Izgorodina, E. I. Generalized spin-ratio scaled MP2 method for accurate prediction of intermolecular interactions for neutral and ionic species. *J. Chem. Phys.* **2017**, *146*, 064108.

(124) Knudtzon, M. N.; Blank, D. A. Photodetachment and Electron Dynamics in 1-Butyl-1-methyl-pyrrolidinium Dicyanamide. *J. Phys. Chem. B* **2020**, *124*, 9144−9153.

(125) Leier, J.; Michenfelder, N. C.; Unterreiner, A.-N. Understanding the Photoexcitation of Room Temperature Ionic Liquids. *ChemistryOpen* **2021**, *10*, 72−82.

(126) Wang, Z.; Zhang, L.; Cukier, R. I.; Bu, Y. States and migration of an excess electron in a pyridinium-based, room-temperature ionic liquid: an ab initio molecular dynamics simulation exploration. *Phys. Chem. Chem. Phys.* **2010**, *12*, 1854−1861.

(127) Becke, A. D. Density-functional exchange-energy approximation with correct asymptotic behavior. *Phys. Rev. A* **1988**, *38*, 3098.

(128) Lee, C.; Yang, W.; Parr, R. G. Development of the Colle-Salvetti correlation-energy formula into a functional of the electron density. *Phys. Rev. B* **1988**, *37*, 785.

(129) Perdew, J. P.; Burke, K.; Ernzerhof, M. Generalized gradient approximation made simple. *Phys. Rev. Lett.* **1997**, *77*, 3865.

(130) Margulis, C. J.; Annapureddy, H. V. R.; De Biase, P. M.; Coker, D.; Kohanoff, J.; Del Pópolo, M. G. Dry excess electrons in room-temperature ionic liquids. *J. Am. Chem. Soc.* **2011**, *133*, 20186−20193.

(131) Roy, S.; Liu, Y.; Topsakal, M.; Dias, E.; Gakhar, R.; Phillips, W. C.; Wishart, J. F.; Leshchev, D.; Halstenberg, P.; Dai, S.; et al. A Holistic Approach for Elucidating Local Structure, Dynamics, and Speciation in Molten Salts with High Structural Disorder. *J. Am. Chem. Soc.* **2021**, *143*, 15298−15308.

(132) Gill, S. K.; Huang, J.; Mausz, J.; Gakhar, R.; Roy, S.; Vila, F.; Topsakal, M.; Phillips, W. C.; Layne, B.; Mahurin, S.; et al. Connections between the speciation and solubility of Ni (II) and Co (II) in molten ZnCl2. *J. Phys. Chem. B* **2020**, *124*, 1253−1258.

(133) Reeves, K. G.; Serva, A.; Jeanmairet, G.; Salanne, M. A first-principles investigation of the structural and electrochemical properties of biredox ionic species in acetonitrile. *Phys. Chem. Chem. Phys.* **2020**, *22*, 10561−10568.

(134) VandeVondele, J.; Hutter, J. Gaussian basis sets for accurate calculations on molecular systems in gas and condensed phases. *J. Chem. Phys.* **2007**, *127*, 114105.

(135) d'Avezac, M.; Calandra, M.; Mauri, F. Density functional theory description of hole-trapping in SiO_2: A self-interaction-corrected approach. *Phys. Rev. B* **2005**, *71*, 205210.

(136) Perdew, J. P.; Zunger, A. Self-interaction correction to density-functional approximations for many-electron systems. *Phys. Rev. B* **1981**, *23*, 5048.

(137) Berthin, R.; Serva, A.; Reeves, K. G.; Heid, E.; Schröder, C.; Salanne, M. Solvation of anthraquinone and TEMPO redox-active species in acetonitrile using a polarizable force field. *J. Chem. Phys.* **2021**, *155*, 074504.

(138) Gansäuer, A.; von Laufenberg, D.; Kube, C.; Dahmen, T.; Michelmann, A.; Behlendorf, M.; Sure, R.; Seddiqzai, M.; Grimme, S.; Sadasivam, D. V.; et al. Mechanistic study of the titanocene (III)-catalyzed radical arylation of epoxides. *Chem.−Eur. J.* **2015**, *21*, 280−289.

(139) Funk, P.; Richrath, R. B.; Bohle, F.; Grimme, S.; Gansäuer, A. Oxidation Under Reductive Conditions: From Benzylic Ethers to Acetals with Perfect Atom-Economy by Titanocene (III) Catalysis. *Angew. Chem., Int. Ed.* **2021**, *60*, 5482−5488.

(140) Weigend, F.; Ahlrichs, R. Balanced basis sets of split valence, triple zeta valence and quadruple zeta valence quality for H to Rn: Design and assessment of accuracy. *Phys. Chem. Chem. Phys.* **2005**, *7*, 3297−3305.

(141) Neese, F. The ORCA program system. *Wiley Interdiscip. Rev. Comput. Mol. Sci.* **2012**, *2*, 73−78.

(142) Hutter, J.; Iannuzzi, M.; Schiffmann, F.; VandeVondele, J. cp2k: atomistic simulations of condensed matter systems. *Wiley Interdiscip. Rev. Comput. Mol. Sci.* **2014**, *4*, 15−25.

(143) Perdew, J. P.; Ruzsinszky, A.; Csonka, G. I.; Vydrov, O. A.; Scuseria, G. E.; Constantin, L. A.; Zhou, X.; Burke, K. Restoring the density-gradient expansion for exchange in solids and surfaces. *Phys. Rev. Lett.* **2008**, *100*, 136406.

(144) Tao, J.; Perdew, J. P.; Staroverov, V. N.; Scuseria, G. E. Climbing the density functional ladder: Nonempirical meta-generalized gradient approximation designed for molecules and solids. *Phys. Rev. Lett.* **2003**, *91*, 146401.

(145) Ling, S.; Slater, B. Primary Basis Sets Optimised from Molecular Calculations. https://fossies.org/linux/cp2k/data/BASIS_MOLOPT_UCL (accessed: 2021-10-09).

(146) Guidon, M.; Hutter, J.; VandeVondele, J. Auxiliary density matrix methods for Hartree- Fock exchange calculations. *J. Chem. Theory Comput.* **2010**, *6*, 2348−2364.

(147) VandeVondele, J.; Krack, M.; Mohamed, F.; Parrinello, M.; Chassaing, T.; Hutter, J. Quickstep: Fast and accurate density functional calculations using a mixed Gaussian and plane waves approach. *Comput. Phys. Commun.* **2005**, *167*, 103−128.

F. A Hybrid Monte Carlo Study of Argon Solidification

Vahideh Alizadeh,* Marco Garofalo † Carsten Urbach,† Barbara Kirchner *

Received: 13 December 2023, accepted: 20 December 2023.

Reprinted in Appendix F (accepted manuscript) with permission‡ from

V. Alizadeh, M. Garofalo, C. Urbach, and B. Kirchner, *Z. Naturforsch.* **2024**, *79*, 283–291, *doi:10.1515/znb-2023-0107.*

For this article, Supporting Information is available free of charge at:
https://www.degruyter.com/document/doi/10.1515/znb-2023-0107/html.

Contributions to the manuscript

- Development of the concept
- Co-performing simulations
- Conducting the analysis, visualizations, and calculations
- Interpretation of the results
- Writing of the manuscript
- Co-implementing HMC code

---

[*] Mulliken Center for Theoretical Chemistry, Clausius Institute for Physical and Theoretical Chemistry, University of Bonn, Beringstr. 4–6, 53115 Bonn, Germany

[†] HISKP (Theory), Rheinische Friedrich-Wilhelms-Universität Bonn, Nussallee 14-16, 53115, Bonn, Germany

[‡] Permission requests to reuse material from this chapter should be directed to De Gruyter.

Vahideh Alizadeh, Marco Garofalo, Carsten Urbach, and Barbara Kirchner

A hybrid Monte Carlo study of argon solidification

https://doi.org/10.1515/znb-2023-0107

Received December 13, 2023; accepted December 20, 2023

Dedicted to Professor Thomas Bredow on the occasion of his 60th birthday

Corresponding author: Barbara Kirchner, Mulliken Center for Theoretical Chemistry, Clausius Institut für Physikalische und Theoretische Chemie, Universität Bonn, Beringstraße 4+6, D-53115 Bonn, Germany; E-mail: kirchner@thch.uni-bonn.de

Vahideh Alizadeh: Mulliken Center for Theoretical Chemistry, Clausius Institut für Physikalische und Theoretische Chemie, Universität Bonn, Beringstraße 4+6, D-53115 Bonn, Germany

Marco Garofalo, Carsten Urbach: Helmholtz-Institut für Strahlen- und Kernphysik (Theory), Bethe Center for Theoretical Physics, Universität Bonn, Nussallee 14-16, 53115, Bonn, Germany

Abstract

A GPU-based implementation of the Hybrid Monte Carlo (HMC) algorithm is presented to explore its utility in the chemistry of solidification at the example of liquid to solid argon. We validate our implementation by comparing structural characteristics of argon fluid-like phases from HMC and MD simulations. Examining solidification, both MD and HMC show similar trends. Despite observable differences, MD simulations and HMC agree within the errors during the phase transition. Introducing voids decreases the solidification temperature, aiding in the formation of a well-structured solids. Further, our findings highlight the importance of larger system sizes in simulating solidification processes. Simulations with a temperature dependent potential show ambiguous results for the solidification which may be attributed to the small system sizes. Future work aims to expand HMC capabilities for complex chemical phenomena in phase transitions.

Keywords: Hybrid Monte Carlo; Lennard-Jones potential; Argon solidification.

1 Introduction

In recent decades, computational methods have revolutionized the field of chemical and material simulations, enabling scientists and researchers to delve deeper into the fundamental properties and behaviors of molecules and materials. The field of computational chemistry and material science has rapidly evolved over the years, driven by advancements in computer hardware, software, and theoretical approaches. [1–3]

Although traditional molecular simulation techniques are highly proficient in probing the dynamics over short time scales through molecular dynamics and exploring regions in configuration space with higher probabilities using Monte Carlo simulations, they encounter inefficiencies when dealing with rare events (transition from one region of phase space to another) such as the folding of a protein, reactions in solvents or a phase transition where longer time scales of simulations and efficient sampling of the phase space are needed.[4–9] Consequently, there grew a need for innovative algorithms and theoretical approaches to overcome this limitation such as local elevation, [10] four-dimensional molecular dynamics, [11] meta dynamics [12, 13], multiple time-scale molecular dynamics [14, 15], transition path sampling [16–19] and advanced Monte Carlo and sampling algorithms. [20–24]

In this context, the Hybrid Monte Carlo (HMC) method has demonstrated a promising utility in condensed matter simulations. [25–28] HMC was originally developed in 1987 by Duane et al. as a groundbreaking approach for numerical simulations in lattice field theory (or within the realm of lattice quantum chromodynamics). [29] In principle, in HMC algorithm, the molecular dynamics technique is applied to guide a Monte Carlo move. As mentioned, HMC already found applications in chemistry with implementations based on existing molecular dynamics packages such as LAMMPS, [30] GROMACS, [31] and NAMD [32] with separate Monte Carlo modules. Alternatively, HMC is implemented for specific chemical applications for instance as part of the TriMem software [33] for efficient simulations of lipid membranes. Though these implementations hold value, they fall short of fully harnessing the potential of HMC algorithms. Consequently, we recognize the necessity for HMC implementations optimized for GPU machines, catering to various applications in the field of chemistry. Therefore, more examples of implementations and applications or case studies in chemistry are needed and with the present work we will make first steps towards this.

As our introductory model in the field of chemistry, we have opted to explore phase transitions in a noble gas like argon (Ar). Lennard-Jones potentials and simulations of noble gases hold fundamental significance in the advancement of theories and methodologies within the field of soft matter physics, and they have been extensively employed since the inception of computer simulations. [34] Lennard-Jones potentials and simulations of noble gases frequently serve as a standard for verifying simulation codes and assessing novel simulation techniques. Despite its uncomplicated nature, the Lennard-Jones model accurately portrays fluids of all kinds [35–38] and it is often applied for the investigation of phase transitions. Phase transitions are important in various fields such as earth and environmental science, [39, 40] biology, [41] material science [42, 43] and chemistry [44, 45].

For example, Bredow and coworkers explored the significance of phase transitions in catalytic reactions and heat storage materials, such as titanium pentoxide (Ti_3O_5). [42, 46] Their findings demonstrated that Ti_3O_5 can release stored energy when pressure is applied, transitioning from a high-energy λ polymorph to a lower-energy β polymorph. Phase transitions occur in both natural phenomena and technological processes when a substance is transformed from one state (solid, liquid, or gas) to another. Each substance has specific conditions of temperature and pressure at which these transitions occur. Importantly, these transitions are not merely reversible: for instance solidification (crystallization) is not simply the reverse of melting and liquids can be cooled below their freezing point without crystallizing.[47–50] Further, phase transitions still pose notorious problems for both traditional molecular dynamics simulations as well as traditional Monte Carlo simulations, which is why alternative approaches are needed. [25, 51] To understand the challenges arising from intrinsic modeling limitations, including sampling efficiency, force field parameters, system size, and the inherent complexity of experimental conditions during phase transitions (such as solidification), in this article, we investigate various systems.

The article is structured as follows: The subsequent section provides a comprehensive description of HMC theory and our specific implementation (section 2.1 and section 2.2). We then elaborate on the Lennard-Jones (LJ) potential used in our simulations (section 2.3) and provide simulation details (section 2.4). Following this, we present consistency checks that validate our HMC implementation (section 3.1). Finally, in the last section (3), we delve into the investigation of the LJ phase transition, specifically exploring considerations related to system size, void effects, and Lennard-Jones parameters by applying HMC simulations.

2 Method

2.1 Theory of Hybrid Monte Carlo

The Hybrid Monte Carlo (HMC) algorithm [29] represents a Markov chain Monte Carlo (MCMC) method. For the scope of this paper it is relevant that it provides a mean to sample from the distribution $\exp(-U(\{\vec{r}_i\}))$, where U is an inter-particle potential depending on the set of particle coordinates $s \equiv \{\vec{r}_i\}$. HMC generates a finite sample of such sets $s_k, k = 0, \ldots, N_t$ distributed according to the aforementioned distribution by introducing so-called canonical momenta $\vec{p}_i$ and an artificial Hamiltonian

$$H(\{\vec{p}_i\}, \{\vec{r}_i\}) \;=\; \sum_i \frac{1}{2}|\vec{p}_i|^2 \;+\; U(\{\vec{r}_i\})\,. \tag{1}$$

Starting with a set of coordinates $s_k, k = 0$, the algorithm consists of the repeated application of the following steps:

1. sample the canonical momenta from a standard normal distribution, i.e. $(\vec{p}_i)_j \sim \mathcal{N}_{0,1}$ for all i and $j \in \{0, 1, 2\}$.

2. integrate Hamilton's equations of motion in artificial time τ

   $$\frac{\mathrm{d}}{\mathrm{d}\tau}\vec{r}_i \;=\; \frac{\partial H}{\partial \vec{p}_i}\,, \qquad \frac{\mathrm{d}}{\mathrm{d}\tau}\vec{p}_i \;=\; -\frac{\partial H}{\partial r_i}\,,$$

   for all i using a reversible and area preserving numerical integration scheme with finite step-size $\Delta\tau$ up to trajectory length τ_0. Denote with s'_k the set of coordinates at the end of the trajectory.

3. set $s_{k+1} = s'_k$ with probability

   $$P_{\text{acc}} \;=\; \min\{1, \exp(-\Delta H)\}\,,$$

   where $\Delta H = H(s'_k) - H(s_k)$. Otherwise set $s_{k+1} = s_k$.

4. set $k = k + 1$ and start over.

If the equations of motion are integrated exactly, the Hamiltonian H is preserved and, therefore, all proposed sets of coordinates are accepted. With finite step-size $\Delta\tau$ this is no longer true in general, but the acceptance rate can be adjusted by adjusting the step-size accordingly. The accept/reject step is required to correct the errors introduced by the numerical integration of the equations of motion: the generated distribution does not depend on $\Delta\tau$ and HMC is exact.

There is a class of numerical integration schemes for which ΔH does not depend on the length of the trajectory τ_0, but only on the step-size $\Delta\tau$. They are called symplectic integration schemes, and the simplest one being also reversible is the well-known Leapfrog scheme. The Leapfrog is a semi-implicit integration scheme, consisting of the following three consecutive steps:

$$\begin{aligned} \vec{p}_i(\tau + \Delta\tau/2) &= \vec{p}_i(\tau) - \frac{\Delta\tau}{2}\frac{\partial U}{\partial \vec{r}_i}(\tau)\,, \\ \vec{r}_i(\tau + \Delta\tau) &= \vec{r}_i(\tau) + \Delta\tau\, \vec{p}_i(\tau + \Delta\tau/2)\,, \\ \vec{p}_i(\tau + \Delta\tau) &= \vec{p}_i(\tau + \Delta\tau/2) - \frac{\Delta\tau}{2}\frac{\partial U}{\partial \vec{r}_i}(\tau + \Delta\tau)\,. \end{aligned} \tag{2}$$

The Leapfrog is a second-order integration scheme, however, schemes of arbitrary order can be constructed [52, 53].

So far we have described the most basic version of HMC. There are generalizations and improvements available in the literature. Examples are the generalisation by Horowitz, [54] preconditioned multi-timescale HMC, [55] or Rieman manifold HMC. [56] One rather basic improvement we are going to discuss and apply in this paper is the usage of improved integration schemes. To be more specific, the so-called Second-order-Minimal-Norm (2MN) integration scheme [53] is constructed to minimize the norm of the residual integration error by means of an additional parameter λ for the price of two additional steps:

$$\begin{aligned}
\vec{p}_i(\tau+\lambda\Delta\tau) &= \vec{p}_i(\tau) - \lambda\Delta\tau\,\frac{\partial U}{\partial\vec{r}_i}(\tau)\,,\\
\vec{r}_i(\tau+\Delta\tau/2) &= \vec{r}_i(\tau) + \frac{\Delta\tau}{2}\,\vec{p}_i(\tau+\lambda\Delta\tau)\,,\\
\vec{p}_i(\tau+(1-\lambda)\Delta\tau) &= \vec{p}_i(\tau+\lambda\Delta\tau) - (1-2\lambda)\Delta\tau\,\frac{\partial U}{\partial\vec{r}_i}(\tau+\Delta\tau/2)\,,\\
\vec{r}_i(\tau+\Delta\tau) &= \vec{r}_i(\tau+\Delta\tau/2) + \frac{\Delta\tau}{2}\,\vec{p}_i(\tau+(1-\lambda)\Delta\tau)\,,\\
\vec{p}_i(\tau+\Delta\tau) &= \vec{p}_i(\tau+(1-\lambda)\Delta\tau) - \lambda\Delta\tau\,\frac{\partial U}{\partial\vec{r}_i}(\tau+\Delta\tau)\,.
\end{aligned} \tag{3}$$

The standard value for the additional parameter is $\lambda \approx 0.19$ [53], but it can be varied to improve the integrator performance for a specific problem. For $\lambda = 0.5$ the 2MN integrator is equivalent to the Leapfrog scheme.

The 2MN scheme can be further generalized to higher orders. In our code, we have also implemented a corresponding fourth-order scheme (OMF4) which has eleven steps in total and four parameters (see Eq. (71) of [53]).

2.2 Implementation

We have implemented HMC using the Kokkos C++ library [57–59], which provides abstractions for both efficient parallel execution of code and data management to write performance-portable applications. The usage of Kokkos, therefore, allows to write code that can be compiled for both CPU and GPU based architectures without modifications while delivering efficient executable code.

Our source code is designed in a modular way, with key components such as force and potential computation functions implemented using the strategy design pattern [60]. The code includes an interface class for particle types, with concrete classes tailored to specific particle instances, each housing distinct strategies.

A strategy, in this context, represents an implementation of the function responsible for computing either force or potential. The interface class delegates the computational workload to a linked strategy object, guided by runtime instructions from an input file. This flexible approach allows for the incorporation of multiple potentials, each with its own set of implementations.

At the current stage, the program supports different integration schemes for integration of the equations of motion, in particular the Leapfrog, 2MN, and OMF4 schemes. While the LJ potential and its corresponding force are currently the sole implementations, the structure of our source code facilitates the straightforward integration of additional potentials.

There are two strategies implemented for the computation of the LJ potential, an explicit computation of the all-to-all contribution to the force or the cell list method for neighbor tracking [2,61,62].

The code is designed to be executed either on a single GPU or a shared memory node. An MPI parallelization is left for future work. All relevant parameters of a particular run can be specified in an input file, which is read at the time of execution. Sets of coordinates $\{r_i\}$ can be read from as well as written to disk.

2.3 Potential used for simulations

The ongoing significance of noble gas and LJ simulations remains a focal point in recent research.[63–66] This interest extends beyond technical simplicity, as it involves noble gas single-atom nature devoid of intra-molecular structures, making noble gas and LJ simulations ideal for tests and benchmarks. [17,67–69] Moreover, the relevance of noble gas simulations, such as argon, in diverse physical contexts drives this interest.[35,70–72]

However, several challenges persist, particularly in formulating the potential and specifying simulation details and conditions. The significance of the potential in molecular simulations is akin to the importance of the simulation technique itself. In this section, we aim to address these critical aspects.

The accuracy of the molecular simulations is limited by the quality of the force field and intermolecular potentials. [73,74] Recently Fischer and Wendland shed light on the history of key intermolecular potentials such as Mie potentials [75], LJ potentials [76], Kihara potential, [77] numerically tabulated [78] and multi-parameter pair potentials [79,80] by Baker and coworkers. [81]

The Mie potential is a pairwise potential as the sum of a repulsive and an attractive part:

$$U(r) = \left(\frac{n}{n-m}\right)\left(\frac{n}{m}\right)^{\frac{m}{n-m}} \varepsilon \left[\left(\frac{\sigma}{r}\right)^{n} - \left(\frac{\sigma}{r}\right)^{m}\right] , \tag{4}$$

where r is the distance between two interacting particles, ε is the depth of the potential well and σ is the distance at which the particle-particle potential energy is zero (collision radius). The n parameter describes the character of repulsion and m describes the attraction. The widely recognized Lennard-Jones potential (12,6-potential) is a simple version of the Mie potential with $n = 12$ and $m = 6$:

$$U(r) = 4\varepsilon \left[\left(\frac{\sigma}{r} \right)^{12} - \left(\frac{\sigma}{r} \right)^{6} \right] . \tag{5}$$

From a technical standpoint, significant discussions revolve around the choice of the potential form, with some alternatives clearly outperforming the LJ potential. Despite this, recent force field design continues to rely on the LJ potential due to its widespread applicability and simplicity, making it an adaptable and easily implementable form for force fields of various materials.[82–84]

An alternative to determining the functional form involves employing an analytical potential function derived from either experimental data or quantum mechanical calculations. Preliminary examples of such potentials include the work of Dymond and Adler[78], as well as the development of multi-parameter pair potentials by Barker and colleagues.[79,80] Also, Huber and coworkers applied ab initio potentials for determining the argon and neon melting curve.[85,86] Furthermore, they explored many-body potential approaches as new functional forms to investigate neon across different states.[87] Their findings indicated that three-body interactions minimally affect the structure and associated thermodynamic properties. Subsequently, this topic was further explored in the literature by Anta et al.[88], Deiters and coworkers[89], Bukowski and Szalewiez,[90] Nasrabad et al.[91,92], Sadus and cowerkers,[93–95] Pahl et al.,[96] Deiters and Sadus,[97, 98]. Recently, Ströker et al. presented a more general approach for the noble gas argon using ab initio potentials for the two-body and non-additive three-body interactions where a single argon atom is one body.[71] Their results indicate that non-additive three-body interactions and quantum effects play a significant role in influencing thermodynamic properties, especially in the liquid and supercritical regions. Notably, near the vapor-liquid phase boundary, three-body interactions have the greatest influence, while at lower temperatures, accounting for quantum effects becomes crucial.

2.4 Simulations details

In this study, the Lennard-Jones (12-6) Potential is applied to calculate each intermolecular interaction in the simulation box for both, MD and HMC simulations. [99]

The simulations can be divided into two primary work packages. Initially, we conducted simulations to validate HMC. This involved selecting a system comprising 500 argon atoms at a temperature of 350 K, utilizing densities of 1744 and 20408 mol $\cdot\, m^{-3}$, as previously outlined in our publication. [100] Interactions between argon atoms were calculated using the LJ potential with

$$\varepsilon = 0.0104223321\,\mathrm{eV}\,, \quad \sigma = 3.40\,\text{Å}\,,$$

and with a cut-off distance of 8.5Å. The MD simulations conducted by LAMMPS [101] were performed in the canonical ensemble, maintaining the system temperature through the use of the Nosé–Hoover thermostat. [102, 103] All systems were equilibrated for $2 \cdot 10^6$ steps and followed by a production run for $2 \cdot 10^7$ steps with 0.5 fs timestep.

To investigate the solidification of argon, we employed a $5 \times 5 \times 5$ face-centered cubic (fcc) supercell. This supercell was constructed using the argon unit cell with a lattice size of 5.36Å. [104] Subsequently, we conducted HMC simulations at elevated temperatures to facilitate the generation of the liquid phase. This liquid phase was then used as the starting structure for each respective temperature in our subsequent investigations. For all simulations that serve to check consistency using MD simulations, the same initial geometry as in HMC simulations has been applied for solidification.

In the subsequent stage, our focus shifted towards studying the solidification of fluid-like argon via HMC simulations. Here, we investigated various factors—such as voids, system size effects, and temperature dependent LJ parameters—impacting the solidification process of fluid-like argon. For the void insertion and defects in order to investigate a possible vacancy formation during solidification, we randomly removed argon atoms from the supercell before generating the liquid phase (see table 1). In the case of HMC simulations, each trajectory runs for $1.1 \cdot 10^5$ sweeps for each temperature after $1 \cdot 10^5$ sweeps thermalizations. Within HMC simulations each trial trajectory corresponds to the equivalent of 20 steps of $5 \cdot 10^{-3}$ fs. Additionally, we conducted simulations with larger system sizes using a $10 \times 10 \times 10$ fcc

	N_{Ar}	L (Å)	T (K)
% void	pure crystal = 500 (5 × 5 × 5)		
0	500	26.80	90 − 250
5	475	26.80	50 − 150
10	450	26.80	30 − 150
15	425	26.80	30 − 150
20	400	26.80	30 − 150
	pure crystal = 4000 (10 × 10 × 10)		
0	4000	53.60	100 − 240
5	3800	53.60	50 − 150

Table 1: Simulation details for argon solidification. Please note the simulations were carried out in steps of 10 K.

supercell and introduced a 5% void in this system. HMC protocol remained consistent with the approach used for small system sizes. In all the simulations periodic boundary conditions were imposed in the XYZ directions.

Furthermore, we studied the LJ parameter modification effect on the solidification of argon. We used temperature dependent interaction parameters given by the following two equations:

$$\sigma = 3.672 - 22.30/T \,, \tag{6}$$

$$\varepsilon/k = 117.655 + 778.012/T \,, \tag{7}$$

where k is the Boltzmann constant and T the temperature. Al-Matar et al. suggested these temperature dependent LJ parameters as improvements in predicting the argon fluid and phase equilibria properties with MD and MC simulations. [105, 106] Note that HMC simulation methodology employed in this section remains consistent with the preceding part, with the sole exception of the LJ parameter, which exhibits temperature dependency.

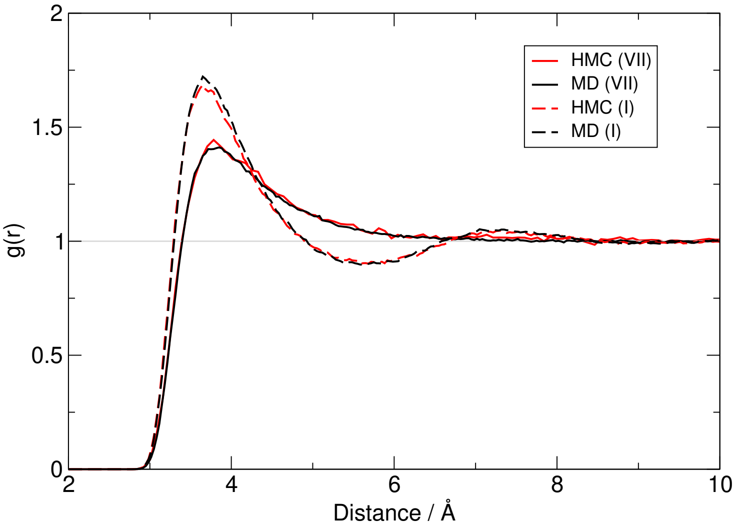

Figure 1: Radial distribution between argon atoms at two different densities from HMC (red) and MD (black) simulations. Please note, VII (solid line) and I (dashed line) are densities taken from Ref. [100]. VII: 1744 mol $\cdot$ m^{-3}; I: 20408 mol $\cdot$ m^{-3}.

3 Results and discussions

3.1 Comparing structure for MD and HMC

We conducted consistency checks to validate the accuracy of our HMC implementation. In Figure 1 we compared the structural properties of liquid argon using HMC simulations to those acquired from MD simulations. Figure 1 shows the radial distribution functions [**?**] (g(r)) for fluid-like systems of argon VII and I, adopted from Ref. [100], at densities of 1744 mol $\cdot$ m^{-3} and 20408 mol $\cdot$ m^{-3}, respectively. As expected, system I, with higher density, exhibited closer interparticle distances compared to system VII, which had lower densities. Both MD and HMC simulation results demonstrated very good agreement.

3.2 Solidification of fluid-like argon

Figure 2 presents a scheme illustrating the relationship between potential energy (shortened in the following to potential) and temperature. The distinct jump of the potential energy from **B** to **C** observed in the black curve in Figure 2 serves as a defining indicator for determining the phase transition point. The high potential energy values (see **A**) on the right side of the

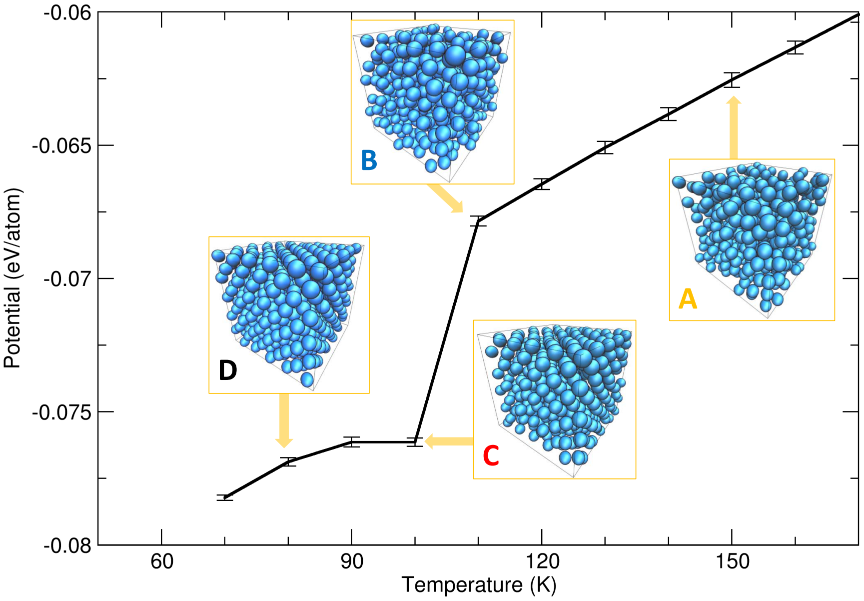

Figure 2: Defining phase states: A liquid, B liquid-like, C solid-like, D solid. Solidification simulation of 4000 argon atoms from HMC. Please note, the representations of the simulation boxes are for 500 argon atoms only to increase visibility.

graph correspond to the liquid phase, while the lower potential energy values (**D**) on the left side represent the solid phase. At point **B** in the black curve the onset of solidification is denoted, marking the transition from the liquid-like state to the solid-like state (point **C**). These defined states and the associated graph will be utilized further to compare MD and HMC methods. Additionally, their application will extend to examining the effects of voids, system size, and the T-dependent LJ parameters.

Figure 3 displays the potential versus the temperature for both the MD and HMC methods to investigate the solidification at two example systems: System A, comprising 500 atoms without voids, and system B, consisting of 475 atoms with a 5% void inclusion. While both simulation techniques exhibit a similar trend and show substantial agreement, it is notable that they do not demonstrate perfect alignment. For example, there is an offset between both methods and the transition region of the void-free simulation displays a plateau like behavior. In the system containing 5% voids (system B), the phase transition occurs within the temperature range of 110 K to 120 K for both MD and HMC methods. However, in

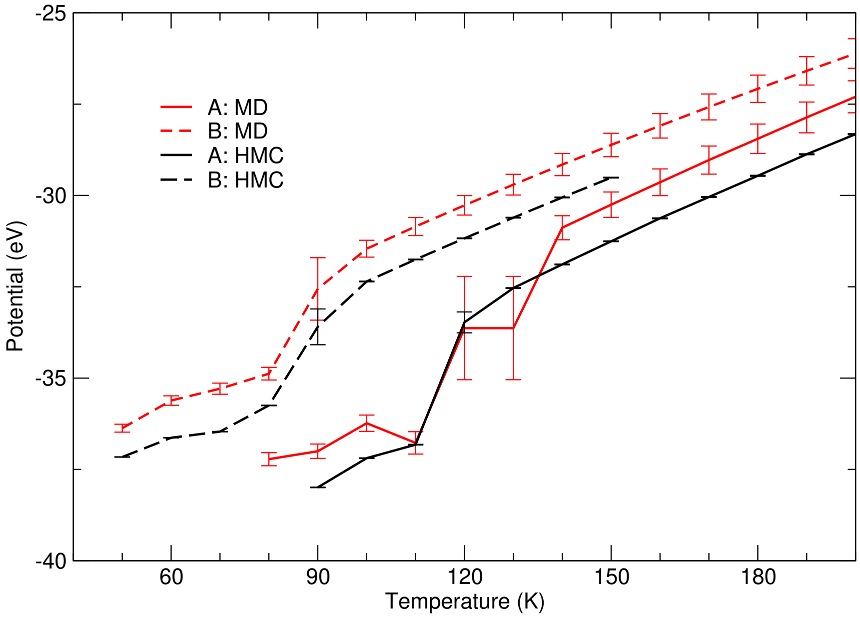

Figure 3: Comparison of solidification from HMC (black) and MD (red) for different systems. A (solid lines): 500 atoms no voids; B (dashed lines): 475 atoms including 5% voids.

system A without voids, the phase transition spans from 110 K to 120 K for HMC and from 110 K to 140 K for MD. Please note, overall the errors are larger for the MD simulations than for HMC simulations and in the transition region the MD errors are rather large. Therefore, it is impossible to assume a clear solidification trend for the MD simulation and we refrain from discussing the mentioned plateau in the transition region as shown by the MD simulation. It is worth noting that, as detailed in section 2.1, HMC method is exact and incorporates an accept/reject step, providing a mechanism to correct errors introduced by the numerical integration of the equations of motion. Another noteworthy observation is that the solidification temperature decreases with the introduction of voids into the system in agreement with the existing literature.[107, 108]

Next, HMC simulations are utilized to explore the impact of voids on the solidification by introducing random voids of 5%, 10%, 15%, and 20% into the system. Our results (see Figure 4 and Figure S1) show that with increased fraction of voids the onset temperature decreases which means less energy requirement. Notably, the solidification onset temperature reaches a plateau at larger void sizes (≈ 15%), potentially indicating favorable conditions for the solidification process. This behavior is in agreement with data from literature where the

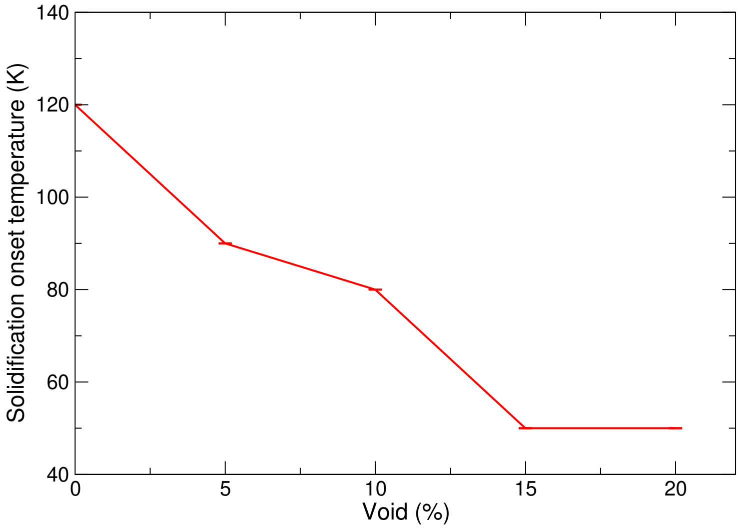

Figure 4: Plot depicting HMC simulated solidification onset temperature (K) against varying void percentages, the system with 500 atoms representing the void-free condition. Solidification curves are given in the SI.

authors studied the melting point of 1-palmitoyl-2-oleoyl-3-stearoyl-sn-glycerol and similar systems. [107]

Subsequently, we computed radial distribution functions (RDFs) [**?**] $g(r)$ and performed a cluster analysis[109] for all systems to elucidate the structural characteristics of each phase state (see Figure 5, 6 and Figure S2, S3). Four temperatures for each system are plotted with each line from higher to lower temperatures representing the liquid (**A**), liquid-like (**B**), solid-like (**C**), and solid (**D**) states. While at higher temperatures the RDFs do not drop to zero at the minima and display broad peaks as is usual for liquids, they show more structure, i.e., they decay to zero and exhibit more pronounced peaks, suggesting enhanced structural order of the solid as compared to the liquid state. The appearance of additional peaks in the RDFs signifies heightened order in the solid state. As anticipated, the RDFs corresponding to the solid-like state closely resemble those of the solid state, while those of the liquid-like state exhibit characteristics similar to the liquid state. [73] A comparison between systems A and B in Figure 5 reveals that the presence of voids leads to a better-ordered solid formation after solidification. Furthermore, a size effect is also visible when comparing system A to system C. We will come back to this below.

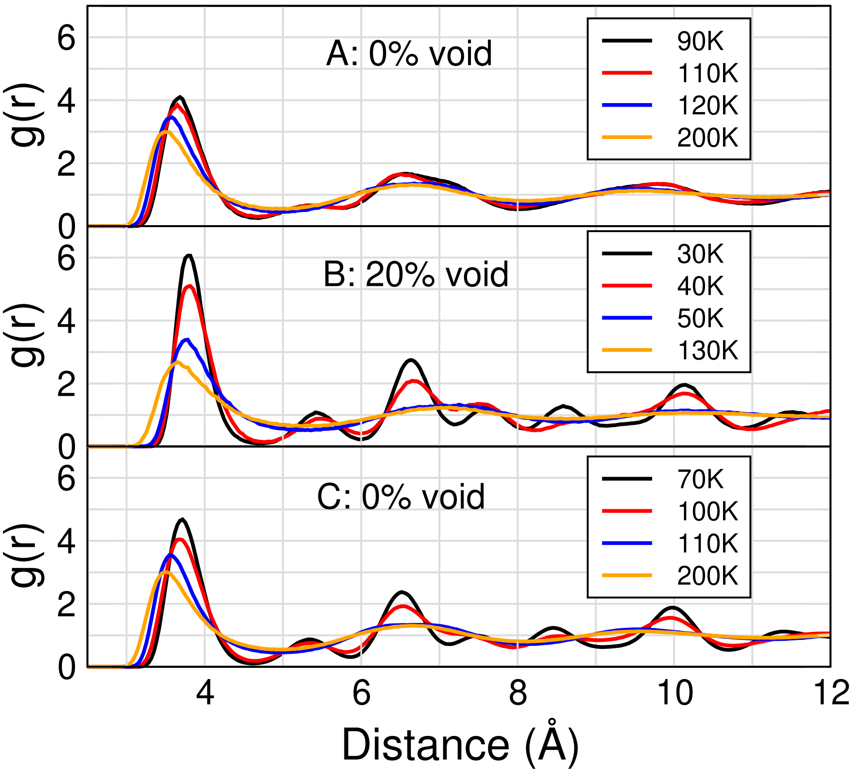

Figure 5: Comparison of radial distribution functions for systems: A: 500 atoms without voids, B: 400 atoms with 20% void, and C: 4000 atoms without voids.

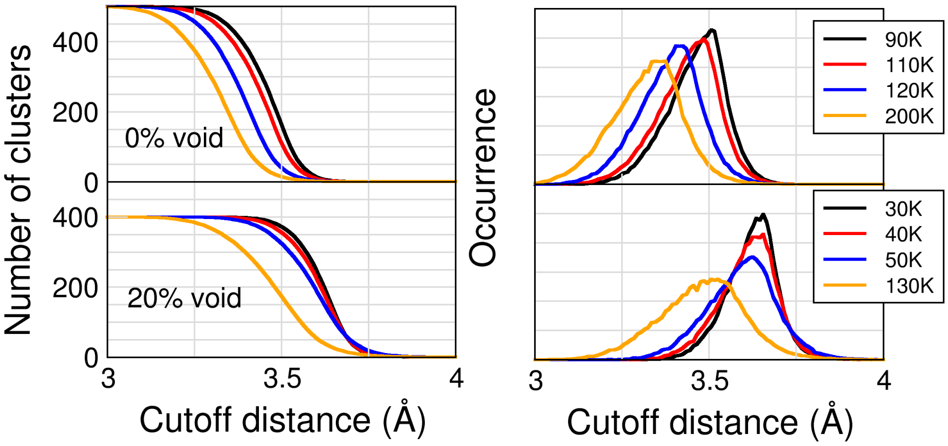

Figure 6: Cluster count (left) and cluster distance distribution functions (right) for 500 atoms without voids above and 400 atoms with 20% void below.

The radial distribution function observations, supported by the cluster analysis (see Figure 6), suggest that larger voids contribute to a better-structured solid, indicated by a narrower peak width in the black line. Moreover, increased void presence corresponds to expanded distances throughout the entire process. The increased void quantity results in larger distances and a noticeable shift in the number and occurrence of clusters towards higher cutoff distances. This potential expansion due to void presence might play a role in facilitating the solidification process. Significantly, these observations are consistent with the solidification onset temperature.

Moreover, as mentioned above the impact of system size on solidification is depicted in Figure 7. Larger systems exhibit a shift in the solidification point to lower temperatures, aligning more closely with literature findings. [110] The radial distribution functions for large system sizes (refer to Figure 5 and Figure S4) emphasize the importance of simulating larger systems. The comparison between graphs A and C in Figure 5 illustrates that larger systems display solid-state structures characterized by long-ranged positional correlations and distinctly identifiable local environments, aspects that are not captured in smaller system

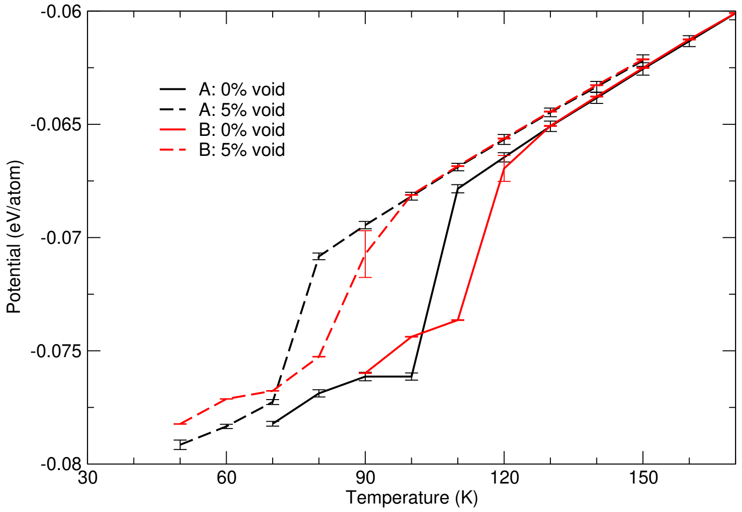

Figure 7: System size effects on the solidification from HMC simulations. A (black): Large systems with 4000 and 3800 (5% void) argon atoms (red); B: Small systems with 500 and 475 (5% voids) argon atoms.

sizes.

The temperature-dependent potential might not accurately represent the solidification process in smaller system sizes or within the temperature range used in our study (see Figure S5). However, in ref [105,106], the reported temperature-dependent LJ parameters for argon were employed in simulating 500 argon atoms across the temperature range of 100 to 800 K. The NPT ensemble was utilized to explore properties related to the liquid-vapor and fluid-like states.

4 Conclusions

We implemented the Hybrid Monte Carlo (HMC) method with the OMF4 integration scheme to allow the exploration of argon solidification. The implementation is based on the Kokkos C++ framework for efficient executable code on GPU and CPU based computer architectures. The validation of our HMC implementation involved comparing the structure of argon fluid-like phases obtained from HMC simulations with those calculated from MD simulations. Subsequently, the argon solidification process was simulated by starting from a higher temperature (liquid state) to a lower temperature (solid state). Both MD and HMC simulations demonstrate a similar trend for the solidification of argon fluid. However, notable differences between HMC and MD manifest in an offset between them and a different behavior in the transition region.

Comparing systems with and without voids showed that the solidification temperature decreased with the introduction of voids. The radial distribution functions indicated that at decreased temperature the solid state is reached by displaying the well known features of the solid compared to the liquid. In addition, it demonstrates that the presence and increasing size of voids contribute to a more well-structured solid. Furthermore, the cluster analysis shows that a larger amount of voids results in increased cluster distances throughout the entire process.

The comparison between very large and small system sizes revealed that achieving solidification satisfactorily is challenging with small system sizes. We observed a smooth solidification curve using 4000 particles that results in a transition at 105 K showing close agreement with findings from literature. This underscores the importance of employing larger system sizes in simulations for solidification processes. The simulations using the temperature-dependent potential did not yield improvements in our results. However, it is important to note that these simulations were so far limited to a small system size.

Future work will involve further implementation in HMC code, expanding its capabilities to explore a broader range of options and conditions, thereby delving into more complex chemical phenomena.

5 Supporting Information

Supplementary material are available online (https://doi.org/10.1515/znb-2023-0107) includes additional figures illustrating the impact of voids on solidification from HMC simulations (Figure S1), RDFs for systems with varying voids and system sizes (Figures S2 and S4), cluster count distribution and cluster distance distribution (Figures S3), along with the influence of temperature-dependent LJ parameters on argon solidification from HMC simulations (Figure S5).

Acknowledgements

This work is supported by the Deutsche Forschungsgemeinschaft (DFG, German Research Foundation) and the NSFC through the funds provided to the Sino-German Collaborative Research Center CRC 110 “Symmetries and the Emergence of Structure in QCD” (DFG Project-ID 196253076 - TRR 110, NSFC Grant No. 12070131001). This work is part of the preparation for the newly funded CRC 1639 NuMeriQS.

References

[1] Frenkel D., Smit B. *Understanding molecular simulation: from algorithms to applications*. Elsevier: Amsterdam 2023.

[2] Allen M. P., Tildesley D. J. *Computer simulation of liquids*. Oxford University Press: Oxford 2017.

[3] Ciccotti G., Dellago C., Ferrario M., Hernández E., Tuckerman M. *Eur. Phys. J. B* 2022, *95*, 1–10.

[4] Hsu W.-T., Piomponi V., Merz P. T., Bussi G., Shirts M. R. *J. Chem. Theory Comput.* 2023, *19*, 1805–1817.

[5] Hénin J., Lelièvre T., Shirts M. R., Valsson O., Delemotte L. *Living J.Comp.Mol.Sci.* 2022, *4*, 1583 (60 pages).

[6] Hassanali A. A., Cuny J., Verdolino V., Parrinello M. *Philos. Trans. R. Soc. A* 2014, *372*, 20120482 (32 papges).

[7] Di Pino S., Perez Sirkin Y. A., Morzan U. N., Sánchez V. M., Hassanali A., Scherlis D. A. *Angew. Chem., Int. Ed.* 2023, *62*, e202306526 (9 pages).

[8] Kao Y.-T., Guo X., Yang Y., Liu Z., Hassanali A., Song Q.-H., Wang L., Zhong D. *J. Phys. Chem. B* 2012, *116*, 9130–9140.

[9] Dreßler C., Kabbe G., Brehm M., Sebastiani D. *J. Chem. Phys.* 2020, *152*, 114114 (14 pages).

[10] Huber T., Torda A. E., van Gunsteren W. F. *J. Comput.-Aided Mol. Des.* 1994, *8*, 695–708.

[11] Beutler T. C., van Gunsteren W. F. *J. Chem. Phys.* 1994, *101*, 1417–1422.

[12] Barducci A., Bonomi M., Parrinello M. *Wiley Interdiscip. Rev. Comput. Mol. Sci.* 2011, *1*, 826–843.

[13] Bussi G., Laio A. *Nat. Rev. Phys.* 2020, *2*, 200–212.

[14] Tuckerman M., Berne B. J., Martyna G. J. *J. Chem. Phys.* 1992, *97*, 1990–2001.

[15] Abreu C. R., Tuckerman M. E. *Mol. Phys.* 2021, *119*, e1923848 (17 pages).

[16] Dellago C., Bolhuis P. G. Transition path sampling and other advanced simulation techniques for rare events. In *Advanced computer simulation approaches for soft matter sciences III*; Holm C., Kremer K., Eds. Springer: Berlin, Heidelberg, 2009; chapter 3, pp. 167–233.

[17] Bolhuis P. G., Swenson D. W. *Adv. Theory Simul.* 2021, *4*, 2000237 (14 pages).

[18] Mullen R. G., Shea J.-E., Peters B. *J. Chem. Theory Comput.* 2015, *11*, 2421–2428.

[19] Van Erp T. S., Moroni D., Bolhuis P. G. *J. Chem. Phys.* 2003, *118*, 7762–7774.

[20] Höllmer P., Maggs A. C., Krauth W. *J. Chem. Phys.* 2022, *156*, 084108 (9 pages).

[21] Haji-Akbari A. *J. Chem. Phys.* 2018, *149*, 072303 (12 pages).

[22] Husic B. E., Pande V. S. *J. Am. Chem. Soc.* 2018, *140*, 2386–2396.

[23] Bürgi R., Kollman P. A., van Gunsteren W. F. *Proteins: Struct., Funct., Bioinf.* 2002, *47*, 469–480.

[24] Griebel M., Zumbusch G., Knapek S. *Numerical Simulation in Molecular Dynamics, Numerics, Algorithms, Parallelization, Applications.* Springer-Verlag: Berlin, Heidelberg 2007.

[25] Prokhorenko S., Kalke K., Nahas Y., Bellaiche L. *npj Comput. Mater.* 2018, *4*, 80 (7 pages).

[26] Mehlig B., Heermann D., Forrest B. *Phys. Rev. B* 1992, *45*, 679–685.

[27] Tagawa T., Kaneko T., Miura S. *Mol. Simul.* 2017, *43*, 1291–1294.

[28] Krieg S., Luu T., Ostmeyer J., Papaphilippou P., Urbach C. *Comput. Phys. Commun.* 2019, *236*, 15–25.

[29] Duane S., Kennedy A. D., Pendleton B. J., Roweth D. *Phys. Lett. B* 1987, *195*, 216–222.

[30] Guo J., Haji-Akbari A., Palmer J. C. *J. Theor. Comput. Chem.* 2018, *17*, 1840002 (19 pages).

[31] Fernández-Pendás M., Escribano B., Radivojević T., Akhmatskaya E. *J. Mol. Model.* 2014, *20*, 1–10.

[32] Barhaghi M. S., Crawford B., Schwing G., Hardy D. J., Stone J. E., Schwiebert L., Potoff J., Tajkhorshid E. *J. Chem. Theory Comput.* 2022, *18*, 4983–4994.

[33] Siggel M., Kehl S., Reuter K., Köfinger J., Hummer G. *J. Chem. Phys.* 2022, *157*, 174801 (14 pages).

[34] Singh A. N., Dyre J. C., Pedersen U. R. *J. Chem. Phys.* 2021, *154*, 134501 (13 pages).

[35] Stephan S., Thol M., Vrabec J., Hasse H. *J. Chem. Inf. Model.* 2019, *59*, 4248–4265.

[36] Mick J., Hailat E., Russo V., Rushaidat K., Schwiebert L., Potoff J. *Comput. Phys. Commun.* 2013, *184*, 2662–2669.

[37] Rutkai G., Thol M., Span R., Vrabec J. *Mol. Phys.* 2017, *115*, 1104–1121.

[38] Chen B., Siepmann J. I., Klein M. L. *J. Phys. Chem. B* 2001, *105*, 9840–9848.

[39] Maruyama M., Takeya S., Yoneyama A., Ishikawa T., Misawa T., Nagayama S., Alavi S., Ohmura R. *Ind. Eng. Chem. Res.* 2023, *131*, 305–314.

[40] Alavi S., Ripmeester J. A. *Angew. Chem., Int. Ed.* 2007, *46*, 6102–6105.

[41] Lee C. F., Wurtz J. D. *J. Phys. D: Appl. Phys.* 2019, *52*, 023001 (21 pages).

[42] Juetten S., Bredow T. *J. Phys. Chem. C* 2022, *126*, 7809–7817.

[43] Von Domaros M., Liu Y., Butman J. L., Perlt E., Geiger F. M., Tobias D. J. *J. Phys. Chem. B* 2021, *125*, 3932–3941.

[44] Zheng C., Simpson R. E., Tang K., Ke Y., Nemati A., Zhang Q., Hu G., Lee C., Teng J., Yang J. K., Wu J., Qiu C.-W. *Chem. Rev.* 2022, *122*, 15450–15500.

[45] Joshi K., Paliwal U., Galav K., Trivedi D., Bredow T. *J. Solid State Chem.* 2013, *204*, 367–372.

[46] Stahl B., Bredow T. *ChemPhysChem* 2022, *23*, e202200131 (11 pages).

[47] Moura Ramos J. J., Diogo H. P. *J. Chem. Educ.* 2006, *83*, 1389–1392.

[48] Viciosa M. T., Correia N. T., Sánchez M. S., Gomez Ribelles J. L., Dionisio M. *J. Phys. Chem. B* 2009, *113*, 14196–14208.

[49] Mendoza-Coto A., Nicolao L., Díaz-Méndez R. *Sci. Rep.* 2019, *9*, 2020 (10 pages).

[50] Hwang H., Weitz D. A., Spaepen F. *Proc. Natl. Acad. Sci.* 2019, *116*, 1180–1184.

[51] Santiso E. E., Trout B. L. *J. Chem. Phys.* 2015, *143*, 174109 (9 pages).

[52] Yoshida H. *Phys. Lett. A* 1990, *150*, 262–268.

[53] Omelyan I., Mryglod I., Folk R. *Comput. Phys. Commun.* 2003, *151*, 272–314.

[54] Horowitz A. M. *Phys. Lett. B* 1991, *268*, 247–252.

[55] Urbach C., Jansen K., Shindler A., Wenger U. *Comput. Phys. Commun.* 2006, *174*, 87–98.

[56] Girolami M., Calderhead B. *J. R. Stat. Soc. B* 2011, *73*, 123–214.

[57] Trott C. R., Lebrun-Grandié D., Arndt D., Ciesko J., Dang V., Ellingwood N., Gayatri R., Harvey E., Hollman D. S., Ibanez D., Liber N., Madsen J., Miles J., Poliakoff D., Powell A., Rajamanickam S., Simberg M., Sunderland D., Turcksin B., Wilke J. *IEEE Transactions on Parallel and Distributed Systems* 2022, *33*, 805–817.

[58] Trott C., Berger-Vergiat L., Poliakoff D., Rajamanickam S., Lebrun-Grandie D., Madsen J., Al Awar N., Gligoric M., Shipman G., Womeldorff G. *Comput. Sci. Eng.* 2021, *23*, 10–18.

[59] Edwards H. C., Trott C. R., Sunderland D. *J. Parallel. Distrib. Comput.* 2014, *74*, 3202 – 3216.

[60] Gamma E., Helm R., Johnson R., Vlissides J. M. *Design Patterns: Elements of Reusable Object-Oriented Software.* Addison-Wesley Professional, Boston 1994.

[61] Quentrec B., Brot C. *J. Comput. Phys.* 1973, *13*, 430–432.

[62] Hockney R. W., Eastwood J. W. *Computer Simulation Using Particles.* Routledge, Oxfordshire 1981.

[63] Pruteanu C. G., Loveday J. S., Ackland G. J., Proctor J. E. *J. Phys. Chem. Lett.* 2022, *13*, 8284–8289.

[64] Losey J., Sadus R. J. *J. Phys. Chem. B* 2019, *123*, 8268–8273.

[65] Heyes D., Dini D., Pieprzyk S., Brańka A. *J. Chem. Phys.* 2023, *158*, 134502 (18 pages).

[66] Nayhouse M., Amlani A. M., Orkoulas G. *J. Chem. Phys.* 2011, *135*, 154103 (10 pages).

[67] Craven G. T., Lubbers N., Barros K., Tretiak S. *J. Chem. Phys.* 2020, *153*, 104502 (13 pages).

[68] Shanks B. L., Potoff J. J., Hoepfner M. P. *J. Phys. Chem. Lett.* 2022, *13*, 11512–11520.

[69] Madin O. C., Boothroyd S., Messerly R. A., Fass J., Chodera J. D., Shirts M. R. *J. Chem. Inf. Model.* 2022, *62*, 874–889.

[70] Chatwell R. S., Vrabec J. *J. Chem. Phys.* 2020, *152*, 094503 (9 pages).

[71] Ströker P., Hellmann R., Meier K. *Phys. Rev. E* 2022, *105*, 064129 (8 pages).

[72] de Gregorio R., Benet J., Katcho N. A., Blas F. J., MacDowell L. G. *J. Chem. Phys.* 2012, *136*, 104703 (12 pages).

[73] Huber H., Dyson A. J., Kirchner B. *Chem. Soc. Rev.* 1999, *28*, 121–133.

[74] van Gunsteren W. F., Daura X., Hansen N., Mark A. E., Oostenbrink C., Riniker S., Smith L. J. *Angew. Chem., Int. Ed.* 2018, *57*, 884–902.

[75] Mie G. *Ann. Phys.* 1903, *316*, 657–697.

[76] Lennard-Jones J. E. *Proc. Phys. Soc.* 1931, *43*, 461–482.

[77] Kihara T. *Rev. Mod. Phys.* 1953, *25*, 831–843.

[78] Dymond J., Alder B. *J. Chem. Phys.* 1969, *51*, 309–320.

[79] Barker J., Pompe A. *Aust. J. Chem.* 1968, *21*, 1683–1694.

[80] Barker J., Fisher R., Watts R. *Mol. Phys.* 1971, *21*, 657–673.

[81] Fischer J., Wendland M. *Fluid Phase Equilib.* 2023, *573*, 113876 (10 pages).

[82] Khabibrakhmanov A., Fedorov D. V., Tkatchenko A. *J. Chem. Theory Comput.* 2023, *19*, 7895–7907.

[83] Stephan S., Staubach J., Hasse H. *Fluid Phase Equilib.* 2020, *523*, 112772 (24 pages).

[84] Méndez-Bermúdez J. G., Guillén-Escamilla I., Méndez-Maldonado G. A., Alva-Tamayo J. A. D. *J. Phys. Commun.* 2022, *6*, 041002 (6 pages).

[85] Solca J., Dyson A. J., Steinebrunner G., Kirchner B., Huber H. *Chem. Phys.* 1997, *224*, 253–261.

[86] Solca J., Dyson A. J., Steinebrunner G., Kirchner B., Huber H. *J. Chem. Phys.* 1998, *108*, 4107–4111.

[87] Kirchner B., Ermakova E., Solca J., Huber H. *Chem. Eur. J.* 1998, *4*, 383–388.

[88] Anta J., Lomba E., Lombardero M. *Phys. Rev. E* 1997, *55*, 2707–2712.

[89] Leonhard K., Deiters U. *Mol. Phys.* 2000, *98*, 1603–1616.

[90] Bukowski R., Szalewicz K. *J. Chem. Phys.* 2001, *114*(21), 9518–9531.

[91] Eskandari Nasrabad A., Laghaei R., Deiters U. *J. Chem. Phys.* 2004, *121*, 6423–6434.

[92] Eskandari Nasrabad A., Laghaei R. *J. Chem. Phys.* 2006, *125*, 084510 (7 pages).

[93] Marcelli G., Sadus R. J. *J. Chem. Phys.* 2000, *112*, 6382–6385.

[94] Wang L., Sadus R. J. *Phys. Rev. E* 2006, *74*, 031203 (5 pages).

[95] Vlasiuk M., Sadus R. J. *J. Chem. Phys.* 2017, *146*, 244504 (9 pages).

[96] Pahl E., Calvo F., Koci L., Schwerdtfeger P. *Angew. Chem., Int. Ed* 2008, *47*, 8207–8210.

[97] Deiters U. K., Sadus R. J. *J. Chem. Phys.* 2019, *150*, 134504 (8 pages).

[98] Deiters U. K., Sadus R. J. *J. Phys. Chem. B* 2021, *125*, 8522–8531.

[99] Woon D. E., Dunning Jr T. H. *J. Chem. Phys.* 1994, *100*, 2975–2988.

[100] Pfleiderer T., Waldner I., Bertagnolli H., Tödheide K., Kirchner B., Huber H., Fischer H. E. *J. Chem. Phys.* 1999, *111*, 2641–2646.

[101] Thompson A. P., Aktulga H. M., Berger R., Bolintineanu D. S., Brown W. M., Crozier P. S., in't Veld P. J., Kohlmeyer A., Moore S. G., Nguyen T. D., others . *Comput. Phys. Commun.* 2022, *271*, 108171 (34 pages).

[102] Nosé S. *J. Chem. Phys.* 1984, *81*, 511–519.

[103] Hoover W. G. *Phys. Rev. A* 1985, *31*, 1695 (3 pages).

[104] Latimer K., Dwaraknath S., Mathew K., Winston D., Persson K. A. *npj Comput. Mater.* 2018, *4*, 40 (7 pages).

[105] Al-Matar A. K., Tobgy A. H., Suleiman I. A. *Mol Simul* 2008, *34*, 289–294.

[106] Al-Matar A. K., Tobgy A. H., Suleiman I. A., Al-Faiad M. A. *Int. J. Comput. Methods* 2015, *12*, 1550003 (14 pages).

[107] Cordina R. J., Smith B., Tuttle T. *J. Comput. Chem.* 2023, *44*, 1795–1801.

[108] Zhang H., Liu F., Yang Y., Sun D. *Sci. Rep.* 2017, *7*, 10241 (8 pages).

[109] Froömbgen T., Blasius J., Alizadeh V., Chaumont A., Brehm M., Kirchner B. *J. Chem. Inf. Model.* 2022, *62*, 5634–5644.

[110] Bocchetti V., Diep H. T. *J. Chem. Phys.* 2013, *138*, 104122 (6 pages).

Acknowledgements

I would like to thank many people without whom this thesis would not have been possible.

Foremost, I thank my dear husband, Sebastian Ehlert, for his patience and support. I thank my parents, Yaghoub and Khoshniyyat, my dear brother, Javad, my dear sister, Zahra, and their families, Anisa, Aynaz, Nazila, and Mehran for supporting me unconditionally over all the years.

I would like to thank my supervisor, Prof. Dr. Barbara Kirchner, for giving me the opportunity to join her research group and for offering scientific freedom and of course thank you for providing all the necessary infrastructure, computational resources, and financial support. Many thanks to Prof. Agilio Padua and Prof. Margarida Costa Gomes for providing guidance, support, and scientific collaborations. Furthermore, I thank Prof. Thomas Bredow for being my second reviewer of this thesis, Prof. Patrycja Kielb for being the head of my Ph.D. committee, and Dr. Gregor Hagelücken for completing my Ph.D. committee. I thank Prof. Ali Hassanali for his support and mentorship during my time in ICTP. Special thanks go to my mentors Prof. Paola Gori Giorgi and Prof. Saman Alavi for supporting me during times of uncertainty. I also like to thank Prof. Nicole Sänger and Dr. Seyed Reza Mosavi Aghdam for saving my life and providing me with hope and direction for the future. Thanks to Prof. Alain Chaumunt for exciting collaborations and inspiring scientific discussions. I want to thank further Kateryna Goloviznina, Mirella Simöes Santos, Jocasta Ávila, and many more friends from the Lyon lab for fruitful scientific collaboration and helpful discussions.

Thanks to all my colleagues and friends at the Mulliken center, especially Prof. Christoph Bannwarth, Katharina Bauerfeind, Jan Blasius, Martin Brehm, Kai Buchmüller, Leo Dick, Eva von Domaros (Perlt), Wenbo Dong, Katrin Drysch, Roman Elfgen, Lars Esser, Tom Frömbgen, Jost Heise, Prof. Oldamur Hollóczki, Johannes Ingenmey, Jeroen Koopman, Claudia Kronz, Joachim Laun, Sarah Löffelsender Roberto Maccieraldo, Friedrich Malberg, Gwydyon Marchelli, Jens Mekelburger, Anna Müller, Hagen Neugebauer, Werner Rekien, Anna Ulpe, Luke Wylie and Paul Zaby.

Special thanks to Prof. Saman Alavi, Sebastian Ehlert, and Johannes Ingenmey for proofreading this thesis and providing feedback and suggestions. Many thanks to my friends Somayeh Faraji, Neda Gayumi Negad, and Farzaneh Alizadeh. I am deeply grateful to my friends, ‘a big Iranian community,’ whose companionship made moments away from home and family joyful and helped me endure hard times.

Finally, I want to express my appreciation to all those who, despite making my life challenging and at times seemingly unbearable, have unknowingly contributed to the development of a stronger and more resilient version of myself. Thank you.